UNIVERSITY OF SOUTHAMPTON

Faculty of Engineering and the Environment
Institute of Sound and Vibration Research

DEVELOPMENT OF A TWO-FREQUENCY TECHNIQUE FOR GAS-BUBBLES SIZING IN MARINE SEDIMENT

by

Agni Mantouka

Thesis submitted for the degree of Doctor of Philosophy

November 2010

UNIVERSITY OF SOUTHAMPTON

ABSTRACT

FACULTY OF ENGINEERING AND THE ENVIRONMENT

Institute of Sound and Vibration Research

Doctor of Philosophy

'DEVELOPMENT OF A TWO-FREQUENCY TECHNIQUE FOR GAS-BUBBLES SIZING IN MARINE SEDIMENT'

by
Agni Mantouka

The aim of this research is to develop an acoustic method to estimate the size distribution of spherical or near-spherical gas bubbles in intertidal sediments. For this purpose, a new inversion method was developed which employs two frequencies. This method is based on monitoring the scattered spectral components, which are generated from nonlinear bubble pulsations under acoustic excitation. Independent transmission acoustic measurements along a hydrophone array were undertaken and inverted following the well-established method of inferring bubble populations from transmission measurements. The first, i.e. the two-frequency, inversion method is able to detect and measure only 'acoustically spherical' bubbles (i.e. bubbles, which can be modelled as monopole sources), whereas the latter inversion method (which will be called the transmission method) assumes that all attenuation originates from 'acoustically spherical' bubbles. Hence, comparison of the two bubble population estimates can be employed to assess the acoustical effects of the non-spherical gas occlusions. *In situ* data were taken at two different intertidal sites of the South coast of England. The first one is a closed muddy region with high organic content and low sand content. The second one has a dynamic environment and the sediment is muddy, with higher sand content and low organic content.

Pre-requisite for the application of the new bubble sizing method is knowledge of the nonlinear bubble response in sediments under acoustic excitation. Current models for bubbles in sediments are limited to the linear regime. A new model suitable for both linear and nonlinear pulsations of bubbles has been developed. The model requires as input

parameters properties of the gas-free water saturated sediment. These unknown parameters were estimated using both laboratory measurements and values found in the literature for similar types of marine sediment.

Water tank tests were carried out to test the performance of the devices and to crosscheck the method against the two-frequency method of inversion of attenuation data, i.e. the transmission method. The experimental conditions in water guaranteed the near-sphericity of the bubbles present. As such, the transmission data provide unambiguous information on the bubble population of the bubbly water. Therefore, good agreement between the two methods proves the ability of the two-frequency method to predict the bubble size distributions. Both set-ups were deployed in the field and the data were inverted in the same manner as the water tank data. The computed bubble distributions showed rather good agreement for the first site, which was a strong indication that most of the gas at the site exists in spherical form. At the second site, a poorer agreement was observed which suggests that only a proportion of the gas has spherical form. These observations are limited to sizes resonant at the frequencies used for the experimental fieldwork, i.e. small gas pockets equal to or at maximum ten times bigger than the size of the grains. The results of this study suggest that using the two-frequency technique, estimation of the size distribution of the 'acoustically spherical' bubbles is possible for the gas situated a few centimetres below seafloor. However the implementation of the two-frequency technique is not sufficient to draw conclusions on the acoustical effects of the gas in non-spherical form. That is, parallel use of the transmission method is needed in order to draw conclusion on the gas phase present in the sediment.

Contents

List of Figures

List of Tables

List of Roman symbols

A_D	bubble gas polytropic coefficient according to Devin (1959)
A_0	amplitude of the DC term resulting from bubble insonification using a series expansion in amplitude and phase representation.
A_{ω_1}	amplitude of the harmonic at ω_1 resulting from bubble insonification using a series expansion in amplitude and phase representation.
A_{ω_2}	amplitude of the harmonic at ω_2 resulting from bubble insonification using a series expansion in amplitude and phase representation.
$A_{2\omega_1}$	amplitude of the harmonic at $2\omega_1$ resulting from bubble insonification using a series expansion in amplitude and phase representation.
$A_{2\omega_2}$	amplitude of the harmonic at $2\omega_2$ resulting from bubble insonification using a series expansion in amplitude and phase representation.
$A_{\omega-}$	amplitude of the harmonic at $\omega_1 - \omega_2$ resulting from bubble insonification using a series expansion in amplitude and phase representation.
$A_{\omega+}$	amplitude of the harmonic at $\omega_1 + \omega_2$ resulting from bubble insonification using a series expansion in amplitude and phase representation.
a	attenuation coefficient (np/m)
a_P	attenuation of compressional waves (dB/m)
a_S	attenuation of shear waves (dB/m)
b_{vis}	bubble viscous damping term
C	ancillary parameter used in Biot equations
C_p	specific heat capacity of gas within bubble at constant pressure
c_0	time invariant speed of sound
c_∞	sound speed in a pure liquid at infinite distance from the bubble centre
c_p	compressional wave velocity
c_{P+}	Biot fast compressional wave
c_{P-}	Biot slow compressional wave
c_s	shear wave velocity

c_w	wave velocity in water
D	ancillary parameter used in Biot equations
D_g	thermal diffusivity of gas
d_m	diameter of mineral grains
$d\Pi_s$	differential scattered power
e	Neper number
F	viscodynamic operator entering Biot equations
f	temporal frequency or form function
f_i	imaging frequency
f_p	pump frequency
G_s	real part of shear modulus of elastic solid or water-saturated sediment
G_s'	imaginary part of shear modulus of elastic solid or water-saturated sediment
G_s^*	complex shear modulus of elastic solid or water-saturated sediment
I_s	scattered intensity
I_i	incident intensity of a plane wave
$I(\omega)$	integrated beam pattern
K_g	thermal conductivity of gas
K_s	bulk modulus of solid or water-saturated sediment
K_m	bulk modulus of mineral grains
K_w	bulk modulus of water
K_f	bulk modulus of sediment drained frame
K_S	constant of proportionality for shear waves (dB/m/kHz)
K_P	constant of proportionality for compressional waves (dB/m/kHz)
$\boldsymbol{k}$	wave vector
k	wave number
k_b	wavenumber of bubbly water or bubbly sediment
$\boldsymbol{k}_0$	wave vector at incident direction
l_D	thermal diffusion length
L_s^*	(complex) first Lamé constant of a solid or sediment

$L_s^{'}$	imaginary part of the first Lamé constant of a solid or sediment
L_s	real part of first Lamé constant of a solid or sediment
n	an integer or number of independent observations
N	number of bubbles per unit volume
N_b	number density of bubbles
n_b	bubble distribution as number of bubbles per micron bin per cubic metre as a continuous function
$\mathbf{n_b}$	bubble distribution as number of bubbles per micron bin per cubic metre in discreet form as a vector
$\hat{\mathbf{n}}_\mathbf{b}$	bubble distribution estimate as number of bubbles per micron bin per cubic metre in discreet form as a vector
p	dimensionless exponential attenuation parameter for compressional waves
s	dimensionless exponential attenuation parameter for shear waves
M	ancillary parameter used in Biot equations
Ma	Mach number
m	an integer
m_{eff}	effective mass term representing the mass displaced by a pulsating bubble in a fluid or solid
O	order of magnitude
$P(t)$	time-varying acoustic pressure
$P_{1,2}$	acoustic pressure amplitudes zero-to-peak of acoustic waves insonifying a bubble
$p(\mathbf{r},t)$	the excess acoustic pressure about the ambient pressure as a function of position and time
$\tilde{p}(\mathbf{r},\omega)$	the excess acoustic pressure about the ambient pressure as a function of position and frequency content
p_b	pressure emitted by single bubble in space-time domain
$\tilde{p}_b$	pressure emitted by single bubble in space-frequency domain
$\tilde{p}_{s\,tot}$	total scattered pressure from an ensemble of particles or bubbles in space-time domain
P_i	pressure amplitude of an incident acoustic wave in space-frequency representation

p_σ	pressure of surface tension
p_s	scattered pressure from particle or bubble smaller than the wavelength in space-time domain
$\tilde{p}_s$	scattered pressure from particle smaller than the wavelength or bubble in space-frequency domain
p_0	bubble ambient liquid pressure
p_g	instantaneous gas pressure in a bubble
p_{g0}	equilibrium gas pressure in a bubble
p_{L}	the liquid pressure at bubble wall
p_{v}	vapour pressure
p_∞	pressure at infinity
Q	Q-factor
Q_{P}	Q-factor of compressional wave
Q_{S}	Q-factor of shear waves
$R(t)$	time-dependant bubble radius
R_0	bubble radius at equilibrium
R_ε	time dependant displacement of bubble radius from the equilibrium such that $R(t) = R_0 + R_{\varepsilon}(t)$
$R_{\varepsilon 0}$	radial displacement amplitude of wall of spherical bubble
$R_{\omega 1}$	time dependant radial displacement of a wall of a spherical bubble from equilibrium at the first pump frequency
$R_{\omega 2}$	time dependant radial displacement of a wall of a spherical bubble from equilibrium at the second pump frequency
$\lvert R_{\omega_1}\rvert, \lvert R_{2\omega_1}\rvert$	amplitude of radius harmonic components, response to the first drive pressure
$\lvert R_{\omega 2}\rvert, \lvert R_{2\omega_2}\rvert$	amplitude of radius harmonic components, response to the second drive pressure
R_-	bubble radius spectral component at the difference frequency $\omega_1 - \omega_2$
$\lvert R_-\rvert$	amplitude of bubble radius spectral component at the difference frequency $\omega_1 - \omega_2$

R_+	bubble radius spectral component at the sum frequency $\omega_1 + \omega_2$
$\lvert R_+ \rvert$	amplitude of radius harmonic component at the sum frequency $\omega_1 + \omega_2$
R_{s0}	the unstrained equilibrium bubble radius for a bubble in an elastic solid
$\boldsymbol{r}$	radial vector
r	radial distance in a spherical coordinate system
r_∞	radial distance at infinite
Sc	Scaling factor for inversions
std	standard error
s_{eff}	effective stiffness of a bubble undergoing linear pulsations in a fluid medium
T	Temperature
T_∞	temperature at infinity
T_{rr}	radial stress tensor
t	time
t'	retarded time
u	instantaneous bubble wall radial velocity
V_g	volume of the bubble gas
V_s	total volume of the sediment
V_w	volume of water in sediment
x	dimensionless radius variation
X	parameter entering the expression of thermal damping

List of Greek symbols

A	ancillary parameter used in Biot equations
B	ancillary parameter used in Biot equations
Γ	ancillary parameter used in Biot equations
α	radius of a spherical volume containing an ensemble of scatterers
α_{τ}	tortuosity factor
α_{p}	pore size parameter
β	regularization parameter
β_{el}	elastic damping constant
β_{rad}	radiation damping constant; 1st order approximation
β_{HK_int}	interfacial damping constant
β_{P_ther}	thermal damping constant according to Prosperetti (1977) analysis
β_{vis}	viscous damping constant
β_{HK_tot}	total damping constant obtained by linearization of the HK equation for elastic solids or sediments
β_{HK_v}	viscous damping constant obtained by linearization of the HK equation
β_{HK_rad}	radiation damping constant obtained by linearization of the HK equation
β_{tot}	total damping constant, the sum of : β_{vis} , β_{rad} and β_{th}
γ	the ratio of specific heat capacity of gas at constant pressure to that at constant volume
δ_{v}	viscous damping parameter
δ	logarithmic decrement
η	dynamic (shear) viscosity of fluid
η_{w}	viscosity of water
η_{P_ther}	effective thermal viscosity according to Prosperetti (1997) analysis
η_{rad}	effective radiation viscosity
η_{s}	shear viscosity of elastic solid or sediment
Θ	change in temperature of gas from equilibrium temperature
θ	ancillary parameter used in small amplitude derivations

ϑ	angle between the incident and the scattered wave vector
ζ	frequency dependant parameter used in Biot theory
K_g	thermal conductivity of gas
κ	polytropic index of bubble gas
κ_P	polytropic index of bubble gas according to Prosperetti (1977)
ξ	sediment porosity
P	Rayleigh probability distribution
$\overline{\rho}$	dynamic density (defined in Biot theory)
ρ_0	fluid density at equilibrium
ρ_g	gas density
ρ_∞	fluid density at infinity
ρ_s	bulk density of the water-saturated sediment or elastic solid medium
ρ_m	mineral density
ρ_w	water density
σ	surface tension
σ_s	total scattering cross section of a bubble
σ_{ds}	differential scattering cross section of a bubble
σ_{ds-}	differential scattering cross section of a bubble for the difference frequency
$\sigma_{ds\ 2\omega_p}$	differential scattering cross section of a bubble for twice the pump frequency
$\boldsymbol{\sigma}_{i\text{-}p}$	matrix containing differential cross sections at difference-frequency
$\boldsymbol{\sigma}_{2p}$	matrix containing differential cross sections at twice the pump frequency
$\boldsymbol{\sigma}_p$	matrix containing differential cross sections at the pump frequency
$\boldsymbol{\tau}$	vector difference of wave vectors
τ	magnitude of the vectorial difference of two wave vectors is space domain description
υ	mode of the Rayleigh probability distribution
Φ	complex function entering the expression of thermal damping when follows the analysis of Prosperetti (1977)
ϕ	phi unit

$\phi_{\omega 1}$ phase of the radius harmonic component at ω_1 resulting from bubble insonification using a series expansion in amplitude and phase representation.

$\phi_{\omega 2}$ phase of the radius harmonic component at ω_2 resulting from bubble insonification using a series expansion in amplitude and phase representation.

$\phi_{2\omega 1}$ phase of the radius harmonic component at $2\omega_1$ resulting from bubble insonification using a series expansion in amplitude and phase representation.

$\phi_{2\omega 2}$ phase of the radius harmonic component at $2\omega_2$ resulting from bubble insonification using a series expansion in amplitude and phase representation.

ϕ_- phase of the radius harmonic component at difference frequency $\omega_1 - \omega_2$ resulting from bubble insonification using a series expansion in amplitude and phase representation.

ϕ_+ phase of the radius harmonic component at $\omega_1 + \omega_2$ resulting from bubble insonification using a series expansion in amplitude and phase representation.

ϕ_K kinetic energy of an oscillator system (specifically of the fluid around a freely pulsating bubble)

ϕ_P potential energy of an oscillator (specifically of the gas in a freely pulsating bubble)

φ phase of insonification wave

ψ phase of combinations of radius harmonic components

Ω solid angle

ω circular frequency

ω_1 circular frequency of first pump wave

ω_2 circular frequency of second pump wave

ω_{p} circular frequency at the pump frequency

$\omega_{2\mathrm{p}}$ circular frequency at twice the pump frequency

ω_- circular frequency of a difference-frequency wave

ω_0 resonance circular frequency of a bubble in a fluid as derived from linearization of the Rayleigh-Plesset equation

ω_{P0} resonance circular frequency of a bubble in a fluid incorporating a complex polytropic index according to the work of Prosperetti (1977)

$\omega_{0\mathrm{s}}$ resonance circular frequency of a bubble in an elastic solid or sediment

ω_{0sP} resonance circular frequency of a bubble in an elastic solid or sediment with the polytropic gas index according to Prosperetti (1977) analysis

ω_{AH} resonance circular frequency of a bubble in sediment according to Anderson and Hampton (1980 a, b)

ω_{HK_s} resonance circular frequency of a bubble in an elastic solid or sediment derived from a Herring-Keller like bubble dynamics equation for media which posses shear.

Υ auxiliary variable in Gassmann equations

X parameter entering the expression of thermal damping

$\wp$ grain shape factor related to tortuosity

Academic Thesis: Declaration Of Authorship

I, Agni Mantouka declare that this thesis and the work presented in it are my own and has been generated by me as the result of my own original research.

DEVELOPMENT OF A TWO-FREQUENCY TECHNIQUE FOR GAS-BUBBLES SIZING IN MARINE SEDIMENT

I confirm that:

1. This work was done wholly or mainly while in candidature for a research degree at this University;

2. Where any part of this thesis has previously been submitted for a degree or any other qualification at this University or any other institution, this has been clearly stated;

3. Where I have consulted the published work of others, this is always clearly attributed;

4. Where I have quoted from the work of others, the source is always given. With the exception of such quotations, this thesis is entirely my own work;

5. I have acknowledged all main sources of help;

6. Where the thesis is based on work done by myself jointly with others, I have made clear exactly what was done by others and what I have contributed myself;

7. Parts of this work have been published as:

Leighton, T. G., Mantouka, A., White, P., and Klusek, Z. (**2008**). "Towards field measurements of populations of methane gas bubbles in marine sediment: An inversion method required for interpreting two-frequency insonification data from sediment containing gas bubbles," Hydroacoustics **11**, 203-224.

Mantouka, A., Leighton, T.G., Best, A.I., Dix, J.K. and White, P.R. (**2009**) "Inferring bubble populations in intertidal sediments from attenuation and scattering measurements," In, Papadakis, J.S. and Bjorno, L. (eds.) Proceedings of the 3rd International Conference on Underwater Acoustic Measurements, Technologies and Results. Third International Conference on Underwater Acoustic Measurements, Technologies and Results Heraklion, Greece, Institute of Applied & Computational Mathematics (IACM), 733-738

Signed: ……
Date: ……

Acknowledgments

This work was carried out as part of a project supported by the Engineering and Physical Science Research Council project (Grant number EP/D000580/1, principal investigator: T. G. Leighton) and I express my gratitude for their funding. My appreciation is also addressed to Institute of Sound and Vibration Research (ISVR) for its Rayleigh Scholarship.

I am indebted to my PhD supervisors, Professor Tim Leighton and Professor Paul White for their support throughout this study. I am also grateful to Dr. Angus Best and Dr. Justin Dix for numerous instances of help and advice on marine sediments and experimental work. I would like to acknowledge the computational input and the experimental work of Dr. Gary Robb and Dr. Paul Fox who participated in the EPSRC project. I am also grateful to Mr. Hugh Dumbrell for providing MATLAB code to solve the Herring-Keller equation and Mr. Paul Doust for support with electronic equipment accompanying sources and receivers for our experiments. I would also like to thank Maureen Mew for proof reading this thesis and Sue Brindle for their secretarial support. Finally, I would like to thank Professor Phil Joseph, Professor Victor Humphrey, Dr Chris Powles and my fellow students for many useful discussions throughout the study.

CHAPTER 1: INTRODUCTION

Gas is a common occurrence in deep sea as well as in organic-rich, muddy sediments of coastal waters and shallow seas (Judd and Hovland, 1992). The depths and horizontal distributions of these gas-charged sediments are usually detected from seismic profiling. Gas in sediments produces excessive reverberation of sound, rendering areas with gas-bearing sediments acoustically impenetrable, a phenomenon called 'acoustic turbidity'. Other terms encountered in seismic terminology to indicate gas-charged sediments are: acoustic masking or blanking, bright spots, wipeouts and pulldowns. Acoustic turbidity makes gas-bearing sediments 'visible' on seismic systems such as echo sounders, high frequency profilers, and side scan sonars, which can map gassy areas (Backus, 1959). For this reason, acoustic turbidity is the most frequently evidence used to infer the presence of gas (Judd and Hovland, 1992, Thießen *et al*., 2006), which is abundant in the top layers of marine sediments (Fleischer *et al.,* 2001).

Current acoustic systems are effective in gas detection (Wever *et al*., 1998) but not in quantification of the gas present or providing shape information of the gas voids in the sediment. Recent scientific research suggests that it is possible to relate the acoustic transmission measurements with bubble sizes (Best *et al.,* 2004; Leighton and Robb, 2008). However to date there is no acoustic method able to give information about the gas shape without supporting CT scanning images. Both the shape and size of the gas voids are important because they influence the sediment loading capacity and stability. The present study aims towards the development of an acoustic system able to both detect and quantify the gas present in marine sediments.

1.1 Gasses in marine sediments

The presence of gas in marine sediments plays an important role in characterising the geotechnical properties of the sea bottom and assessing geohazards for offshore structures (Geyer, 1983). *In situ* gas generation may have a pronounced effect on sediment stability as well as environmental consequences. As mentioned by Judd *et al.* (2002) in geological environments, such as deep-water basins, continental margins and polar slopes, methane

can be mediated from methane hydrates [1] , which are widespread in water depths greater than a few hundred metres. In these environments, an increase in temperature or a decrease in pressure will cause hydrate to dissociate and release methane as a gas, weakening the sediment by removing hydrate, which is a cementing agent, and, in sediments of low permeability, by raising fluid pressure. This makes the sediment prone to the formation of submarine slumps and, in the case of an oil platform, weakens the foundations. Additionally, part of this methane can find various pathways to escape through natural gas seeps and be released in the atmosphere, thereby presenting a possible issue for global climate change consideration (Judd *et al.*, 2002). However, it is not only the gas in the deep sea but also the shallow marine gas that has profound scientific, engineering and environmental significance. Fleischer *et al.* (2001) and Judd and Hovland (1992) estimate that methane from shallow water emissions accounts for up to 20 % of the total atmospheric emissions. The previously mentioned references are just a few examples, which demonstrate importance of quantifying the gas present in marine sediments. Estimations of gas (mainly methane) and gas hydrate concentrations in marine sediments is a topic of current research and as mentioned by Milkov (2003) these concentrations change over the time.

The most common gas encountered in marine sediments is methane, which is considered to originate mainly from one of two sources: the microbial degradation of organic matter in shallow sediments, or the thermocatalytic breakdown of complex organic molecules as part of the petroleum-generating processes occurring deep within sedimentary basins (Judd, 2004). Other sources include atmospheric air entrainment for shallow sediments and submarine volcanoes, which are connected with deep geological faults for deep sediments (Judd *et al.*, 2002).

In shallow marine sediments, which are of interest in this study, the gases that may be encountered are: oxygen (O_2) carbon dioxide (CO_2), nitrogen (N_2), ammonia (NH_3), hydrogen sulphide (H_2S) and methane (CH_4). Their production is mainly controlled by biogeochemical processes associated with the bacterial remineralisation of labile [2] organic matter (Mechalas, 1974) and (Claypool and Kaplan, 1974). The process of organic matter

[1] methane hydrate is a solid, ice-like, clathrate of water and methane

[2] liable to change, unstable

remineralisation depends on the available oxidant that yields the greatest free energy and determines the dominant process at a particular horizon (Claypool and Kaplan, 1974). If O_2 is present, aerobic decomposition is the major reaction to occur. Upon depletion of dissolved O_2, organic matter degradation shifts to nitrate reduction. Once nitrate is fully utilized, metal oxides (MnO_2 and Fe_2O_3) serve as oxidants. When metal oxides are no longer available, organic matter remineralisation proceeds through sulphate (SO_4^{2-}) reduction. In this zone sulphate-reducing bacteria produce black smelly sediment rich in H_2S. Hydrogen sulphide is highly corrosive and will react quickly with minerals to form iron sulphides, thus its presence indicates freshly deposited organic matter as mentioned on page 2 of Kaplan (1974). Below the sulphate reduction zone methanogenic bacteria continue the process of organic material decomposition resulting in methane production which occurs after the sulfate has been exhausted (Martens and Berner, 1974). Investigations have shown (for example Martens *et al.*, 1998) that in organically rich environments the aerobic zone extends 1-2 cm below the sea floor and the sulfate reduction zone extends to depths of 50 cm to 1 m. Below the depth of 1 m methanogenic bacteria dominate.

The preceding discussion reveals that each gas-production zone reflects a certain type of ecological system, because each type of gas is linked with the presence of a different type of microbe. A simplified typical division of the upper few metres of a shallow organic-rich sedimentary environment is shown in Figure 1.1 (Claypool and Kaplan, 1974). Although in the top sediment layer more than one gas may exist, the dominant ones are oxygen and aerobic respiration products in the aerobic zone, sulphate (and sulfur compounds) in the sulphate-reducing zone and methane in the carbonate reducing zone, as shown in Figure 1.1 and discussed in Claypool and Kaplan (1974). Nitrogen is not considered as a major gas in these zones. As mentioned by Martens *et al.* (1998) and discussed by Reeburgh (1983), nitrate reduction is thought to be a minor oxidant for organic carbon owing to its low concentration in overlaying water.

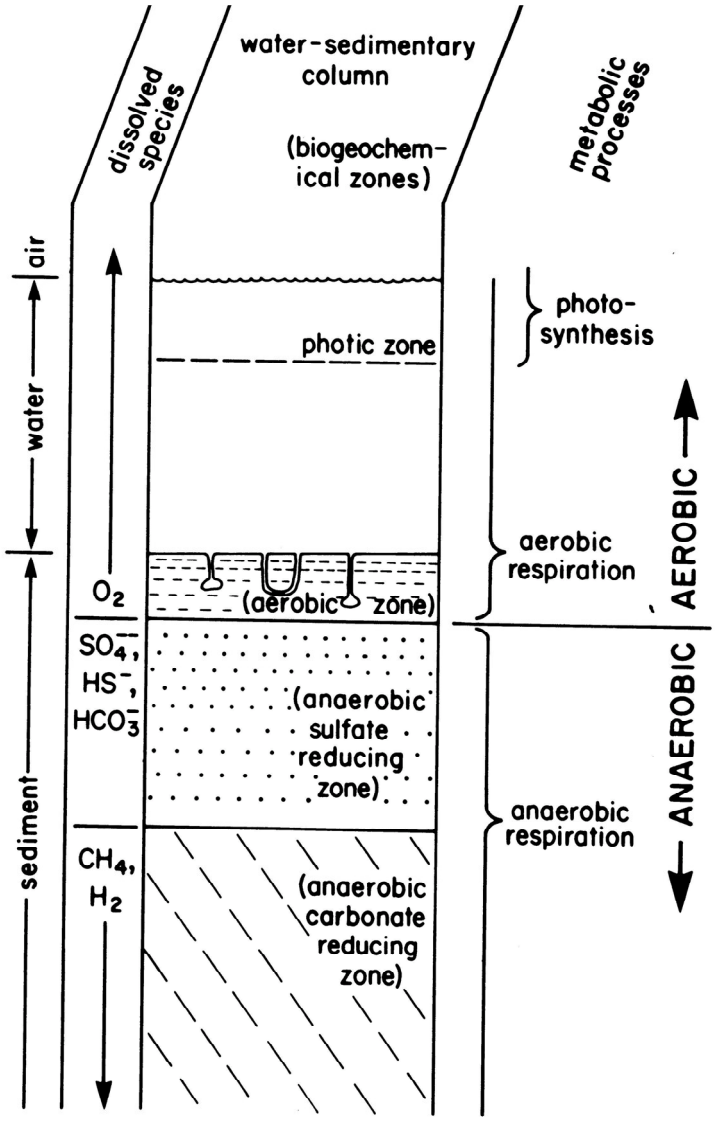

Figure 1.1: An idealised diagrammatic cross-section of a typical sediment/water column showing the major biogeochemical zones and the corresponding compounds present (Claypool and Kaplan, 1974).

1.2 The shape of gas in marine sediments

As discussed in the previous paragraph, most gas in the shallow seafloor results from biochemical processes. Gas concentrations dissolve initially in the pore water. The maximum gas concentrations that can be dissolved in the pore water are controlled by the pressure, temperature, and salinity conditions (Wever et al, 1998, Abegg and Anderson, 1997, Thießen et al., 2006). When the saturation levels are exceeded the gas forms a

distinct phase (the gas phase) in the sediment. Gas occurs in a variety of forms, ranging from near-spherical bubbles to coin- and slab-like gas inclusions (Abegg and Anderson, 1997; Anderson et al., 1998).

According to Anderson *et al*. (1998), bubbly sediments can be separated into three types which are depicted in Figure 1.2. The first type is the interstitial bubbles, in which the gas bubble size is smaller than the interstitial spaces of the sediment skeletal frame. Such bubbles may either float in the pore water or adhere to walls of a pore space. The second type is the gas reservoir, where the sediment framework remains essentially unaltered by the free gas. This type of bubbles has sizes greater than the pore space. The third type, the sediment displacing bubble, in which the sediment framework is deformed actually, displaced by the bubble. This type of bubble is larger than the type I bubbles and, as mentioned in Anderson *et al.* (1998), this is the most commonly observed type of bubble. The three types of bubbles according to Anderson *et al*. (1990) assume a spherical bubble shape. However, gas investigations in muddy sediments showed that gas is found in form of cracks and prolate spheroids. For example, results from *in situ* CT scan in Ekkernförde Bay in Germany (Lyons *et al*., 1996; Tang, 1996) showed that in muddy sediments bubbles tend to be non-spherical, filling fractures in the sediment like a coin standing on its edge.

Another study by Best *et al*. (2004) supported the evidence that gas voids in muds can form cracks or fissures in the sediment. In addition, previous investigations of cores taken from Chesapeake Bay, which is characterised by the presence of fine grain sediments, revealed the presence of both spherical cavities and fissures (Schubel, 1974). The phenomenon of presence of cracks is explained partially by the brittle fractural behaviour of cohesive sediments. The independent study of Boudreau (2005) explains in more detail the growth of bubbles in mud by fracture and the formation of prolate spheroids. Also it was observed that gas bubble non-sphericity increases with the bubble size in investigations with X-ray CT scanning; the smallest detectable size of the scan was 0.5 mm. Sizes greater than a millimetre are involved in studies of Boudreau (2005) as well as in the work of Best *et al*., (2004). Hence questions on very small (i.e. order of micron) bubbles are left unresolved.

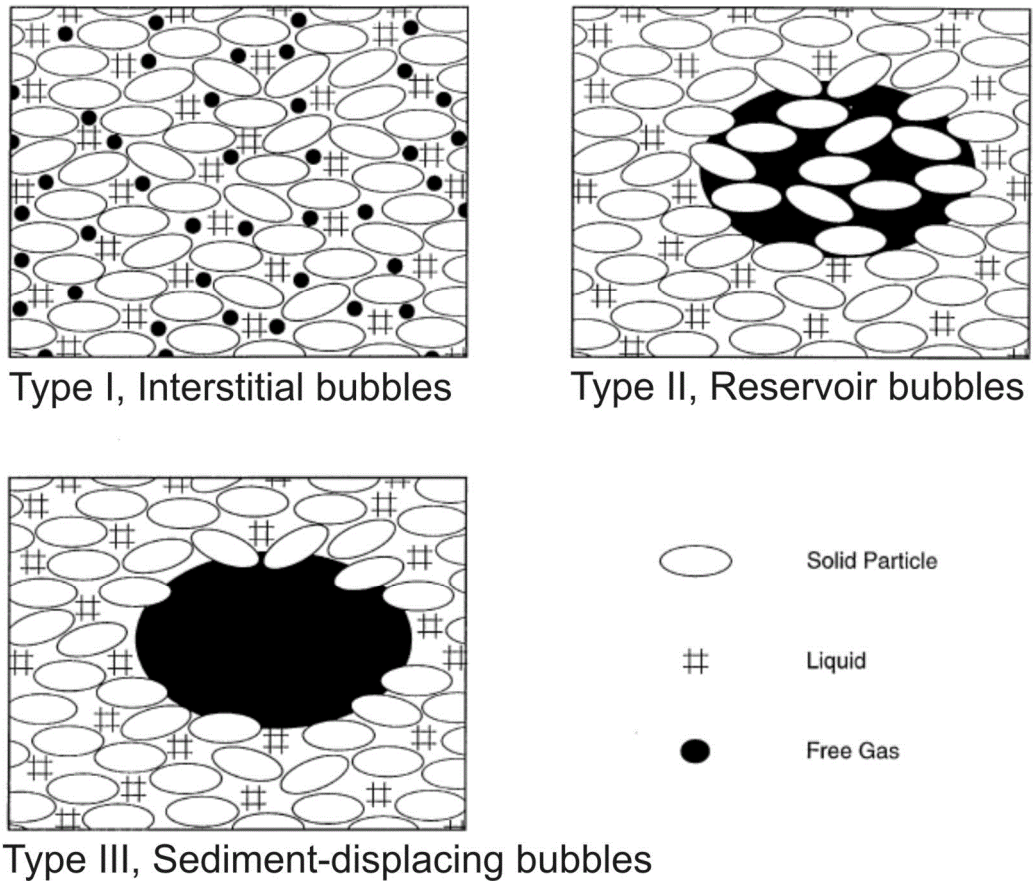

Figure 1.2: The characterisation by Anderson et al. (1998) of bubbles in gassy sediments, into three types. Type I bubbles ("interstitial bubbles"), are necessarily small, and may be free-floating or adhering to one or more solid particles, or stabilized within a crevice within a particle. In type II ("reservoir bubbles"), the gas pockets displace liquid but do not significantly affect the distribution of the solid particles. In type III ("sediment-displacing bubbles") the gas pockets displace both liquid and sediment, with a bubble wall formed from material which is substantially similar to the bulk sediment. Reproduced from Anderson et al. (1998)

1.3 Bubble sizing techniques and their application to sediments

Acoustic bubble sizing techniques are based on resonance properties of bubbles. Spherical and near- spherical shapes (i.e. ellipsoid with low ellipticity[3] ratio), insonified with acoustic wavelengths larger than their size, have the potential to strongly resonate (more details follow in sections 5.3 and 7.1). Such bubbles will be termed 'acoustically spherical'

[3] ellipticity is defined as the ratio of the major to minor axis of revolution of a spheroid.

in this thesis, to distinguish from the 'geometrically spherical' bubbles, which conform to a perfect sphere. In this work, making use of the resonance property, it is attempted to estimate the size distribution of the gas portion, which is contained within such 'acoustically spherical' bubbles and which therefore behave as a monopole source using acoustic measurements. The thesis will also attempt to estimate the attenuation caused by entities other than 'acoustically spherical' gas bubbles (such entities include gas cracks, flora and fauna). This is linked to the assumption of the commonest technique (i.e. the inversion of propagation data) for producing oceanic bubble size distributions. This technique would connect acoustic attenuation to 'acoustically spherical' bubbles in order to produce bubble size distributions ignoring the fact that attenuation in sediments can be caused by many other factors.

Typically acoustic bubble sizing techniques employ resonance characteristics of bubbles which pulsate under insonification. These are classified in two broad categories. The first one employs transmission measurements (i.e. measurements of speed and attenuation of sound waves propagating through a bubbly medium) whilst the second one uses (back) scattering measurements to infer the bubble size distributions (Clay, 1977). Commonly, the first type of bubble sizing techniques involves single frequency bubble insonification and linear approximation of the bubble pulsations as found in Medwin (1977), Commander and Prosperetti (1989), Duraiswami *et al*. (1998) and Terrill and Melville, (2000). An exception is the nonlinear propagation method developed by Leighton *et al*. (2004). Bubble size distributions inferred from (back) scattering measurements may involve single or dual insonification of the bubbles. Such single frequency scattering bubble sizing methods are encountered as either linear (Vagle and Farmer, 1992) or as nonlinear (Miller, 1981). Dual frequency scattering methods are mostly described as nonlinear methods because a pressure component which is generated from the nonlinear interaction of the bubbles with the two insonifying waves is used to estimate the bubble sizes. Examples of works using such a nonlinear method are: Koller *et al*., (1992), Phelps and Leighton, (1998) and Sutin *et al*., (1998).

The above mentioned acoustic techniques have been developed to measure air bubble distributions in sea water or applied for biomedical purposes. Efforts have been made to apply similar linear (Anderson and Hampton, 1980 a, b) and nonlinear (Boyle and Chotiros, 1998) techniques to sediments. However, the transition from water to sediments

is not straightforward because water is a homogenous medium and does not possess shear strength like sediments. In some cases, as will be discussed in chapter 7, the interpretation of measurement data is based on a rather *ad hoc* modification of bubble natural frequency and damping to accommodate the shear effects. In practice, it is possible to apply this ad hoc approach successfully for linear bubble sizing techniques only. During this PhD study, a nonlinear technique was developed for bubble sizing in sediments. For this purpose a new model for bubble pulsations in sediments was developed which can be used for interpretation of linear as well as nonlinear acoustic measurements.

1.4 Aims, objectives and novelty of the thesis

The aim of the work described in this thesis is the development of an acoustic bubble sizing technique that can be used to predict the size distribution of the gas the form of spherical or near-spherical bubbles in shallow marine sediments. This acoustic technique uses the characteristics of nonlinear resonances of bubbles under two frequency insonification. Since in marine sediments the bubble shape, which controls the characteristics of resonant bubbles, is not known, the validity of the technique was first tested in bubbly water before application to intertidal marine sediments. To achieve the aim, three fundamental objectives are addressed. The first is to understand current bubble dynamics models for water and sediments. The second objective is to establish the theory and procedures for the new bubble sizing technique and compare the results with a well-established bubble sizing technique in water. Having checked for the validity of the new technique in water; its application to marine sediments is straightforward. However study of current bubble models for sediments reveals the necessity to develop a suitable bubble dynamics model for sediments and in particular for muddy sediments which were studied here. The third objective of this thesis is related to the development of a new nonlinear bubble dynamics model for muddy sediments. To develop such a model the geoacoustic properties of sediments had to be studied and well understood.

1.5 Thesis structure

This report presents models, methods and experimental results for bubble sizing in water and gassy sediments. Chapter 2 is devoted to bubble models suitable for fluid media. Initially chapter 2 discusses two basic bubble equations: the Rayleigh and Rayleigh-Plesset. In this chapter analytical and numerical solutions of these equations are compared to conclude on the applicability of each type of solution in fluids. Then higher order models are studied that encompass more rigorously the physics of media with shear properties and have the potential to be applied in sediments. Chapter 3 discusses a new bubble model, which can be applied to linear and nonlinear scattering from bubbles in sediments. Chapter 4 clarifies the concept of coherent and incoherent scattering, which is essential for the modelling of the response of an ensemble of bubbles to acoustic waves as well as for the inversion. In this chapter the theory for the forward and the inverse incoherent scattering problem is formulated. These formulations will be used in chapter 5, where the nonlinear two-frequency bubble sizing technique is described together with experimental and theoretical results. In the same chapter, inversion results of this two-frequency technique are compared to independent inversion results of a linear inversion method, the so-called transmission method. This is done in water, where all bubbles in the generated population are acoustically spherical, to validate the acoustic techniques. Since both the two-frequency technique and the transmission technique give the same bubble population predictions, the validity of the first one is assured. Chapter 6 gives background information about geoacoustic properties of gas-free sediments. Current models for gas-free sediments are studied and compared with measurement results found in the literature. This chapter is focused on shallow non-gassy marine sediments. Chapter 7 presents propagation and scattering measurements in intertidal muddy sediments. Datasets from both kinds of measurements are inverted in order to estimate the size distribution of the acoustically spherical bubbles and conclude on the gas shape of these environments. Conclusions and recommendations for future work addressed in chapter 8.

CHAPTER 2: BUBBLE MODELS FOR FLUID MEDIA

In this chapter, bubble dynamics equations are studied. The study is focused on the bubble response under two frequency insonification and the appearance of the nonlinearly generated spectral components. The study pays attention to the generation of the difference-frequency component by gas bubbles insonified in water. This nonlinear spectral component is one of the nonlinear components, which will be used for the bubble sizing technique developed here. For the type of insonification under consideration, existing analytical solutions have limited applicability. Initially bubble equations of the Rayleigh-Plesset family are studied and the possibility of using analytical solutions in order to solve these equations is explored. Then higher order bubble models are studied and compared with a Rayleigh-Plesset- like equation. All models discussed in this chapter describe bubble pulsations in media that cannot carry shear forces. However they form the basis for the development of bubble models for media that do possess shear strength and, in particular, the sediments that are of interest in this work.

2.1 The Rayleigh and Rayleigh-Plesset equations

2.1.1 Theory

The first nonlinear bubble dynamics equation was derived by Lord Rayleigh while studying the creaking noise produced by a kettle just before boiling. This equation is thoroughly discussed in chapter 3 of Leighton (1994) and here only some of the basic principles are mentioned.

Consider a gas bubble with initial radius R_0 filled with an ideal gas of pressure p_g in an infinite incompressible liquid medium. The liquid medium has an equilibrium density ρ_0 and pressure p_0 near the bubble wall (Figure 2.2) whereas these properties at infinity are ρ_∞ and p_∞ respectively.

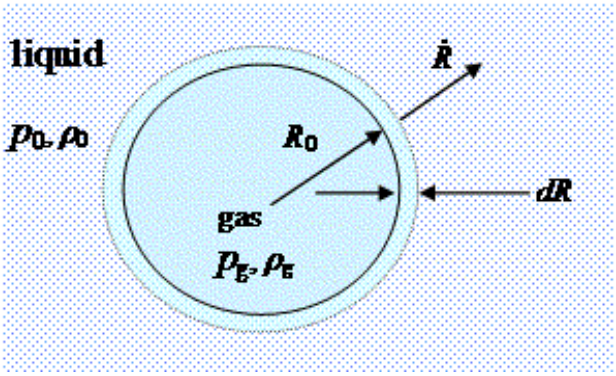

Figure 2.1: A bubble of radius R_0 containing a gas of density ρ_g at a pressure p_g. The bubble wall has expanded by dR and has acquired a velocity $\dot{R}$. The bubble is surrounded by a liquid with equilibrium density ρ_0 and pressure p_0.

Assuming that the bubble wall has acquired a velocity $\dot{R}$ by expanding by dR, then, from the conservation of mass the instantaneous velocity u at radial distance r from the centre of the bubble is given by (Leighton, 1994):

$$u = \frac{R^2}{r^2}\dot{R}. \tag{2.1}$$

Throughout this document, the dots above variables denote time derivatives. Strictly speaking the material derivative should be used in (2.1) but here it is assumed that the convective terms are negligible. A small perturbation of the equilibrium state of the system air cavity-liquid will cause the liquid surrounding the bubble to acquire kinetic energy ϕ_K, which can be expressed as:

$$\phi_K = \int_R^\infty 4\pi\rho_0 r^2 \dot{r}^2 dr \Rightarrow \phi_K = 2\pi\rho_0 R^3 \dot{R}^2. \tag{2.2}$$

The bubble is assumed to remain spherical at all times and the density of the liquid at infinity equal to the equilibrium density of the liquid, i.e. $\rho_\infty \simeq \rho_0$. Under these assumptions the corresponding change of the gas potential energy, ϕ_P is:

$$\phi_P = -\int_{V_o}^{V(R)} p_g dV = -\int_{R_o}^{R} p_g 4\pi r^2 dr. \tag{2.3}$$

Equating (2.2) and (2.3) the original Rayleigh equation is obtained:

$$R\ddot{R}+\frac{3}{2}\dot{R}^2=\frac{1}{\rho_0}\left(p_{\mathrm{g}}-p_0\right). \tag{2.4}$$

In fact the pressure entering in equation (2.3) is the pressure at the bubble wall p_{L} and not of the gas itself (p_g) but under the conditions of this derivation (i.e. ignoring surface tension and vapour pressure of the gas) these two pressures coincide, i.e. $p_{\mathrm{L}} \simeq p_{\mathrm{g}}$. Also the pressure p_0 is actually the pressure at infinity p_∞, the later being equal to the sum of the bubble ambient pressure plus an external acoustic pressure $P(t)$, if present:

$$p_\infty = p_0 + P(t) \tag{2.5}$$

Thus equation (2.4) takes the form:

$$R\ddot{R}+\frac{3}{2}\dot{R}^2=\frac{1}{\rho_0}\left(p_{\mathrm{L}}-p_0-P(t)\right) \tag{2.6}$$

Equation (2.6) is only of theoretical interest because it does not include any form of dissipation and for this reason will not be considered further. Since Rayleigh's derivation various extensions and modifications of the original equation have being made in order to take into account additional physical effects; most notably the effect of dissipation. Such a bubble dynamics equation is the Rayleigh-Plesset-Noltingk-Neppiras-Poritsky (RPNNP) equation. This equation takes into account the pressure due to the liquid surface tension p_σ and the vapour pressure p_{v}. Considering these, the pressure in the liquid at the bubble wall equals:

$$p_{\mathrm{L}} = p_{\mathrm{g}} - p_\sigma + p_{\mathrm{v}}. \tag{2.7}$$

Assuming that the gas in the bubble follows a polytrophic gas law, the pressure in the gas changes as:

$$p_{\mathrm{g}} = p_{\mathrm{g0}} \left(\frac{R_0}{R} \right)^{3\kappa}. \tag{2.8}$$

where κ is the polytropic index of the gas and p_{g0} is the gas pressure at equilibrium:

$$p_{\mathrm{g0}} = p_0 + \frac{2\sigma}{R_0} - p_{\mathrm{v}}. \tag{2.9}$$

Substitution of equations (2.9), (2.8) and (2.7) in (2.5) and addition of the viscosity effects at the bubble liquid boundary leads to the Rayleigh-Plesset equation in the following form:

$$\rho_0 R\ddot{R} + \frac{3}{2}\rho_0 \dot{R}^2 = \left(p_0 + \frac{2\sigma}{R_0} - p_{\mathrm{v}} \right) \left(\frac{R_0}{R} \right)^{3\kappa} + p_{\mathrm{v}} - \frac{2\sigma}{R} - \frac{4\eta\dot{R}}{R} - p_0 - P(t), \tag{2.10}$$

where σ is the surface tension at the bubble boundary and η the shear viscosity. The polytropic index κ equals γ if the bubble gas expands and contracts adiabatically. The Rayleigh-Plesset equation (2.10) is referenced throughout this document as the RP equation. This equation assumes that:

1) the liquid surrounding the bubble is fluid (cannot sustain shear forces) and infinite in extent
2) the gas is ideal and follows the polytrophic gas law: PV^{κ} = constant;
3) the temperature and pressure have uniform spatial distribution within the bubble;
4) the ambient (hydrostatic) pressure, surface tension and vapour pressure are constant;
5) the bubble carries out zero order oscillations;
6) no mass or heat transfer between the two phases takes place;
7) the viscous forces are the only source of energy dissipation and act only on the bubble boundary;
8) the liquid is incompressible.

The RP equation has limited practical application for the modelling of air bubbles in water. This is because, firstly, thermal effects are neglected and, secondly, the liquid is assumed to be incompressible (i.e. no radiation losses), having a time-invariant density ρ_0 which is greater than the density of the gas in the bubble. The lack of thermal damping is a source

of small or large errors, depending on the bubble size and ambient conditions. The second assumption is valid only so long as the velocity of the bubble wall is very much smaller than the sound speed, i.e. the acoustic Mach number of the bubble wall is much less than unity, i.e.:

$$Ma = \dot{R}/c_0 << 1, \tag{2.11}$$

where c_0 is the speed of sound in a bubble-free liquid under linear conditions. However this equation demonstrates many physical characteristics of pulsating bubbles and it is a good starting point for the formulation of analytical solutions as is discussed in the following section.

2.1.2 Analytical and numerical solutions

Analytical solutions for the Rayleigh-Plesset equation were first found for single frequency insonification (Miller, 1981) and later for dual frequency insonification (Newhouse and Shankar, 1984). These solutions were found by the method of asymptotic expansion with the following change of variables:

$$R(t) = R_0(1+x), \tag{2.12}$$

where the dimensionless variable x (x<<1) is the sum of the harmonics which are assumed present in the steady state pulsations of the bubble. According the works of Miller (1981) and (Newhouse and Shankar, 1984) the perturbation of the bubble wall in response to the driving field is approximated by an asymptotic series expansion in amplitude and phase representation. The expression (2.12) can be seen as:

$$R = R_0 + R_\varepsilon(t), \tag{2.13}$$

where $R_\varepsilon(t)$ is the displacement of bubble radius from the equilibrium. Equating the right sides of equation (2.12) and (2.13) the equivalence of the two representations is obtained in time domain:

$$R_\varepsilon(t) = R_0 x(t). \tag{2.14}$$

Approximating x with a finite number of terms is equivalent to assuming a certain spectrum in the frequency response of the bubble. The spectrum of the radius displacement

$R_\varepsilon(t)$, denoted in the subsequent text as R_ω, is readily obtained by multiplying the corresponding spectral components of $x(t)$ by R_0. This spectrum is also equal to the frequency spectrum of $R(t)$ if the term R_0 is added to the DC component of the spectrum of $R_\varepsilon(t)$. Consequently, the amplitude spectrum of the radius response, denoted as $|R_\omega(t)|$, which as it will be shown in Chapter 4 is of main interest in this work, is obtained by multiplication of the amplitude spectrum, x with R_0.

To obtain first order non-linear solutions for single frequency insonification, following the notation of Miller (1981), the dimensionless variable x is set equal to:

$$x = A_0 + A_{\omega_1}\cos(\omega_1 t + \phi_{\omega_1}) + A_{2\omega_1}\cos(\omega_2 t + \phi_{2\omega_1}). \tag{2.15}$$

For two frequency insonification, according to the work of Newhouse and Shankar (1984), the dimensionless variable x has the following terms:

$$\begin{aligned} x = {} & A_0 + A_{\omega_1}\cos(\omega_1 t + \phi_{\omega_1}) + A_{2\omega_1}\cos(\omega_2 t + \phi_{2\omega_1}) \\ & + A_{\omega_2}\cos(2\omega_1 t + \phi_{\omega_2}) + A_{2\omega_2}\cos(2\omega_2 t + \phi_{2\omega_2}) \\ & + A_{\omega_+}\cos((\omega_1+\omega_2)t + \phi_+) + A_{\omega_-}\cos((\omega_1-\omega_2)t + \phi_-) \end{aligned} \tag{2.16}$$

In the works of Miller (1981) and Newhouse and Shankar (1984) the phase information is not mentioned. For this reason and to gain insight on the assumptions leading to these solutions another small amplitude expansion has been undertaken in terms of sines and cosines (see appendix A). In the remainder of this document expressions in terms of amplitude and phase are used.

Substitution of (2.15) and retaining up to the second order terms leads to the following equivalent expression for the Rayleigh-Plesset equation (2.10):

$$\underbrace{\ddot{x} + 2\beta_{\text{vis}}\dot{x} + \omega_0^2 x}_{\text{linear}} \underbrace{- \frac{3\kappa+1}{2}\omega_0^2 x^2 - \frac{2\kappa\sigma}{\rho_0 R_0^3}x^2}_{\text{quadratic nonlinearity}} \underbrace{+ \frac{3}{2}\dot{x}^2 + \ddot{x}\,x}_{\text{dynamic nonlinearity}} + \underbrace{2\beta_{\text{vis}}\,\dot{x}\,x}_{\substack{\text{nonlinear viscous} \\ \text{damping}}} = -\frac{P(t)}{\rho_0 R_0^2}, \tag{2.17}$$

where $P(t)$ is the insonifing acoustic plane wave having the form:

$$P(t) = P_1 \cos(\omega_1 t), \tag{2.18}$$

ω_0 is the bubble eigenfrequency equal to

$$\omega_0^2 = \frac{3\kappa\left(p_0 + \frac{2\sigma}{R_0} - p_v\right) - \frac{2\sigma}{R_0}}{\rho_0 R_0^2} \tag{2.19}$$

and β_{vis} is the viscous damping constant equal to

$$\beta_{vis} = 2\eta / \rho_0 R_0^2. \tag{2.20}$$

Under the observation that the term $\frac{2\kappa\sigma}{\rho_0 R_0^3}$ is negligible because of the R_0^3 in the denominator, the equation can be considered equivalent to:

$$\underbrace{\ddot{x} + 2\beta_{vis}\dot{x} + \omega_0^2 x}_{\text{linear}} - \underbrace{\frac{3\kappa+1}{2}\omega_0^2 x^2}_{\text{quadratic nonlinearity}} \underbrace{+\frac{3}{2}\dot{x}^2 + \ddot{x}\,x}_{\text{dynamic nonlinearity}} + \underbrace{2\beta_{vis}\,\dot{x}\,x}_{\text{nonlinear viscous damping}} = -\frac{P(t)}{\rho_0 R_0^2}. \tag{2.21}$$

Alternatively, the linear part of equation (2.17) can be written in the standard form of a linear damped oscillator:

$$m_{eff}\ddot{x} + 2b_{vis}\dot{x} + s_{eff}\,x = P(t), \tag{2.22}$$

where the effective mass term m_{eff}, the viscous damping term b_{vis} and the effective stiffness term s_{eff} are given by:

$$m_{eff} = \rho_0 R_0^2, \tag{2.23}$$

$$b_{vis} = 2\eta \tag{2.24}$$

and

$$s_{eff} = 3\kappa\left(p_0 + \frac{2\sigma}{R_0} - p_v\right) - \frac{2\sigma}{R_0}. \tag{2.25}$$

Moreover using standard terminology of linear systems (Kinsler, 1999), a Q-factor can be defined for the linear system defined by equation (2.22) as:

$$\frac{1}{Q} = \frac{2b_{vis}}{\omega_0} \tag{2.26}$$

Assuming single frequency insonification, the solution of (2.22) is the first order term of equation (2.15), i.e. the term $A_{\omega_1}\cos(\omega_1 t+\phi_{\omega_1})$. Substitution of this term in (2.12) gives the time radius solution as first order approximation:

$$R(t)=R_0(1+A_{\omega_1}\cos(\omega_1 t+\phi_{\omega_1})), \tag{2.27}$$

where the amplitude and phase terms are expressed according to the derivation in appendix A as:

$$A_{\omega_1}=\frac{P_1}{\rho_0 R_0^2\sqrt{\left(\omega_0^2-\omega_1^2\right)^2+\left(2\beta_{\text{vis}}\omega_1\right)^2}} \tag{2.28}$$

and

$$\tan\phi_{\omega_1}=-\frac{2\beta_{\text{vis}}}{\omega_0^2-\omega_1^2}. \tag{2.29}$$

Using (2.14) and (2.27) the amplitude radius spectral component at the primary frequency is:

$$\left|R_{\omega_1}\right|=R_0A_{\omega_1}\ . \tag{2.30}$$

Substituting the term $A_{\omega 1}$ into (2.27) the following expression for the radius time response is obtained:

$$R(t)=R_0\left(1+\frac{P_1}{\rho_0 R_0^2\sqrt{\left(\omega_0^2-\omega_1^2\right)^2+\left(2\beta_{\text{vis}}\omega_1\right)^2}}\cos(\omega_1 t+\phi_{\omega_1})\right). \tag{2.31}$$

Equation (2.31) is just the steady state solution of the classic linear bubble dynamics equation, for a bubble displacing a shell of the surrounding liquid with equivalent mass m_{eff} when insonified by a pressure $P(t)=P_1\cos(\omega_1 t)$; see for example chapter 3 of Leighton (1994). This explains the characterization of the region of validity of asymptotic solutions as 'quasi linear': That is, in this regime where the analytical solution is valid, they predict a bubble response at the primary frequency which is the same as the one predicted by the use of linear theory.

The DC term A_0 and the second harmonic predicted by (2.15) have the expressions given by equation (2.32) and (2.33) respectively (for the derivation see appendix A).

$$A_0 = \frac{A_{\omega_1}^2}{2\omega_0^2 \rho_0 R_0^2}\left[\left(\frac{1}{2}\rho_0\omega_0^2 R_0^2 - \frac{1}{4}\rho_0\omega_1^2 R_0^2\right) + \frac{9\kappa^2}{2}\left(p_0 + \frac{2\sigma}{R_0} - p_v\right) - \frac{2\sigma}{R_0}\right], \tag{2.32}$$

$$A_{2\omega_1} = \frac{1}{2}A_{\omega_1}^2 \sqrt{\frac{\left(2.5\omega_1^2\rho_0 R_0^2 + 1.5\kappa(3\kappa+1)\left(p_0 + \frac{2\sigma}{R_0} - p_v\right) - \frac{4\sigma}{R_0}\right)^2 + \left(2\beta_{vis}\omega_1\right)^2}{\left(\left(\rho_0 R_0^2\right)^2\left(\omega_0^2 - 4\omega_1^2\right)^2 + \left(4\beta_{vis}\omega_1\right)^2\right)}} \tag{2.33}$$

When a two-frequency acoustic field is applied, it can be assumed to have the general form:

$$P(t) = P_1\cos(\omega_1 t) + P_2\cos(\omega_2 t + \psi)\ . \tag{2.34}$$

In the dual insonification case the solution to the linear problem follows from the principle of superposition and it is the sum of the bubble radius response to the first and the second insonifying waves, i.e.:

$$R(t) = R_0(1 + A_{\omega_1}\cos(\omega_1 t + \phi_1) + A_{\omega_2}\cos(\omega_2 t + \phi_2))\,, \tag{2.35}$$

where the terms A_{ω_2} and ϕ_2 are given by (for the derivations see appendix A):

$$A_{\omega_2} = \frac{P_2}{\rho_0 R_0^2\sqrt{\left(\omega_0^2 - \omega_2^2\right)^2 + \left(2\beta_{vis}\omega_2\right)^2}} \tag{2.36}$$

and

$$\tan\phi_{\omega_2} = -\frac{\frac{2\beta_{vis}}{\omega_0^2 - \omega_2^2} + \tan\psi}{\frac{2\beta_{vis}}{\omega_0^2 - \omega_2^2}\tan\psi - 1}\,. \tag{2.37}$$

The expressions (2.36) and (2.37) have an analogous form with the expressions (2.28) and (2.29), if the phase of the second insonifying wave is set equal to zero. Similarly here the amplitude radius spectral component at the second primary frequency is:

$$\left|R_{\omega_2}\right| = R_0 A_{\omega_2} . \tag{2.38}$$

The nonlinear components predicted from the small amplitude solutions are components from the second harmonics of the primary frequencies as well as the cooperative harmonics of sum and difference frequencies. The latter, which are of interest for this work, are expressed analytically using equations (2.12) and (2.16) as:

$$R_{-} = R_0 A_{\omega_-} \cos((\omega_1 - \omega_2)t + \phi_{-}) \tag{2.39}$$

where the dimensionless amplitude term A_{ω_-} equals:

$$A_{\omega_-} = \frac{A_{\omega_1} A_{\omega_2}}{\sqrt{\left(\omega_0^2 - (\omega_1 - \omega_2)^2\right)^2 + \left(2\beta_{\text{vis}}(\omega_1 - \omega_2)\right)^2}} \left(\left(\frac{1}{2}\left(\omega_1^2 + \omega_2^2\right) - \frac{3}{2}\omega_2\omega_1 + \frac{\frac{3}{2}\kappa(3\kappa+1)\left(p_0 + \frac{2\sigma}{R_0} - p_v\right) - \frac{2\sigma}{R_0}}{\rho_0 R_0^2} \right)^2 + \left((\omega_1 - \omega_2)^2 \delta_R^2\right) \right)^{1/2}. \tag{2.40}$$

Its amplitude, denoted by $\left|R_{-}\right|$, is simply:

$$\left|R_{-}\right| = R_0 A_{\omega_-} \tag{2.41}$$

The phase ϕ_{-} of the spectral component at difference frequency equals:

$$\tan\phi_{-} = -\frac{(1+\theta)}{(1-\theta)}, \tag{2.42}$$

where the ancillary parameter θ equals:

$$\theta = \frac{2\beta_{\text{vis}}\frac{\omega_1-\omega_2}{\omega_0}\left(\tan\psi\left(\frac{\omega_1^2+\omega_2^2}{\omega_0^2}-3\frac{\omega_2\omega_1}{\omega_0^2}+\frac{3\kappa(3\kappa+1)\left(p_0+\frac{2\sigma}{R_0}-p_{\text{v}}\right)-\frac{4\sigma}{R_0}}{2\rho_0R_0^2\omega_0^2}\right)+2\beta_{\text{vis}}\frac{\omega_1-\omega_2}{\omega_0}\right)}{\left(1-\left(\frac{\omega_1-\omega_2}{\omega_0}\right)^2\right)\left(\left(\frac{\omega_1^2+\omega_2^2}{\omega_0^2}-3\frac{\omega_2\omega_1}{\omega_0^2}+\frac{3\kappa(3\kappa+1)\left(p_0+\frac{2\sigma}{R_0}-p_{\text{v}}\right)-\frac{4\sigma}{R_0}}{2\rho_0R_0^2\omega_0^2}\right)-2\beta_{\text{vis}}\frac{\omega_1-\omega_2}{\omega_0}\tan\psi\right)} \tag{2.43}$$

The analytical solutions can be characterised as quasi-linear solutions because the spectral components at the primary frequencies are the same with those found when the linear problem is solved, in other words it is assumed that the energy dissipated in nonlinear generation is so small that it leaves the linear solutions unaltered. Additionally, as observed in equations (2.36), (2.37), (2.40) and (2.43) the phase of the insonifing field enters only the radius phase spectrum and not the amplitude spectrum. As the nonlinear systems theory dictates dependence between the type of excitation and the system response, the validity of the analytical solutions depends, among others, on the amount of energy pumped into higher harmonics. In section 2.2.2, this is discussed for the special cases of interest for this PhD work. Here it must be noted that the bubble dynamics models and their solutions are studied for the purposes of the development of a scattering bubble sizing technique. As it will be explained in chapter 4, the relevant quantity for scattering equations is the mean square amplitude of the pressure wave scattered from bubbles, or equivalently the power scattered at the frequency of interest. As it will be explained in chapter 4, this quantity depends on the amplitude of the radius spectral component and not on the phase. For this reason, the studies of the subsequent paragraphs are focused only on the amplitude spectral components. Moreover the subsequent studies are focussed on resonant bubbles because those bubbles are causing the greatest sound scattering. This is the reason; most acoustic bubble sizing techniques are based on resonant scattering rather than geometric scattering of sound.

Since resonant bubbles are important, modelling correctly the damping entering the bubble dynamics equations becomes also important. The Rayleigh-Plesset equation in the form of (2.10) or (2.17) is of limited practical interest here because it encompasses only viscous dissipation effects and therefore predicts unrealistically large pulsations for small pressure

amplitudes. This is demonstrated here with an example of single frequency insonification. Figure 2.2 shows the time series response of a single air bubble undergoing adiabatic pulsations ($\gamma = 1.4$) in fresh water with equilibrium radius R_0 equal to 20 microns which is insonified for 1 ms by a 155 kHz sound field of pressure amplitude P_1=10 kPa (zero-to-peak). The insonification frequency coincides with the bubble natural frequency.

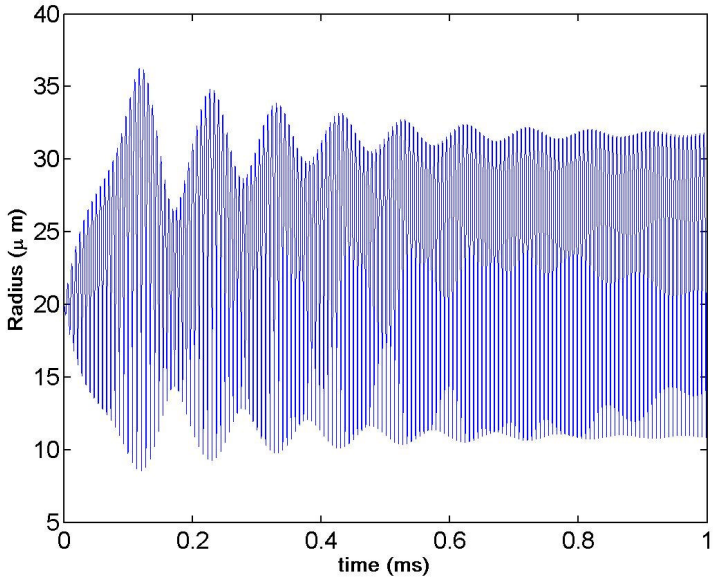

Figure 2.2: Radius time plot of an air bubble in water of equilibrium radius R_0 =20 micron in water of temperature 20 ℃ and under one atmospheric pressure. The bubble was insonified by a 155 kHz sound field of pressure amplitude P_1 =10 kPa.

As shown in Figure 2.2 the bubble expands up to 1.75 times its original size and the transient remains for a long time, effects not observed in practice for bubbles under these conditions. The time series solution shown in Figure 2.2 is obtained using the Matlab® ode45 solver. Unless otherwise stated, this solver is used for the numerical simulations of this report involving numerical solutions of nonlinear bubble dynamics equations. Some basic characteristics related to this solver are discussed in the rest of this section.

Numerical solutions can be employed here to check analytical solutions as the former ones are not limited to small amplitude response or the existence of certain harmonics in the response spectrum. The analytical solutions are approximations to the solution under the assumption that certain frequencies are important whereas others that possibly exist are negligible. Therefore these solutions are limited to predicting certain states of the system

and are not suitable for systems that exhibit instabilities or/and possibly chaotic phenomena. In this report, the validity of the analytical solutions for bubble equations is checked by solving numerically the equation by the ode45, Matlab® Ordinary Differential Equation (ODE) solver.

Numerical solutions to bubble dynamics equations (which have the general form: $f(R,\dot{R},\ddot{R},R\ddot{R},\dot{R}^2)=0$) are computed by converting the second order equation of motion into state representation i.e. into a coupled pair of first order expressions in matrix form. Then this system of first order equations is solved for the radius state-space vector $\left[R_1\ R_2\right]$, where $R_1 = R$ and $R_2 = \dot{R}$ by numerical integration. For example, the Rayleigh-Plesset equation (2.10) is converted to the following set of coupled equations:

$$\begin{aligned}\dot{R}_1 &= R_2 \\ \dot{R}_2 &= \frac{1}{\rho_0 R_1}\left(\left(p_0+\frac{2\sigma}{R_0}-p_v\right)\left(\frac{R_0}{R_1}\right)^{3\kappa}+p_v-\frac{2\sigma}{R_1}-\frac{4\eta R_2}{R_1}-p_0-\frac{3}{2}\rho_0 {R_2}^2-P(t)\right).\end{aligned} \tag{2.44}$$

This is a general method of solving second or higher order differential equations numerically (Forsythe, 1977) and any higher order differential equation can be expressed as a system of simultaneous equations with this method. The accuracy of the numerical solution depends on the numerical integration method. The Matlab ode45 solver is based on an explicit Runge-Kutta (4, 5) formula and it is a variable one-step solver. Generally, it is applied for non-stiff problems when medium accuracy is required. There is relatively limited control on the numerical errors because the error control properties of the solver are limited to the estimation of the *local* error (Golubitsky and Deliniz, 1999). As stated in the Matlab help directory, the parameter Relative Tolerance (RelTol) indicated the number of correct digits of each solution step, whereas the option AbsTol is a threshold below which the value of a solution component is unimportant. Thus assuming a solution of n steps the error of each step has an upper bound that depends on these settings and the norm of the solution according to:

$$\left|\text{error}(n)\right| \le \max(\text{RelTol}\left|\text{R}\right|, \text{AbsTol}(n)) \ . \tag{2.45}$$

Lowering the local error upper bound does not necessarily increase the accuracy of the whole solution. It may even worsen the accuracy of the solution because it leads to an increase of the cumulative solution error (Biran, 1999). For the simulations presented here both tolerance settings were set to 10^{-6}. Improvement of the solution accuracy is possible by setting cumulative error bounds. However, such bounds cannot be set in the options command of the ODE solver. The ode113 is a multistep solver and thus more accurate than ode45. However it was not selected because it is time consuming and the relatively low amplitude pulsations studied here (for example phenomena such as cavitation are excluded) do not pose high demands on the solver.

2.2 The Rayleigh-Plesset model with pseudo viscosity terms

2.2.1 Theory

Apart from the viscous losses at the bubble boundary there are two other important sources of energy loss: the acoustic radiation losses and the thermal losses. The nature of these is thoroughly described in chapter 3 of Leighton (1994). Briefly, thermal losses are caused by irreversible heat conduction between the gas and the liquid and radiation losses account for the energy radiated out from the bubble as a result of its pulsation. These losses can be approximately incorporated in the Rayleigh-Plesset equations in form of pseudo viscosity terms (Prosperetti, 1977). That is, the shear viscosity η entering the shear dissipation term $4\eta\dot{R}/R$ of equation (2.10) is replaced by the sum: $\eta+\eta_{\text{rad}}+\eta_{\text{P\_ther}}$, where η_{rad} is the effective radiation and $\eta_{\text{P\_ther}}$ is the effective thermal viscosity term. The viscosity terms η_{rad} and $\eta_{\text{P\_ther}}$ are linked to the bubble radiation and thermal damping constants (Prosperetti, 1977) as:

$$\beta_{\text{rad}}=\frac{2\eta_{\text{rad}}}{\rho R_0^2} \text{ and} \tag{2.46}$$

$$\beta_{\text{P\_term}}=\frac{2\eta_{\text{P\_ther}}}{\rho_0 R_0^2} \text{ respectively.} \tag{2.47}$$

Expressions for the linear bubble damping constants were derived for bubbles at resonance by Devin (1959). Later, the work of Devin was extended for the off-resonance case by

Eller (1970). Here these expressions are used with the form appearing in later works as for example (Prosperetti *et al*., 1988) and (Duraiswami *et al*., 1998):

viscous loss damping constant: $\beta_{\text{vis}} = \dfrac{2\eta}{\rho_0 R_0^2}$ (2.48)

radiation loss damping constants: $\beta_{\text{rad}} = \dfrac{\omega^2 R_0}{2c_0}$ (2.49)

thermal loss damping constant: $\beta_{\text{P\_ther}} = \dfrac{p_0 + \dfrac{2\sigma}{R_0} - p_{\text{v}}}{2\rho_0 \omega R_0^2} \operatorname{Im}\Phi$ (2.50)

The complex function Φ of equation (2.50) equals:

$$\Phi = \frac{3\gamma}{1 - 3(\gamma - 1)\, jX \left[(jX)^{1/2} \coth((jX)^{1/2}) - 1 \right]} \tag{2.51}$$

and depends on the thermal diffusivity of the gas in the bubble D_{g} through the parameter X:

$$X = \frac{D_g}{\omega R_0^2}. \tag{2.52}$$

The expression (2.51) is an approximation of the original expression for the complex function Φ (Prosperetti, 1977) and is valid only when the thermal diffusion length (l_{D}) in the gas is much greater than the thermal diffusion length in the liquid. The expression (2.51) is encountered in Prosperetti *et al*. (1988) and for air bubbles in water, equation (2.51) is a good approximation as discussed further in section 2.3.

The study proceeds with the incorporation of bubble damping constants, given by equations (2.48), (2.49) and (2.50), in the dimensionless Rayleigh-Plesset equation (2.17), by substituting the viscous damping constant by the total damping constant β_{tot}:

$$\beta_{\text{tot}} = \beta_{\text{vis}} + \beta_{\text{rad}} + \beta_{\text{P\_ther}} \ . \tag{2.53}$$

The thermal damping expression was derived through the use of a polytropic relationship. The polytropic index according to Prosperetti (1977) is expressed as:

$$\kappa_{\mathrm{P}} = \frac{1}{3}\mathrm{Re}\,\Phi\,, \tag{2.54}$$

and takes a value between unity and γ (the ratio of the specific heat of the gas at constant pressure to its value at constant volume). However whilst the condition $1 \le \kappa \le \gamma$ allows heat flow across the bubble wall, if κ is constant during the cycle then that heat flow is reversible, and there is no net loss of heat from the bubble, and no thermal damping in the thermodynamic sense. Moreover the use of the polytropic index modifies the expression for the bubble natural frequency which becomes:

$$\omega_{\mathrm{P0}}^2 = \frac{\mathrm{Re}\,\Phi\left(p_0 + \dfrac{2\sigma}{R_0} - p_{\mathrm{v}}\right) - \dfrac{2\sigma}{R_0}}{\rho_0 R_0^2}. \tag{2.55}$$

Substitution of expression (2.55) for the bubble natural frequency ω_0 and of the total damping, equation (2.53), for the viscous damping in the Rayleigh-Plesset equation (2.17), leads to a bubble dynamics equation which includes thermal effects with a first order approximation:

$$\underbrace{\ddot{x} + 2\beta_{\mathrm{tot}}\dot{x} + \omega_{\mathrm{P0}}^2 x}_{\text{linear}} - \underbrace{\frac{3\kappa+1}{2}\omega_{\mathrm{P0}}^2 x^2}_{\text{quadratic nonlinearity}} \underbrace{+\frac{3}{2}\dot{x}^2 + \ddot{x}\,x}_{\text{dynamic nonlinearity}} + \underbrace{2\beta_{\mathrm{tot}}\,\dot{x}\,x}_{\substack{\text{nonlinear viscous}\\ \text{damping}}} = -\frac{P(t)}{\rho_0 R_0^2}. \tag{2.56}$$

Equation (2.56) will be used for comparison with more advanced bubble models in section 2.3. The benefit of this modified formulation of the Rayleigh-Plesset equation, abbreviated by RPmod, is that the analytical solutions mentioned in section 2.1.2 are also solutions of (2.56) if β_{vis} and ω_0 are substituted by β_{tot} and ω_{P0} respectively. For example, using this substitution and retaining the assumption that the solution of (2.56) has the form of equation (2.16), the first order $A_{\omega 1}$ term equals:

$$A_{\omega_1} = \frac{P_1}{\rho_0 R_0^2 \sqrt{\left(\omega_{\mathrm{P0}}^2 - \omega_1^2\right)^2 + \left(2\beta_{\mathrm{tot}}\omega_1\right)^2}}, \tag{2.57}$$

the term $A_{2\omega_1}$ equals:

$$A_{2\omega_1} = \frac{1}{2} A_{\omega_1}^2 \sqrt{\frac{\left(2.5\omega_1^2\rho_0 R_0^2 + 1.5\kappa(3\kappa+1)\left(p_0 + \frac{2\sigma}{R_0} - p_v\right) - \frac{4\sigma}{R_0}\right)^2 + \left(2\beta_{tot}\omega_1\right)^2}{\left(\left(\rho_0 R_0^2\right)^2\left(\omega_{P0}^2 - 4\omega_1^2\right)^2 + \left(4\beta_{tot}\omega_1\right)^2\right)}} \tag{2.58}$$

and the term A_{ω_-} equals:

$$A_{\omega_-} = \frac{A_{\omega_1} A_{\omega_2}}{\sqrt{\left(\omega_{P0}^2 - (\omega_1 - \omega_2)^2\right)^2 + \left(2\beta_{tot}(\omega_1 - \omega_2)\right)^2}} \left(\left(\frac{1}{2}\left(\omega_1^2 + \omega_2^2\right) - \frac{3}{2}\omega_2\omega_1 + \frac{\frac{3}{2}\kappa(3\kappa+1)\left(p_0 + \frac{2\sigma}{R_0} - p_v\right) - \frac{2\sigma}{R_0}}{\rho_0 R_0^2} \right)^2 + \beta_{tot}^2 (\omega_1 - \omega_2)^2 \right)^{1/2} \tag{2.59}$$

The above described *ad hoc* modification of the Rayleigh-Plesset equation is necessary when the thermal and radiation damping are more important than the viscous damping.

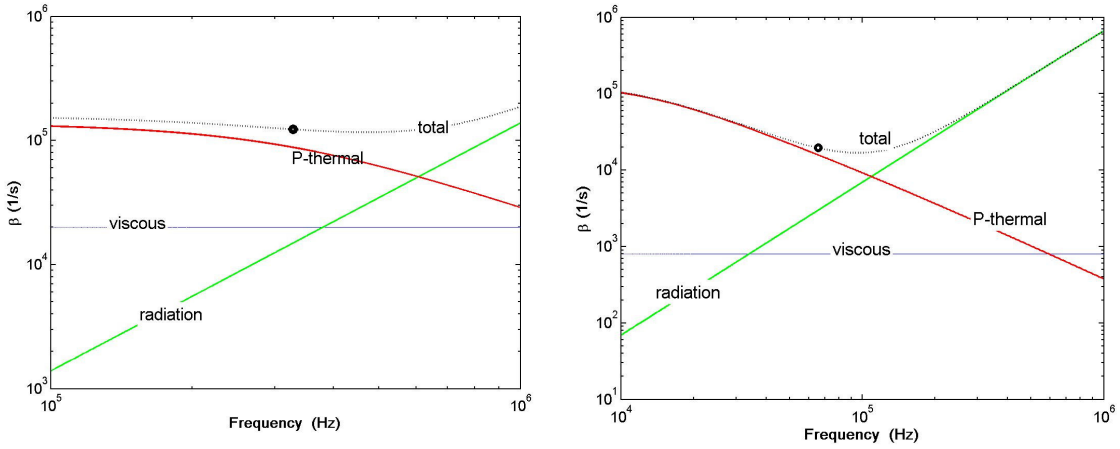

(a) *(b)*

Figure 2.3: Dimensional damping constants versus frequency for a gas bubble in fresh water at 20º C and atmospheric ambient pressure with equilibrium radius (a) 10 µm and (b) 50 µm. The dot indicates the resonance frequency of the bubble.

The relative importance of the damping constants depends on the gas and medium properties as well as the bubble size under consideration. The damping constants for a gas bubble in fresh water at atmospheric ambient pressure are plotted as a function of

frequency for a bubble with equilibrium radius 10 microns and 50 microns on figures 2.3 (a) and (b) respectively. The thermal damping constant is marked as 'P-thermal' because it was simulated according to Prosperetti *et al.* (1988) analysis using equation (2.50). The dot on both figures indicates the bubble resonance frequency. As shown in these figures, the viscous damping is constant and much smaller than the thermal damping. In particular, at or near resonance frequency, β_{vis} has the smallest contribution to the bubble damping. This indicates the importance of studying higher order bubble models that incorporate radiation and thermal effects in a rigorous way. The damping near or at resonance frequency is of importance because resonant bubbles are efficient scatterers and therefore resonant bubbles are used for most bubble sizing techniques. This is demonstrated in Figure 2.4 (a) and (b), which show the scattering cross section (solid line) and the geometrical cross section (dotted line) as function of a range of air bubbles in fresh water insonified at 100 kHz and 30 kHz respectively. The scattering cross section was calculated by equation (4.28) using the expressions (2.55) and (2.53) for the bubble natural frequency and damping respectively. As shown in Figure 2.4 the scattering cross section has a local peak at the radius corresponding to resonance at the insonification frequency, on the same figures the geometrical cross section is plotted for comparison. Figure 2.4 will be discussed further together with the development of the bubble sizing technique in chapter 5.

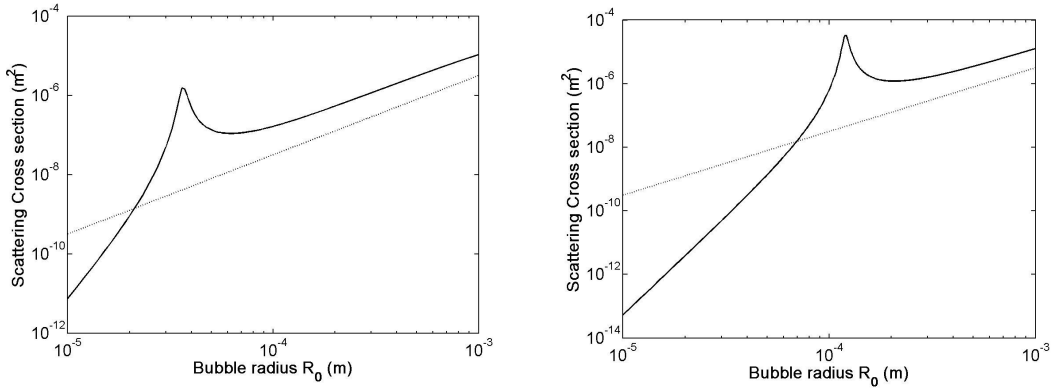

(a) *(b)*

Figure 2.4: Scattering cross section (solid line) and geometrical cross section (dashed line) for a range of air bubble sizes in fresh water insonified at (a) 100 kHz and (b) 30 kHz. The analytical expression (4.28) was used for the calculations.

Bubble scattering which is a millstone for the development of a bubble sizing technique is studied in chapter 4. Prior to this study, the analytical solutions are compared with the numerical solutions of equation (2.56).

2.2.2 Analytical versus numerical results

Inspection of equation (2.16) shows that analytical solutions are limited to a system where a priori knowledge exists that the certain harmonics (i.e. the ones taken into account for the asymptotic expansion) are the only ones present in the frequency spectrum of the bubble response. Additionally in these analytical solutions the additional nonlinear effects of the drive pressures on the solutions are neglected. That is, the first harmonics are always proportional to the corresponding applied pressure and the harmonic at the difference frequency is always proportional to their product, hence the asymptotic solutions concerns limited states of the oscillating nonlinear system bubble gas and surrounding liquid. Effects due to a pressure increase include the generation of many harmonic components which are combinations of the insonification frequencies, $f_2 - f_1, f_2 + f_1, f_2 - 2f_1, f_2 + 2f_1$ as well as multiples ($2f_1$, $2f_2$, $4f_1$, $4f_2$ etc) and fractions (sub harmonics) of the insonification frequencies ($1/2\, f_1$ $1/3\, f_1$,$1/2\, f_2$, $1/3\, f_2$ etc). In general, subharmonic generation takes place when the drive pressure exceeds a threshold (see, for example, Eller (1969), Nayfeh, (1933) and Prosperetti, (1976)) whereas higher order harmonics are present for any value of the driving signal, although they may be negligible when the input is sufficiently small (Juel, 1997). A complete study on the appearance of sub-or other combination harmonics employs chaos theory which falls out of the scope of this work. Nevertheless it is necessary to know whether the analytical solutions of equation (2.56) are a good approximation for the solution of this nonlinear equation or numerical solutions must be employed for bubble related calculations. This is studied in this section by means of looking at the amplitude spectrum of the bubble radius response $R(t)$. The cases examined are those encountered at the experiments of this PhD work.

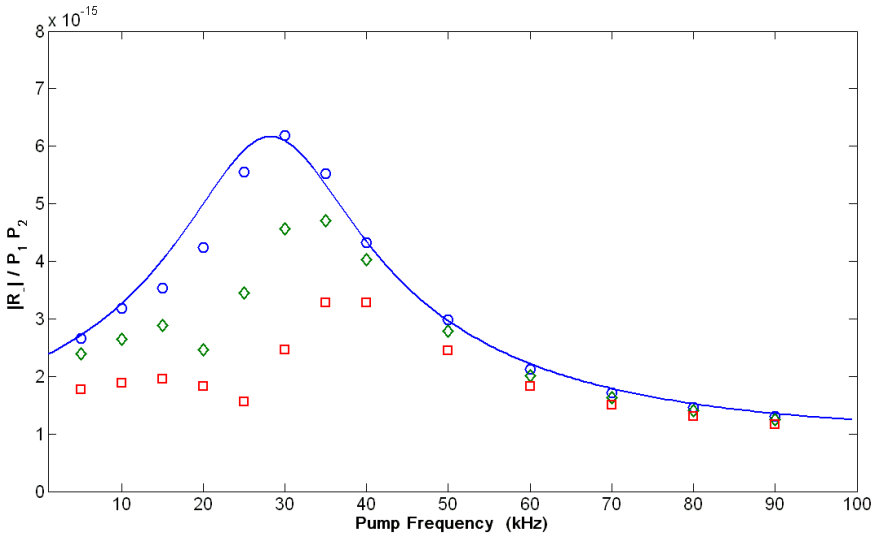

(a)

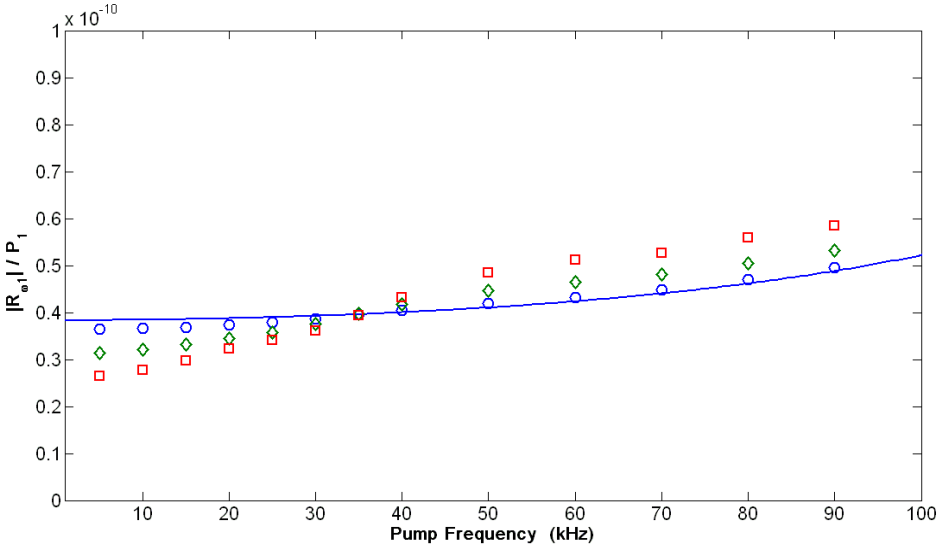

(b)

Figure 2.5: Comparison of normalised analytical (continuous lines) and numerical results (markers) for insonification (zero-to-peak) pressures $P_1 = P_2 = 10$ kPa (circles), 20 kPa (diamonds) and 30 kPa (squares); (a) The ordinate axis shows the amplitude of the difference frequency radius component divided by the product of the pressure amplitude of each wave($|R_-|/P_1P_2$) and (b) The ordinate axis shows the amplitude of the radius component at the first insonification frequency divided by its amplitude($|R_{\omega_1}|/P_1$). In both figures the frequency of the pump wave varies on the abscissa from 1 kHz to 100 kHz whereas the imaging frequency is kept constant at 220 kHz. For all computations a single gas bubble (with $R_0 = 18$ microns) in fresh water (20ºC) at a depth of 0.5 m is considered.

Assume first a single air gas bubble of equilibrium radius 18 microns in fresh water and at a half metre depth in fresh water under two frequency insonification: the one frequency is a low frequency (or pump frequency f_{p}) and is allowed to vary from one to 100 kHz. The second frequency (imaging frequency) is kept constant at 220 kHz. The bubble size under consideration is resonant at approximately 180 kHz which is equal to the difference frequency (f_{-}) when the pump frequency emits at approximately 40 kHz.

In Figure 2.5 (a) the radius amplitude spectral component at the difference frequency normalised by the product of the pressure amplitudes ($|R_{-}|/P_1P_2$) is plotted versus pump frequencies. The continuous line shows the result as predicted from the analytical solution, equation (2.41), whereas the markers show the numerical results for the $|R_{-}|/P_1P_2$ component. These numerical solutions were obtained as follows: First the dimensionless variable x of equation (2.56) was computed in the time domain using the Matlab ode45 solver as outlined in section 2.1.2. Then the amplitude spectral component $A_{\omega_{-}}$ was computed using Fourier transformation. The required spectral component $|R_{-}|$ was then obtained by equation (2.41). Similarly for the radius spectral components at the pump frequency, the amplitude spectral component A_{ω_1} was computed and then the amplitude radius spectral component at the pump frequency was obtained by equation (2.30).

In Figure 2.5 the circles, diamonds and squares indicate simulations where both acoustic amplitudes (zero- to-peak) are set equal to 10 kPa, 20 kPa and 30 kPa respectively. According to the small amplitude approach the normalised numerical results at the difference frequency would coincide because the difference frequency component appears to be proportional to the product P_1P_2

(a)

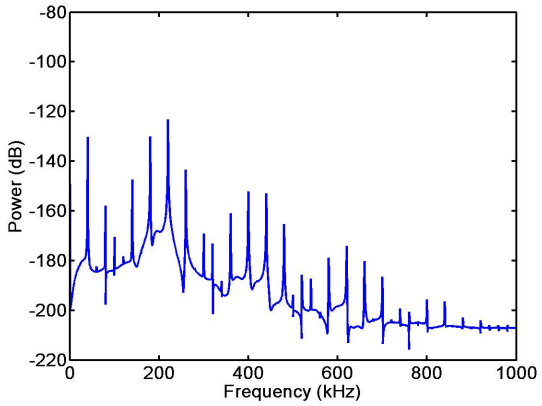

(b)

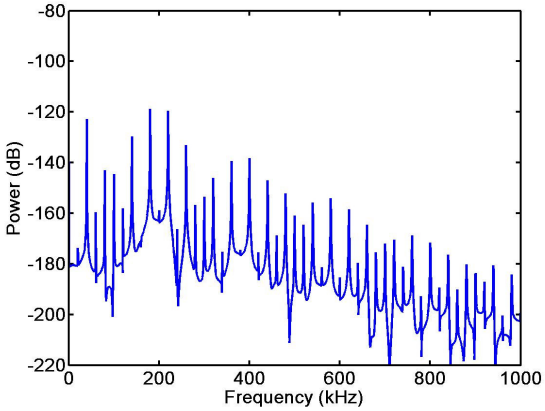

(c)

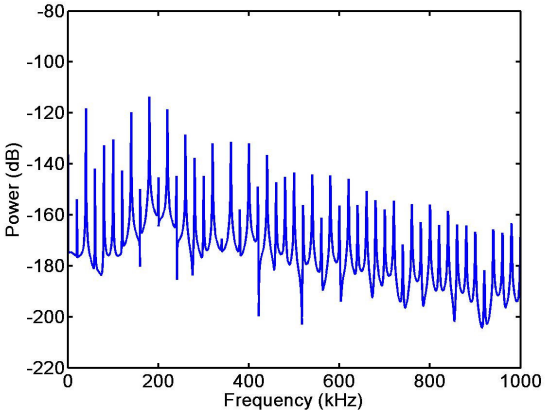

Figure 2.6: The mean-square power spectrum plotted in dB scale with (reference of acoustic power equals one) is plotted against frequency for a bubble resonant at $f_1 - f_2$ *=180 kHz (* $R_0 = 18\ \mu m$ *) under two- frequency insonification. Both waves have a zero-to-peak pressure amplitudes of (a) 10 kPa, (b) 20 kPa and (c) 30 kPa. The imaging and pump frequency are 220 kHz and 40 kHz respectively. All other conditions as in Figure 2.5.*

However this is not the case for frequencies around f_{-}=180 kHz, i.e. at or near the bubble resonant frequency, because energy is spread via the harmonic generation. This is shown in Figure 2.6 where the mean-square power spectrum of the bubble radius response is plotted against frequency for insonification waves of 40 kHz and 220 kHz, both having a zero-to-peak amplitude of (a) 10 kPa, (b) 20 kPa and (c) 30 kPa. Owing to energy spreading via harmonic generation; the magnitude of the difference frequency components reduces as the insonification pressure increases. For the same reason, as shown in Figure 2.5 (a), the analytical solution for the quantity $|R_{-}|/P_1P_2$ predicts higher values than the numerical solutions around f_{-}=180 kHz.

Moreover the corresponding analytical and numerical solutions for the radius amplitude components at the first, or pump, frequency are also not in a good agreement with each other as shown in Figure 2.5 (b) but the effect is not so pronounced. For frequencies up to 40 kHz, increasing the acoustic pressure results in a decrease of the radius spectral component due to the above mentioned energy spreading. For pump frequencies between 50 and 100 kHz the bubble size under consideration is resonant neither at the pump or the imaging frequency nor at the difference frequency, and the pressure increase of the insonification waves results in increase of the radius spectral components at these frequencies. This suggests that acoustic energy stays at the same frequencies. The impact of the above mentioned phenomena in predicting the corresponding scattered pressure is discussed further in section 4.2. Since the scattered pressure is proportional to the source level, the deviations shown in Figure 2.5 lead to significant discrepancies in interpretation of scattering measurements, especially for the nonlinear components.

The above discussed features are characteristics of nonlinear systems heading towards chaos at an instability state (i.e. system resonance) by the change of a system variable, namely the pressure. A complete treatment of the problem would require three dimensional phase portraits as, for example, in Maksimov (2000). These phenomena stem from bifurcations of equation (2.56) and do not necessarily reflect what is observed in practice. For example, insonification with two frequencies both having amplitudes zero-to-peak 30 kPa would first bring about other nonlinear phenomena. This is explained further with observations on the appearance of subharmonics. The instability threshold predicts relatively high pressures for their appearance whereas other physical effects (surface

waves, higher modes of pulsation, etc) may result in the appearance of these subharmonics below the predicted threshold, see for example Maksimov (1997) and Ramble (1997). The literature on nonlinear and chaotic systems is so extensive that it would be impossible to make a full analysis for all possible cases encountered in bubble population in the sea or sediments. Here, examining cases pertinent to bubble sizing in the water tank, we are focused on sufficiently low pressure amplitudes. The use of relatively low pressure renders non bubble mediated nonlinearities, such as surface waves (Phelps and Leighton, 1997), negligible. The relevant simulation results show that the analytical solutions are not giving sufficient accuracy.

By contrast when the insonification is of a 'parametric type', that is when the two insonifying frequencies are close to each other and much higher than the difference-frequency, then the analytical solutions as predicted by equation (2.41), there is closer agreement with the numerical answers. For this type of insonification there is a limited energy loss in harmonic component generation between the difference and the primary frequencies. This is demonstrated in Figure 2.7 where the radius amplitude spectral component at the difference frequency normalised by the product of the pressure amplitudes ($|R_-|/P_1P_2$) is plotted versus the first primary frequency. Here the response of a single air gas bubble of equilibrium radius 18 microns under a parametric type of insonification (f_1=1 MHz and f_2=1.18 MHz) is studied. The continuous line shows the result as predicted from the analytical solution, equation (2.41), whereas the markers show the numerical results for the $|R_-|/P_1P_2$ component, as resulted from numerical solutions using equation (2.56) and the procedures described earlier in this section. The circles, diamonds and squares indicate simulations where both acoustic amplitudes (zero-to-peak) are set equal to 10 kPa, 20 kPa and 30 kPa respectively. As in the example of Figure 2.5, three different frequencies (f_2=1.16 MHz, 1.18 MHz and 1.20 MHz) of the one insonification wave are tested by keeping the other frequency constant at 1 MHz. As previously, according to the small amplitude approach these normalised numerical results would coincide because the difference frequency component appears to be proportional to the product P_1P_2. In this case, although the markers corresponding to the same frequency of insonification frequencies do not coincide, the results are much closer to the theoretical predictions. Here energy spreading due to harmonic generation is less.

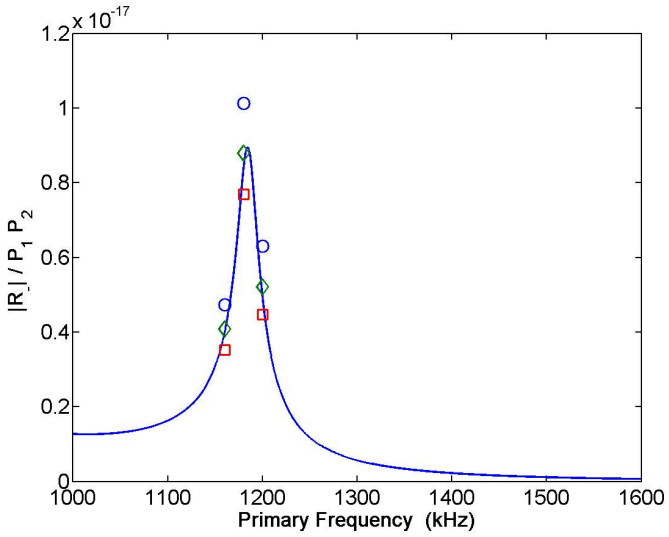

Figure 2.7: The ordinate axis shows the scattered pressure component at the difference frequency normalized by the pressure product P_1P_2 and on the abscissa the first primary frequency varies from 1MHz to 1.60 MHz. The second primary frequency stays constant at 1MHz. Both insonification (zero-to-peak) pressures are $P_1 = P_2 = 10$ kPa (circles), 20 kPa (diamonds) and 30 kPa (squares). All conditions are the same as in Figure 2.5.

An example of the mean-squared power spectrum of the radius bubble response is shown in Figure 2.8. The spectrum has been computed for the same bubble with primary frequencies at 1 MHz and 1.18 MHz, both having 30 kPa zero-to-peak amplitude. The bubble is resonant at the difference frequency (approximately 180 kHz) just as in the previously examined cases shown in Figure 2.6 and all other simulation conditions were kept the same. Figure 2.8 shows much less spectral components in comparison to Figure 2.6 (c). The radius spectral components appearing in Figure 2.8 are similar to those predicted by (2.16), i.e. the small amplitude expansion has enough terms to approximate the true solution. Even at relatively high pressure amplitudes harmonic or subharmonic generation at frequencies other then those predicted by (2.16) does not take place. As such analytical solutions are suitable for this type of bubble insonification.

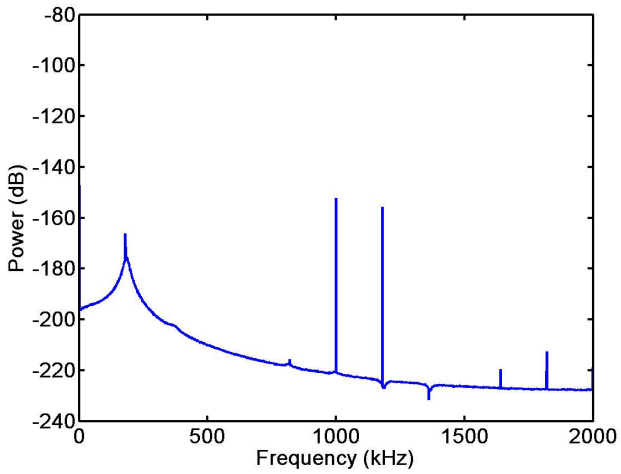

Figure 2.8: The mean-square power spectrum is plotted in dB scale with reference the unity acoustic power for a radius response of a single bubble of size resonant at $f_1 - f_2$ *=180 kHz (* R_0 *=18 microns). Both waves have a 30 kPa 0-peak pressure amplitudes. The insonification frequencies are at 1 MHz and 1.180 MHz. All other input parameters as in figures 2.4, 2.5 and 2.6.*

2.3. Advanced bubble dynamics models

In this section two advanced bubble dynamics models are studied and compared with the modified Rayleigh-Plesset equation. The one is of the family of Herring-Keller-Miksis equations. The other is based on the same equation but it includes the thermal effects according to the work of Prosperetti *et al*. (1988). The aim of this section is to compare these models with the Rayleigh-Plesset equation with pseudo viscosity terms, equation (2.56), abbreviated with RPmod, in order to choose a suitable model for the bubble inversions.

2.2.3 Elements of theory

Several equations have been formulated to include explicitly the medium compressibility in the bubble-dynamics equations. First works were from Keller-Kolonder (1956), Herring (1941) and Keller and Miksis (1980). In this work the formulation of Keller and Miksis (1980) is used. Following this formulation the bubble dynamics equation which relates the bubble radius R and wall velocity $\dot{R}$ to the inertial, forcing and dissipative terms is:

$$\left(1-\frac{\dot{R}}{c_0}\right)R\ddot{R}+\frac{3}{2}\dot{R}^2\left(1-\frac{\dot{R}}{3c_0}\right)=\left(1-\frac{\dot{R}}{c_0}\right)\frac{1}{\rho_0}\left[p_{\mathrm{L}}(t)-p_0-P_{\mathrm{I}}\sin\left(\omega\left(t+\frac{R}{c_0}\right)\right)\right]+\frac{R}{\rho_0 c_0}\frac{\mathrm{d}p_{\mathrm{L}}(t)}{\mathrm{d}t} \tag{2.60}$$

where:

$$p_{\mathrm{L}}(t)=\left(p_0+\frac{2\sigma}{R_0}\right)\left(\frac{R_0}{R}\right)^{3\kappa}-\frac{2\sigma}{R}-\frac{4\eta\dot{R}}{R}. \tag{2.61}$$

The consideration of a finite, time invariant speed of sound (c_0) in the medium at the bubble wall allows for energy losses through acoustic radiation to the medium. This formulation does not include explicitly thermal damping. However, the radius time derivatives create damping and stiffness terms; among those is a pseudo thermal damping. These terms are explained by considering the linear problem and are not significant for air bubbles encountered in shallow fresh water but they can become important when the bubble host medium is other than water. To demonstrate this, the method of small amplitude expansion is used, following the method outlined in section 2.1.2. The time dependent bubble radius in the form of equation (2.12) is substituted in (2.60). Linearising the power terms and keeping terms up to second order gives the following expression in terms of the dimensionless radius variations x:

$$\begin{aligned}&\rho_0 R_0^2(1+x)\ddot{x}+\frac{3}{2}\rho_0 R_0^2\dot{x}^2=\left(p_0+\frac{2\sigma}{R_0}-p_{\mathrm{v}}\right)\left(1-3\kappa x+\frac{3\kappa}{2}(3\kappa+1)x^2\right)-\\&\left(p_0+\frac{2\sigma}{R_0}\left(1+x+x^2\right)\right)-4\eta(\dot{x}-x\dot{x})+\frac{R_0}{c_0}\left[3\kappa\dot{x}\left(p_0+\frac{2\sigma}{R_0}-p_{\mathrm{v}}\right)\left(3\kappa x+\frac{R_0}{c_0}\dot{x}-1\right)\right.\\&\left.+4\eta\left(\dot{x}^2-\ddot{x}+\frac{R_0}{c_0}\dot{x}\ddot{x}\right)+2\sigma\dot{x}\left(\frac{1}{R_0}-\frac{x}{R_0}-\frac{\dot{x}}{c_0}\right)\right]-P(t)-\frac{\dot{x}R_0}{c_0}P(t)\end{aligned} \tag{2.62}$$

If a solution were to be found to the nonlinear problem by substitution of x (equation (2.15) or (2.16)) into (2.62), then a great number of terms are generated rendering this approach impracticable. However if the linear problem is considered, then only the terms contributing to x, $\dot{x}$ and $\ddot{x}$ are retained and important features can be easily highlighted. For

the purposes of solving the linear problem, the excitation term $P(t)$ can be written using exponential representation: $P(t) = P_1 e^{j\omega t}$. The driving pressure of the

term $\dot{x}R_0 P(t)/c_0$ is equivalent to the bubble radiation at the bubble wall. To find the equivalent expression for the amplitude P_1 we consider the spatial dependence of the pressure emitted by a monopole source which is pulsating with a uniform surface velocity $\dot{R}$:

$$p(r) = \frac{\rho_s c_P k R_0 (kR_0 - i) R_0 \dot{R}}{(kR_0)^2 + 1} \frac{e^{ik(R-R_0)}}{r}, \tag{2.63}$$

where k is the wavenumber in the bubble host medium. For $kR_0 \ll 1$, the emitted pressure of (2.63) is approximated by:

$$p(r) \simeq -i\rho_0 c_0 k R_0^2 \dot{R} \frac{e^{ikR}}{r} \tag{2.64}$$

And therefore the amplitude of the acoustic pressure at the bubble wall $r = R_0$ is approximated by:

$$P_1 \simeq -\rho_0 \omega^2 R_0^2. \tag{2.65}$$

Using expression (2.65) for the amplitude of the driving pressure and grouping the linear terms the equation of a linear bubble oscillator is obtained:

$$\ddot{x} + 2\beta_{HK}\dot{x} + \omega_{HK}^2 x = -\frac{P(t)}{m_{HK}}. \tag{2.66}$$

The terms characterising the bubble pulsations β_{HK}, ω_{HK} and m_{HK} have acquired different expressions comparing to those derived from the Rayleigh-Plesset equation. The effective oscillating mass m_{HK} equals to:

$$m_{HK} = \rho_0 R_0^2 + \frac{4\eta_s R_0}{c_s}. \tag{2.67}$$

The total damping constant β_{HK} is the summation of the following damping terms:

the radiation damping:

$$\beta_{\mathrm{HK\_rad}} = \frac{\omega^2 \rho_0 R_0^3}{2c_0} \Bigg/ \left(\rho_0 R_0^2 + \frac{4\eta R_0}{c_0} \right) \tag{2.68}$$

the viscous damping:

$$\beta_{\mathrm{HK\_v}} = 2\eta \Bigg/ \left(\rho_0 R_0^2 + \frac{4\eta R_0}{c_0} \right) \tag{2.69}$$

the thermal damping:

$$\beta_{\mathrm{HK\_th}} = 3\kappa p_{\mathrm{g0}} R_0 \Bigg/ 2c_0 \left(\rho_0 R_0^2 + \frac{4\eta R_0}{c_0} \right), \tag{2.70}$$

the interfacial damping, which is a negative damping term:

$$\beta_{\mathrm{HK\_int}} = -\sigma \Bigg/ c_0 \left(\rho_0 R_0^2 + \frac{4\eta R_0}{c_0} \right) \tag{2.71}$$

and the bubble natural frequency, ω_{HK}, in (2.66) is:

$$\omega_{\mathrm{HK}}^2 = \left(3\kappa p_{\mathrm{g0}} - \frac{2\sigma}{R_0} \right) \Bigg/ \left(\rho_0 R_0^2 + \frac{4\eta R_0}{c_0} \right). \tag{2.72}$$

If water is the bubble ambient medium, the term $4\eta R_0 / c_0$ is negligible and the expression for the radiation damping $\beta_{\mathrm{HK\_rad}}$ becomes the same as the expression (2.49), i.e. the radiation damping as derived by Prosperetti (1977). Also the expressions for the viscous damping $\beta_{\mathrm{HK\_v}}$, becomes the same as the viscous damping present in the RP equation (2.17). Additionally in the long wavelength assumption and the small values of water for the surface tension render the interfacial damping ($\beta_{\mathrm{HK\_int}}$) negligible for gas bubbles in water. This damping is negative, i.e. stores instead of consumes energy and arises from the changes of the bubble surface tension pressure term ($2\sigma / R$) which is a function of the time dependent bubble radius. The surface tension σ for gas (air)-fresh water interface takes values around 0.072 N/m which renders the expression of equation (2.71) negligible.

From the discussion of the previous paragraph, it is concluded that the damping constants as well as the eigenfrequency and effective mass predicted by linearization of the HK

equation are well approximated by the corresponding terms discussed in section 2.2.1. The shortcoming of the HK model is lack of thermal damping, or more precisely the thermal losses resulting from heat conduction which as shown in Figure 2.3 is, for gas bubbles in water, the most important effect. The linear damping constants and natural frequency as these are resulting from the Herring-Keller equation will be revisited in Chapter 3 where bubble dynamics models for viscoelastic media are discussed.

An exact solution of the bubble dynamics with thermal effects was formulated by Prosperetti *et al.* (1988), which is called throughout this report the nonlinear Prosperetti model (NLP). In that paper the bubble dynamics equation (2.60) is solved simultaneously with the thermal equation for conduction describing the temperature distribution in the bubble. The gas temperature is assumed to vary spatially (radially) in the bubble. The main assumptions of this model are:

1) the pressure is spatially uniform in the bubble;
2) the gas exhibits ideal gas behaviour;
3) the bubble remains spherical all the time;
4) no mass transfer takes place at the bubble boundary;
5) the bubble wall temperature is always equal to the liquid temperature at infinity;
6) the vapour pressure is negligible.

The original numerical solution according to Prosperetti *et al.* (1988), was found to have limited accuracy (estimated 0.1% error). The accuracy is improved by the use of the spectral method of Chebyshev polynomials (Kamath and Prosperetti, 1989). The thermal losses were modelled using the common one dimensional conduction model which in spherical coordinates is:

$$\frac{\partial^2 (r\Theta)}{r^2 \partial r^2} = \frac{1}{D_g} \frac{\partial \Theta}{\partial t}, \tag{2.73}$$

where the term D_g denotes the thermal diffusivity of gas which equals to:

$$D_{\mathrm{g}} = \frac{K_{\mathrm{g}}}{\rho_g C_{\mathrm{p}}}, \tag{2.74}$$

where K_{g} is the thermal conductivity of gas within a bubble , ρ_g the density of gas in a bubble and C_{p} specific heat capacity of gas within a bubble at constant pressure. The variable Θ is the change in temperature of gas $T(r,t)$ from equilibrium temperature at infinity T_∞.

$$\Theta = T(r,t) - T_\infty . \tag{2.75}$$

Equation (2.73) was solved in Prosperetti *et al*. (1988), assuming that the temperature of the liquid remains unperturbed. This assumption is valid for air-gas bubbles in water because the thermal diffusion length (l_{D}) in the water is two to three orders of magnitude smaller than in the gas. For gas the diffusion length equals:

$$l_{\mathrm{D}} = \sqrt{D_{\mathrm{g}} / 2\omega} . \tag{2.76}$$

To find the corresponding diffusion length in the bubble surrounded by the liquid, the thermal diffusivity of gas must be replaced with that of the liquid. The Table 2.1 and Table 2.2 show typical values of thermal properties of air and water respectively.

Table 2.1: Thermodynamic properties of air

T (°C)	ρ (kg/m^2)	C_p (kJ kg^{-1}K^{-1})	K (Wm^{-1}K^{-1})
0	1.293	1.005	0.0243
20	1.205	1.005	0.0257

Table 2.2: Thermodynamic properties of air-free fresh water

T (°C)	ρ (kg/m^2)	C_p (kJ kg^{-1}K^{-1})	K (Wm^{-1}K^{-1})
0.01	999.8	4.210	0.561
20	998.3	4.183	0.673

The model presented in the work of Prosperetti *et al*. (1988) can be used for bubbles under a single frequency excitation and not under two (or more) frequencies. The limitation originates from the treatment of the temperature profile Θ. Specifically, the temperature

profile described by equation (2.75) is considered to take the following boundary condition at $r = R$:

$$\Theta(R,t) = T_0 \cos(\omega_1 t) - T_\infty \text{ and } \lim_{r\to\infty} \Theta(r,t) = 0 \tag{2.77}$$

When the bubble undergoes two frequency insonification the corresponding temperature fluctuations at the boundary are:

$$\Theta(R,t) = T_0 \cos(\omega_1 t) + T_0 \cos(\omega_2 t) - T_\infty . \tag{2.78}$$

Thus the boundary layer has two time scales (here it is assumed that heat effects are linear phenomena and the superposition principle applies). Hence the algorithm of Prosperetti *et al.* (1988), which considers one time scale for the excitation, is no longer adequate. In this work, this code was used for a two frequency insonification under the assumption that only one frequency component of the bubble response spectrum is of interest. In this case the thermal effects at the bubble boundary are computed with the timescale corresponding to the frequency of interest. For example, when the frequency of interest is the difference frequency ω_-, which is generated from nonlinear pulsations of the bubble boundary, the bubble thermal boundary condition becomes at the bubble wall: $\Theta(R,t) = T_0 \cos(\omega_- t) - T_\infty$. This condition will underdamp the primary frequencies because the thermal diffusion length equation (2.76), is greater for the primaries than for the difference frequency and therefore the time lagging of the primaries is greater than for the difference frequency. In the next section numerical examples which demonstrate these effects are shown.

2.2.4 Numerical simulation results

In these paragraphs numerical results using the three bubble dynamics models HK, NLP and RPmod, are shown to highlight important features of bubble pulsations. For a single bubble under a single frequency of insonification the HK equation models viscous and radiation losses exactly and NLP model computes all three damping losses exactly. The RPmod equation incorporates radiation damping and thermal damping as first order as discussed in section 2.2. Initially the implementations of the Matlab codes for the HK and NLP models were tested via reproducing results of the publication of Prosperetti *et al.*

(1988). Figure 2.9 shows the figure 5 of Prosperetti *et al*. (1988). This figure shows the normalised bubble radius response R/R_0 versus the normalised time of bubble pulsation defined as the elapsed time multiplied but the radial insonification frequency $\omega: t \cdot \omega$.

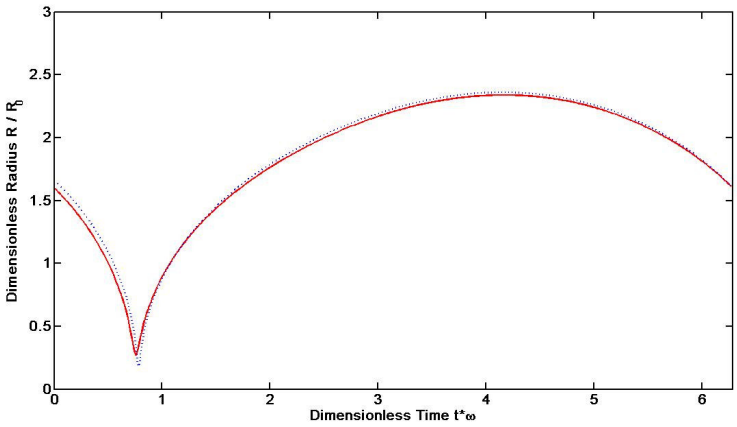

Figure 2.9: Normalised radius-time curves simulated with the NLP code (red solid line) and the HK code (blue dotted line) for steady pulsations of a 10 μm bubble driven at a pressure amplitude 0.6 times the ambient pressure with an insonification frequency 0.8 f_0, reproduction from Prosperetti et al. (1988).

Simulation results for the RPmod model in the form of equation (2.56) are not encountered in literature. Its correctness will be verified by comparison of the RPmod code with the NLP code.

The first set of simulations are concerned with an air bubble, R_0 =50 μm resonant bubble in fresh water at 20ºC at a depth of half metre. The surface tension was taken into account and no vapour is assumed to be present for the HK and RPmod models for a fair comparison with the NLP model. The time response was simulated for 80 pump cycles assuming that the bubble is at rest at $t = 0$.

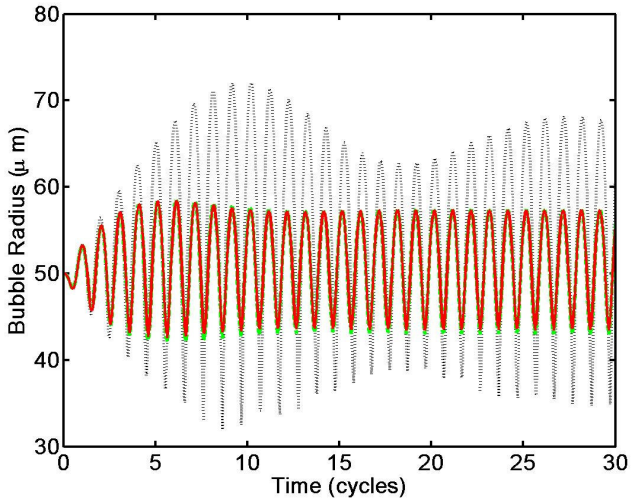

Figure 2.10: Bubble radius time response of an air bubble (R_0=50 μm) in fresh water at a depth of half metre under near-resonance frequency of insonification (68 kHz) of a pressure waves (10 kPa, zero-to-peak), computed using HK equation (black dotted line), NLP code (red line) and RPmod equation (green dashed line). The last curve is hardly discernible because it overlaps with the solid line resulted from the NLP code.

Figure 2.10 shows bubble radius time response during the first 30 cycles as computed by the HK equation (black dotted line, the NLP code (red solid line) and the RPmod equation (dashed green line). The last curve is hardly distinguishable because it overlaps with the solid line. The bubble response predicted from the HK equation exhibits much larger amplitudes and a sustaining transient which indicates the lack of thermal damping. As shown in Figure 2.3 the thermal damping is the most prominent of the three types of damping and therefore determines the accuracy of the model. For this reason the HK model is not considered in the examination of the amplitude response spectra shown in Figure 2.11. In Figure 2.11 the bubble radius amplitude response spectrum as computed from the NLP model (black solid line) and the RPmod equation (dashed blue line), are plotted against frequency.

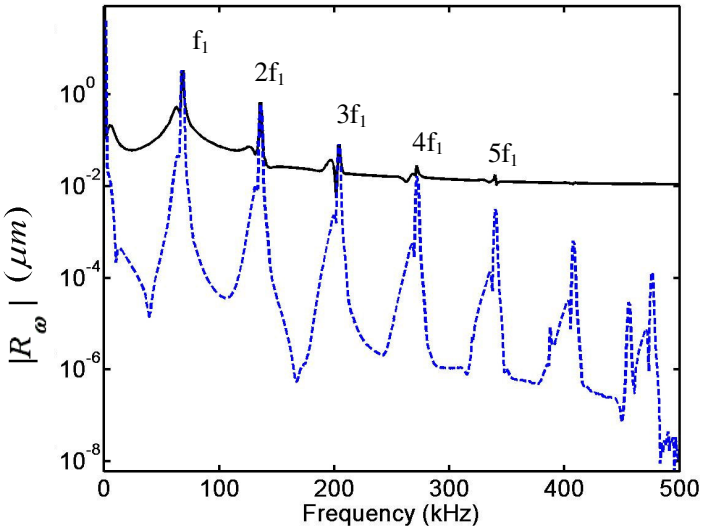

Figure 2.11: Amplitude spectra of radius response of an air bubble (R_0 =50 μm) computed using the NLP and the RPmod model (solid and dashed line respectively) all conditions as in Figure 2.10

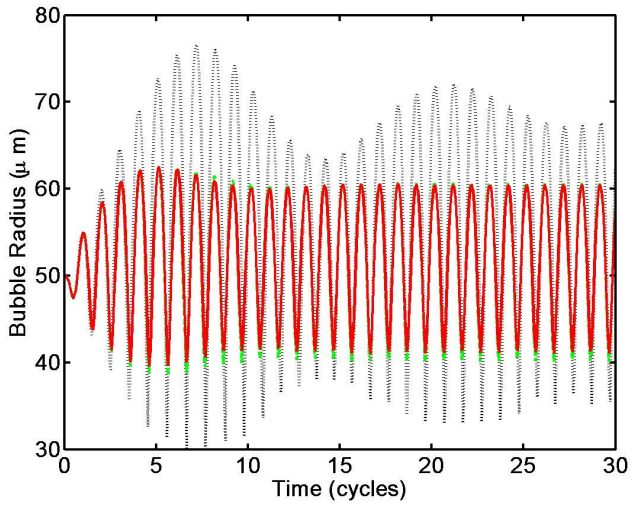

Figure 2.12: Bubble radius time response of an air bubble (R_0=50 μm) in fresh water at a depth of half metre under near-resonance frequency of insonification (68 kHz) of a pressure waves (15 kPa, zero-to-peak), computed using the HK equation (black dotted line), NLP code (red line) and RPmod equation (green dashed line). The last curve is hardly discernible because it overlaps with the solid line resulting from the NLP code.

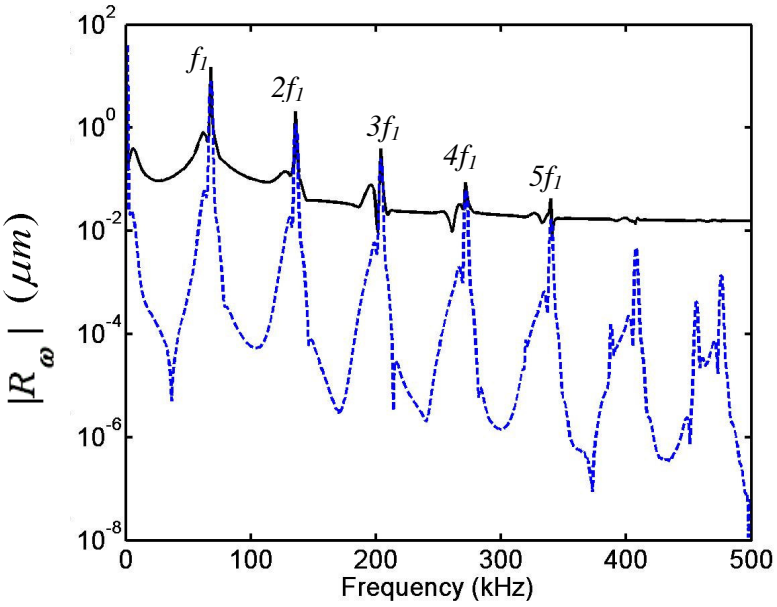

Figure 2.13: Amplitude spectra of radius response an air bubble (R_0 =50 μm) computed using the NLP and the RPmod model (solid and dashed line respectively) all conditions as in Figure 2.12

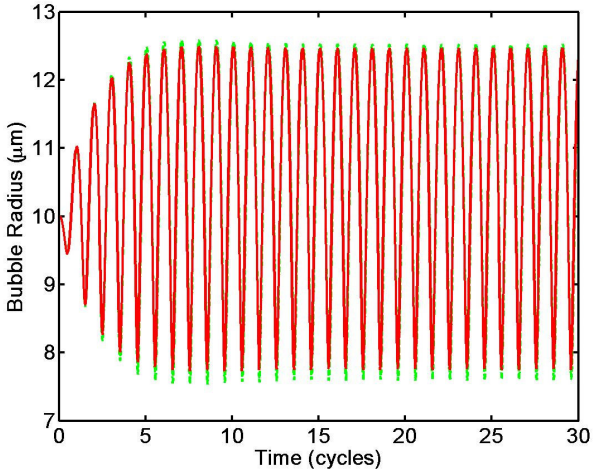

Figure 2.14: Bubble radius time response of an air bubble (R_0=10 μm) in fresh water at a depth of half metre under near-resonance frequency of insonification (32 kHz) of a pressure waves (15 kPa, zero-to-peak), computed NLP code (red line) and RPmod equation (green dashed line). The last curve is hardly discernible because it overlaps with the solid line resulting from the NLP code

These numerical simulation tests were repeated for a resonant bubble of the same size and ambient conditions. The only input changed is the acoustic pressure which was increased from 10 kPa to 15 kPa (zero-to-peak) amplitude. The radius time responses are shown in

Figure 2.12 and the corresponding amplitude spectra in Figure 2.13. As in the first example the NLP code shows a good agreement with the RPmod for the primary frequency, f_1 and the $2f_1$ and $3f_1$ the nonlinear generated harmonic components. On the whole the RPmod equation overdamps the higher harmonics which is rather expected because the thermal damping is based on a first order approximation.

To demonstrate the good agreement of the NLP code with the RPmod another resonant bubble size ($R_0 = 10\ \mu$m) is examined for single frequency insonification. Figure 2.14 shows the radius time response. As previously, the bubble was simulated for 80 pump cycles and the first 30 cycles are shown. Figure 2.13 shows the amplitude spectra resulted for the radius time series as predicted from NLP code (continuous line) and from RPmod code (dashed line). As shown in Figure 2.14, there is good agreement for the low end of the frequency spectrum whereas the discrepancy becomes considerable at frequencies $6f_1$ and higher.

The simulations presented in the remainder of this section concern a single bubble under two frequency insonification. The NLP model is no longer exact because the thermal boundary has two time scales as discussed at the end of section 2.3.1. The examples refer to frequencies used in the experimental work. It was assumed that the bubble pulsates in response to insonification by a two- frequency primary pressure field having the form: $P(t) = P_1 \cos(2\pi f_1 t + \pi/2) + P_2 \cos(2\pi f_2 t + \pi/2)$, with $P_1 = P_2 = 15$ kPa, and $f_1 = 220$ kHz and $f_2 = 55$ kHz, which begins at time t=0 (the insonifying pressure field is zero for all earlier times). As already mentioned, the phase doesn't influence the amplitude spectrum of the bubble response, this choice insonification pressure facilitated the numerical calculations because at t=0, $P(t)$ equals also zero.

First the response of a bubble size resonant at the difference frequency, $R_0 = 20$ μm, was computed using the NLP and the RPmod codes. The results in the time and frequency domain are shown in Figure 2.16 and Figure 2.17 respectively. The dashed line represents the results from the RPmod equation and the solid line the results from the NLP code.

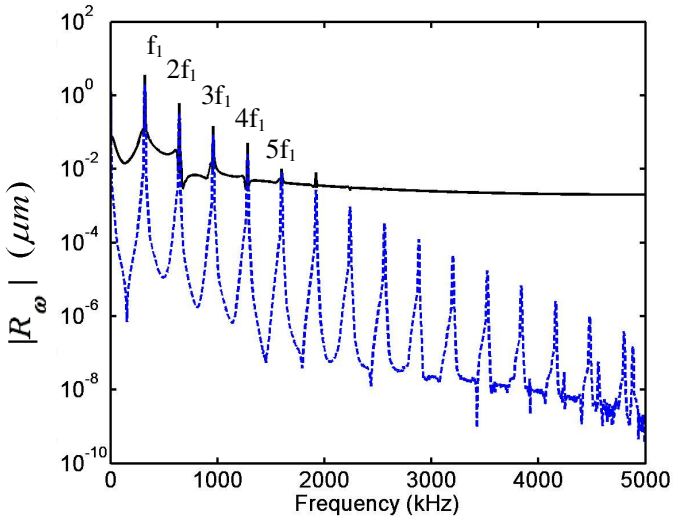

Figure 2.15: Amplitude spectral components of radius response of an air bubble (R_0 =10 μm) computed using the NLP and the RPmod model (solid and dashed line respectively). All conditions as in Figure 2.14.

For the same type of two-frequency insonification and bubble ambient conditions, the time and spectral response of a bubble with R_0=64 μm (a bubble size resonant at the primary frequency f_2) was computed in the same manner. The results in frequency domain are shown in Figure 2.18. The time series results are not shown because there the two curves overlap and the difference is not visible. Now the spectral component of interest is the one at $f_1 - f_2$. Therefore the frequency entering the expression of polytropic index of equation (2.54) and thermal damping of equation (2.50) is the difference frequency of the insonifying fields. As shown in Figure 2.18 the two models predict similar radius time responses.

In all examined cases the predictions of the RPmod and NLP models agree within 0.2 % for the frequencies of interest in this work. The two models disagree in the high frequency range which is not of interest here. It was chosen to use the RPmod for the theory accompanying the inversion method of thesis as the simulation time of the RPmod is much shorter than that of the NLP code.

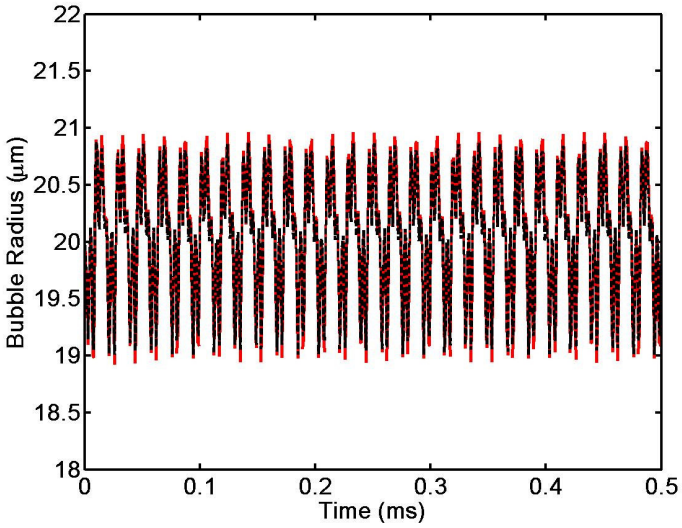

Figure 2.16: Radius time response for the first 0.5 ms of an air bubble (R_0=20 μm) in fresh water under 106 kPa ambient pressure, for two frequency insonification (f_1=220 kHz and f_2 =55 kHz) where each of the primary fields has a zero-to-peak pressure amplitude of 15 kPa. The response computed NLP code (red line) and RPmod equation (black dashed line). The last curve is hardly discernible because it overlaps with the solid line resulting from the NLP code.

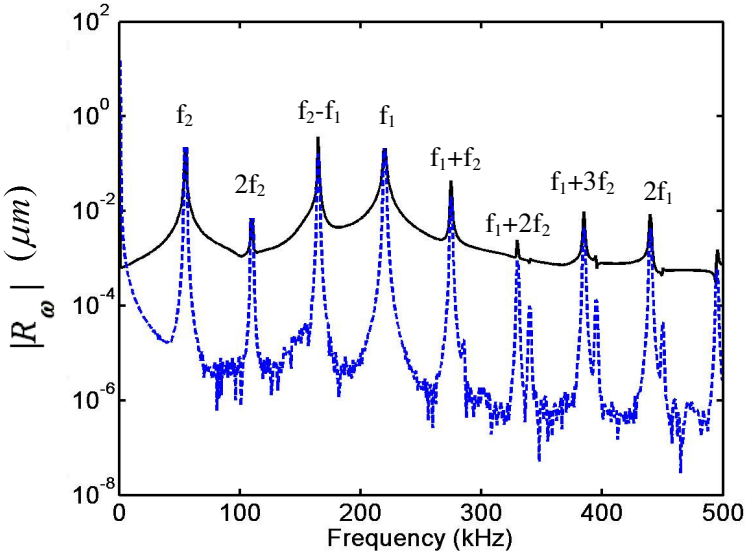

Figure 2.17: Amplitude spectral components of the response of the air bubble of Figure 2.16 (i.e. R_0 =20 μm in water under two frequency insonification (f_1 =220 kHz and f_2 =55 kHz) for primary waves both having zero-to-peak pressure amplitudes of 15 kPa); computed using the NLP and the RPmod model (solid and dashed line respectively) The spectrum is computed for all 1.1 ms of data.

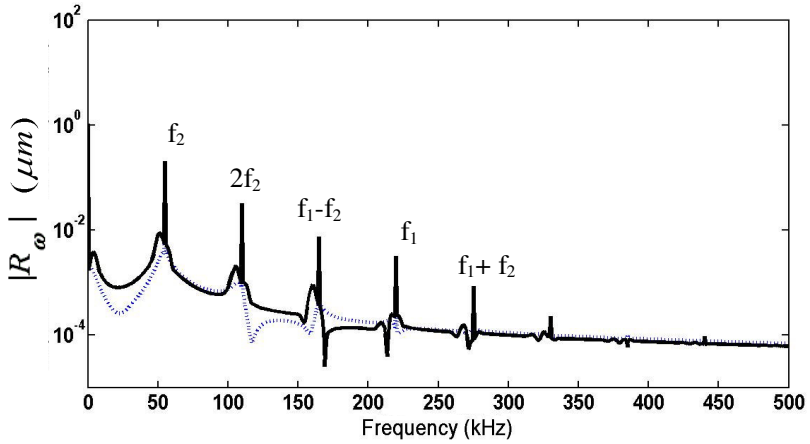

Figure 2.18: Amplitude spectral components of the response of the air bubble of R_0 =64 μm in water under two frequency insonification (f_1=220 kHz and f_2 =55 kHz) for primary waves both having zero-to-peak pressure amplitudes of 15 kPa). The spectrum is computed using the NLP and the RPmod model (solid and dashed line respectively) for all 1.1 ms of data.

2.3 Summary

Bubble dynamics models were studied in this chapter. The study was focused on the use of a simpler bubble dynamics model, the modified Rayleigh-Plesset model (abbreviated as RPmod) as alternative to the time consuming finite element model of Prosperetti *et al*. (1988). Numerical simulations showed that for the cases of interest in this PhD thesis the RPmod cast in the form of equation (2.56) is a good alternative to the bubble dynamics model of Prosperetti *et al*. (1988). Hence the equation (2.56) will be used thought out this work to predict the bubble radius response for bubbles pulsating in water.

Moreover, study reveals they are suitable for single frequency bubble frequency insonification because the thermal damping is modelled through the thermal diffusion length which depends only on one frequency as expressed by equation (2.76). Thus only one time scale is involved in the modelling of the thermal effects. Since the bubble sizing method studied in this PhD work is based on the use of two insonification frequencies, fitting of the damping to the frequencies of interest was applied. This approach consists of

substituting the nonlinearly generated frequency of interest to the damping expressions which are frequency dependent, i.e. the thermal damping given by equation (2.50) and the radiation damping given by equation (2.49). In this way when for example the difference frequency f_- is of interest, then the frequency entering equations (2.50) and (2.49) is $\omega = 2\pi f_-$.

A great part of this chapter was devoted to finding analytical solutions and examining their suitability. Although analytical solutions are easier and straightforward to use, the study reveals that are not suitable for the cases of interest here. Namely these solutions limit themselves to the cases where the insonification pressures are so low that only the few a priori know spectral components appearing in equation (2.16) are present in the bubble response spectrum. In this work numerical solutions were employed in order to predict the bubble response because higher acoustic pressures are of interest. The use of higher acoustic pressure produces signals with high signal-to-noise ratio as shown in the experimental results of chapter 5. The employment of numerical solutions for solving equation (2.56) introduces another step, the application of a Fourier transform. This stems from the fact that for the interpretation of bubble scattering, as explained in chapter 4, requires the bubble amplitude spectral components, i.e. the bubble response in the frequency domain.

CHAPTER 3: BUBBLE MODELS FOR VISCOELASTIC MEDIA AND THEIR APPLICATION TO SEDIMENTS

This chapter discusses two bubble models applicable to media that possess shear strength and have the potential to be applied to sediments. The first one is based on the Rayleigh-Plesset equation and the second on the Herring-Keller equation. Both models assume that the bubble ambient medium behaves as a linear viscoelastic Voigt model and that the gas inside the bubble follows the polytropic gas law. However the latter encompasses more physical phenomena associated with bubble oscillations and hence it is more reliable for use in the study of nonlinear scattering from bubbles in sediments which is the topic of chapter 7. The last section discusses the application of this Herring-Keller like equation to sediments and the advantages over existing bubble models for sediments.

3.1 Rayleigh-Plesset model with shear components

Leighton (2007) derived a bubble dynamics equation for bubble dynamics in elastic solids. His work is based on the approach of Church (1995) and follows the formulation of the Rayleigh-Plesset equation. Accordingly, the assumptions two to eight as listed in section 2.1.1 for the Rayleigh-Plesset equation for fluid media are valid here for the analogous Rayleigh-Plesset equation for elastic media. The equation in Leighton (2007) reads:

$$\rho_s R\ddot{R} + \frac{3}{2}\rho_s \dot{R}^2 = p_g - \frac{2\sigma}{R} - \frac{\partial \sigma}{\partial R} - \frac{4}{R}\left(G_s\left(R - R_{s0}\right) + \eta_s \dot{R}\right) - p_\infty(t), \tag{3.1}$$

where ρ_s is the density of the surrounding solid medium. The shear forces acting on the bubble boundaries have been taken into account through the medium shear modulus G_s. In equation (3.1), the surface tension effects have acquired an extra term $\partial\sigma/\partial R$ which represents surface tension variations at the bubble boundaries. Here this term is set equal to zero because the number of particles at the bubble boundaries is assumed constant at all times. The term

R_{s0} denotes the unstrained bubble radius which equals the equilibrium radius R_0 because no mass exchange takes place at the bubble boundaries:

$$R_{s0} = R_0 \tag{3.2}$$

Under these assumptions, at the beginning of bubble insonification, t=0, the gas pressure in the bubble p_g, is in equilibrium with the ambient pressure according to equation (2.7). Thus equation (3.1) can be written as:

$$\rho_s R\ddot{R} + \frac{3}{2}\rho_s \dot{R}^2 = \left(p_0 + \frac{2\sigma}{R_0} - p_v \right)\left(\frac{R_0}{R} \right)^{3\kappa} - \frac{2\sigma}{R} - \frac{4}{R}\left(G_s \left(R - R_0 \right) + \eta_s \dot{R} \right) - p_0 - P(t) \tag{3.3}$$

When a small amplitude series expansion is applied to equation (3.3), (following the same procedure as outlined section 2.1.1), the equation takes the following dimensionless form:

$$\underbrace{\ddot{x} + 2\beta_{vis}\dot{x} + \omega_{0s}^2 x}_{\text{linear}} \underbrace{- \left(\frac{3\kappa+1}{2}\omega_{0s}^2 - \frac{4G_s}{\rho_0 R_0^2} \right) x^2}_{\text{quadratic nonlinearity}} + \underbrace{\frac{3}{2}\dot{x}^2 + \ddot{x}\,x}_{\text{dynamic nonlinearity}} + \underbrace{2\beta_{vis}\,\dot{x}\,x}_{\substack{\text{nonlinear viscous} \\ \text{damping}}} = -\frac{P(t)}{\rho_s R_0^2} \tag{3.4}$$

where ω_{0s} is the bubble eigenfrequency in the (visco-) elastic solid:

$$\omega_{0s}^2 = \frac{3\kappa\left(p_0 + \frac{2\sigma}{R_0} - p_v \right) - \frac{2\sigma}{R_0} + 4G_s}{\rho_s R_0^2}. \tag{3.5}$$

The only form of damping present is the viscous damping which has the expression of equation (2.48). If the surface tension and the vapour pressure are set equal to zero, equation (3.5) becomes identical with the expression derived by Andreeva (1964) for the fundamental pulsation frequency of a gas bubble in fish tissue:

$$\omega_{0s}^2 = \frac{3\kappa p_0 + 4G_s}{\rho_0 R_0^2}. \tag{3.6}$$

The limiting factor in applying this equation is the assumption of the medium incompressibility, in other words the lack of radiation damping. For this reason a Keller-Miksis like model would be more suitable. This model is discussed in the following paragraphs.

3.2 Keller-Miksis bubble model with shear components

The bubble model discussed in this section combines the general form of the Keller-Miksis equation, equation (2.60) with the linear Voigt model. It was first proposed by Yang and Church (2005) to study the dynamics of bubbles in soft tissue. This model was modified further in this PhD work for application to sediments. Here the theory of this equation is discussed whereas the application to sediments is elucidated in the section 3.4 of this chapter. The particular equation of the Herring-Keller-Miksis family used by Yang and Church (2005) relates the bubble radius R and wall velocity $\dot{R}$ to the inertial, forcing and dissipative terms through equation (2.60). The form of this equation is discussed here.

The shear strength of the medium affects the pressures p_{L} and p_{∞}. The pressure at the bubble wall is evaluated according to Leighton (2007) as:

$$p_{\mathrm{L}} = p_{\mathrm{g}} - p_{\sigma} + T_{\mathrm{rr}}(R,t), \tag{3.7}$$

where $T_{\mathrm{rr}}(R,t)$ is the stress tensor at the bubble boundary. The pressure far from the bubble equals to:

$$p_{\infty}(t) = p_0 + P(t) + T_{\mathrm{rr}}(R,t) + 3\int_R^{\infty} (T_{\mathrm{rr}}/r)dr\,. \tag{3.8}$$

The integral $\int_R^{\infty} (T_{\mathrm{rr}}/r)dr$ is the sum of the near and far field radial components of the stress tensor which comprises the elastic and lossy (viscous) parts of the tensor. Because of the

assumed spherical symmetry, the radial stress component depends only on the radial deformation of the medium at distance r from the bubble centre. For a Hookean medium the elastic part of the tensor component T_{rr} is expressed in terms of the radial strain $\varepsilon_{\mathrm{rr}}$ as (Reismann, 1980):

$$T_{\mathrm{rr\_elastic}} = (\lambda_{\mathrm{s}} + 2G_{\mathrm{s}})\frac{\partial \varepsilon_{\mathrm{rr}}}{\partial r} + 2\lambda_{\mathrm{s}}\frac{\varepsilon_{\mathrm{rr}}}{r}, \tag{3.9}$$

where λ_{s} is the first Lamé constant and G_{s} is the modulus of rigidity (the dynamic shear modulus, or second Lamé constant). In incompressible conditions, spherical divergence or convergence of particle velocity gives the radial strain $\varepsilon_{\mathrm{rr}}$ through conservation of mass, equation (2.1).

Assuming small deformation rates, the viscous dissipation is proportional to the viscosity of the medium. As a result, the viscous part of the radial stress tensor can be expressed as a function of the shear viscosity η_{s} of the host medium outside of the bubble wall as

$$T_{\mathrm{rr\_viscous}} = 2\eta_{\mathrm{s}}\frac{\partial \varepsilon_{\mathrm{rr}}}{\partial t}. \tag{3.10}$$

The radial strain rate is approximated using equation (2.1) according to:

$$\begin{aligned} &\frac{\partial \varepsilon_{\mathrm{rr}}}{\partial t} \cong \frac{\partial u}{\partial r} \Rightarrow \\ &\frac{\partial \varepsilon_{\mathrm{rr}}}{\partial t} = -2\frac{R^2}{r^3}\dot{R}. \end{aligned} \tag{3.11}$$

Evaluation of the elastic stress component depends on the approximation for the medium strain. For small amplitudes, the radial strain component is approximated as follows:

$$\varepsilon_{\mathrm{rr}} \cong \frac{\Delta r}{r} = \left(\frac{R}{r}\right)^2 \frac{\Delta R}{r} \Rightarrow \tag{3.12}$$

$$\frac{\Delta r}{r} = \left(\frac{R}{r}\right)^2 \frac{\left(R - R_0\right)}{r}.$$

Hence the expression of instantaneous strain of equation (3.12) becomes:

$$\varepsilon_{\mathrm{rr}} \cong \frac{R^2}{r^3}\left(R - R_0\right). \tag{3.13}$$

Substituting the expression of equation (3.13) into (3.9) leads to cancellation of the terms containing the first Lamé parameter and the elastic components $T_{\mathrm{rr\_elastic}}$ becomes:

$$T_{\mathrm{rr\_elastic}} = 2G_{\mathrm{s}} \frac{\partial \varepsilon_{\mathrm{rr}}}{\partial r}. \tag{3.14}$$

Taking both the elastic and lossy characteristics of the medium together (equations (3.14) and (3.10)) (Church, 1995), the radial component of the stress tensor is:

$$T_{\mathrm{rr\_SA}} = -4\frac{R^2}{r^3}\left(G_{\mathrm{s}}\left(R - R_0\right) + \eta_{\mathrm{s}}\dot{R}\right), \tag{3.15}$$

and the integral for the medium in equation (3.8) can be evaluated with equation (3.15) (Leighton, 2007):

$$3\int_R^\infty \frac{T_{\mathrm{rr}}}{r} dr = -4G_{\mathrm{s}} \frac{R - R_0}{R} - 4\eta_{\mathrm{s}} \frac{\dot{R}}{R}. \tag{3.16}$$

For large amplitude pulsations equation (3.15) is not valid. In this case the radial strain is better approximated by equation (3.17) (Yang, 2005):

$$\varepsilon_{\mathrm{rr}} = -\frac{2}{3r^3}\left(R^3 - R_0^3\right). \tag{3.17}$$

For the viscous part of the radial strain of equation (3.9) we keep the same approximation because the stress rates involved are relatively small. Hence taking both the lossy and elastic characteristics of the medium together the radial component of the stress tensor becomes:

$$T_{\mathrm{rr\_LA}} = -\frac{4}{r^3}\left(\frac{G_\mathrm{s}\left(R^3 - R_0^3\right)}{3} + \eta_\mathrm{s} R^2 \dot{R}\right). \tag{3.18}$$

The stress tensor integral of equation (3.8) results from integration of (3.18) at R according to:

$$3\int_R^\infty \frac{\mathrm{T}_{rr}}{r} dr = -\frac{4}{3} G_\mathrm{s} \frac{R^3 - R_0^3}{R^3} - 4\eta_\mathrm{s} \frac{\dot{R}}{R}. \tag{3.19}$$

Both the small and large amplitude assumptions, equations (3.15) and (3.19) respectively give the general form for the radial stress tensor acting on a Voigt solid:

$$3\int_R^\infty \frac{T_{\mathrm{rr}}}{r} dr = -4\left(G_\mathrm{s}\varepsilon_{\mathrm{rr}} + \eta_\mathrm{s}\frac{\partial \varepsilon_{\mathrm{rr}}}{\partial t}\right). \tag{3.20}$$

Since this Herring-Keller like model was studied in this thesis for large amplitudes, the tensor in the form of equation (3.19) will be used rather than from equation (3.15). The model presented in this report results by substitution of equations (3.7), (3.8), (3.18) and (3.19) in (2.60):

$$\begin{aligned}
&\left(1 - \frac{\dot{R}}{c_\mathrm{P}}\right) R\ddot{R} + \left(1 - \frac{\dot{R}}{3c_\mathrm{P}}\right)\frac{3}{2}\dot{R}^2 = \\
&\left(1 + \frac{\dot{R}}{c_\mathrm{P}}\right)\frac{1}{\rho_\mathrm{s}}\left[p_\mathrm{g} - \frac{2\sigma}{R} - \frac{4G_\mathrm{s}\left(R^3 - R_0^3\right)}{3R^3} - \frac{4\eta_\mathrm{s}\dot{R}}{R} - p_0 - P_1 \sin\left(\omega\left(t + \frac{R}{c_\mathrm{P}}\right)\right)\right] + \\
&\qquad \frac{R}{\rho_\mathrm{s} c_\mathrm{P}}\left[\left(-3\kappa p_\mathrm{g} + \frac{2\sigma}{R}\right)\frac{\dot{R}}{R} - 4G_\mathrm{s}\frac{R_0^3 \dot{R}}{R^4} - 4\eta_\mathrm{s}\left(\frac{\ddot{R}}{R} - \frac{\dot{R}^2}{R^2}\right)\right]
\end{aligned} \tag{3.21}$$

The sound speed entering equation (3.21) is the compressional (or P-wave) sound speed in the bubble- free solid medium which is the equivalent sound speed propagating in liquids. When liquids were considered this clarification was not necessary because liquids posses only

bulk modulus and therefore only compressonal waves can propagate through them. As such liquids cannot bear shear forces and therefore no shear wave can propagate. However in solids and marine sediments more then one waves can propagate as they posses both bulk and shear properties. In particular for application to sediments the assumption of the existence of one pressure wave must be examined, this is done in Chapter 6.

To study the linear bubble dynamics problem and discuss the importance of the damping effects encompassed in equation (3.21), a linear bubble dynamics equation is derived from equation (3.21) using the same methods with those used to derive the linear bubble dynamics equation from the Herring-Keller equation (2.60). Using equation (2.12) and following the procedures outlined in 2.2.3, the linear part of the problem can be defined through the bubble damping constants and natural frequency. The resulting equation has the typical form of a linear oscillator. In analogy with equation (2.66):

$$\ddot{x}+2\beta_{\mathrm{HK\_s}}\dot{x}+\omega_{\mathrm{HK\_s}}^2 x=-\frac{P(t)}{m_{\mathrm{HK\_s}}}, \tag{3.22}$$

where the bubble natural frequency $\omega_{\mathrm{HK\_s}}$ equals:

$$\omega_{\mathrm{HK\_s}}^2=\left(3\kappa p_{\mathrm{g0}}-\frac{2\sigma}{R_0}+4G_{\mathrm{s}}\right)\Bigg/\left(\rho_{\mathrm{s}}R_0^2+\frac{4\eta_{\mathrm{s}}R_0}{c_{\mathrm{s}}}\right). \tag{3.23}$$

The damping, $\beta_{\mathrm{HK\_s}}$, is the sum of the damping constants as appear in equations (2.69) to (2.71) plus an additional damping term stemming from the elasticity of the surrounding medium. This is the elastic damping which has the expression:

$$\beta_{\mathrm{el}}=\frac{2G_{\mathrm{s}}}{\left(c_{\mathrm{P}}\rho_{\mathrm{s}}R_0+4\eta_{\mathrm{s}}\right)}. \tag{3.24}$$

Assuming $P(t)=P_1\cos(\omega_1 t)$, equation (3.22) has the standard solution of a first order linear equation:

$$x = \frac{P_1}{\rho_0 R_0^2 \sqrt{\left(\omega_{\mathrm{HK\_s}}^2 - \omega_1^2\right)^2 + \left(2\beta_{\mathrm{HK\_s}}\omega_1\right)^2}} \cos(\omega_1 t + \phi_{\omega_1}) \tag{3.25}$$

Where the phase term is: (3.26)

$$\tan\phi_{\omega_1} = -\frac{2\beta_{\mathrm{HK\_s}}}{\omega_{\mathrm{HK\_s}}^2 - \omega_1^2}.$$

In Figure 3.1 (a) and (b) these linear damping terms are plotted as function of insonification frequency for a single bubble with equilibrium radius $R_0 = 10$ μm and $R_0 = 50$ μm respectively. These plots were produced using the input parameters of Yang and Church (2005), given in Table 3.1. The damping terms for $R_0 = 10$ μm was examined also in the paper of Yang and Church (2005) and Figure 3.1 (a) is reproduction of figure 2 of their publication.

Table 3.1: Input parameters for the computations of Figures 3.1, 3.2 and 3.3.

Property	Value
Depth (m)	-
p_0 (kPa)	101
ρ_s (kg/m^3)	1060
c_P (m/s)	1540
G_s (MPa)	1
η_s (Pa.s)	0.015
σ (N)	0.056
κ (-)	1.4
D_g (-)	2.1e-5

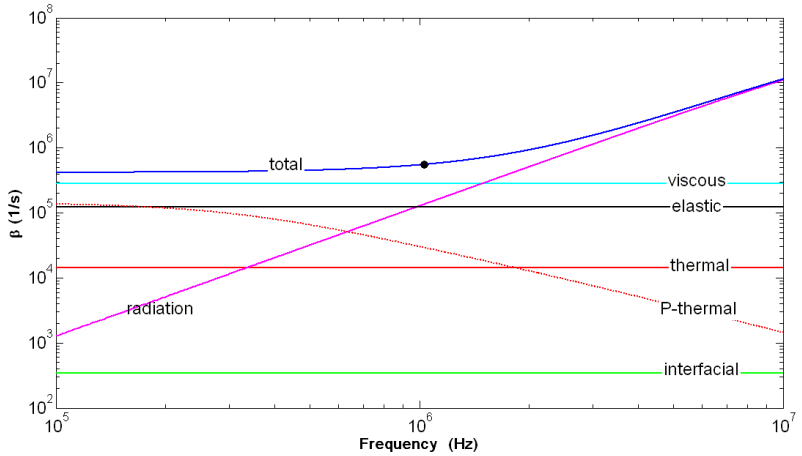

(a)

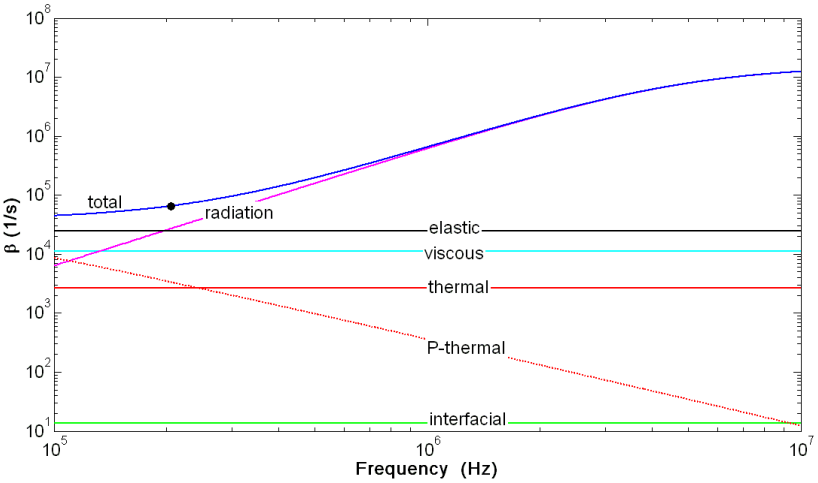

(b)

Figure 3.1 Dimensional damping constants versus frequency for bubble equilibrium (a) 10 μm and (b) 50 μm, for the parameters listed in table 3.1. The dot indicates the resonance frequency of the bubble.

The plots of Figure 3.1 show that for near-resonant gas bubbles in viscoelastic media the viscous and elastic forces are more than the thermal effects, as opposed to near-resonant gas bubbles in a fluid medium (compare with Figure 2.3). The next important damping mechanism to consider is the acoustic radiation damping which near resonance takes values of the same order of magnitude and the viscous damping. In Figure 3.1, the thermal damping constant according to Prosperetti (1977) analysis, equation (2.54), denoted by P-thermal, has been

plotted (dotted lines) for comparison. The damping factors will be discussed further in section 3.4 with input parameters for marine sediments.

3.3 Numerical examples

In this section the two bubble dynamics equation for viscoelastic media, equations (3.1) and (3.21) are compared using numerical simulations. In Figure 3.2 (a) and (b) the time-series of the radius response and emitted pressure of a single bubble of R_0 =10 microns respectively is plotted versus time. In Figure 3.3 the same quantities are plotted for a bubble with R_0 =50 microns.

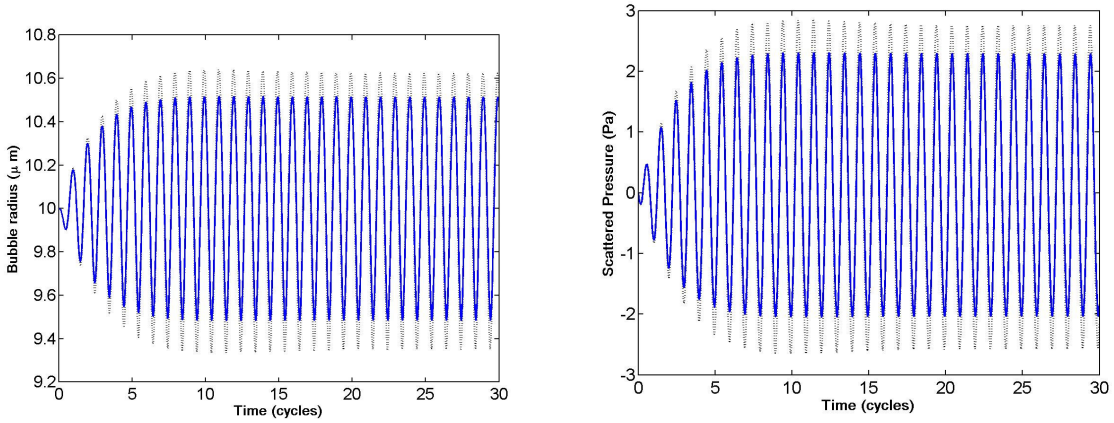

(a) *(b)*

Figure 3.2:Bubble radius time response (a) and the corresponding emitted pressure at 1 m (b) of an air bubble (R_0=10 μm) in a viscoelastic medium under near-resonance frequency of insonification (1 MHz) of a pressure wave (30 kPa, zero-to-peak), computed using the HK like equation (blue solid line) and the Rayleigh-Plesset like equation (black dotted line).

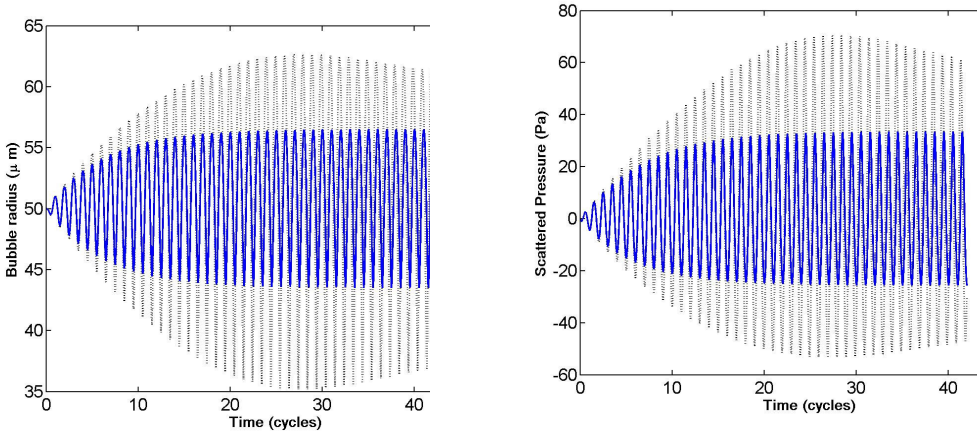

(a) *(b)*

Figure 3.3: Bubble radius time response (a) and the corresponding emitted pressure at 1 m (b) of an air bubble (R_0=50 μm) in a viscoelastic medium under near-resonance frequency of insonification (200 kHz) of a pressure waves (30 kPa, zero-to-peak), computed using HK like equation (blue solid line) and the Rayleigh-Plesset like equation (black dotted line).

The blue lines indicate the numerical results using equation (3.21) whilst the black dotted lines indicate numerical results using equation (3.1). The input parameters used for the numerical simulations are given in table 3.1 (Yang and Church, 2009). These examples are used here only to highlight some general features because the input parameters of Table 3.1 are borrowed from ultrasonics and therefore they are not applicable to sediments. For this reason only two computational examples are shown below. The scattered pressure in the time domain was computed by substitution of the radius time series information in equation (4.29), assuming 1 m radial distance from the centre of the bubble. In Figures 3.2 and 3.3 the importance of including dissipation mechanisms becomes evident. Using the information of Figures 3.1, it can be inferred that the significant difference between the two models, shown in Figures 3.2 and 3.3 is caused mainly from the radiation damping.

For the two models the gas is assumed to undergo adiabatic compression and expansion ($\kappa = \gamma$). A complex polytropic index (κ_P) could have been introduced similar to the treatment described in section 2.3. However in this case the models are bound to be considered as approximations. Additionally as shown in Figure 3.1, the thermal damping factor has much

smaller value compared to the elastic, viscous and radiation damping factors. Hence the accuracy of modelling the bubble response depends mainly on modelling the elastic, viscous and radiation damping factors rather than the thermal damping. The damping factors for bubbles in marine sediments are discussed in the next section.

3.4 Application of the Herrring-Keller bubble model with shear components to sediments

The bubble dynamics theory developed in this PhD work in order to interpret sound scattering and propagation from gassy sediments is based on equation (3.21). This equation is used to predict the single bubble response. The collective effect, i.e. the sound speed and scattering from a bubble distribution is discussed in conjunction with scattering theory in chapter 4. Geoacoustic properties and models of gas-free sediments, which are discussed in chapter 6, help finding the correct parameters entering the bubble model of equation (3.21). This model assumes the bubble host medium to be viscoelastic. Literature study, carried out in chapter 6 suggests that this assumption is valid only for muds, limiting the model of equation (3.21) to muddy sediments. Additionally the model of equation (3.21) requires as input parameters the density, shear modulus and viscosity and the compressional wave speed in the gas-free sediment which substitute the counterpart parameters of the viscoelastic medium. Laboratory measurements provided the values for the density and shear modulus. Literature experimental data gave indicative values for the compressional wave speed for gas-free sediments. The viscosity of the sediment was inferred from shear wave attenuation values, which where found in literature. Details of these parameters are explained in chapters 6 and 7. In this section the study is focused on single bubble response using input values acquired experimentally or from literature as detailed in Chapters 6 and 7.

A literature review for existing bubble models in sediments reveals the necessity to develop a new model. The most widely used bubble model, the one of Anderson and Hampton (1980 a, b), was developed for linear scattering interpretation. This model is based on the approach of fitting linear bubble damping constants to the well know expression for the linear scattering

cross section using equations 54-56 of Anderson and Hampton (1980 a). This approach may be a reasonable approximation for linear scattering as it is shown later in this section with Figure 3.7 but it cannot be extended for the interpretation of nonlinear scattering from bubbles either under one or two frequency insonification.

Boyle and Chotiros (1998) presented a model for the interpretation of nonlinear scattering from gas bubbles in sandy sediments. Their model uses analytical solutions of the nonlinear bubble model of Zabolotskaya and Soluyan (1967), which was derived for gas bubbles in water. There are two main reasons for not applying this model here. The first is that their formulation involves analytical solutions, which as discussed in chapter 2 are bound to be not suitable for bubbles in water under a two-frequency insonification with frequencies neither very close nor very far apart in frequencies. The second is that the shear strength of the medium is not taken into account for the bubble dynamics model. Specifically it is known that the shear properties of the bubble ambient medium, here sediment, modify the bubble natural frequency (Andreeva, 1964; Anderson and Hampton, 1980 b) as well as the viscous damping coefficient (Anderson and Hampton, 1980 b). In line with the approach of Boyle and Chotiros (1998), Tegowski *et al.* (2006) used the nonlinearly generated spectral component at the sum frequency to interpret back scattering experiments from the muddy seafloor of the Gulf of Gdansk. The limitation of their model is the same as the limitation of the model of Boyle and Chotiros (1998), i.e. the assumption of treating the mud as fluid.

To apply equation (3.21) for bubbles in sediments, the bubble host medium is considered first. For the cases examined in this work, the bubble host medium, i.e. the gas-free sediment is mud but not with such a high water content that it may be characterised as 'fluid'. In general, the mud at intertidal sites may have such high water content, 90% or more, when first exposed by the retreating tide that it may considered as fluid (McAnally *et al.*, 2007) and various rheological models are used to characterise the mud flow (Whitehouse *et al.*, 2000). However, the experiments took place one to three hours after tidal exposure and the measured density ($\rho_s = 1640 \pm 50\,\mathrm{kg/m^3}$) suggests sediment porosity between 60% and 70%. Consequently, the medium surrounding the bubble is assumed to be an elastic solid framework and a viscoelastic model is assigned to it in order to model the internal friction losses. The assumption that the

medium surrounding the bubble be an elastic solid implies no relative motion between the mineral grains and the pore water. This is valid because, given that small strains are involved in acoustic excitations (according to Stoll (1985) these are approximately 10^{-6}), the low permeability of the mud precludes dynamic relative motion of the pore fluid relative to the skeletal frame (Curtis, 1992). That is, the global flow phenomena become unimportant (see also discussion at the end of section 6.2.2). For this reason the mud surrounding the gas bubble can be modelled as an effective viscoelastic material consisting of the mineral grains plus the pore water and its bulk density is given by equation (6.2). These assumptions for the sediment surrounding the bubble are also found in Anderson and Hampton (1980 b), and Lyons *et al*. (1996). However their approach to incorporating the bubble effects in acoustic scattering differs from the approach of this PhD work as discussed in the rest of this section.

To apply the bubble dynamics model of equation (3.21), the Voigt model was modified to conform to the shear wave attenuation behaviour observed in gas-free muddy sediments, which as it will be discussed in chapter 6 follows by good approximation a linear dependence with frequency. This is achieved, by considering the bubble host medium, i.e. the gas-free sediment, to have a complex shear modulus:

$$G_s^* = G_s + jG_s^{'}, \tag{3.27}$$

and a frequency dependent shear viscosity according to:

$$\eta_s = \frac{G_s^{'}}{\omega}, \tag{3.28}$$

rather than a constant viscosity.

The Voigt model either with constant or frequency dependent viscosity, is applicable to single frequency only. In order to apply the modified Voigt model when more than one frequency is involved, the viscosity η_s, which represents the dissipation in shear, was fitted for the frequencies of interest (i.e. the difference-frequency or twice the pump frequency) using equation (3.28). The value of $G_s^{'}$ is calculated from equation (6.7) by setting the logarithmic decrement equal to 0.2 according to Hamilton (1976). Table 3.2 summarises the input model

parameters. These values will be inserted in the appropriate equation of chapter 4 in order to predict the sound speed, attenuation and scattering from the gas in the form of bubbles.

As published work for nonlinear acoustic scattering from resonant bubbles under the sea bed appears to neglect the sediment shear properties, the new model is compared with existing works for linear scattering and then the effect of shear is discussed. According to Anderson and Hampton (1980 b), the bubble natural frequency has the expression:

$$\omega_{\mathrm{AH}} = \frac{1}{R_0}\left(\frac{3\gamma p_0}{A_{\mathrm{D}}\rho_{\mathrm{s}}} + \frac{4G_{\mathrm{s}}}{\rho_{\mathrm{s}}}\right)^{1/2}, \tag{3.29}$$

where A_{D} is the gas polytropic coefficient (Devin, 1959), which accounts for the heat flow across the bubble boundary. The quantities κ_{P}, equation (2.54) and γ / A_{D} are different expressions for the gas polytropic index. These expressions account for the fact that the bubble gas expansions and contractions are neither purely adiabatic nor isothermal and take values between 1 and γ.

As mentioned by Prosperetti (1977), the expressions γ / A_{D} and κ_{P} are in good agreement when the quantity X, equation (2.52), is less than approximately 50. For values of X greater than 50 the predictions of the two expressions begin to deviate and when the parameter X greater than 100, then Devin's expression for the bubble gas polytropic index tends to infinity (Prosperetti, 1977). As for the cases of interest here the quantity X is bound to be greater than 50, in order to compare like-with-like, the polytropic index follows the expression of Prosperetti (1977), thus the quantity γ / A_{D} is substituted by κ_{p} and the equivalent expression of (3.29) becomes:

$$\omega_{0\mathrm{sP}} = \frac{1}{R_0}\left(\frac{3\kappa_{\mathrm{P}} p_0}{\rho_{\mathrm{s}}} + \frac{4G_{\mathrm{s}}}{\rho_{\mathrm{s}}}\right)^{1/2}. \tag{3.30}$$

With this consideration, the discussion proceeds with comparison of the formulas presented by Anderson and Hampton (1989 a, b) with first order formulas resulting from first order approximations of the model of equation (3.21). Equation (3.23) differs from equation (3.30) in the polytropic index entering these equations and in including surface tension and vapour pressure effects. The polytropic index depends on the gas of the bubble.

In Table 3.2 values of γ for commonly encountered gasses in shallow sediments are given (Kaye and Laby, 1972). Given that for the cases of interest here the bubble gas is of biogenic origin being O_2, CO_2, H_2S and possibly CH_4 (see section 1.1), the vapour pressure is not a relevant quantity.

Table 3.2: Values for the ratio of the principal specific heat capacities for gasses commonly encountered in shallow sediments (Kaye and Laby, 1972).

gas	γ (-)
O_2	1.400
H_2S	1.34
CH_4	1.313
H_2	1.407
N_2	1.401
CO_2	1.300
NH_3	1.336

The bubbles are expected to have surface tension and its value is expected to be closer to the value for bubbles in sea than in fresh water. Additionally, the term $4\eta_s R_0 / c_P$ is negligible for the cases of interest here. Consequently, the equation (3.23) is simplified to:

$$\omega_{0s}^2 = \left(3\kappa \left(p_0 + \frac{2\sigma}{R_0} \right) - \frac{2\sigma}{R_0} + 4G_s \right) \Big/ \rho_0 R_0^2 \ . \tag{3.31}$$

The sensitivity of expressions (3.30) and (3.31) to variations of the polytropic index and the presence of surface tension is examined first. In Figure 3.4 the bubble resonance radius as calculated from equation (3.31) (black line) is compared with the one predicted from equation (3.30) (red dots) with input model parameters as given in Table 3.3. The bubble gas is assumed to be O_2 because this gas is predominantly present in the first top metre of the seafloor where the experiments of this PhD work took place as described in chapter 7. The graph of Figure 3.4 shows that the two expressions are in good agreement. Although not visible, the maximum deviation in their predictions does not exceed the 0.6 %. This is an expected result as the shear modulus is the dominant input parameter and variation of the polytropic index and/or the presence of surface tension do not influence the result in this case.

Table 3.3: Input parameters for the bubble model. The gas is O_2 and the host medium is mud found in Calshot or Mercury site.

Property	Value
Depth below sea floor (m)	0.35
ρ_s (kg/m^3)	1640 ± 50
c_P (m/s)	1450 ± 20
G_s (MPa)	2.6 ± 0.1
$G_s^{'}$ (MPa)	0.16 ± 0.08
p_0 (kPa)	101
σ (N)	0.036
D_g (m^2/s)	1.9e-5
κ (-)	1.4

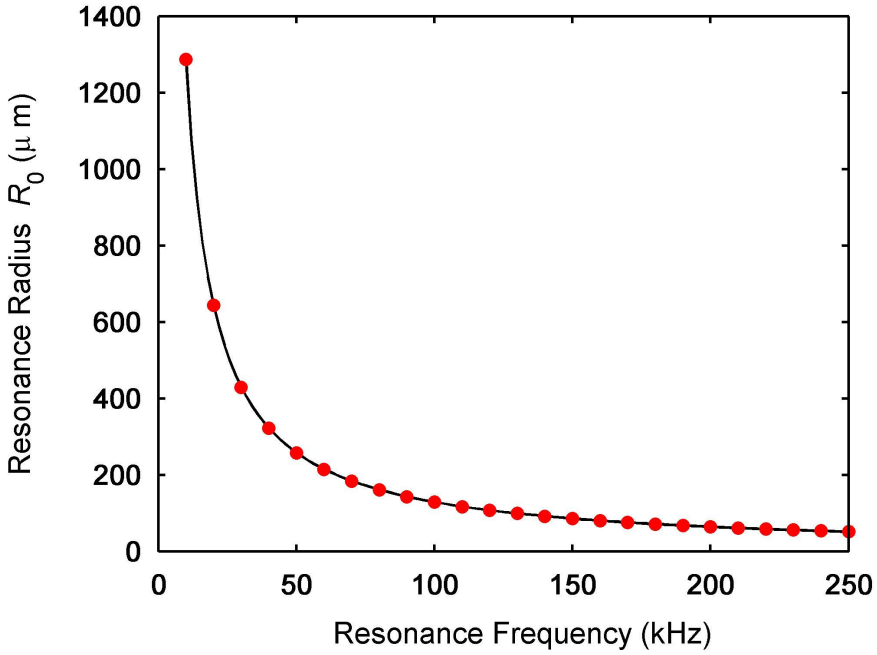

Figure 3.4: Plot showing the bubble resonant size (R_0) versus natural frequency where the solid line is calculated by equation (3.31) and the dots are calculated from equation (3.30), the input parameters for both equations are shown in Table 3.3

To examine the sensitivity of equation (3.30) to variations of the polytropic index, the resonant radius was calculated for two limiting values of κ and a lower value for the shear modulus (G_s =100 kPa). The results are plotted in Figure 3.5; the black line corresponds to κ=1.4 and the red line to κ=1. These values of κ correspond to two limiting cases for the polytropic index; the maximum value corresponds to the adiabatic whilst the minimum value corresponds to isothermal expansions and contractions of the bubble gas. In this case the maximum difference between these two predictions is 10%. On the same figure the resonant bubble sizes when the medium is considered fluid (G_s =0) is plotted for comparison. The green and blue lines show the bubble resonant size as function of resonant frequency for gas bubbles in water for κ=1.4 and κ=1 respectively.

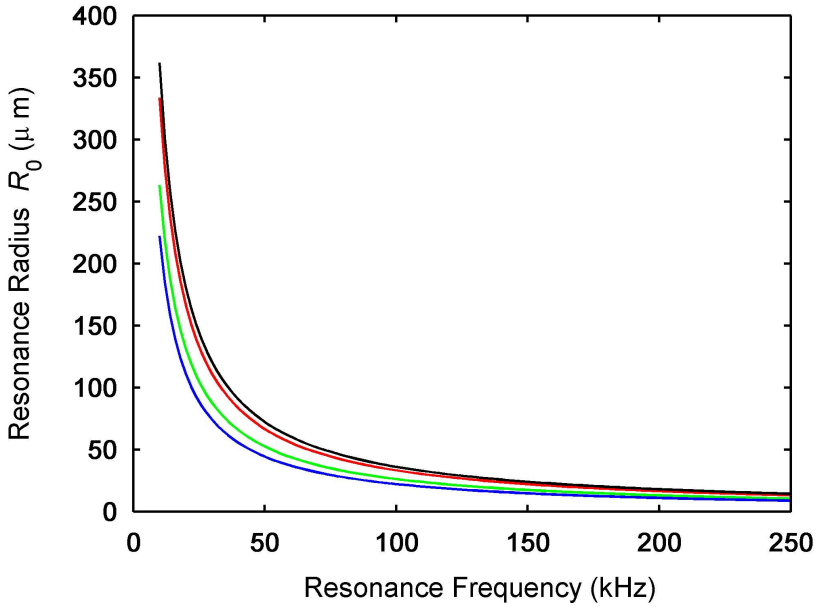

Figure 3.5: Plot showing the bubble resonant size (R_0) versus natural frequency where the black and red solid lines were computed from equation (3.31) for $\kappa = 1.4$ and $\kappa = 1$ respectively. The green and blue lines were computed by the same equation assuming a fluid medium ($G_s = 0$) and $\kappa = 1.4$ (green line) and $\kappa = 1$(blue line). All other input parameters are as shown in Table 3.3

Apart from the natural frequency, the damping constants are the next important quantities to be computed with the new model for bubble pulsations in sediments. These damping terms are plotted for a bubble with equilibrium radius 130 and 400 microns in Figure 3.6 (a) and (b) respectively, using the values given in Table 3.3. For comparison the thermal damping according to the theory of Prosperetti (1977) is plotted with a dotted line with the label P-thermal. As for viscoelastic media, the elastic and viscous damping effects are the most important and the third important damping constant to consider is the radiation damping, whereas the interfacial damping stemming from the surface tension is of least importance. As expected, in Figure 3.6 the viscous damping is inversely proportional to the frequency as the viscosity is also inversely proportional to frequency.

Using information from Figure 3.4 and Figure 3.6 the Q-factor, given by equation (2.26), is estimated to be between 5 and 6 in contrast to water which lies approximately between 15 and 25. Additionally using these figures, it is observed that thermal effects are not of great importance and therefore, ignoring the exact composition of the gas in the sediment would not

introduce significant errors in calculations. Here it has to be noted that these observations are valid when the gas-free sediment surrounding the bubble has the properties listed in Table 3.3. To extent such statements to other sediments, the bubble damping factors and natural frequency have to be computed for the frequencies of interest.

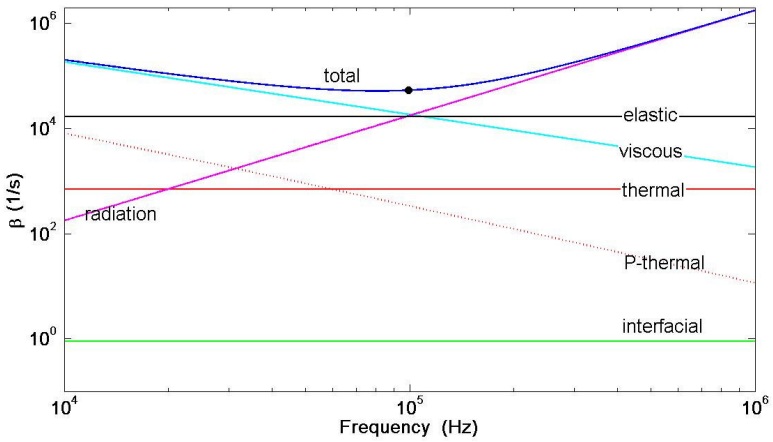

(a)

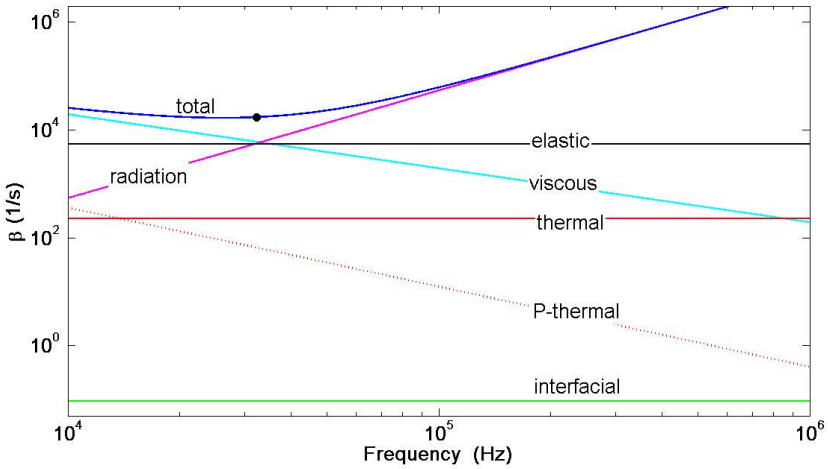

(b)

Figure 3.6: Dimensional damping constants versus frequency for bubble equilibrium (a) 130 μm and (b) 400 μm, for the parameters listed in Table 3.3. The dot indicates the resonance frequency of the bubble.

Differences in expressions used to calculate single bubble damping factors manifest in calculations of the sound speed in bubbly water and of linear scattering cross sections. In this chapter these differences are briefly discussed when only one bubble is under consideration. The results will be extended for a bubble population in Chapter 4. The next set of simulations aims to compare the Anderson and Hampton (1989 a, b) approach with the model presented in this work in terms of bubble scattering cross sections. The analytical expression (4.28) was used for the calculation of a single bubble cross section as function of equilibrium bubble radius for 100 kHz and 30 kHz of acoustic excitation, shown in Figure 3.7 (a) and (b) respectively. The red lines indicate the scattering cross sections as calculated by substitution of the sum the three bubble damping coefficients (i.e. the viscous, radiation and thermal damping) in the analytical expression for the scattering cross section according to the approach of Anderson and Hampton (1989 a,b)[4].

The black lines indicate the scattering cross sections as calculated using equation in (4.28) by substituting for β_{tot}, the term $\beta_{\text{HK\_s}}$ as predicted from the model of (3.22) (the surface tension was ignored). The difference between the two approaches is the additional damping term given by equation (3.24). As shown in Figure 3.7 the two approaches differ at resonance. This difference depends on the bubble size and is more pronounced for smaller bubbles. If the plots of Figure 3.7 were to be compared those of Figure 2.4, i.e. to compare the scattering cross sections of bubbles sediment and water, then the difference between the geometric cross section of the resonant bubbles in sediment and in water must be taken into account. As bigger bubbles have larger geometric cross sections, comparing the dimensionless quantity $\sigma_s / \pi R_0^2$ for sediment and water would give a better estimate of the relative scattering efficiency. Using this dimensionless quantity and Figure 2.4 (b) and Figure 3.7 (b), the scattering efficiency of a resonant bubble at 30 kHz in water is about 5 times greater than that of the corresponding resonant size in sediments with properties given in Table 3.3.

[4] As for the bubble natural frequency, the thermal damping follows the expression of Prosperetti (1977) instead of Devin (1959).

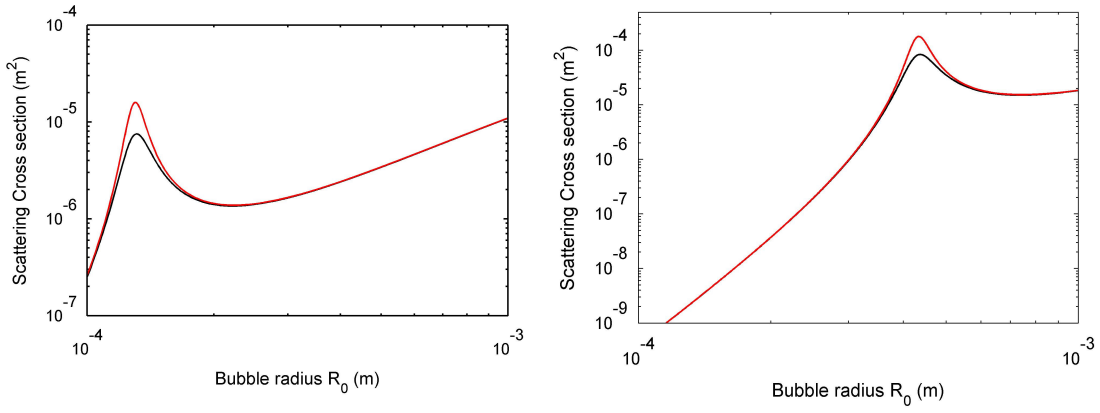

(a) *(b)*

Figure 3.7: Scattering cross section as calculated from equation using the damping factors following the Anderson and Hampton approach (red line) and using the damping factors of the new model (black line), for a range of O_2 bubble sizes in mud insonified at (a) 100 kHz and (b) 30 kHz. The surface tension was not taken into account; all other input parameters are given in Table 3.3.

3.5 Summary and discussion

In this chapter two bubble dynamics models applicable to viscoelastic media were studied. The first model resembles to the Rayleigh-Plesset equation and the second to the Herring-Keller equation both widely applied to bubbles in water and discussed in Chapter 2. The additional effect taken into account here is the shear strength of the bubble host medium. Numerical examples showed that for viscoelastic media the medium elasticity plays dominant role in determining the bubble natural frequency and damping. The next important damping term appeared to be the radiation damping. Based on these observations, it was chosen to apply the model of equation (3.21) to sediments retaining the assumption that the bubble gas follows the adiabatic gas law during pulsation. For the first time the model of equation (3.21) was applied to sediments. Literature review reveals that there are no other nonlinear bubble dynamics models for sediments. The landmark paper of Anderson and Hampton (1980 a,b) deals with linear bubble pulsations. To compare the new model with this of Anderson and Hampton (1980 a,b), equation (3.21) was linearised by retaining terms up to the first order. Expressions for the linear bubble damping and natural frequency were derived and compare

with those used by Anderson and Hampton. Simulation results showed that the linear quantities are in close agreement which reassured the use of this new equation for modelling nonlinear bubble scattering which is of interest for this work. Numerical solutions of equation (3.21) will be employed to interpret the nonlinear scattered pressure from each bubble size. The theory to interpret the collective effect of sound scattering by bubbles is elaborated in the next chapter.

CHAPTER 4: ACOUSTIC SCATTERING FROM AN ENSEMBLE OF BUBBLES AND BUBBLE SIZING METHODS

The previous chapters were focused on the modelling of the response of a single bubble to an external acoustic field. This is the first step in modelling the acoustic scattering from a medium that contains bubbles. The next step, which is discussed here, is the prediction of the collective response of an ensemble of bubbles from the individual bubble responses. The following paragraphs aim to underline the assumptions made in order to solve the forward and the inverse scattering problem, the latter being the basis of the incoherent bubble sizing techniques. The chapter outlines the theory of scattering from an ensemble of small particles (scatterers) and describes the inversion techniques which were used to infer bubble populations in water and sediments.

In the literature, inversion techniques are sometimes referred to as coherent or incoherent. This categorization reflects the manner in which the data are interpreted. The coherent techniques use the method of averaging to interpret the bubble size distributions from attenuation and sound speed measurements of sound propagated through a bubble cloud. The incoherent techniques interpret the (back) scattered intensity and the scattering cross sections, which are the relevant measured quantities. To apply these techniques in bubble sizing the concept of coherent and incoherent scattering is clarified and expressions for the ensemble scattering cross sections are derived for the case of resonant bubbles in water and sediment.

4.1 Coherent and incoherent scattering

Consider the case when bubbles (or other scatterers) are present randomly over the propagation path of an acoustic wave. Each bubble scatters the sound with different phase. The scattered sound which is spatially and temporally correlated with the incident wave is the coherent part, whilst the phase of the incoherent part is stochastically related to the phase of the incident waves. The spatial incoherency, which is of interest for this work, depends on the

bubble spacing and the relation of this spacing with the wavelength. As mentioned by Sarkar and Prosperetti (1994), the transition between the coherent and incoherent regime is continuous. Here the two limiting cases are considered: the incoherent regime where the scattered power is proportional to the number of scatterers N and coherent regime where the scattered power is proportional to N^2. The physics of scattering from an ensemble of scatterers is explained in chapter 11 of Morse (1953). Here the main points are repeated in order to extend the theory to bubbles and underline the assumptions made for the interpretation of the experimental scattering data.

To simplify the analysis, the medium of propagation is considered non-dispersive and lossless. The incident pressure field $p(\boldsymbol{r},t)$ is assumed a single-frequency plane wave and it is considered within a limited time period. During this limited time period the ensemble of bubbles is considered frozen in space (in practice this is achieved with the use of a short pulse as explained in paragraph 5.2). Under these assumptions the analysis proceeds with the equivalent description of the incident pressure field in the frequency domain: $\tilde{p}(\boldsymbol{r},\omega)$. The problem is described using Figure 4.1. In this figure N identical scatterers are assumed to be randomly distributed inside a small spherical region of radius a. The point O is the reference point located in the centre of this region and it is assumed to have zero phase in the vector space. The n^{th} scatterer is located at a distance $\boldsymbol{r}_n$ from this centre. The problem has no azimuthal dependence and the polar (zenith) angle ϑ suffices for the description of the problem. Under these assumptions the plane wave incident on the whole ensemble is:

$$\tilde{p}(\boldsymbol{r},\omega) = P_{\text{i}}(\omega)\, e^{ikr\cos\vartheta}, \tag{4.1}$$

where $P_{\text{i}}(\omega)$ is the pressure amplitude, k is the magnitude of the wave vector $\mathbf{k}$ at the direction of the observation point P and r is the radial distance from the centre of the sphere to the observation point. Each scatterer in the ensemble scatters the incident wave with angular distribution function $f(\omega,\vartheta_n)$ (in the literature, the function f is also encountered as 'form function' or 'scattering length'), which depends on the nature of the scatterer and on the frequency of the incident wave.

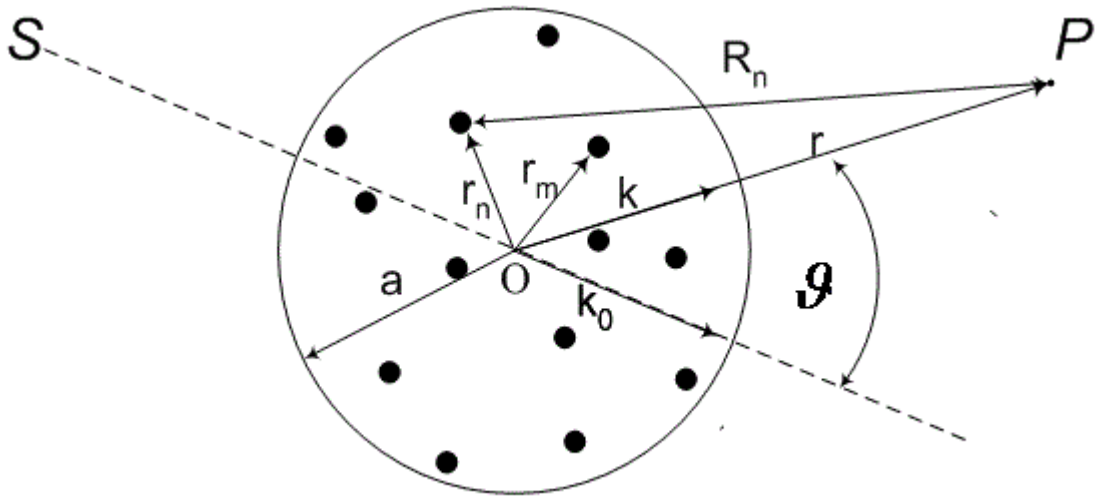

Figure 4.1: Modelling an ensemble of random scatterers. The ensemble is assumed to be spherical and the reference point with zero phase is its centre. The incident wave originates from a point S whilst the measurement point is at P on the same plane with S and O at an angle ϑ.

Assuming negligible attenuation of the medium, the scattered pressure from each scatterer at the point P is (Morse, 1953):

$$\tilde{p}_{\mathrm{s}}(\boldsymbol{r},\omega) = P_{\mathrm{i}}(\omega) f(\omega,\vartheta_n) \frac{e^{i(\mathbf{k}_0\cdot\mathbf{r}_n + kR_n)}}{R_n}. \tag{4.2}$$

For the subsequent derivations, it is assumed that all scatterers are identical having the same form function. Also the observation point is located at a much larger distance relative to the radius of the ensemble region ($r >> a$) so that the distance of each scatterer to the observation point R_n, is approximately equal to the distance of the centre of the ensemble with respect to the observation point, i.e.: $R_{\mathrm{n}} \sim r$. Then equation (4.2) is approximated by:

$$\tilde{p}_{\mathrm{s}}(\boldsymbol{r},\omega) = P_{\mathrm{i}}(\omega) \frac{e^{ikr}}{r} f(\omega,\vartheta) e^{i\boldsymbol{\tau}\cdot\mathbf{r}_n}, \tag{4.3}$$

where the vector quantity $\boldsymbol{\tau}$ corresponds to the difference of the wave vector of the incident wave $\boldsymbol{k}_0$ and the wave vector of the scattered wave $\boldsymbol{k}$, i.e. $\boldsymbol{\tau} = \boldsymbol{k}_0 - \boldsymbol{k}$ and has magnitude $\tau = 2k\sin(\vartheta/2)$. The total pressure field at point P is:

$$\tilde{p}_{\mathrm{s\,tot}}(\boldsymbol{r},\omega) = P_{\mathrm{i}}(\omega)\frac{e^{ikr}}{r} f(\omega,\vartheta)\sum_{n=1}^{N} e^{i\boldsymbol{\tau}\cdot\boldsymbol{r}_n} . \tag{4.4}$$

In equation (4.4) each component of the wave at P has its own phase and the net result of the vector summation depends on the degree of regularity of positioning of the scatterers. When the scatterers are distributed in a non-regular manner, it is easier to see the resulting field characteristics by considering the power of the field. Multiplying equation (4.4) with its complex conjugate results in:

$$\left|\tilde{p}_{\mathrm{s\,tot}}(\boldsymbol{r},\omega)\right|^2 = P_{\mathrm{i}}^2(\omega)\frac{\left|f(\omega,\vartheta)\right|^2}{r^2}\sum_{m,n=1}^{N} e^{i\boldsymbol{\tau}\cdot\boldsymbol{r}_{mn}} , \tag{4.5}$$

where $\boldsymbol{r}_{mn} = \boldsymbol{r}_m - \boldsymbol{r}_n$ is the vector from the n$^{\mathrm{th}}$ to the m$^{\mathrm{th}}$ scatterer. After separation of the terms $m = n$, equation (4.5) can be written as:

$$\left|\tilde{p}_{\mathrm{s\,tot}}(\boldsymbol{r},\omega)\right|^2 = P_{\mathrm{i}}^2(\omega)\frac{\left|f(\omega,\vartheta)\right|^2}{r^2}\left[N + \sum_{m\neq n} e^{i\boldsymbol{\tau}\cdot\boldsymbol{R}_{mn}}\right]. \tag{4.6}$$

Equation (4.6) can be seen as a summation of two terms. The first term $N\frac{\left|f(\vartheta)\right|^2}{r^2}P_{\mathbf{i}}^2(\omega)$ is the incoherent part of the scattered field and the second term $\frac{\left|f(\vartheta)\right|^2}{r^2}P_{\mathbf{i}}^2(\omega)\sum_{m\neq n} e^{i\boldsymbol{\tau}\cdot\boldsymbol{R}_{mn}}$ is the coherent part of the scattered field, which takes into account the phase relations between the various scattered waves. If the value of τ is large enough so that the dot product $\boldsymbol{\tau}\cdot\boldsymbol{R}_{mn} > \pi/2$ for most values of n and m and if the scatterers are randomly and symmetrically distributed around the point O, then the exponentials in the double sum will

cancel out and leave only the incoherent term. If this is true, then backscattering from random scatterers such as bubbles at sea is incoherent.

However, if τ is small enough, there is still a coherent part which will predominate in the forward direction. Without repeating the analysis here, it was shown in paragraph 11.3 of Morse (1953) that in this case the signal scattered power can be approximated as:

$$\left|\tilde{p}_{\mathrm{s\,tot}}\right|^2 = P_{\mathrm{i}}^2(\omega)N^2\frac{\left|f(\omega,\vartheta)\right|^2}{r^2}\left[1-\frac{2}{5}\frac{N-1}{N}k^2a^2\sin^2\left(\vartheta/2\right)\right]. \tag{4.7}$$

Equation (4.7) shows that even when the scatterers are randomly spaced, coherent scattering can dominate when $\tau a << 1$ or equivalently $2\pi a\sin\vartheta/2 << \lambda$. In the special case where the term $\sin\left(\vartheta/2\right)$ equals zero, i.e. in the forward direction, then the scattered power is equal to $P_{\mathrm{i}}^2(\omega)N^2\frac{\left|f(\omega,\vartheta)\right|^2}{r^2}$, that is the field is coherent for all wavelengths.

According to the work of Foldy (1945) and Lax (1951), the forward propagating wave through an ensemble of N scatterers of radius R_0 has an effective wave number k_{b} given by:

$$k_{\mathrm{b}}^2 = k^2 + N_{\mathrm{b}}4\pi f(\omega,R_0), \tag{4.8}$$

where k is ,as in Figure 4.1, the medium wavenumber, i.e. the wave number of the propagating wave if scatterers were not present, the complex quantity $f(\omega,R_0)$ is the scattering length of each scatterer and N_{b} the number dencity of bubbles, defined as:

$$N_{\mathrm{b}} = \int_V NdV, \tag{4.9}$$

Here the dependence of the scattering length on the range is neglected under the previous assumption that the ensemble is confined in a small region $a << r$. This forward propagating wave is used for the interpretation and inversion of acoustic propagation data from a tenuous bubbly medium.

The analysis of the previous paragraphs showed that in the case of randomly distributed scatterers, i.e. incoherent scattering, the total scattered spectral power from an ensemble of scatterers equals the sum of the scattered spectral power from each scatterer:

$$\left|\tilde{p}_{\mathrm{s\,tot}}(\boldsymbol{r},\omega)\right|^2 = NP_{\mathrm{i}}^2(\omega)\frac{\left|f(\omega,\vartheta)\right|^2}{r^2} \tag{4.10}$$

For most applications, it is not the absolute number N of interest but the number density, defined by (4.9). In this case the incoherent scattered wave is computed assuming that the scattering volume consists of the sum of elementary volumes dV :

$$\left|\tilde{p}_{\mathrm{s\,tot}}(\boldsymbol{r},\omega)\right|^2 = \int_V N_{\mathrm{b}}P_{\mathrm{i}}^2(\omega)\frac{\left|f(\omega,\vartheta)\right|^2}{r^2}dV\,. \tag{4.11}$$

Equation (4.11) involves the power of the signal (i.e. the acoustic pressure signal, $\left|\tilde{p}_{\mathrm{s\,tot}}(\boldsymbol{r},\omega)\right|$), which is in practice the ensemble average (i.e. expected value) of the amplitude squared of the pressure:

$$\left|\tilde{p}_{\mathrm{s\,tot}}(\boldsymbol{r},\omega)\right|^2 = \left\langle\left|p_{\mathrm{s\,tot}}(\boldsymbol{r},t)\right|^2\right\rangle. \tag{4.12}$$

This holds because the signal power is a quantity which is linked to the experimental data using the ensemble scattering statistics. The statistical approach consists of treating a given measurement as one realisation of a random process. One aims at evaluating the statistical moments of the scattered waves in order to characterise the medium (i.e. background medium with scaterrers). In practice, the measured acoustic waves are measured for a short period of

time. As already mentioned, for this time period, i.e. experimental realisation, the bubbles are assumed frozen in space, however for every measurement, the scattered signal vary due to the random phase of the returns of the scatterers, here the bubbles. The amplitude fluctuation of a scattered signal from the superposition of random phase waves is uniformingly distributed over 2π and has a Rayleigh probability distribution:

$$\mathrm{P}(|\tilde{p}_{\mathrm{s\,tot}}|) = \frac{|\tilde{p}_{\mathrm{s\,tot}}|}{\upsilon^2} e^{-|\tilde{p}_{\mathrm{s\,tot}}|^2/2\upsilon^2}, \tag{4.13}$$

where υ is the mode of the Rayleigh probability distribution (also named reverberation variance). For n independent observations, the theoretical variability of the distribution can be expressed in terms of the standard deviation (*std*), as:

$$std = \left((4-\pi)/4n\right)^{1/2} |\tilde{p}_{\mathrm{s\,tot}}|. \tag{4.14}$$

In paragraph 5.4, equation (4.14) is used to estimate the theoretical random error of the bubble population measured in bubbly water.

Equations (4.11) and (4.13) are the basis for the interpretation of wave scattering from a tenuous distribution of scatterers (Ishimaru, 1978). Equation (4.11) will be extended to bubbles in the following section.

4.2 Single bubble scattering and scattering cross sections

In this section, expressions for the form function and scattering cross sections will be derived for a single bubble in order to underline limitations of applying existing analytical expressions to predict bubble scattering. All derivations below assume $kR_0 << 1$.

The total acoustic scattering cross section σ_s is defined as the ratio of the total power scattered at a reference distance to the intensity of the incident plane wave, see for example chapter 8 of Morse (1968). Assuming a receiver with finite aperture at the point P of Figure 4.1, only a fraction of the scattered power is sampled. The relevant measure then is the differential cross section per unit solid angle Ω: $\sigma_{ds} = d\sigma_s / d\Omega$. This quantity is found from the ratio of the differential scattered power $d\Pi_s$ and the incident intensity I_i. An expression for $d\Pi_s$ is obtained assuming a spherical scattered wave with a sinusoidal time dependence:

$$p_s(\boldsymbol{r},t) = P_i \frac{e^{ikr}}{r} f(\omega,\vartheta)\sin(\omega t), \tag{4.15}$$

and the fact that p_s is a spherical wave:

$$d\Pi_s = \frac{\left\langle |p_s|^2 \right\rangle}{\rho_0 c} r^2 d\Omega, \tag{4.16}$$

which leads to:

$$d\Pi_s = \frac{P_i^2 d\Omega}{2\rho_0 c} |f(\omega,\vartheta)|^2. \tag{4.17}$$

The incident intensity of a plane wave is: $\langle I_{\mathrm{i}} \rangle = \dfrac{\left\langle |p_{\mathrm{i}}|^2 \right\rangle}{\rho_0 c}$ (Kinsler, 1999), hence using the definition, the differential scattering cross section is:

$$\sigma_{\mathrm{ds}} = \frac{d\Pi_{\mathrm{s}}}{I_{\mathrm{i}} d\Omega} \Rightarrow \tag{4.18}$$

$$\sigma_{\mathrm{ds}} = \left| f(\omega, \vartheta) \right|^2 \tag{4.19}$$

If the scattering is isotropic the total scattering cross section is obtained by integrating over the surface of radius r in azimuth (ϕ) and zenith (ϑ) angles:

$$\sigma_{\mathrm{s}} = \int_0^{2\pi} d\phi \int_0^{\pi} \sigma_{\mathrm{ds}} \sin\vartheta d\vartheta \Rightarrow \sigma_{\mathrm{s}} = 4\pi\sigma_{\mathrm{ds}} \tag{4.20}$$

Until this point the analysis does not distinguish between hard and soft boundary scatterers. Modal solutions for the scattering problem from spheres indicate that the scattering is omnidirectional for hard (Morse, 1968; Clay 1977) as well as soft boundaries (Anderson, 1950) as long as $kR_0 << 1$. Therefore equations (4.18) and (4.20) can be applied for gas bubbles and the scattered power and incident intensity can be written in terms of time averages. Under these observations, the definition for the total bubble scattering cross section becomes:

$$\sigma_s = 4\pi r^2 \frac{\left\langle {p_{\mathrm{b}}}^2 / \rho_0 c_0 \right\rangle}{\langle I_{\mathrm{i}} \rangle}, \tag{4.21}$$

where p_{b} is the pressure scattered from a single bubble. Assuming that the bubble is an acoustic monopole source, the pressure p_{b} is related to the time-varying bubble volume $V_{\mathrm{g}}(t)$ with (Landau and Lifshiz, 1959):

$$p_{\mathrm{b}}(r,t)=\frac{\rho_0}{4\pi r}\frac{\partial^2 V_{\mathrm{g}}}{\partial t^2}. \tag{4.22}$$

For the derivation of the bubble scattering cross sections the reference distance is $r=R_0$ and therefore there is no need to use retarded time in equation (4.22). When linear scattering is considered, the volume velocity $\frac{\partial V_{\mathrm{g}}}{\partial t}$ is approximated by:

$$\frac{\partial V_{\mathrm{g}}}{\partial t}\simeq 4\pi R_0^2\dot{R} \tag{4.23}$$

Substitution of equation (4.23) in (4.22) yields the following expression for the pressure emitted by a bubble:

$$p_{\mathrm{b}}(r,t)=\frac{\rho_0}{4\pi r}\left(4\pi R_0^2\right)\ddot{R}(t). \tag{4.24}$$

Using the expression of equation (2.27), equation (4.24) becomes:

$$p_{\mathrm{b}}(r,t)=\frac{\rho_0}{4\pi r}4\pi R_0^3 A_{\omega_1}\omega_1^2\cos(\omega_1 t+\phi_{\omega_1}). \tag{4.25}$$

This can be written in exponential form as:

$$p_{\mathrm{b}}(t)=\frac{\rho_0}{4\pi r}\left(4\pi R_0^3\right)\omega_1{}^2 A_{\omega_1}e^{j\left(\omega t+\phi_{\omega_1}\right)}. \tag{4.26}$$

Substitution of (2.15) in (4.26) and then in (4.21) leads to:

$$\sigma_s=4\pi r^2\frac{\left\langle p_b^2\right\rangle/2\rho_0 c_0}{\left|P_{\mathrm{i}}\right|^2/2\rho_0 c_0}\Rightarrow\sigma_s=4\pi\frac{\left(\omega_1{}^2\rho_0 R_0^3\right)^2 A_{\omega 1}^2}{\left|P_{\mathrm{i}}\right|^2}. \tag{4.27}$$

The expression for the total scattering cross section of a single bubble is readily obtained by substitution of the analytical expression for $A_{\omega 1}$, see equation (2.28):

$$\sigma_s = \frac{4\pi R_0^2}{\left(\omega_0^2/\omega_1^2 - 1\right)^2 + \left(2\beta_{\text{tot}}/\omega_1\right)^2} \tag{4.28}$$

Setting the quantity $2\beta_{\text{tot}}/\omega_1$ equal to the quantity called the damping coefficient, equation (4.28) leads to the alternative expression for a single bubble scattering cross section frequently encountered in literature, as for example in Sarkar and Prosperetti (1994).

Equations (4.27) to (4.28) reveal that scattering cross sections explicitly depend on the bubble equilibrium resonance and insonification frequency ω_1 (ω_0 is not considered as an extra parameter because it is a function of R_0), i.e. $\sigma_{\text{ds}} = \sigma_{\text{ds}}(\omega_1, R_0)$. To avoid confusion when using definitions for nonlinear scattering cross sections, the frequency and radius dependence is explicitly mentioned. Also the nonlinear frequency, in which the differential cross section refers to, appears in the subscript in order to emphasise that the expression for the nonlinear scattering cross section is different to that given by equation (4.28).

The above-mentioned approach for obtaining the linear bubble scattering cross sections can be extended for nonlinear scattering cross sections. In this case the emitted pressure from the bubble is given by equation (4.29) (see Vokurka (1985) and p. 153 of Leighton (1994) for a detailed discussion).

$$p_b(r,t) = \frac{\rho_0}{r}\left(2R\dot{R}^2 + R^2\ddot{R}\right). \tag{4.29}$$

If, for example, the nonlinear generated difference-frequency is of interest, then the expression for the corresponding pressure spectral component at that frequency, i.e. $\left|\tilde{p}_{\text{b}}(r,\omega)\right|_{\omega=\omega_-}$, will have the bubble spectral components that give rise to this difference-frequency. Subsequently analytical expressions for the scattering cross sections can be derived for ω_- in a manner analogous to the derivation of the linear scattering cross sections. For example, to derive an analytical expression for the scattering cross section using the analytical solutions of chapter 2

and appendix A, first the bubble emitted pressure at ω_- equation (4.29), is written in terms of the dimensionless variable x:

$$p_b(r,t) = \frac{\rho_0}{r} R_0^3 \left(\ddot{x} + 2\dot{x}^2 + 2x\ddot{x} \right). \tag{4.30}$$

As the terms $\dot{x}^2$ and $x\ddot{x}$ are not negligible, to find the pressure emitted at the difference frequency $\omega_1 - \omega_2$, we have to look at the last two rows of table A.1 where the contributions of $\dot{x}^2$ and $x\ddot{x}$ are given in terms of sins and cosines. After some manipulation of the terms, equation (4.30) gives for the difference frequency:

$$p_b(r,t) = \frac{\rho_0}{r} \left(\omega_1 - \omega_2 \right)^2 R_0^3 \left(A_{\omega_1} A_{\omega_2} + A_{\omega_-} \right). \tag{4.31}$$

The terms $A_{\omega_1} A_{\omega_2}$ and A_{ω_-} entering equation (4.31) were defined in section 2.2.1. Using the definition of scattering cross section as given by equation (4.21), the intensity of two incident waves has to be taken into account. Using expression (4.31), the bubble scattering cross section at difference frequency is formulated in terms of the analytical solutions:

$$\sigma_{s_-}(\omega_-, R_0) = 4\pi \frac{\left(\left(\omega_1 - \omega_2 \right)^2 \rho_0 R_0^3 \right)^2 \left(A_{\omega_1} A_{\omega_2} + A_{\omega_-} \right)^2}{\left| P_1^2 + P_2^2 \right|}. \tag{4.32}$$

In the past, analytical expressions have been used by many authors for the interpretation of nonlinear backscattering from bubbles (Newhouse and Shankar, 1984) in water as well as in sediments (Lyons *et al.*, 1996; Boyle and Chotiros, 1998; Tegowski *et al.*, 2006). However, as discussed in chapter 2, analytical expressions for the difference frequency are not suitable for the conditions examined in this work. Here, in order to interpret nonlinear scattering, the pressure field emitted by a bubble, $p_b(r,t)$, was computed numerically using the bubble model of equation (2.56) for water and the model of equation (3.21) for sediments. Then its

frequency amplitude spectrum $\left|\tilde{p}_{\mathrm{b}}(r,\omega)\right|$ was computed using the Fourier transform method. For the difference frequency the corresponding differential cross section σ_{ds} is computed using the pressure spectral component emitted at the difference frequency ($\left|\tilde{p}_{\mathrm{b}}(r,\omega)\right|_{\omega=\omega_-}$):

$$\sigma_{\mathrm{ds}-}(\omega_-,R_0)=r^2\frac{\left|\tilde{p}_{\mathrm{b}}(r,\omega)\right|^2_{\omega=\omega_-}}{\left|P_{\mathrm{i}}\right|^2}. \tag{4.33}$$

Similarly expressions are obtained for any nonlinear scattering component of interest, for example for the component at twice the pump frequency, the corresponding backscattering cross section is:

$$\sigma_{\mathrm{ds}\ 2\omega_{\mathrm{p}}}(2\omega_{\mathrm{p}},R_0)=r^2\frac{\left|\tilde{p}_{\mathrm{b}}(r,\omega)\right|^2_{\omega=2\omega_{\mathrm{p}}}}{\left|P_{\mathrm{i}}\right|^2}. \tag{4.34}$$

Based on Parseval's theorem, the total scattering cross section of a single bubble, when the nonlinear harmonics are not negligible, is the sum of the scattering cross sections at all frequencies at which the bubble is emitting. For example, the cross section of a single bubble under insonification with a pump frequency ω_{p}, which has non-negligible harmonics up to the second order, is:

$$\sigma_s=\sigma_{\mathrm{s}}(\omega_{\mathrm{p}},R_0)+\sigma_{\mathrm{ds}\ 2\omega_{\mathrm{p}}}(2\omega_{\mathrm{p}},R_0). \tag{4.35}$$

Similarly, the cross section of a single bubble under two frequency insonification, ω_{p} and ω_{i}, which has non-negligible harmonics up to the second order, is:

$$\begin{aligned}\sigma_s=\sigma_{\mathrm{s}}(\omega_{\mathrm{p}},R_0)+\sigma_{\mathrm{ds}\ 2\omega_{\mathrm{p}}}(2\omega_{\mathrm{p}},R_0)+\sigma_{\mathrm{s}}(\omega_{\mathrm{i}},R_0)+\sigma_{\mathrm{ds}\ 2\omega_{\mathrm{p}}}(2\omega_{\mathrm{i}},R_0)\\ +\sigma_{\mathrm{ds}\text{-}}(\omega_-,R_0)+\sigma_{\mathrm{ds}+}(\omega_+,R_0)\end{aligned} \tag{4.36}$$

The combinations of pump-imaging frequencies, which should be taken into account, depend on the relative magnitude of ω_p and ω_i, as discussed in chapter 2. If the two frequencies are close enough (as in the example of Figure 2.8) then the terms of (4.36) are sufficient to approximate the total single bubble scattering cross section.

4.3 Scattering from an ensemble of bubbles: the forward and the inverse problem

In this section the general theory of section 4.1 will be applied to scattering from an ensemble of gas bubbles. Retaining the assumption $kR_0 \ll 1$, the forward and the inverse scattering problem will be discussed for an ensemble of bubbles.

The forward problem, which is the calculation of the scattered field from a known bubble cloud, is easily solved using by substitution of equation (4.19) in (4.11) if the bubble cloud were to have N_b bubbles per unit volume with the same equilibrium radius.

$$\left|\tilde{p}_{s\,tot}(\boldsymbol{r},\omega)\right|^2 = \int_V N_b P_i^2(\omega)\frac{\sigma_{ds}(\omega,R_0)}{r^2}dV\,. \tag{4.37}$$

Equation (4.37) is not of practical use because the finite beam widths of the receiver and the transmitter have not been taken into account. Moreover the medium attenuation is neglected, which may be a plausible assumption when the background medium is water. Taking into account the directivities of the transmit and receive devices as well as the medium attenuation, equation (4.37) becomes:

$$\left|\tilde{p}_{s\,tot}(\boldsymbol{r},\omega)\right|^2 = \int_V N_b P_i^2 \sigma_{ds}(\omega,R_0)\frac{r_0^2\Omega_r^2\Omega_t^2}{r_r^2 r_t^2}e^{-2\alpha(r_r+r_t)}dV\,, \tag{4.38}$$

where P_i is the pressure amplitude of the incident wave, α is the attenuation of the background medium, r_r and r_t is the distance from the receiver and transmitter to the centre of the scattering volume and Ω_r and Ω_t are the directivities of the receiver and transmitter

respectively. The radial distance r_0 is the distance along the acoustic axis of the transmitter to the point at which the sound pressure level is P_i . Equation (4.38) gives the pressure for bistatic scattering. Application of equation (4.38) to the experimental set up used in this work will be discussed in the subsequent paragraphs after discussing the way of applying this equation when scatterers of different sizes are present.

Usually bubbles produced in a tank or found in marine environments have a range of R_0 , i.e. a size distribution $n_\mathrm{b}(R_0)$ is present. Retaining the incoherency assumption, equation (4.37) becomes for a bubble distribution:

$$\left|\tilde{p}_{\mathrm{s\,tot}}(\boldsymbol{r},\omega)\right|^2 = \int_0^\infty n_\mathrm{b}(R_0)\sigma_\mathrm{ds}(\omega,R_0)dR_0 \int_V P_\mathrm{i}^2 \frac{r_0^2\Omega_\mathrm{r}^2\Omega_\mathrm{t}^2}{r_\mathrm{r}^2 r_\mathrm{t}^2} e^{-2\alpha(r_\mathrm{r}+r_\mathrm{t})} dV \,. \tag{4.39}$$

As the transmitter and receiver directivities depend on the frequency, equation (4.39) shows that the scattering volume is frequency dependent. Also, in practice, the sizes R_0 of the bubble population n_b do not extend from zero to infinity but there is a minimum and maximum detectable size. With these considerations equation (4.39) can be written as:

$$\left|\tilde{p}_{\mathrm{s\,tot}}(\omega)\right|^2 = I(\omega)\int_{R_{0\,\min}}^{R_{0\,\max}} n_\mathrm{b}(R_0)\sigma_\mathrm{ds}(\omega,R_0)dR_0 \,, \tag{4.40}$$

where $I(\omega)$ is the frequency dependent volume integral:

$$I(\omega) = \int_V P_\mathrm{i}^2 \frac{r_0^2\Omega_\mathrm{r}^2\Omega_\mathrm{t}^2}{r_\mathrm{r}^2 r_\mathrm{t}^2} e^{-2\alpha(r_\mathrm{r}+r_\mathrm{t})} dV \,, \tag{4.41}$$

and will be computed numerically. The evaluation of this integral depends on the experimental set up discussed in chapter 5.

The size range entering equation (4.40) depends on the incident frequencies and the measured spectral components. Traditionally when linear scattering is considered, the smallest and biggest bubble size resonant determines the upper and lower distribution limits (Commander and McDonald, 1991). The insonifing frequency range is usually covering the size range likely to be present in the volume. If it is assumed that a number of frequencies p are used to estimate a bubble population, then for every incident frequency $\omega^{(p)}$ the following integral equation is satisfied:

$$\left|\tilde{p}_{\text{s tot}}\left(\omega^{(p)}\right)\right|^2 = I^{(p)} \int_{R_{0\,\min}}^{R_{0\,\max}} n_{\text{b}}(R_0)\sigma_{\text{ds}}(\omega^{(p)}, R_0)dR_0, \tag{4.42}$$

where the superscript p indexes the number of frequencies (pump frequencies when nonlinear scattering is considered) interrogating the ensemble of bubbles. To find the inverse problem, i.e. finding the bubble size distribution from measured spectra at different frequencies, the set of integral equations (4.42), are reduced into summations by discreetising the bubble size distribution $n_{\text{b}}(R_0)$ in radius bins. Then these summations are performed over the bubble radii of the bubble population from the minimum size $R_{0\,\min} = R_0^{(1)}$ to the maximum size $R_{0\,\max} = R_0^{(p)}$. Every bin contains $N_{\text{b}}(R_0)$ number of bubbles:

$$N_{\text{b}}(R_0) = n_{\text{b}}(R_0)dR_0. \tag{4.43}$$

In the literature it is common to set dR_0 equal to 1 μm and present the bubble size distribution as number per cubic metre per micron. This representation will be adopted also in this PhD work.

The matrix equation resulting from equation (4.42) is:

$$\mathbf{P}_{\text{p}} = \boldsymbol{\sigma}_{\text{p}}\mathbf{n}_{\text{p}}. \tag{4.44}$$

where the column matrix $\mathbf{P}_{\mathrm{p}}$ contains the measured scattered pressure spectra at the incident frequencies multiplied by the inverse of the quantity $I^{(p)}$, which contains the frequency dependent information for the device directivities and scattering volume:

$$\mathbf{P}_{\mathrm{p}} = \left[\frac{\left| p_{\mathrm{s\,tot}}(\omega^{(1)}) \right|^2}{I^{(1)}}, \frac{\left| p_{\mathrm{s\,tot}}(\omega^{(2)}) \right|^2}{I^{(2)}}, \ldots\ldots\ldots\ldots, \frac{\left| p_{\mathrm{s\,tot}}(\omega^{(p)}) \right|^2}{I^{(p)}} \right]^{\mathrm{T}}. \tag{4.45}$$

The superscript T represents transpose of matrix. The $\boldsymbol{\sigma}_{\mathrm{p}}$ matrix contains the differential scattering cross sections:

$$\boldsymbol{\sigma}_{\mathrm{p}} = \begin{bmatrix} \sigma_{\mathrm{ds}}(\omega^{(1)}, R_0^{(1)}) & \ldots & \ldots & \sigma_{\mathrm{ds}}(\omega^{(1)}, R_0^{(p-1)}) & \sigma_{\mathrm{ds}}(\omega^{(1)}, R_0^{(p)}) \\ \sigma_{\mathrm{ds}}(\omega^{(2)}, R_0^{(1)}) & \ldots & \ldots & \ldots & \sigma_{\mathrm{ds}}(\omega^{(2)}, R_0^{(p)}) \\ \ldots & \ldots & \ldots & \ldots & \ldots \\ \sigma_{\mathrm{ds}}(\omega^{(p-1)}, R_0^{(1)}) & \ldots & \ldots & \ldots & \sigma_{\mathrm{ds}}(\omega^{(p-1)}, R_0^{(p)}) \\ \sigma_{\mathrm{ds}}(\omega^{(p)}, R_0^{(1)}) & \ldots & \ldots & \sigma_{\mathrm{ds}}(\omega^{(p)}, R_0^{(p-1)}) & \sigma_{\mathrm{ds}}(\omega^{(p)}, R_0^{(p)}) \end{bmatrix}, \tag{4.46}$$

and $\mathbf{n_b}$ is the column vector with the unknown bubble sizes:.

$$\mathbf{n_b} = \left[n_{\mathrm{b}}(R_0^{(1)}), n_{\mathrm{b}}(R_0^{(2)}), \ldots\ldots n_{\mathrm{b}}(R_0^{(p)}) \right]^{\mathrm{T}}. \tag{4.47}$$

In order to solve the system of (4.44) without any other information, the matrix $\boldsymbol{\sigma}_{\mathrm{p}}$ must be square. For linear scattering this is ensured by choosing the frequencies $\omega^{(p)}$ to cover the resonant sizes present in bubble population (Commander and McDonald, 1991). In this case, the diagonal elements of $\boldsymbol{\sigma}_{\mathrm{p}}$ represent the scattering from resonant bubbles and the off-diagonal elements account for the off-resonant contributions of bubbles.

If nonlinear incoherent scattering is considered then similar expressions for the forward and inverse scattering problem are obtained by considering the energy of nonlinear frequency of interest in the measuring signal. Assume that two frequencies insonify the ensemble of

bubbles: a high frequency ω_i which is kept fixed at some frequency and a low varying frequency ω_p . In this work we are interested in the nonlinearly scattered component at the difference frequency $\omega_- = \omega_i - \omega_p$ and twice the pump frequency $\omega_{2\mathrm{p}}$ instead of the scattering at ω_p . These will be indicated as superscripts of the difference-frequency signal and twice the frequency with $i-p$ and $2p$ respectively. The nonlinear scattering cross section is given for each of these combinations from equations (4.33) and (4.34). Again assuming incoherent scattering, the total received power is the sum of the power scattered from each bubble for the frequency component under question. For example for the difference frequency $\omega_- = \omega_i - \omega_p$ the measured scattered power at every measure difference frequency is:

$$\left|\tilde{p}_{\mathrm{s\,tot}}\left(\omega_-^{(i-p)}\right)\right|^2 = I^{(i-p)} \int_{R_{0\,\min}}^{R_{0\,\max}} n_{\mathrm{b}}(R_0)\sigma_{\mathrm{ds\text{-}}}(\omega_-^{(i-p)}, R_0)dR_0 \,. \tag{4.48}$$

The scattering volume covered for each frequency depends on the transmitter and receiver characteristics; therefore the volume integral $I^{(i-p)}$ on the combination of high and low transmitted frequencies. Complicating more the integral (4.41) due to the presence of third device can be avoided by observing the geometry of the scattering experiment. The difference frequency can be generated only in the space where the beam patterns of the pump and the imaging frequencies overlap, thus the beam pattern of the transmitter with the narrowest beam determines the scattering volume for the difference frequency. This is explained in detail in chapter 5 together with the configuration of the experimental set up. The detectable size range with a minimum size $R_{0\,\min} = R_0^{(i-1)}$ and a maximum size $R_{0\,\max} = R_0^{(i-p)}$ depend on the bubble sizes that give rise to scattered peaks at the difference frequency ω_- .

Similarly with the linear scattering analysis the integral expression of (4.48) is converted to a system of linear equations with the matrix expression:

$$\mathbf{P}_{\text{i-p}} = \boldsymbol{\sigma}_{\text{i-p}}\mathbf{n}_{\mathrm{b}} \,, \tag{4.49}$$

where the column matrix $\mathbf{P}_{\text{i-p}}$ contains the relevant measured scattered pressure spectra at the difference frequency corrected by the scattering volume integral:

$$\mathbf{P}_{\text{i-p}} = \left[\frac{\left| p_{\text{s tot}}\left(\omega^{(i-1)}\right)\right|^2}{\left(I^{(i-1)}\right)^2}, \frac{\left| p_{\text{s tot}}\left(\omega^{(i-2)}\right)\right|^2}{\left(I^{(i-2)}\right)^2}, ..., \frac{\left| p_{\text{s tot}}\left(\omega^{(i-p)}\right)\right|^2}{\left(I^{(i-p)}\right)^2} \right]^{\text{T}}, \tag{4.50}$$

the $\boldsymbol{\sigma}_{\text{i-p}}$ matrix contains the differential scattering cross sections at difference frequency $\sigma_{\text{ds-}}$, numerically computed using the definition (4.33):

$$\boldsymbol{\sigma}_{\text{i-p}} = \begin{bmatrix} \sigma_{\text{ds-}}(\omega^{(i-1)}, R_0^{(i-1)}) & \dots & \dots & \sigma_{\text{ds-}}(\omega^{(i-1)}, R_0^{(i-1)}) & \sigma_{\text{ds-}}(\omega^{(i-1)}, R_0^{(i-p)}) \\ \sigma_{\text{ds-}}(\omega^{(i-2)}, R_0^{(i-2)}) & \dots & \dots & \dots & \sigma_{\text{ds-}}(\omega^{(i-2)}, R_0^{(i-p)}) \\ \dots & \dots & \dots & \dots & \dots \\ \sigma_{\text{ds-}}(\omega^{(i-p-1)}, R_0^{(1)}) & \dots & \dots & \dots & \sigma_{\text{ds-}}(\omega^{(i-p-1)}, R_0^{(i-p)}) \\ \sigma_{\text{ds-}}(\omega^{(i-p)}, R_0^{(1)}) & \dots & \dots & \sigma_{\text{ds-}}(\omega^{(i-p)}, R_0^{(i-p-1)}) & \sigma_{\text{ds-}}(\omega^{(i-p)}, R_0^{(i-p)}) \end{bmatrix}, \tag{4.51}$$

and $\mathbf{n_b}$ is the column vector with the unknown bubble sizes:

$$\mathbf{n_b} = \left[n_{\text{b}}(R_0^{(i-1)}), n_{\text{b}}(R_0^{(i-2)}), ...n_{\text{b}}(R_0^{(i-p)}) \right]. \tag{4.52}$$

The correspondence between R_0 and $\omega_{-}^{(i-p)}$ depends on the nonlinear behaviour of each bubble size, i.e. the nonlinear resonances of each bubble size. That is, if only one size gave rise to the difference frequency then the matrix $\boldsymbol{\sigma}_{\text{i-p}}$ would be diagonal. For the cases examined in this work more than one size contribute to the generation of nonlinear components and therefore a full matrix inversion is needed just as for the case of linear scattering. The formulation of the matrix $\boldsymbol{\sigma}_{\text{i-p}}$ is further discussed in conjunction with the development of the combination-frequency technique in chapter 5 where the nature of the matrix $\boldsymbol{\sigma}_{\text{i-p}}$ is discussed and the scattered pressure is plotted against the low varying frequency (pump frequency) for a range

of bubble sizes (Figure 5.10). Analogously, the matrix equation for the nonlinear scattering at twice the pump frequency is formulated as $\mathbf{P}_{2p} = \boldsymbol{\sigma}_{2p}\mathbf{n}_b$. The vector is:

$$\mathbf{P}_{2p} = \left[\frac{\left| p_{s\,tot}\left(\omega^{(2p)}\right)\right|^2}{\left(I^{(2p)}\right)^2}, \ldots\ldots\ldots, \frac{\left| p_{s\,tot}\left(\omega^{(1)}\right)\right|^2}{\left(I^{(1)}\right)^2} \right]^T, \tag{4.53}$$

and the matrix $\boldsymbol{\sigma}_{2p}$ is diagonal as it is explained in section 5.2.

The formulation of a matrix equation, like equations (4.44) or (4.49), from an integral set of equations is a well known approach for the computation of integral equations, which typically leads to an inherently ill-conditioned system. The theory of regularization for linear problems is heavily researched; however the success of any practical approach depends on the nature and the physics of the problem. In bubble acoustics, the inverse problem of finding the bubble distribution from attenuation or scattering measurements has been discussed in many works, see for example Vagle and Farmer (1992), Commander and McDonald (1991), Duraiswami *et al.* (1998), Terrill and Melville (2000) and Leighton *et al.* (2004). Although many regularisation schemes have been studied, results showed that there is no holy grail as to the best regularisation approach. The regularisation method used in this work is a variation of the well known Tikhonov method (Tikhonov, 1977). It relies upon the standard method of adding a diagonal matrix (denoted by *diag*), scaled by β a regularisation parameter, to the matrix to be inverted. According to the variation used in this work, the system of equations, for example for the linear scattering, (4.44) takes the form:

$$\left(\boldsymbol{\sigma}_p{}^T\boldsymbol{\sigma}_p + \beta \mathrm{diag}(\boldsymbol{\sigma}_p{}^T\boldsymbol{\sigma}_p)\mathbf{I}\right)\hat{\mathbf{n}}_\mathbf{b} = (\boldsymbol{\sigma}_p)^T\mathbf{P}_p, \tag{4.54}$$

where $\mathbf{I}$ is the identity matrix. This regularisation method is outlined in the thesis of Coles (2009). In this section, this regularisation method is described using the notation for scattering at the pump frequency. The bubble size distribution $\hat{\mathbf{n}}_\mathbf{b}$ resulting from (4.54) is an estimate of $\mathbf{n}_\mathbf{b}$ and consequently substituting this value in (4.44) gives a forward fitted value, estimate of $\mathbf{P}_p$:

$$\hat{\mathbf{P}}_{\mathrm{p}} = \boldsymbol{\sigma}_{\mathrm{p}} \hat{\mathbf{n}}_{\mathbf{b}} . \tag{4.55}$$

The estimation error $\left|\hat{\mathbf{n}}_{\mathbf{b}} - \mathbf{n}_{\mathbf{b}}\right|$ depends on the choice of regularisation parameter β. A commonly used method of determining the optimal amount of regularisation to add to ill-conditioned matrices is the L-curve method, explained in chapter 14 of Linz and Wang (2003). The L-curve method is based on minimising the estimation error and has been used for bubble inversions, as for example in the work of Leighton *et al*. (2004). The main drawback of this solution is that it does not guarantee always a physically meaningful answer, i.e. positive values for all elements of $\hat{\mathbf{n}}_{\mathbf{b}}$. For this reason the criteria used for the inversions undertaken in this work were (a) the elements of $\hat{\mathbf{n}}_{\mathbf{b}}$ to be positive for all sizes and (b) the forward fitted values $\hat{\mathbf{P}}_{\mathrm{p}}$ be as close as possible to the initially inputted values for $\mathbf{P}_{\mathrm{p}}$. The second of these two constrains to the problem was posed through a scaling parameter Sc. The matrix equation which was solved in this work for the inverse problem is:

$$Sc\left(\boldsymbol{\sigma}_{\mathrm{p}}{}^{\mathrm{T}}\boldsymbol{\sigma}_{\mathrm{p}} + \beta diag(\boldsymbol{\sigma}_{\mathrm{p}}{}^{\mathrm{T}}\boldsymbol{\sigma}_{\mathrm{p}})\mathbf{I}\right)\hat{\mathbf{n}}_{\mathbf{b}} = \boldsymbol{\sigma}_{\mathrm{p}}{}^{\mathrm{T}}\mathbf{P}_{\mathrm{p}}, \tag{4.56}$$

instead of equation (4.54). The scaling factor Sc minimises the difference $\left|\hat{\mathbf{P}}_{\mathrm{p}} - \mathbf{P}_{\mathrm{p}}\right|$ in the least square sense and this is the criterion for choosing the value Sc for all the inversions presented in this work. This regularisation scheme will be discussed further in section 4.4.

The above mentioned approach for interpreting scattering from an ensemble of bubbles in a medium that possesses no shear can be extended to a medium that does possess shear and in particular to sediments. The shear property of the medium enters equation (4.39) only through the scattering cross section, which in turn depends on the bubble model used to interpret p_{b} using equation (4.29). Therefore the above described inversion method will be used for bubble sizing in sediments.

4.4 Testing of the nonlinear inversion method with an artificial bubble population

To test the inversion method based on equation (4.56) for the nonlinear scattering bubble sizing method developed in this work, a uniform bubble size distribution (1320 bubbles per micron radius bin per m^3) of air bubbles was assumed in fresh water. The insonification frequencies are the same with those used for the experiments carried out in this work: the pump frequency was varying from 30 kHz to 100 kHz with 5 kHz frequency steps and the imaging frequency is kept constant. Using these frequencies the resonant bubble sizes covered by the difference frequency and the pump frequency are shown in Figure 4.2. Here it has to be mentioned that the nonlinear pressure component at twice the pump frequency originates only from the bubbles resonant at the pump, which is the reason for estimating the bubble sizes resonant at the pump frequency although the measured component is at twice the pump frequency.

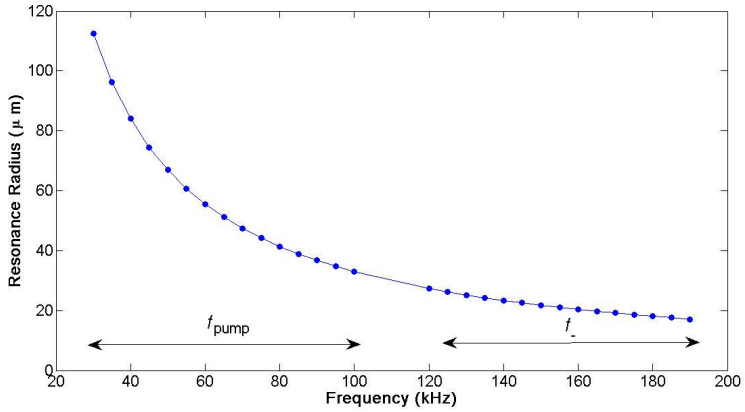

Figure 4.2: Plot showing the bubble resonant size (R_0) versus natural frequency where the solid line is calculated by equation (2.55) and the dots indicate the resonant sizes at the nonlinear frequencies used for the scattering experiments of this work.

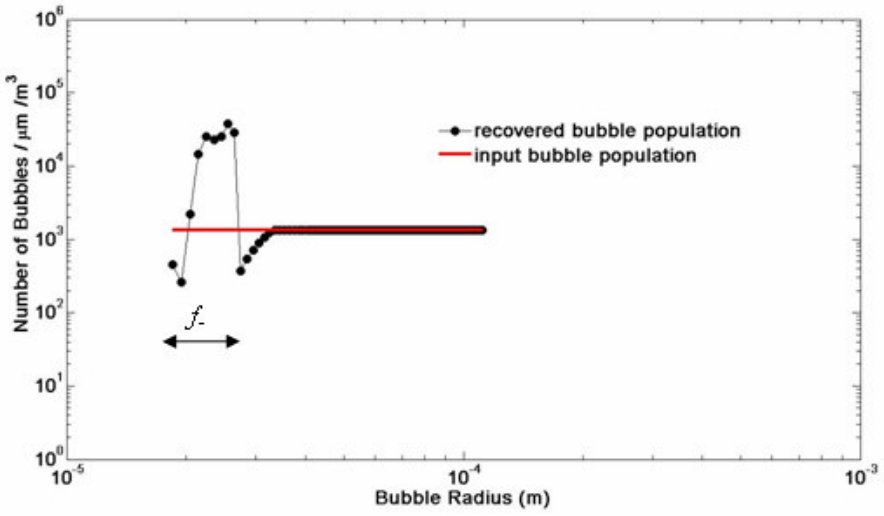

Figure 4.3: Bubble population plotted as number of bubbles per cubic metre per micrometer radius range versus bubble size. The red solid line represents the artificial bubble population which was input for the forward problem. The inversion black dotted line represents the recovered population from the inverse problem using (4.56). The arrow indicates that proportion of the population that resulted predominately from the difference frequency.

To carry out the inversion using nonlinear components and the inversion scheme of (4.56) the linear scattering matrix of equation (4.56) was substituted with the nonlinear scattering matrix composed by the nonlinear scattering matrix at difference frequency and twice the difference frequency. The matrix formulation resulted from melding these two nonlinear formulations into a single matrix equation is:

$$\begin{bmatrix} \mathbf{P}_{\text{i-p}} \\ \mathbf{P}_{2\text{p}} \end{bmatrix} = \begin{bmatrix} \boldsymbol{\sigma}_{\text{i-p}} \\ \boldsymbol{\sigma}_{2\text{p}} \end{bmatrix} \mathbf{n_b}\,, \tag{4.57}$$

where the vector $\mathbf{n_b}$ contains all the resonant sizes, marked with dots in Figure 4.2:

$$\mathbf{n_b} = \left[n_{\text{b}}(R_0^{(i-1)}), n_{\text{b}}(R_0^{(i-2)}), ...n_{\text{b}}(R_0^{(i-p)}), n_{\text{b}}(R_0^{(p)}), n_{\text{b}}(R_0^{(p-1)}), ...n_{\text{b}}(R_0^{(1)}) \right]. \tag{4.58}$$

In the following sections, the scattering matrix $\begin{bmatrix} \boldsymbol{\sigma}_{\text{i-p}} \\ \boldsymbol{\sigma}_{2\text{p}} \end{bmatrix}$ will be denoted by $\boldsymbol{\sigma}$ for brevity.

The evaluation of the inversion code was done as follows: First assuming the above mentioned uniform bubble size population $\mathbf{n_b}$ the columned matrix $\begin{bmatrix} \mathbf{P}_{\text{i-p}} \\ \mathbf{P}_{2\text{p}} \end{bmatrix}$ was obtained from (4.57), i.e.

the forward problem. Then this matrix $\begin{bmatrix}\mathbf{P}_{\text{i-p}}\\ \mathbf{P}_{\text{2p}}\end{bmatrix}$ was inserted into the inversion matrix equation (4.56) to recover a bubble population $\hat{\mathbf{n}}_{\mathbf{b}}$, which is considered the best estimate of $\mathbf{n}_{\mathbf{b}}$. Inserting the estimated population $\hat{\mathbf{n}}_{\mathbf{b}}$ into results in the forward fitted vector $\begin{bmatrix}\hat{\mathbf{P}}_{\text{i-p}}\\ \hat{\mathbf{P}}_{\text{2p}}\end{bmatrix}$ .The regularisation parameter and the scaling factor are not free parameters but chosen by the constrains for positive bubble population and minimum error in the least square sense of the quantity: $\left\|\begin{bmatrix}\mathbf{P}_{\text{i-p}}\\ \mathbf{P}_{\text{2p}}\end{bmatrix}-\begin{bmatrix}\hat{\mathbf{P}}_{\text{i-p}}\\ \hat{\mathbf{P}}_{\text{2p}}\end{bmatrix}\right\|$.

The recovered population is drawn with black dotted lines in Figure 4.3. The code achieves high accuracy at the larger bubbles, which come from resonant bubbles at the pump frequency whilst it exhibits oscillatory behaviour at the smaller sizes. This is attributed to the fact that the submatrix matrix $\boldsymbol{\sigma}_{\text{i-p}}$ is ill-conditioned with many off-diagonal elements of relatively large magnitude whilst the submatrix $\boldsymbol{\sigma}_{\text{2p}}$ is diagonal and thus well-conditioned (the elements of these submatrices are discussed section 5.2.2), As indicated by the regularisation scheme of equation (4.56), the regularisation parameter beta reduces the effect of the singular vectors associated with very small singular values of the scattering matrix. Standard Tikhonov regularisation inflates the leading diagonals of a matrix by adding a (small) fixed quantity to its diagonal elements. This serves to inflate the singular value by that fixed amount. In this work, using a variation of this regularisation scheme, the diagonal elements of the matrix are inflated by an amount which is proportional to their size. The result is that the singular values are similarly inflated, with smaller singular values being increased by a lesser amount than bigger ones, albeit that the singular values are not inflated by amount which is proportional to their original size. Nevertheless, since these small singular values are oscillatory, adding such a regularisation term to the matrix $\boldsymbol{\sigma}^{\text{T}}\boldsymbol{\sigma}$ is expected to reduce this undesired effect. However, getting a smooth solution depends on the smoothness of the singular vectors associated with the large singular values (Linz and Wang, 2003). If these large singular valued did not contain rapidly varying components then the solution would be smooth. As shown schematically in Figure 5.10, it is the submatrix which, as a consequence of its irregular form contains rapidly

varying components, which result in the oscillatory behaviour of the bubble distribution at small bubble sizes. The constraint imposed by the requirement that the result of the inversion contain only positive bubble populations, affect the choice of the regularisation parameter beta, which, as mentioned, is associated with the small singular values of the scattering matrix. Thus there is no direct influence on the smoothness of the solution.

Improvement the inversion scheme to result into a less oscillatory behaviour falls out of the scope of this work. It is known that increasing the regularisation parameter would give a smoother curve by adding damping in larger singular values of the scattering matrix, however with the current inversion scheme such an increase would increase the error $\left\| \begin{bmatrix} \mathbf{P}_{\text{i-p}} \\ \mathbf{P}_{\text{2p}} \end{bmatrix} - \begin{bmatrix} \hat{\mathbf{P}}_{\text{i-p}} \\ \hat{\mathbf{P}}_{\text{2p}} \end{bmatrix} \right\|$.

The inversion scheme of equation (4.56) will be kept for predicting bubble populations in water and in sediments. Keeping in mind the inherent highly oscillatory behaviour occurring at small bubble sizes, inversion results from measure bubble populations in water will be discussed further at the end of chapter 5.

4.5 A reference to the coherent inversion technique

Single frequency acoustic sizing techniques are based on assigning the bubbly medium an effective wave number. Pioneering work of Foldy (1945) explains in detail the derivation of equation (4.8), which assigns the bubbly medium an effective complex wave number. As mentioned in the work of Cartensen and Foldy (1947), the scattering length of gas bubbles in water equals:

$$f(R_0, \omega) = \frac{\omega^2 R_0}{\omega_0^2 - \omega^2 + j2\beta_{\text{tot}}\omega}. \qquad (4.59)$$

When a bubble distribution is present in the ensemble the effective wave number becomes:

$$k_{\mathrm{b}}^2 = k^2 + 4\pi \int_{R_{0\,\max}}^{R_{0\,\max}} \frac{\omega^2 R_0 n(R_0)}{\omega_0^2 - \omega^2 + j2\beta_{\mathrm{tot}}\omega} dR_0 \,. \tag{4.60}$$

From equation (4.60), the sound speed in the bubbly medium is derived:

$$\frac{c_0^2}{c_{\mathrm{b}}^2} = 1 + 2\pi {c_0}^2 \int_{R_{0\,\max}}^{R_{0\,\max}} \frac{R_0 n(R_0)}{\omega_0^2 - \omega^2 + 2j\beta_{\mathrm{tot}}\omega} dR_0 \,. \tag{4.61}$$

To invert (4.61) the right side of equation is set equal to (Commander and Prosperetti, 1989; Duraiswami *et al*., 1998):

$$\frac{c_0}{c_{\mathrm{b}}} = u - jv \,. \tag{4.62}$$

The phase velocity and the attenuation (expressed as dB/m) of the bubbly medium are respectively:

$$c_{\mathrm{b}} = \frac{c_0}{u} \tag{4.63}$$

$$A = 20\left(\frac{\omega v}{c_{\mathrm{water}}}\right)\log_{10}(e) \tag{4.64}$$

Detailed discussion of this method falls out of the scope of this thesis. This method is a well established method for estimation of bubble distributions and in this work it was used as a cross check for the bubble distribution results from the scattering method. Equation (4.61) is also an integral equation similar to equation (4.37), i.e. a Fredholm integral of first kind. To estimate bubble populations using attenuation data from propagation measurements, equation (4.64) was employed. The inversion method was applied in the same manner to the one applied for the inversion of scattering data.

Equation (4.61) has been used many times in the past for bubble sizing in water (Duraiswami *et al.,* 1998; Commander and Prosperetti, 1989; Terrill and Melville, 2000; Coles and

Leighton, 2007). However a state of art for bubble sizing in marine sediments follows another root. Bubbles in sediments using linear bubble dynamics are currently inferred according to the theory presented at the double paper by Anderson and Hampton (1980 a, b). Their formulation for sound speed and attenuation in gas-bearing sediments, is based on the work of Spitzer (1943) and Silberman (1957), leaves ambiguities for the inverse problem because of the double plus/minus sign entering the expression of the complex sound speed (equation 49 of Anderson and Hampton, 1980 a). As mentioned by Silberman (1957), the choice of the sign depends on the number of resonant bubbles and the bubble resonance frequency. In this work, this ambiguity is eliminated using the formulation of Foldy (1944), equation (4.61), for the complex sound speed of a wave propagating through random scatterers. The characteristics of the bubble pulsations, as derived from the nonlinear bubble dynamics model, enter Foldy's formulation through the scattering form function as it is explained in chapter 7.

4.6 Summary

In this chapter the theory behind coherent and incoherent scattering was outlined. The two-frequency inversion method developed during this PhD work is based on incoherent scattering and the bubble scattering cross sections are the key quantities for this inversion. Analytical expressions for linear and nonlinear scattering from bubbles were discussed as well as the derivation of numerically computed scattering cross sections. The last paragraphs of this chapter summarised the procedure of converting the integral equations for incoherent scattering into a linear system of equations using matrix formulation. This linear system is inherently ill-conditioned; therefore this matrix has to be regularised before being inverted. A variation of the standard regularisation methods which gives always meaningful, i.e. positive bubble population results was described and tested for an artificial bubble population. The simulation results showed that choosing the minimum beta that gives positive bubble populations results into a highly oscillatory curve. This oscillatory behaviour is observed at small bubble sizes and stems from the highly ill-conditioned submatrix $\boldsymbol{\sigma}_{\text{i-p}}$. Nevertheless this choice minimises the error $\left|\hat{\mathbf{P}}-\mathbf{P}\right|$ and will be used in this work.

CHAPTER 5: COMBINATION FREQUENCY INVERSION TECHNIQUE

This chapter describes a new bubble sizing technique that employs two frequencies, both in the kHz range. This frequency choice allows the application of this technique using the same devices in water as well as in sediments. Here the discussion and analysis is limited to bubble sizing in fresh water and it is extended to gassy sediments in Chapter 7. The first sections describe application and calibration of the rig designed to employ the combination frequency technique to measure the size distribution of air bubbles in water. It details how the returned signal is related to the size and number of bubbles and how parameters such as the sensing volume were numerically estimated. Then the underlying assumptions and possible error sources are discussed. The chapter concludes with tank measurements and bubble distribution results. The inversion results from the combination frequency technique are compared with independent inversion results. The latter ones were obtained using a single frequency bubble sizing technique which employs the inversion of attenuation data of sound propagating through a bubble cloud. The very good agreement of the predictions from these two techniques in water (where the bubbles are predominantly spherical) supports the efficacy of this combination frequency technique.

5.1 The combination frequency apparatus

The two-frequency technique developed during this work is based on simultaneous insonification of the bubble population with a lower frequency signal f_p (pump frequency) and a higher frequency, fixed acoustic signal with frequency f_i (the imaging signal). The apparatus used for the experiments is shown in Figure 5.1. The imaging source and receiver (A and C in the photograph) have a common focus point F; which is the point where their acoustic axes intersect each other at 90°, their axes being 45° either side of the axis of the pump transmitter (B in the photograph which is also the axis of symmetry of the device). The relative position of the devices is shown in Figure 5.2.

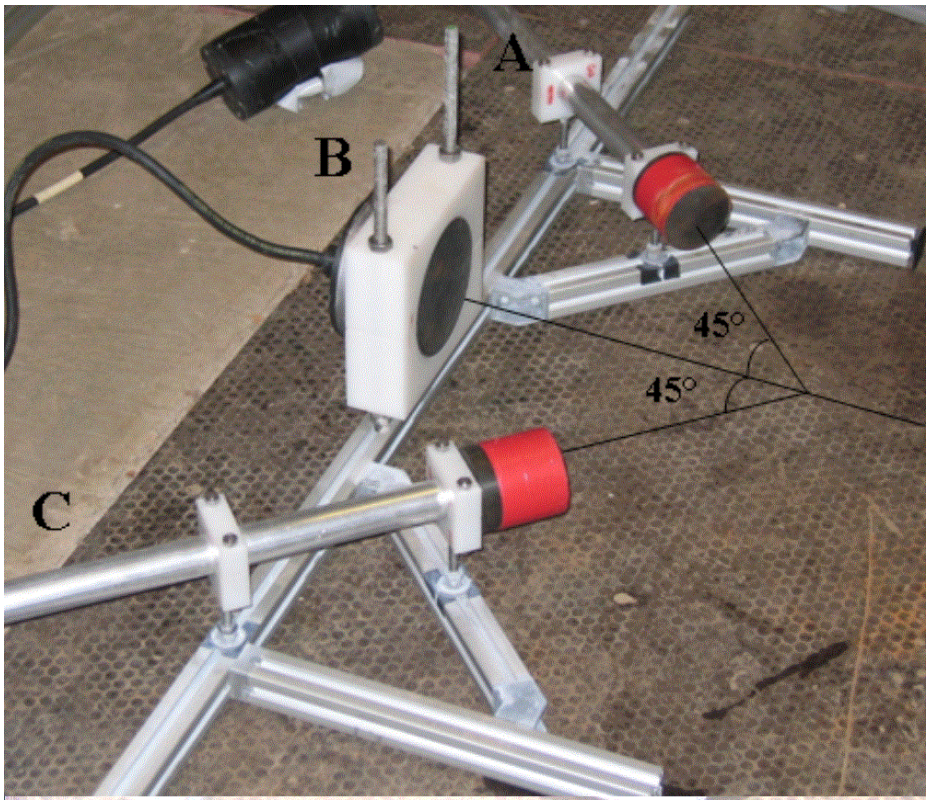

Figure 5.1: The combination-frequency apparatus: the three devices, the high (imaging) frequency transmitter (A), the pump source (B) and the high (imaging) frequency receiver (C) are mounted on a rig so that the devices have a common focus point. The imager and the receiver have equal angular distances (45°) from the pump axis.

The measurements taken with this device in the tank were aiming to cross-check the combination frequency technique against the well-established propagation inversion technique. Both methods were employed to measure the same bubble distribution. The bubbles were generated in a small container with a Venturi system designed to produce a population similar to that encountered at sea (Coles, 2007). The bubbly water was pumped via a hose from the container to the bottom of a tank with dimensions 8 m x 8 m x 5 m (deep), which contained fresh water at a temperature between 12 ºC and 15 ºC. The rig was placed horizontally in the tank at a depth of 2 m and the bubbles allowed to rise through the measurement volume. The experimental tank set up is shown diagrammatically in Figure 5.3.

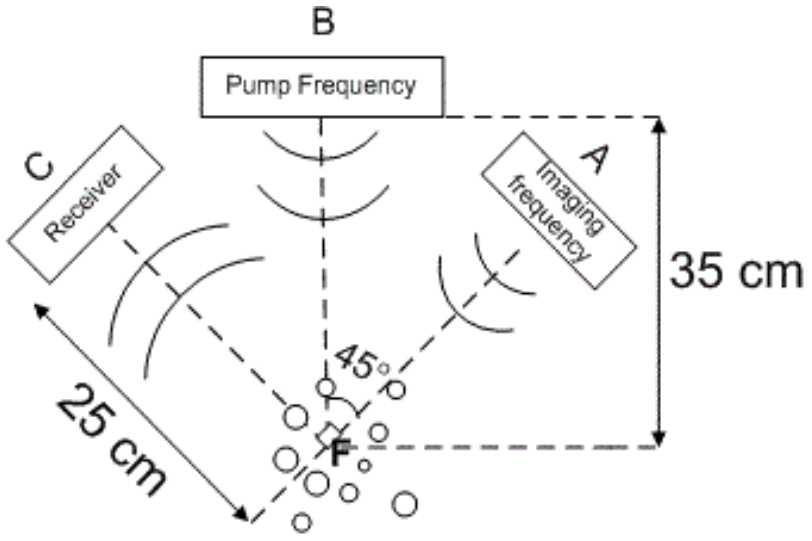

Figure 5.1: Top view of the combination-frequency apparatus with gas bubbles at the common focus point showing schematically the relative distance of the three devices which are depicted in Figure 5.1.

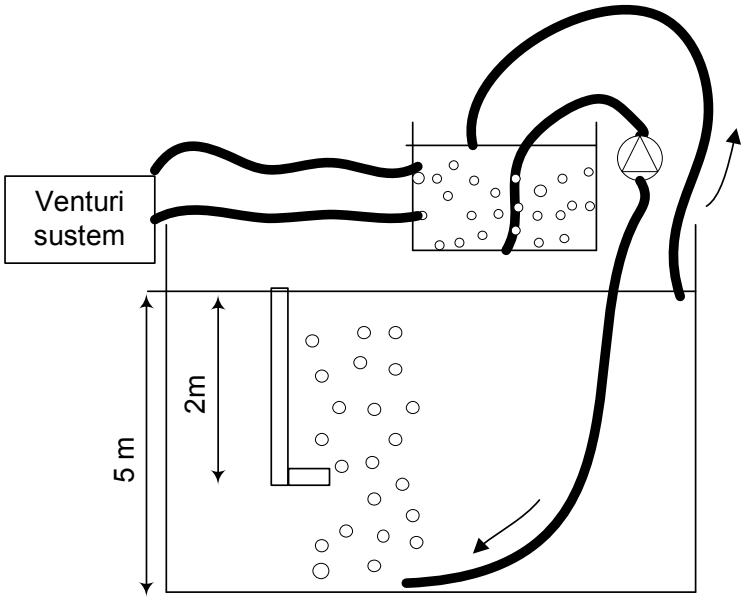

Figure 5.3: Schematic (not to scale) of the experimental set up. The combination frequency apparatus was placed at a depth of approximately 2 m. Bubbles were formed in the small tank by a Venturi system. The bubbly water was pumped to the bottom of the big tank in front of the test rig.

For all the scattering measurements the imaging frequency, f_i was kept constant at 220 kHz and the pump frequency f_p varied from 30 kHz to 100 kHz in increments of 5 kHz.

The acoustic sources were adjusted such that at the focus point F of the rig the pressure stayed constant at 15 kPa (zero-to-peak amplitude) for all frequencies. This is the calibration pressure for the combination frequency device and the value of the term P_{i} entering the volume integral (4.41) is the sum of these pressures averaged .These two signals were generated as a 2 ms square pulse. Simulations showed (see chapter 2) that this pulse length is long enough for the bubbles to reach the steady state. Additionally this time length is short enough for the bubbles to be considered frozen in the space confined by the sensing volume because their terminal velocity is so low. This terminal velocity for spherical bubbles lies between 2 cm/s and 7 cm/s according to Figure 7.3, p172 of Clift (1978). Thus the bubbles need at least 100 times the pulse length to move across the measuring volume. The scattered signal was recorded using an acquisition card with a sampling frequency of 2 MHz. The advantage of the device configuration described above is that it allows accurate spatial localisation because the measuring volume is well defined in space. The frequency range of all devices was chosen as low as possible in order to use the same set up for bubble sizing in sediments where the attenuation is much higher than in water. As mentioned in Chapter 4, the scattered spectral components, which will be used to estimate the bubble populations are the nonlinearly generated ones at the difference frequency ($f_{\mathrm{i}} - f_{\mathrm{p}}$) and the second harmonic of the pump frequency ($2f_{\mathrm{p}}$).

The volume integral corresponding to the difference frequency spectral components, ($I^{(i-p)}$), was calculated by computing the pressure field of the two high frequency transducers (i.e. the imaging source and receiver) by performing a Rayleigh integral over their surfaces. The volume expression, equation (4.41) , is repeated here:

$$I(\omega) = \int_V P_{\mathrm{i}}^2 \frac{r_0^2 \Omega_{\mathrm{r}}^2 \Omega_{\mathrm{t}}^2}{r_{\mathrm{r}}^2 r_{\mathrm{t}}^2} e^{-2\alpha(r_{\mathrm{r}} + r_{\mathrm{t}})} dV \,, \tag{4.41}$$

The difference frequency can be generated in the space where the beam patterns of the pump and the imaging frequencies overlap, see Figure 5.2, thus the beam pattern of the transmitter with the narrowest beam determines the scattering volume for the difference frequency. This is

the device of the imaging frequency (device A). The distance r_t entering equation (4.41) is the distance from the centre of the transmitter to the point F and the distance r_r is the distance from the centre of the receiver (device C) to the same point. These two devices have equal radiating surfaces (a diameter of 60 mm) and are located symmetrically with respect to the point F, thus $r_r = r_t = r_0$. As such spatial multiplication of these beam patterns results in a nearly symmetrical common sensing volume. Neglecting here the medium attenuation, the quantity that has to be integrated over the space is $\frac{\Omega_r^2 \Omega_t^2}{r_r^2 r_t^2}$. This is found by correlation of the pressure fields of the two devices in the time domain. The pressure field of the devices were computed numerically using the impulse response method developed by (Lockwood and Willette, 1973). Having evaluated the combined pressure field, the integral (4.38) was computed numerically using the coordinates of the points in space which had 3dB reduction of the intensity relative to the pressure at point F (see Figure 5.2). This is the so-called in this thesis 3dB common sensing volume. The above mentioned procedure was repeated for every combination of imager source-receiver because for every frequency pair the beam patterns and therefore the common sensing volume is different. Figure 5.4(a) shows the resulting combined beam pattern for $f_i - f_p$ =120 kHz.

Similarly the sensing volume for the scattering spectral components at twice the pump (primary) frequencies ($I^{(2p)}$) is calculated in the same way by the correlation of the beam patterns of the pump source (with a radiating diameter of 100 mm) with the receiver. In this case the distance r_t entering equation (4.41) is the distance from the pump source to the focus point F and the beam pattern is the one corresponding to this device. In this case the imaging frequency plays no role in the nonlinear generation of these component thus for the measurement at the difference frequency the experiment is a purely bistatic scattering experiment. In this case the resulting measurement volume is much greater.

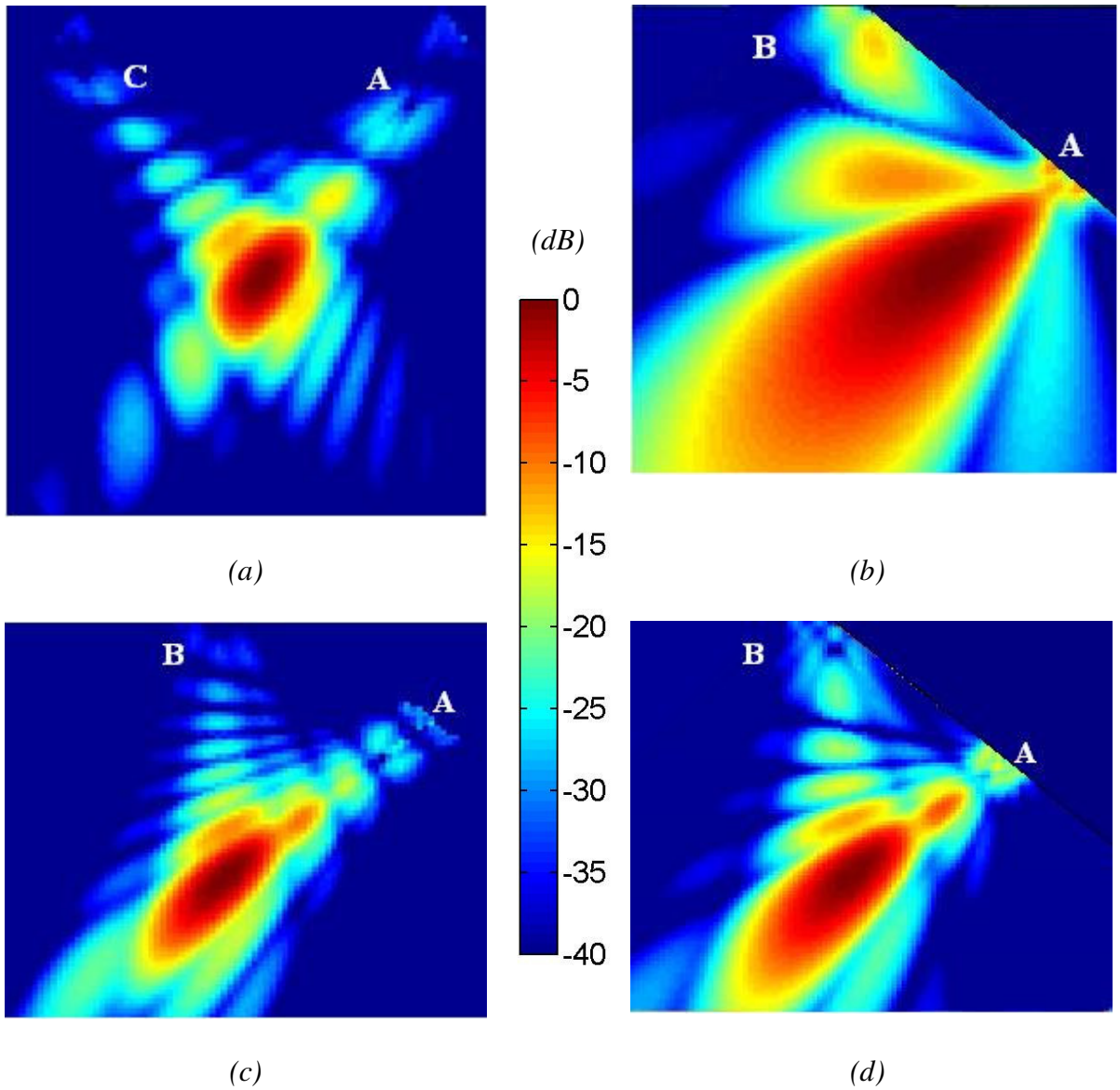

Figure 5.4: Measurement volume as resulted from correlation of beam patterns of (a) imager and receiver at difference frequency ($f_i - f_p$) of 120 kHz, (b) for pump frequency (f_p) 30 kHz and receiving frequency 60 kHz, (c) for pump frequency 40 kHz and receiving frequency 80 kHz and (d) for pump frequency 100 kHz and receiving frequency 200 kHz. The letters indicate the devices as in Figure 5.1. The relative position of the devices is shown in Figure 5.2. The colorbar shows the intensity fall-off from the reference common focus point F (dB).

Examples are shown in Figure 5.4 (b)-(d), where the correlated beam patterns are shown for (b) pump frequencies 30 kHz and receiving frequency 60 kHz, (c) 40 kHz and receiving frequency 80 kHz and (d) 100 kHz and receiving frequency 200 kHz. It is observed , as for

example in Figure 5.4 (b), that for low pump frequencies the transmitter beam is so wide that the greatest section of the receiving device corresponds to the common sensing volume. As already mentioned, the measuring volume for each frequency component of interest is defined by the 3 dB fall off limits of this sensing volume maximum value with respect to the reference common focus point F (see Figure 5.2). The accuracy of this estimated sensing volume is based on the accuracy of the numerical code to compute the beam patterns. The code was first tested to predict the directivities of each device separately. Example of these calculated beams for the pump source are shown in Appendix B where they are compared with calibration beam patterns obtained from the device manufacturer. It was observed that within the 3dB beam width the code predicts within 1 degree accuracy the calibrated beam patterns. For larger beam widths the error increases. For example at 30 kHz, the computed 10 dB beam width deviates approximately 16 degrees from the measured directivity. This occurs because the beam pattern computations with the use of the Rayleigh integral are based on the assumption that the vibrating surface is flat and part of an infinite baffle. It is well known that such calculations are accurate within a limited range of off-acoustic axis angles because diffraction effects are neglected (Sinayoko *et al*., 2009). As already noted by Herrin and Wu (2000), the accuracy is better at high frequencies. This is mainly because the beam has high directionality. Therefore calculations of the common sensing volume for the 3dB volume frequencies are considered without errors. As it will be described later in this chapter, to test the effect of taking into account bigger sensing volumes, inversions using a 6 dB beamwidth were carried out but these are interpreted with caution as contain frequency-dependent errors.

5.2 The inversion technique

5.2.1 Computations of single bubble nonlinearity

The inversion technique is based on the principle that bubbles can oscillate nonlinearly whilst retaining their spherical shape. Thus the source of nonlinearity considered for the development of this technique is the nonlinear character of the bubble dynamics equations which describe the bubble pulsations. When bubbles are subjected to very small acoustic pressure amplitudes they will respond with small oscillations about their equilibrium radius. Naturally for these

pulsations, their response will have the same frequency response components with the insonification spectrum. Increasing the driving amplitude will bring about effects of nonlinearity manifesting themselves as the occurrence of several simultaneously excited resonances. These nonlinearities arise from the volume pulsations of the bubble. This effect has been studied previously for a single insonification frequency using the Rayleigh-Plesset equation (Lauterborn, 1976). These studies showed that bubbles of different equilibrium radius, R_0, will respond differently to the same sound field and under the same ambient conditions. This results in a large amount of combinations of acoustic field-bubble sizes that must be examined for a bubble sizing experiment. As stated by Lauterborn (1976): 'the situation is very complex and …it is impossible to calculate a nearly sufficient variety of what may happen'; for this reason here a range of cases of interest were numerically studied. The algorithm used for these numerical studies and for the interpretation of acoustic data in terms of bubble counts was the modified Rayleigh-Plesset equation discussed in 2.2. The numerical results were obtained using the Matlab® ode45 solver, discussed in 2.2.2. The corresponding bubble spectra were obtained by taking the fast Fourier transform of the computed solution.

Owing to the complexity of the problem, it was not attempted to derive analytical solutions. Instead numerical simulations were used to predict the response of a range of bubble sizes of interest for every frequency pair used for the experiments. Also these simulations served to get insight about the correspondence between the bubble mediated nonlinear components and the bubble size. This is explained below using the following numerical simulation examples shown in Figure 5.5 to Figure 5.8. These numerical results were obtained for: f_p =30 kHz and f_i = 220 kHz with pressure amplitude of 15 kPa (0-peak). All simulation conditions are the same as those used for the tank experiments. These simulations show the scattered amplitude spectra for bubble sizes resonant at: (a) $f_i - f_p$ =190 kHz, i.e. $R_0 \approx 18\mu$m, (b) f_p =30 kHz i.e. $R_0 \approx 116\ \mu$m, (c) f_i = 220 kHz i.e. $R_0 \approx 16\ \mu$m, and (d) $f_i + f_p$ =250 kHz, i.e. $R_0 \approx 14\ \mu$m. This set of simulations is focused on the difference frequency generation using the bubble dynamics equation (2.56). Therefore the frequency term entering the damping

terms (2.49) and (2.50) is $f_i - f_p$. As a consequence of this approach the only spectral component which is predicted rigorously is the one at the difference frequency $f_i - f_p$.

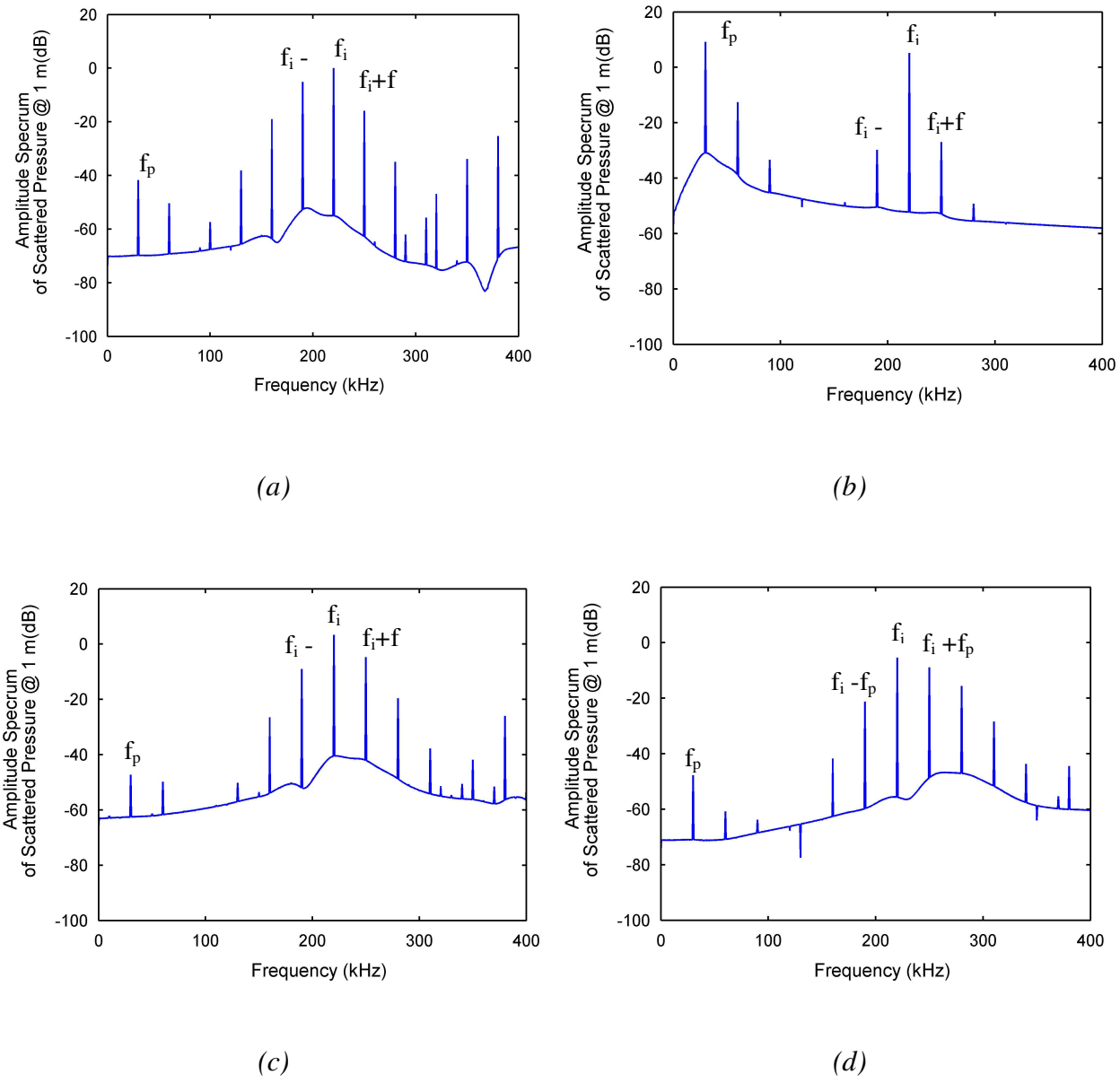

Figure 5.5: Amplitude spectrum (with a common dB reference) of scattered pressure at 1 m from a single bubble of size resonant at (a) $f_i - f_p$ =190 kHz, (b) f_p =30 kHz (c) f_i = 220 kHz and (d) $f_i + f_p$ =250 kHz. The bubble is insonified by a wave at 30 kHz and another at 220 kHz. Both waves have pressure amplitude of 15 kPa (0-peak). Note that for the simulations the damping terms have been modified to accommodate the difference frequency by substituting the difference frequency $f_i - f_p$ for the damping terms in equations (2.49) and (2.50).

In other words the damping is fitted for the difference frequency. Thus frequency components at frequencies lower than the difference frequency are overdamped whereas frequency components at higher frequencies are underdamped. For this reason these figures are not suitable to draw conclusions for frequencies other than the difference frequency. As shown in these figures, the single bubble that is resonant at the difference frequency shown in Figure 5.5 (a) dominates the detected signal at $f_i - f_p$ compared to the scattering at $f_i - f_p$ from a resonant bubble at the pump frequency f_p shown in Figure 5.5 (b) and it is greater than the scattering at $f_i - f_p$ from a size resonant at the imaging f_i ,Figure 5.5 (c), and the sum frequency, Figure 5.5 (d).

Another example of simulation results is shown in Figure 5.6 (a)-(d). The numerical results are obtained for: f_p =55 kHz and f_i = 220 kHz, both having a pressure amplitude of 15 kPa (0-peak). The simulations show the scattered power spectra for a bubble resonant at: (a) $f_i - f_p$ =165 kHz, i.e. $R_0 \approx 21.5\ \mu$m, (b) f_p =55 kHz i.e. $R_0 \approx 64\ \mu$m, (c) f_i = 220 kHz i.e. $R_0 \approx 16\ \mu$m, and (d) $f_i + f_p$ =275 kHz, i.e. $R_0 \approx 12\ \mu$m. As for the simulations of Figure 5.5, this set of simulations is focused on the difference frequency generation and the damping entering the simulations was adjusted accordingly. However in contrast to the example of Figure 5.5, in the case of single bubble that is resonant at the difference frequency, shown in Figure 5.6(a), emits at the difference frequency almost the same amount of acoustic energy as another one resonant at the pump Figure 5.6 (b) or the imaging frequency, shown in Figure 5.6(d).

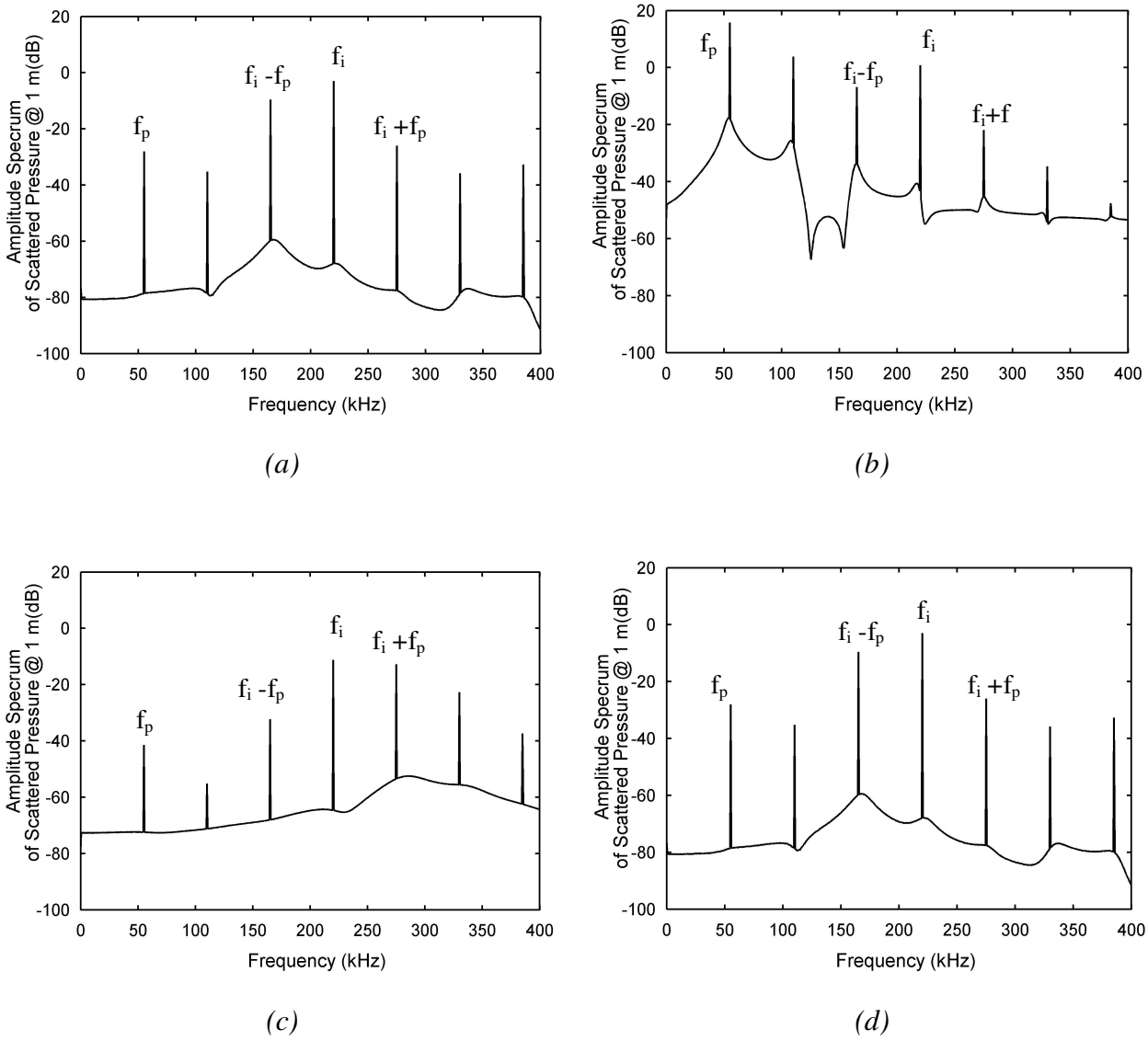

Figure 5.6: Amplitude spectrum (with a common dB reference) of scattered pressure at 1 m form a single bubble of size resonant at (a) $f_i - f_p$ =165 kHz, (b) f_p =55 kHz (c) f_i =220 kHz and (d) $f_i + f_p$ = 275 kHz. The bubble is insonified by a wave at 55 kHz and another at 220 kHz. Both waves have pressure amplitude of 15 kPa (0-peak). Note that for the simulations the damping terms have been modified to accommodate the difference frequency by substituting the difference frequency $f_i - f_p$ for the damping terms, equations (2.49) and (2.50).

As no one-to one mapping between the resonant bubble sizes and the pressure component at difference frequency ($\left|\tilde{p}_{\mathrm{b}}(r,\omega)\right|^2_{\omega=\omega-}$) exists; the only way to carry out such an inversion is to monitor simultaneously another frequency component. This frequency component must cover

the bubble sizes contributing to the difference-frequency component in order to have an equal number of measured spectral components and unknown bubble sizes. It was chosen to monitor the nonlinear signal scattered at twice the pump frequency ($\left|\tilde{p}_{\mathrm{b}}(r,\omega)\right|_{\omega=2\omega_{\mathrm{p}}}$) because it can be uniquely related to the bubbles resonant at the pump frequency and does not depend on the presence of the second acoustic frequency. Having these characteristics, it adds information on the bubble sizes being resonant at the pump frequency without introducing more unknowns. These features are illustrated through the simulation results shown in Figure 5.7 (a)-(b) and Figure 5.8 (a)-(b). Here the frequency of interest is the $2f_{\mathrm{p}}$ and therefore this frequency enters the thermal and acoustic radiation damping terms, equations (2.49) and (2.50) . The numerical results shown in Figure 5.7 are obtained for: f_p =55 kHz and f_i = 220 kHz. All other simulation conditions are kept the same with Figure 5.5 and Figure 5.6. These simulations show the scattered amplitude spectra for bubble sizes resonant at (a) $2f_p$ =110 kHz, i.e. $R_0 \approx 32\ \mu$m and at f_p =55 kHz.

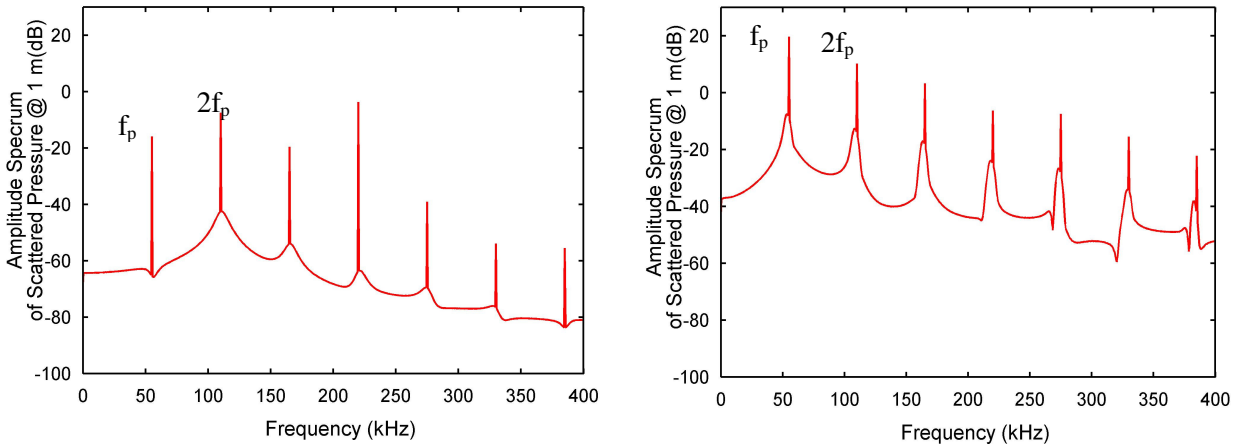

(a) *(b)*

Figure 5.7: Amplitude spectrum (with a common dB reference) of scattered pressure at 1 m from a single bubble of size resonant at (a) $2f_p$ =110 kHz and, (b) f_p =55 kHz under two frequency insonification (f_p =55 kHz and f_i =220 kHz).

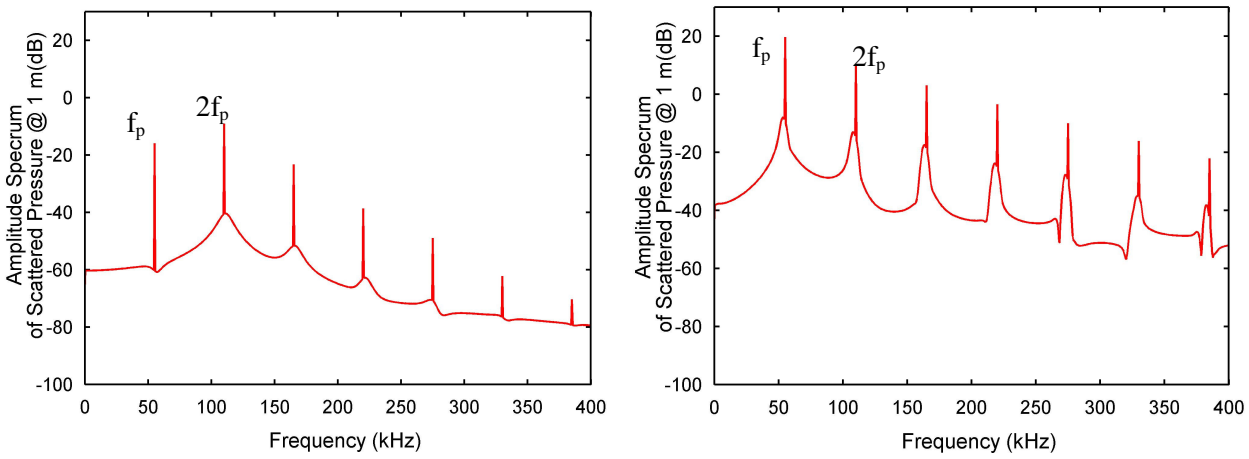

Figure 5.8: Amplitude spectrum (with a common dB reference) of scattered pressure at 1 m from a single bubble of size resonant at (a) =110 kHz and, (b) =55 kHz under a single frequency insonification at 55 kHz.

Clearly nonlinear generation at $2f_p$ results form bubbles resonant at the pump frequency whilst bubbles resonant at twice the pump frequency give negligible pressure spectral components at $2f_p$. As shown in Figure 5.8, a single bubble resonant at f_p gives about 10 dB greater signal than the size resonant at $2f_p$. Thus it can be assumed that only bubbles resonant at f_p contribute to the measured signal at $2f_p$. These observations suggest that there is one-to-one correspondence between the bubbles resonant at the frequencies interrogating the scattering volume and the measure spectral component at $2f_p$. The simulations of Figure 5.7 were repeated after setting the imaging pressure equal to zero. Comparison of the spectra in Figure 5.8 (a) and (b), suggest that the generation of the $2f_p$ component is not influenced by the presence of the second acoustic wave.

5.2.2 Formulation of the inversion matrix

The inversion method is developed based on the observation that resonant bubbles at the insonification frequencies and their combinations contribute the most. As bubble size

distribution will be present in the insonification volume; this type of insonification is expected to lead to the generation of a series of harmonics and combination frequencies between the pump and the imaging frequency, such as $2f_p, 2f_i, f_i - f_p$, $f_i + f_p, f_i - 2f_p, f_i + 2f_p$ etc). This was observed experimentally as shown in Figure 5.9 (a)-(c). In these figures bubble-free spectra from fresh water measurements are also shown as a black line, with grey lines to indicate the upper and lower error bounds. These measurements show that the components generated from the medium nonlinearity are considerably lower than the bubble mediated nonlinearity.

In order to relate the bubble sizes with the measured difference frequency, the bubble spectral component at the difference frequency was computed and stored in a matrix. A three dimensional representation of this matrix is shown Figure 5.10 where linear axes have been used for all dimensions.

(a)

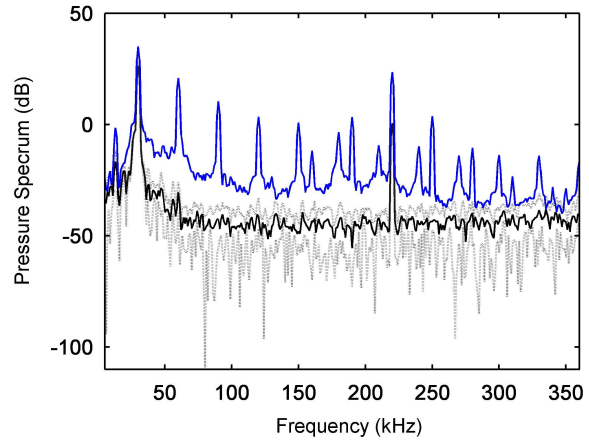

(b)

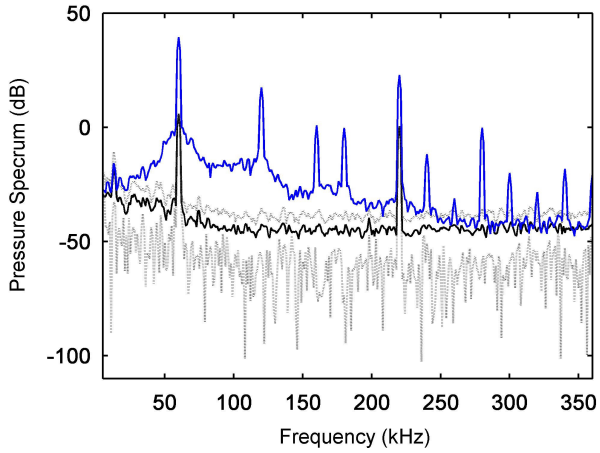

(c)

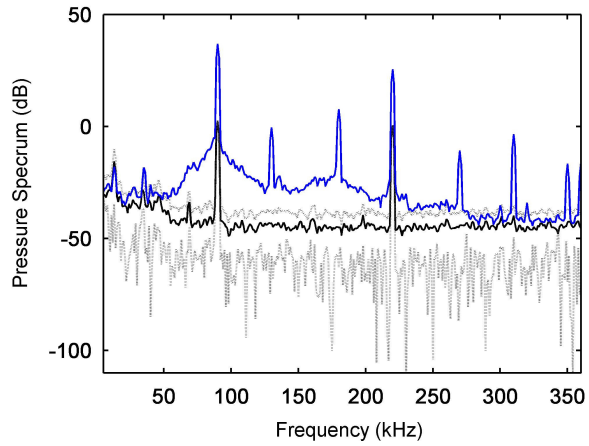

Figure 5.9: Mean spectral components (with a common dB reference) in fresh water (black line) and in bubbly water (blue line) of the measured pressure at the receiver , for imaging frequency of 220 kHz and pump frequency of (a) 30 kHz, (b) 60 kHz and (c) 90 kHz. The light grey dotted lines indicate the maximum and minimum signal variations measured in fresh water. The spectral frequencies between 5 kHz and 360 kHz are shown.

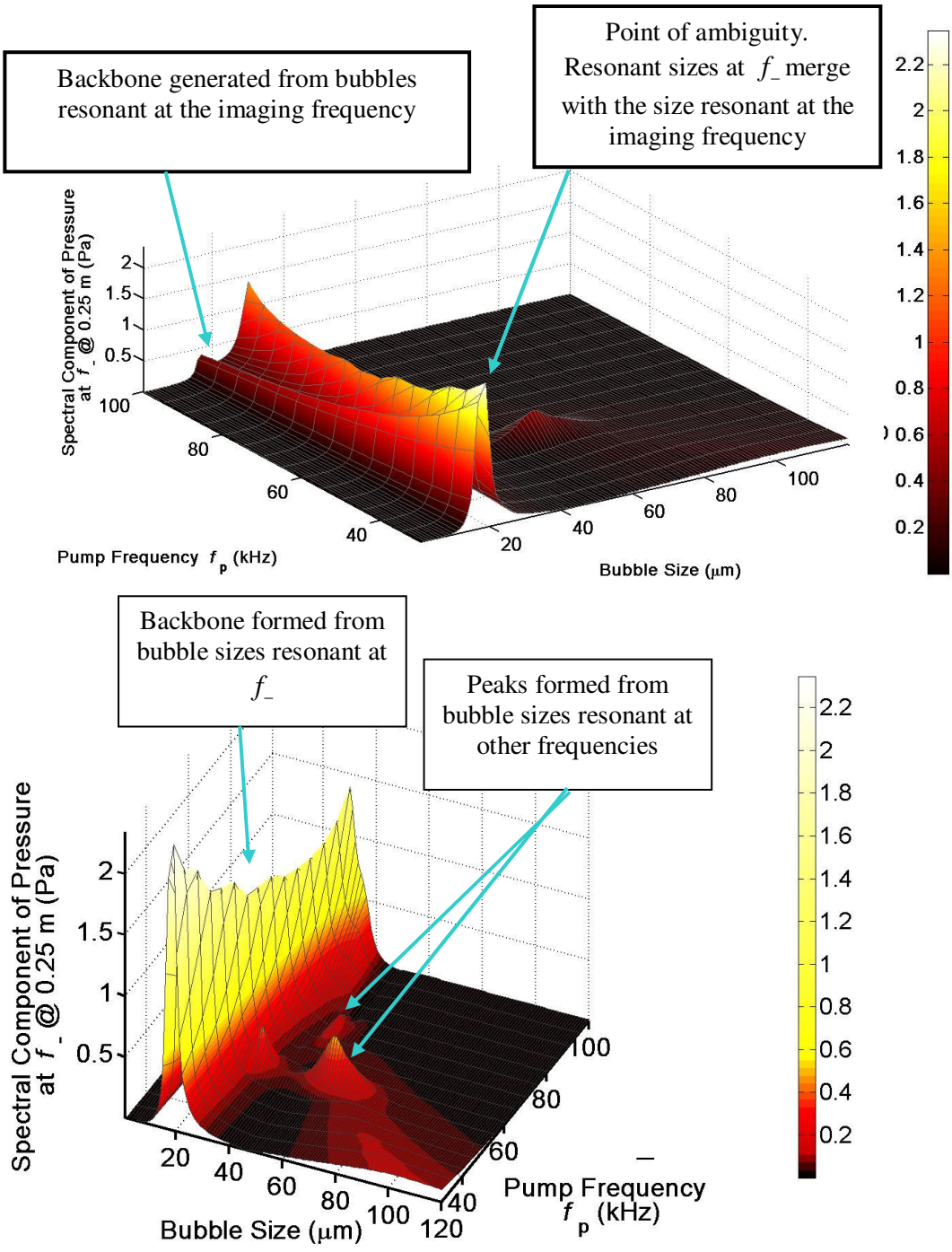

Figure 5.10: Three dimensional representation of the difference frequency scattered spectra corresponding to the conditions of the tank experiments undertaken with the combination frequency device. The pressure emitted at difference frequency (vertical axis) was computed for bubble sizes ranging form 1 to 120 micron using one micron bins and for pump frequencies ranging from 30 kHz to 100 kHz with increments of 5 kHz. The two plots show the same results but are drawn with different colorscales to highlight the magnitude of the backbone and the constant peak of bubbles resonant at 220 kHz(upper plot) and of the nonlinear peaks for other sizes (lower plot).

The matrix is depicted with two different colour scales. The vertical axis shows the scattered pressure from a single bubble, whereas every point of the grid of the horizontal plane represents the bubble size/pump frequency combinations. As shown in Figure 5.10, there is not a one-to-one mapping between the difference-frequency spectral component and the bubble size for every $f_i - f_p$ frequency pair. The greater peaks forming the backbone of the surface shown in Figure 5.10 occur for bubble sizes resonant at the difference frequency $f_i - f_p$ .if these were the only ones present the method would resemble the parametric kind of excitation (see end of section 2.1.2).

However the other peaks shown in Figure 5.10 cannot be ignored in the inversion as they have similar order of magnitude. These peaks are mediated from bubbles resonant at the pump frequency or other combinations of imager-pump frequencies. Additionally there is a constant contribution of the bubbles resonant at the imaging frequency. As shown in the first view of Figure 5.10, this contribution is merging with the contribution of the difference frequency when the pump source emits at 30 kHz. Hence the spectral component at $f_i - f_p$ =190 kHz can be assumed to give the total number of bubbles resonant at the imaging frequency f_i ($R_0 \approx 16\ \mu$m) as a size bin merged with the bubbles resonant at $f_i - f_p$, i.e. $R_0 \approx 18\ \mu$m . For the rest of the pump-imaging frequency pairs the inversion matrix was formulated using the information of the matrix shown in Figure 5.10. First the nonlinear scattering cross sections were computed and then they were stored in a matrix $\boldsymbol{\sigma}_{i\text{-}p}$ as defined by equation (4.51). This led to a matrix formulation where each row of this matrix gives the contribution of each bubble bin size at the difference frequency under consideration whereas each column of this matrix gives the importance of a certain bubble size for the difference frequency ($f_i - f_p$) range under consideration. As already mentioned, more than one bubble size contributes to that difference frequency component, thus the matrix $\boldsymbol{\sigma}_{i\text{-}p}$ is not square. As resulted from simulations, it has twice as many columns than rows. This is explained by the fact that a component at the difference frequency stems predominantly from sizes resonant at the difference frequency and another at the pump frequency. The information about the sizes resonant at pump frequencies is complemented by monitoring the component at twice the

pump frequency, which as mentioned in section 5.2.1 results mainly form bubbles resonant at the pump frequency.

In the same manner a matrix with the nonlinear cross sections at the double pump frequency, $\boldsymbol{\sigma}_{2\mathrm{p}}$, was formulated using numerical computations for the corresponding spectral component, i.e. $\left|\tilde{p}_{\mathrm{b}}(r,\omega)\right|_{\omega=2\omega_{\mathrm{p}}}$. This is a diagonal matrix because, as already discussed, a peak at $2f_{\mathrm{p}}$ is uniquely related to a resonant bubble size at f_{p}. The final inversion matrix was formed by simply the merging of the matrices $\boldsymbol{\sigma}_{2\mathrm{p}}$ and $\boldsymbol{\sigma}_{\mathrm{i\text{-}p}}$, into one larger matrix under the assumption of isotropic scattering:

$$\boldsymbol{\sigma}=\begin{bmatrix}
\sigma_{\mathrm{ds\text{-}}}(\omega^{(i-1)},R_0^{(i-1)}) & \dots & \sigma_{\mathrm{ds}}(\omega^{(i-1)},R_0^{(i-p)}) & \sigma_{\mathrm{ds\text{-}}}(\omega^{(i-1)},R_0^{(1)}) & \dots & \dots & \sigma_{\mathrm{ds\text{-}}}(\omega^{(i-1)},R_0^{(p)}) \\
\dots & \dots & \dots & \dots & \dots & \dots & \dots \\
\dots & \dots & \dots & \dots & \dots & \dots & \dots \\
\sigma_{\mathrm{ds\text{-}}}(\omega^{(i-p)},R_0^{(i-1)}) & \dots & \sigma_{\mathrm{ds\text{-}}}(\omega^{(i-p)},R_0^{(i-p)}) & \sigma_{\mathrm{ds\text{-}}}(\omega^{(i-p)},R_0^{(1)}) & \dots & \dots & \sigma_{\mathrm{ds\text{-}}}(\omega^{(i-p)},R_0^{(p)}) \\
0 & 0 & 0 & 0 & 0 & 0 & \sigma_{\mathrm{ds}\,2\omega_{\mathrm{p}}}(\omega^{(2p)},R_0^{(p)}) \\
0 & 0 & 0 & 0 & 0 & \dots & 0 \\
0 & 0 & 0 & 0 & \dots & 0 & 0 \\
0 & 0 & 0 & \sigma_{\mathrm{ds}\,2\omega_{\mathrm{p}}}(\omega^{(1)},R_0^{(1)}) & 0 & 0 & 0
\end{bmatrix}$$

The superscript p denotes the varying pump frequency and i the imaging frequency. The partition of the inversion matrix with zeros expresses the fact that no bubble sizes resonant at the difference frequency give raise to frequency components at twice the pump frequency. Thus the bubbles resonant at f_p give uniquely rise to the nonlinear component $2f_p$. Note that the partition of the matrix with the $2f_p$ components is anti diagonal to maintain the bubble sizes in ascending order; because as the difference frequency decreases the pump frequency increases.

5.3 Assumptions of the two-frequency inversion technique

The combination frequency technique for water exploits simultaneously many bubble sizes using nonlinear scattering cross sections. This technique is more unambiguous than other bubble sizing techniques using linear scattering because linear cross sections exhibit a local maximum whereas nonlinear ones exhibit a global maximum at the resonant bubble size (Figure 2.4). Although resonant bubbles are very efficient scatterers because their scattering cross sections are much larger than their geometric cross section (Medwin, 1977); ambiguities in the linear scattered spectra may occur if big bubbles are present. If large bubbles are present, they have the potential to scatter incident sound more strongly than the resonant smaller ones. This is demonstrated in Figure 2.4 (a) and (b), which show the scattering cross section (solid line) and the geometrical cross section (dotted line) as function of a range of bubble sizes insonified at 100 kHz and 30 kHz respectively. As shown in Figure 2.4 the scattering cross section has a local peak at the radius corresponding to resonance at the insonification frequency. The curve has a strongly growing tail which can be of the same order of magnitude as the peak. That is for linear scattering the resonance peak is not a global maximum as opposed to the nonlinear scattering cross sections (see Figure 5.10). This ambiguity appears when big bubbles are present. For example, if a bubble cloud has a bubble size distribution comprising bubbles of R_0=36 microns and R_0=300 microns and it is insonified with an acoustic wave of 30 kHz, then according to Figure 2.4 (a) the resonant scattering from each bubble of R_0=36 microns will equal the geometrical scattering from each bubble of R_0=300 microns. Thus this scattering may be interpreted as either sizes.

Moreover, the formulation of the scattering matrix and the example of Figure 2.4 rely on the assumption that all bubbles pulsate, that is, they maintain their spherical shape. This is a valid assumption as long as $kR_0 \ll 1$. Larger bubbles violate this condition and as the kR_0 value increases, the scattering directivity begins to deviate from being omnidirectional. Before proceeding with the scattering directivity analysis, it must be noted that the biggest bubble size considered for the following analysis has R_0=0.5 mm; bigger bubbles deviate significantly

from a spherical form; they take an ellipsoidal form, see chapter 7 of Clift (1978). Such bubbles are not likely to be encountered in the tank as these rise quickly to the surface of the small tank (see Figure 5.3) where the bubbles were generated instead of being transported down to the big tank. To examine the limiting case of kR_0 approaching unity, a modal series solution was employed for the calculation of scattering from gas bubbles according to the approach of Anderson (1950). In this approach, viscous and thermal bubble losses are not taken into account. Nevertheless it is a good approximation because the bubble sizes under consideration here are insonified by a frequency much greater than their resonance frequency and in this case scattering is the dominant loss mechanism (Nishi, 1975). The polar plots show the change of directionality, normalised by $\sqrt{\pi R_0}$, as kR_0 approaches unity. These numerical results show that the assumptions of omnidirectional (or isotropic) scattering can be satisfactory for less than $kR_0 = 0.2$. For bigger kR_0 values the backscattered field will be much less than if the scattering were isotropic, Figure 5.11 (c). Thus the predictions of the bubble dynamics model are correct for bubbles sizes up to approximately 0.3 mm. For all the calculations shown in Figure 5.11 the first seven modes were used for the computations.

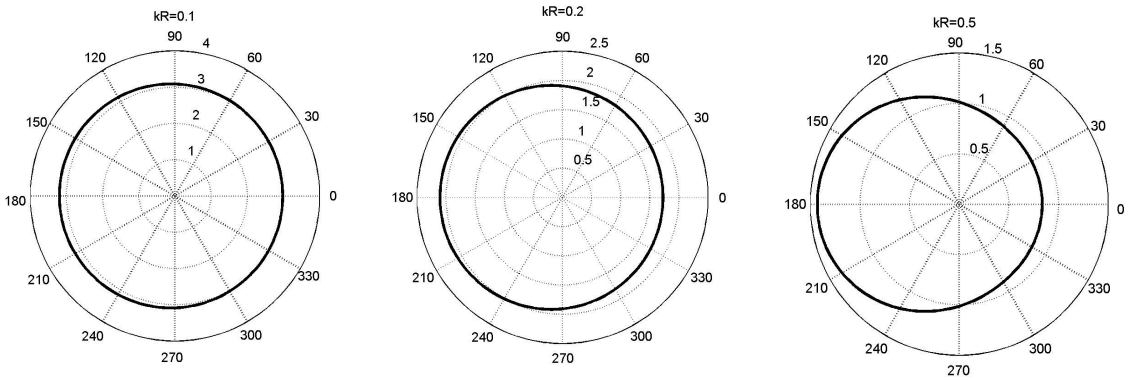

(a) *(b)* *(c)*

Figure 5.11: Directivity of the scattering from an air-filled bubble normalised by $\sqrt{\pi R_0}$ *for (a)* kR_0 *=0.1, (b)* kR_0 *=0.2 and (c)* kR_0 *=0.5. The plane wave is incident from the right at 0º.*

5.4 Experimental inversion results

The propagation measurements and inversion results shown in this section were carried out by P. Fox. The inversion code was programmed by Prof. P. White and extended by P. Fox to optimum regularisation parameter selection. The scattering data collection, processing and interpretation belong to this PhD work.

In this section inversion results from experiments that took place in a bubbly water tank are presented. Figure 5.12 shows two bubble population estimates as the number of bubbles per cubic metre per micrometer radius range. The two curves resulted from two independent sets of measurements using different bubble sizing methods. The red curve resulted using the classic method of inverting attenuation data from propagation experiments (Medwin, 1977). This method relies on the fact that bubbles dramatically increase the attenuation of wave propagating through a bubble cloud (Duraiswami *et al.*, 1998). It is a single frequency coherent method (Sarkar and Prosperetti, 1994) and requires the a priori assumption that the void fraction is not greater than 10^{-5} (Kargl, 2002) and that no big scatterers ($kR_0 \sim 1$ or larger) are present in the propagation path. This method has been discussed extensively elsewhere (Meers, 2005; Coles, 2009) and such a discussion is not part of the work for this thesis. Employment of this method was a cross-check for the combination–frequency method. For this reason a wide range of frequencies was employed (from 10 kHz to 290 kHz) making it possible to obtain an estimate for number of bubbles having a minimum equilibrium radius equal to ~10 microns and a maximum equilibrium radius of approximately 345 microns; covering in this way most bubble sizes present in the tank. The inversion results are shown with red line in Figure 5.12 together with the inversion results from the scattering experiment (blue line). The inversion of the propagation data was performed using equation (4.61) which led to a formulation of a matrix equation in the form of matrix equation (4.54). The regularisation parameter was chosen by the numerical code as the minimum value that gave a positive number of bubbles for all frequencies and the best forward data fit as discussed in section 4.2 (equation (4.55). The raw attenuation data were filtered, prior to being inverted, using a third order Savitzky-Golay smoothing filter. The raw data, the filtered data and the forward fitted data are shown in Figure 5.13 with blue, green and red curves respectively.

The blue line of Figure 5.12 represents inversion results using the combination-frequency technique, which as shown exhibited a very good agreement with the red curve. The smaller bubbles, i.e. the part of the population indicated by the arrow, result predominantly from the difference frequency whereas the rest of the population resulted only from the pump frequency. The data were taken in sets of 10 repetitions. For each measurement set, the pump source repeatedly emitted pulses ranging from 30 kHz to 100 kHz in 5 kHz steps. The data were acquired as 10 consecutive pulses of the same pump frequency with a 2 ms pause between each pulse. This allowed the assumption that the bubble size distribution of the cloud is consistent across data sets. To estimate the bubble distribution of the tank, nine of such data sets were acquired in succession on the same day.

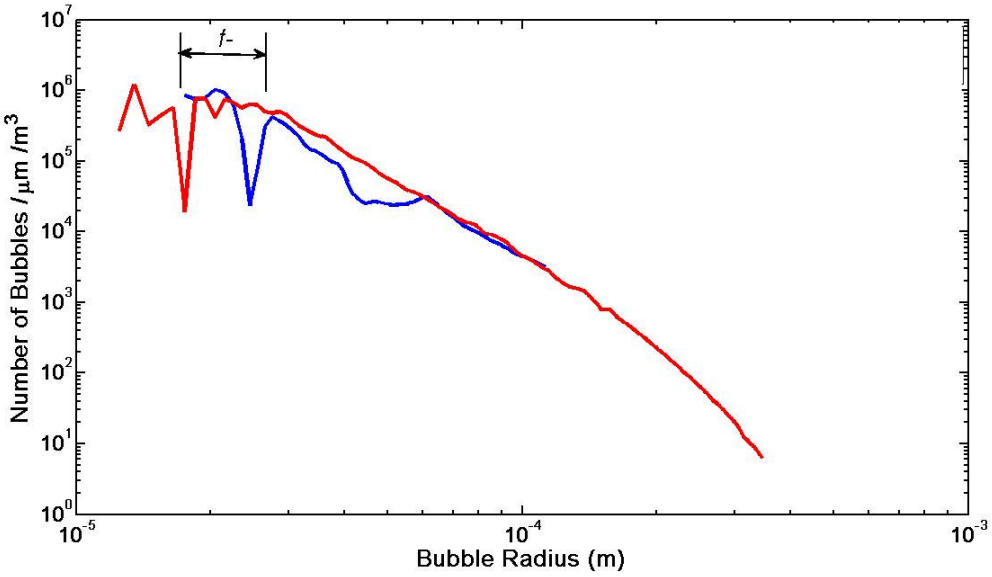

Figure 5.12: Bubble population estimate plotted as number of bubbles per cubic metre per micrometer radius range versus bubble size. The two curves resulted from two independent sets of measurements: The red and blue line represent inversion results using single frequency attenuation and scattering measurements respectively. The arrow indicates that proportion of the population of the blue curve that resulted predominately from the difference frequency.

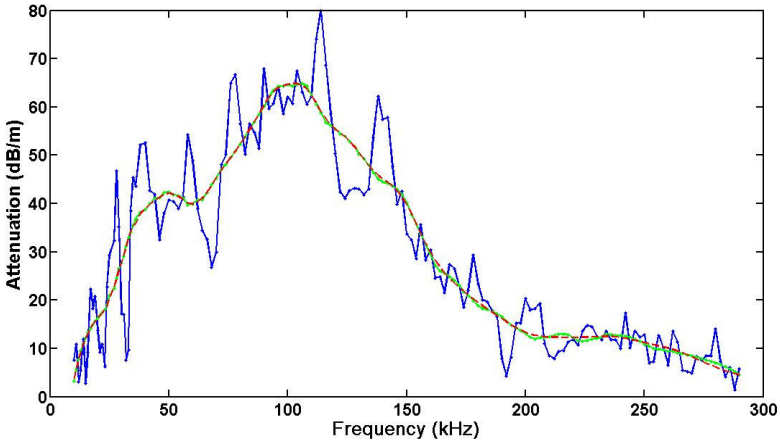

Figure 5.13: Attenuation (dB/m) versus frequency measured in the water tank with bubbly water: raw data (blue lines), filtered data (green lines) and forward fitted data (red lines).

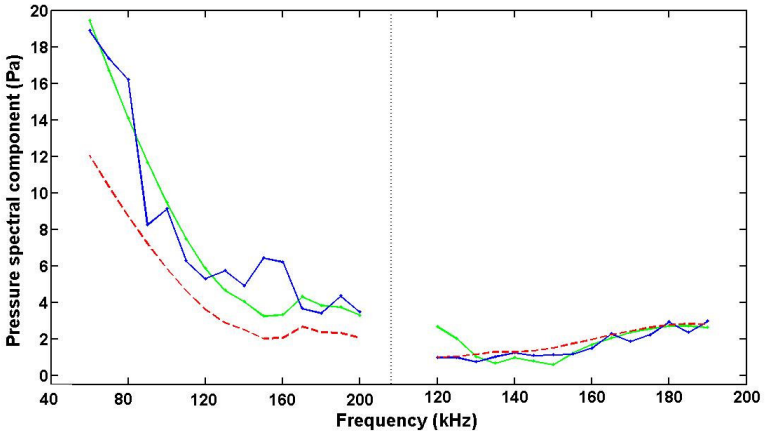

Figure 5.14: Raw (blue line), filtered (green line) and forward fitted (red dashed line) data versus frequency range from the scattering experiment. For the scattering experiment the data is presented as amplitude spectral component (Pa) for the primary (30-100 kHz) and the difference frequency (120-190 kHz) range. Note that the two components of the same colour are derived at the same inversion (see equation (4.57) and (4.58).

The spectra of all acquired waveforms were averaged and then the average spectral components at $2f_{\mathrm{p}}$ and $f_{\mathrm{i}} - f_{\mathrm{p}}$ from all frequency combinations were used in the inversion. These averaged spectra were then filtered prior to being inverted using a third order Savitzky-Golay smoothing filter which has many advantages against other filters as detailed in section 8.3.5 of Orfanidis (1996). This filter minimizes the least-squares error in fitting a third order polynomial to frames of noisy data. In Figure 5.14 the raw scattering data are plotted with blue lines, the filtered inversion input data with green lines and the forward fitted data with red

lines. These data were melded together in a column matrix for the inversion, see equation (4.57). Here they are presented separately in order to indicate which spectra belong to the difference frequency (right hand side of the figure) and which to twice the pump frequency (left hand side of the figure).

This paragraph discusses two approaches to assess the uncertainty of the bubble distribution that was computed from the scattering experiment. The first involves the variability of the acquired signal. The second approach invokes the statistics of the returns from the scatterers. The first approach was based on finding the standard deviation of the measured pressure spectral components at each frequency. Adding this standard deviation as perturbation to the average spectral component and computing the bubble distribution in the same way (which was keeping the minimum value for beta that gives non negative bubble populations and letting the algorithm choose the optimum value for the scaling parameter), the upper and the lower bounds of the inversion were found. The results are shown as cyan block plot in Figure 5.15. The second approach attempts to assess the error of the bubble distribution using the statistics of the random phase arrivals from the bubbles. This approach was followed by Thorne *et al.* (1993) to estimate sediment concentrations in marine suspensions. As in the case of a homogeneous suspension of fixed concentration, so for homogeneous bubbly water, the signal is not constant but it is variable due to the random phase of the returns of the scatterers, here the bubbles. As discussed at the end of paragraph 4.1, the outcome of the superposition of signal with random phases leads to a Rayleigh distribution. Equation (4.14) was used to estimate the standard error of the mean amplitude form n independent observations. From equation (4.14), it can be seen that 6% accuracy in the signal amplitude was obtained from the $n=90$ independent measurements taken at each frequency combination. As previously to estimate impact on the bubble population computations, the standard error was added as perturbation to the mean value. The results are shown in Figure 5.16 with the green blockplot. The error bounds of the population as computed with the first approach are also shown for comparison with the blue blockplot.

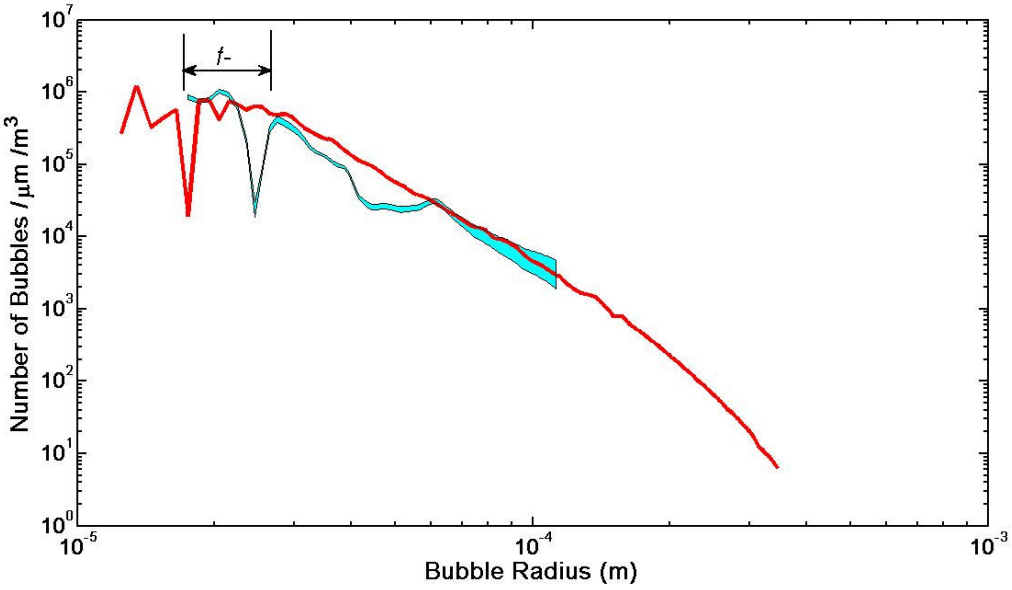

Figure 5.15: Bubble population estimate plotted as number of bubbles per cubic metre per micrometer radius range versus bubble size. The two curves resulted as in Figure 5.12, from two independent sets of measurements: The red line represent inversion results using single frequency attenuation measurements. The cyan area represents the error bounds for the blue line of Figure 5.12, as calculated from the standard deviation of the measured signal from the scattering experiment. The arrow indicates that proportion of the population of the cyan that resulted predominately from the difference frequency.

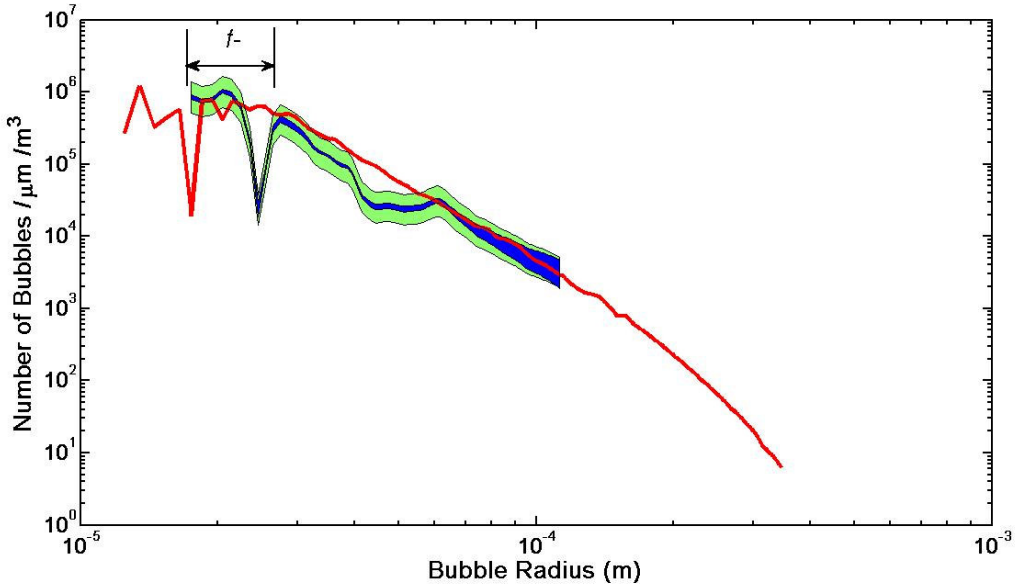

Figure 5.16: As in Figure 5.15. The green blockplot has been added which shows the theoretical error of the bubble population estimate resulted from the combination frequency measurements.

The results show that the measured signal variation was smaller than the theoretical value of the signal standard deviation for the higher frequencies. Interestingly at the lower frequencies, which correspond to the bigger bubble sizes, the theoretical error and measured signal variation agree are in good agreement.

The last paragraph of this section discusses two completely different aspects which cause the same effect on the inversion results: Shifting of the bubble distribution curve vertically on the graph. The first aspect is the effect of the regularisation parameter. It would be possible to obtain a smoother curve by increasing the value of beta and keeping the algorithm constrain for minimum error $\left|\hat{\mathbf{P}}-\mathbf{P}\right|$ to select the appropriate value for the scaling parameter Sc. This approach was tested by doubling the minimum beta value. The results are shown with blue intermitted line in Figure 5.17, where the distributions of Figure 5.12 are also shown for comparison. This choice would shift the results to lower bubble distribution values. The second aspect investigated, was the effect of the sensing volume. The 6 dB sensing volume was computed in the same way as the 3 dB volume described in section 5.1. As shown in Figure 5.18, increasing the sensing volume will give a smaller bubble size distribution. This is an expected result as the inversion result is inversely proportional to the bubble size distribution, see equations (4.42) and (4.50). It is difficult to asses the computation error for larger sensing volumes because beam patterns at off-axis angles cannot be computed accurately (see discussion at the end of section 5.1). However in either cases the bubble distribution curves agree within an order of magnitude with the bubble distribution computed with the propagation method.

All figures of this section, exhibit a dip, which is an artefact of the inversion. Increasing the regularisation parameter smoothes the bubble distribution curve but also increases the estimation error. The effect of increasing the regularisation parameter was demonstrated here by doubling the optimum beta corresponding to the combination frequency experiments. As shown in Figure 5.17, doubling the regularisation parameter smoothes the deep dip of the combination inversion results (blue dotted curve) but worsens the agreement with the curves which resulted by the optimal minimum beta (solid line).

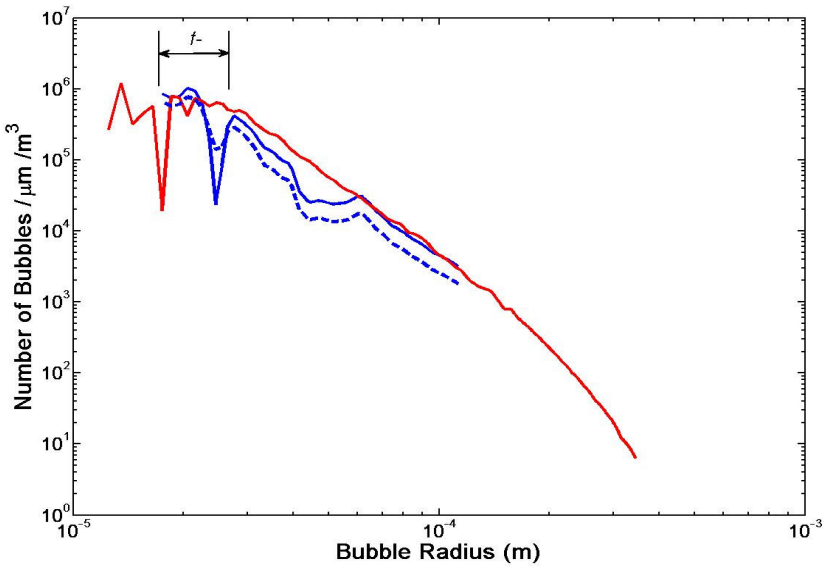

Figure 5.17: Bubble population estimates plotted as number of bubbles per cubic metre per micrometer radius range versus bubble size. The red and blue lines represent inversion results from single frequency attenuation and scattering measurements respectively, using the minimum value for the regularisation parameter. The arrow indicates that proportion of the population of the blue curve that resulted predominately from the difference frequency. The blue dotted curve shows the bubble population which results from scattering measurements by doubling the regularisation parameter.

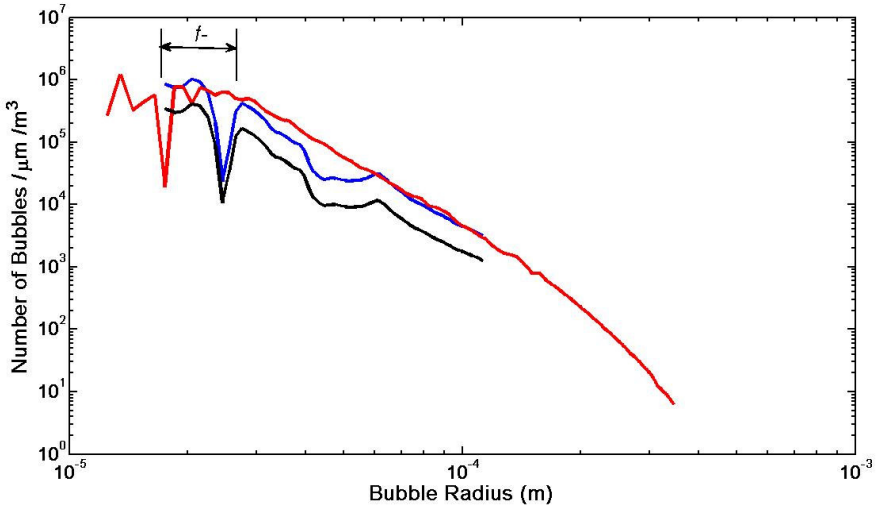

Figure 5.18: Bubble population estimates plotted as number of bubbles per cubic metre per micrometer radius range versus bubble size. The red and blue lines represent inversion results from single frequency attenuation and scattering measurements respectively, using the minimum value for the regularisation parameter. The arrow indicates that proportion of the population of the blue curve that resulted predominately from the difference frequency. The black curve shows the bubble population which results from scattering measurements by doubling the sensing volume.

Moreover this dip is an artefact of the inversion and thus may be ignored. For this reason the criterion of having the minimum beta with the best data fit was kept thought out this work.

5.5 Summary

This chapter has presented the two-frequency inversion scattering method developed during this work. First the apparatus and the experimental set up were described as well as the underlying assumptions for using such an inversion method. The most important assumption of omindirectional scattering, that is the quantity kR_0 should be smaller than unity. The method requires accurate knowledge of the insonificaton volume for each pair of frequencies, which is an extra source of errors when the beam patterns have to be computed beyond the 3dB beam width.

The chapter then went on to present details of the inversion matrix formulation. The matrix was composed from numerically computed bubble scattering cross sections at the difference frequency and twice the pump frequency. Since numerical simulations showed that there is no one-to one mapping between the difference frequency and the bubble resonances, the use of a second scattering component was necessary to add information on the bubble sizes present, making in this way the scattering matrix square. Interestingly, simulations showed that the nonlinear pressure component at twice the pump frequency doesn't depend on the presence of the imaging frequency. This component exhibits an one-to-one correspondence with the bubbles resonant at the pump frequency, hence it could have been used alone for bubble sizing. The reason of using the difference frequency component is to extent the measurable bubble sizes.

The chapter concludes by presenting bubble size distribution results from bubbly water experiments at a laboratory tank. The results were compared with results from a bubble population resulting from inversion of transmission measurements using attenuation data, taken under the same experimental conditions. The very good agreement of the two methods proves the efficacy of the new method.

CHAPTER 6: GEOACOUSTIC PROPERTIES OF SHALLOW MARINE SEDIMENTS

This chapter discusses geotechnical and acoustical properties of gas-free seafloor sediments. Initially these geotechnical properties are defined. Then the properties of phase velocity and attenuation for both compressional (or P-waves) and shear waves (or S-waves) are examined. Relevant geoacoustic models and empirical relationships are studied with the focus on intertidal sediments, which are of interest for this work. The experimental work carried out during this study took place at intertidal sites on the south coast of England, environments where the sediment is characterised as mud and falls into the category of cohesive sediments.

Knowledge of the geoacoustic characteristics of the gas-free sediments is a prerequisite to modelling the acoustic behaviour of their gassy counterparts using the theory outlined in Chapter 3. Like the bubble model of Yang and Church (2005), equation (3.21) assumes the existence of one compressional wave in the bubble surrounding medium and, as already mentioned, it was assumed that the bubble host medium behaves in shear according to the Voigt viscoelastic model. The question is whether these assumptions are valid for the case when the host medium of bubbles in sediments (i.e. the medium surrounding the bubble in question) is itself bubble-free sediment. As this work is focused on cohesive sediments of the top metre of the seafloor for the frequency range of 10 kHz-500 kHz, the geoacoustic behaviour for these conditions is reviewed in the following paragraphs with focus to these conditions. The shear properties of the gas-free sediment are obtained by assigning a viscoelastic model to the gas-free sediments. To find a representative model, observations of shear sound speed and attenuation are employed. Moreover the possibility of assigning a viscoelastic model to Biot theory is examined. The last section discusses basic viscoelastic models and their potential to model shear wave propagation.

6.1 Geotechnical properties pertinent to geoacoustic models

Sediment physical properties are termed by civil engineers as ‘geotechnical’ properties. Here the following properties, which are linked to the acoustic properties of the sediments,

are briefly discussed: grain size, packing, porosity, density, permeability, tortuosity and shear strength.

Sediment classification is commonly based on two criteria (a) the mineral grain size and (b) the sorting i.e. the mineral grain size distribution. In this thesis, the Wentworth grade scale is used (Wentworth, 1922) for the classification of sediments according to their mineral grain size. The grain size limits of this scale are shown in the Table 6.1 expressed in mm of the grain size diameter and in phi (ϕ) units. The phi (ϕ) unit is defined by: $\phi = -\log_2 d_m / d_0$ where d_m is the sediment particle diameter in mm and d_0 is the 'standard' grain diameter equal to 1 mm. Another sediment classification is based on the silt-sand-clay ratios present and follows Shepard's ternary diagram as shown in Figure 6.1 (Shepard, 1954). Historical geoacoustic data compilations, for example, Hamilton (1970) and Shumway *et al*. (1956) and this report follow Shepard's definitions when more than one grade is present. Furthermore, characterisation as coarse, medium or fine follows the indications of the Wentworth grade scale (Wentworth, 1922). 'Mud' is another term frequently encountered in the literature and used here to indicate all sediments finer than 4ϕ, i.e. silt and clay (Flemming, 2000).

Table 6.1: Grain sizes named according to Wentworth grade scale (Wentworth, 1922)

Name	Grade limits stated as particle diameters (mm)	Phi (ϕ)
coarse sand	1.00-0.50	0-1
medium sand	0.50-0.25	1-2
fine sand	0.25-0.125	2-3
very fine sand	0.125-0.0625	3-4
coarse silt	0.0625-0.0313	4-5
medium silt	0.0313-0.0156	5-6
fine silt	0.0156-0.0078	6-7
very fine	0.0078-0.004	7-8
clay	<0.004	>8

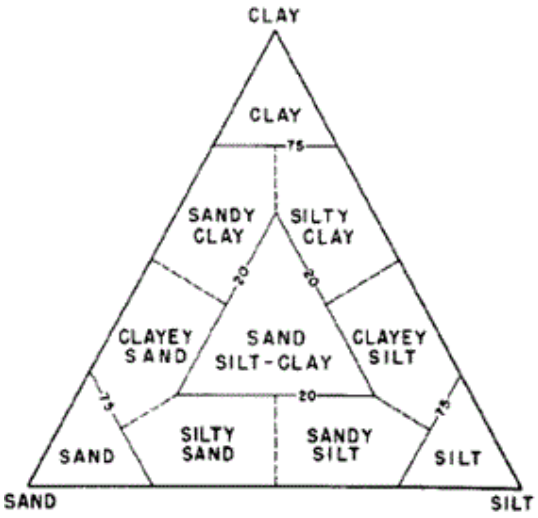

Figure 6.1: Sediment classification based on sand-silt-clay ratio from Shepard (1954).

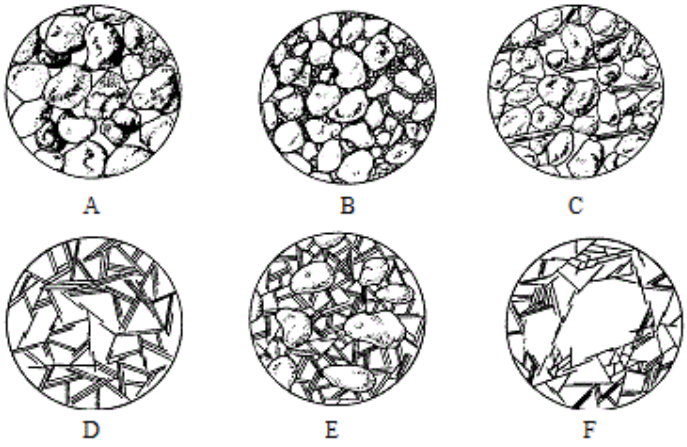

Figure 6.2: Typical sediment structures: a well-sorted sand (A), a mixture of sand and clay (B and E), bridging effect of mineral particles (C) and fine grained –muddy-sediments forming flocks and card-house structure (D and F) structures (Hamilton, 1970).

Apart from the grain size and the sorting, grain sphericity, grain roundness and packing (i.e. the arrangement of the mineral grains) as well as the mineralogy all play an important role in characterising sediment structure and therefore bulk sediment properties. The sphericity and roundness are two distinct characterisations for the grain shape. In particular, the sphericity is a measure of how closely the shape of a grain resembles the shape of a sphere. As defined by Wadell (1935), the sphericity of a grain is the ratio of the surface area of a sphere (with the same volume as the given grain) to the surface area of the

grain and takes values between 0 and 1 (sphere). The term roundness describes the shape of the corners on a grain of sediment. These mineral grain properties are interrelated: pure sands and gravels will have rather spherical and rounded grains whereas finer soils such as clays are typically flaky in shape. Owing to their granular nature, sands and silts are characterised as cohesionless sediments. In these types of sediment, it is the frictional forces and the interlocking of grain contacts that inhibit the grain relative motion. In contrast, clay minerals display cohesion that is the tendency for the clay particles to stick together and resist disruption due to surface forces of an electrochemical nature. More on this topic can be found in textbooks such as Allen (1992) and Whitehouse *et al*. (2000). Although pure silts are granular sediments, the presence of even a small percentage of clay mineral (less than 10%) can give them a cohesive character (Whitehouse *et al*., 2000). Figure 6.2 shows common sediment structures (Hamilton, 1970).

Packing and sediment structure are characteristics related to the sediment porosity. Porosity (ξ) is the parameter describing the amount of open space in a geological material, denoted throughout this document by ξ. Porosity is presented either as a volume fraction (0 to 1.0) or as a percentage (0 to 100) of the total volume. The porosity is presented here as fraction:

$$\xi = \frac{V_w}{V_s}, \qquad (6.1)$$

where V_w is the volume of pore spaces and V_s the total volume of the sediment. The bulk density of the water saturated sediment ρ_s is calculated from:

$$\rho_s = \xi\rho_w + (1-\xi)\rho_m, \qquad (6.2)$$

where ρ_w is the water density and ρ_m the grain mineral density for the water-saturated sediments. The density of pore water of seafloor sediments stays nearly constant in marine environments and takes values between 1000 and 1030 kg/m^3 (Stoll, 1985; Courtney and Mayer, 1993). The mineral density depends on the sediment type. Sands typically comprise quartz minerals with density equal to 2650 kg/m^3 (Mavko *et al*., 1998). Muds comprise various minerals (kaolinite, illite est.) having densities from 2600 kg/m^3 to 2800 kg/m^3

(Whitehouse *et al.* 2000). In marine sediments, the porosity varies between 0.35 and 0.90 (Hamilton and Bachman, 1982) and generally increases inversely proportionally with the mean grain size. In Figure 6.3 the relationship between porosity and mean grain size for a range of 1-1000 microns is shown according to Hamilton and Bachman (1982). The data were taken from samples from three general sediment environments of continental shelf (circles), abyssal hills (squares) and abyssal plain (triangles). Diamonds represent data from diatomaceous [5] samples from the Bering and Okhotsk Seas.

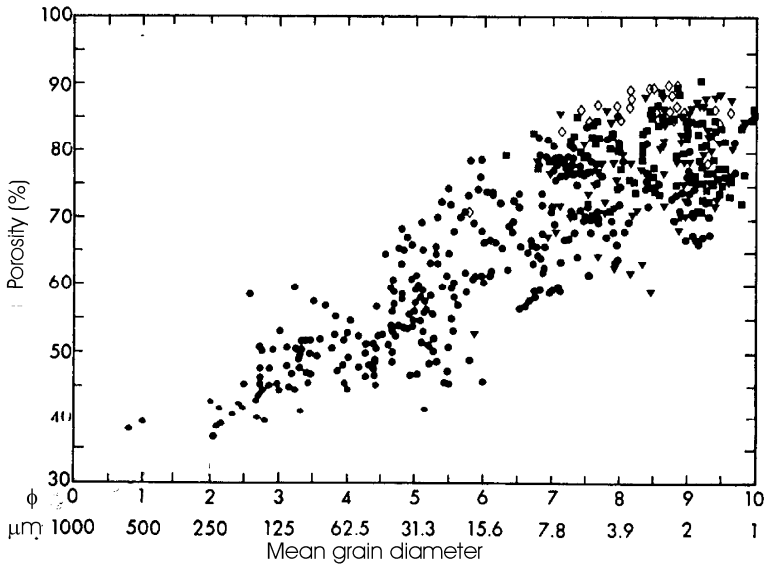

Figure 6.3: Relationship between porosity and mean grain size for a range of samples for the three general sediment environments of continental shelf (circles), abyssal hills (squares) and abyssal plain (triangles). Diatomaceous sediments are displayed as open diamonds and mean grain diameter is expressed in units of ϕ and μm. From Hamilton and Bachman (1982).

The high porosity and the cohesiveness explain, in part, the bridge-like, house-of-cards and packing in chain arrangements, which predominate (like the structures D and F of Figure 6.2) in muddy sediments. These sediments can have porosities of up to 0.90 or even higher according to Whitehouse *et al.*, (2000). In this case, they are characterised as 'fluid' and possess shear viscosity but not rigidity. Fluid mud with such high water content, can exhibit large strain pseudo-plastic, viscoplastic, and/or viscoelastic flow properties which arise from a space-filling network structure and depends on the hydrodynamic conditions and characteristics of the mud (McAnally *et al.*, 2007). The relationship between low-shear viscosity and density is shown in Figure 6.4 for several estuarine muds.

[5] a naturally occurring, siliceous sedimentary rock which consists of fossilized remains of diatoms (a type of hard-shelled algae).

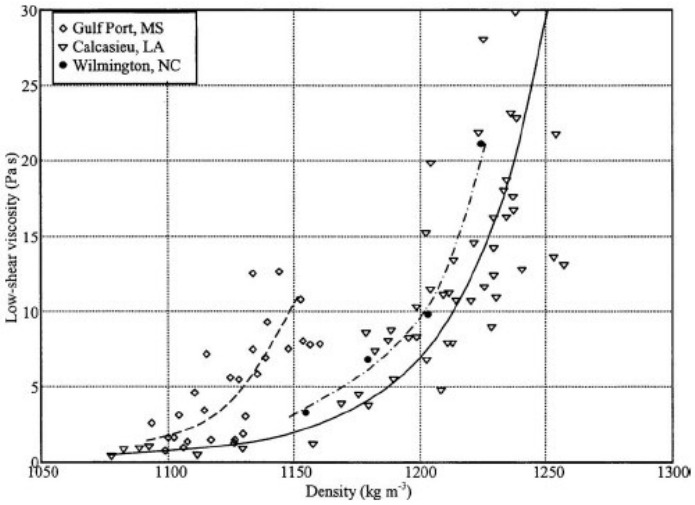

Figure 6.4: Low-shear viscosity in relation to density for some natural estuarine cohesive sediments from (McAnally et al., 2007)

The porosity stands out as the most important geotechnical factor which affects sound speed in sediments because it determines the density and the state of the saturated sediment. Additionally its importance stems from the difference in compressibility between the compressibility of the pore water and the sediment frame, i.e. the structure formed by the minerals (Shumway 1960; Hamilton 1971). Experimental work (Hamilton *et al.*, 1970; Hamilton 1971) showed that the higher the porosity the lower the value of the sediment bulk modulus whereas for the shear modulus there is no clear monotonic relationship. The relationship between porosity and bulk modulus is discussed further in section 6.2

Permeability and the tortuosity are sediment properties that characterize the flow of the fluid through the skeletal frame pores. The permeability is an average sediment property that measures the ability of the medium to transmit fluid through it (Bear, 1972). By contrast tortuosity is a local medium property that measures the deviation of the flow streamline from the straight path. The permeability (denoted here by B) takes values between 10^{-12}-10^{-14} m^2 for silts, it is less than 10^{-15} m^2 for clays and greater than 10^{-12} m^2 for sands. The tortuosity factor (denoted here by α_τ) is related to the sediment porosity with the following relation (Berryman, 1980):

$$\alpha_\tau = 1 - \wp(1 - 1/\xi) \,. \qquad (6.3)$$

The factor $\wp$ is a microscopic frame parameter which ranges from 0 to 1 and equals 0.5 for spheres. Previous work of Stoll and Bryan (1969) used the term 'structure factor' instead of 'tortuosity factor'. According to their work the structure factor has a theoretical value of 3 if the sediment with grain arrangement (skeletal frame) is isotropic. Equation (6.3) was derived assuming a granular sediment texture hence it may not be applicable to muds. An analytical model for the tortuosity of marine muds has been derived by Boudreau and Maysman (2006). Their model relates the tortuosity with the porosity assuming the mud consists of disks arranged in a block like structure. For porosity values encountered in muds, equation (6.3) and the model of Boudreau and Maysman (2006) both predict values for α_τ between 1 and 1.7.

6.2 Acoustic models for gas-free sediments

Current geoacoustic models for saturated sediments fall into two broad groups. The first assumes the sediment, i.e. mineral grains plus water, is a continuum with effective viscoelastic behaviour. The second group considers the sediments to be a two-phase medium. Wave propagation according to the latter treatment depends on the individual constituents of the sediment as well as the structural characteristics of the skeletal frame. Hamilton's model (Hamilton, 1971) belongs to the first group whereas the Biot model (Biot, 1956 a, b) belongs to the second one. These two models are discussed in the next paragraphs.

6.2.1 Hamilton model

Background theory

When small amplitudes are of interest, acoustic measurements are employed to extract information on the stress-strain behaviour. In other words sound wave attenuation and velocity are a way to infer intrinsic energy dissipation and elastic characteristics of a solid material (or sediment). The relevant measured quantities are: the compressional (or P-wave) and the shear (or S-wave) sound speeds (denoted by c_P and c_S respectively) and the

corresponding attenuation coefficients (denoted by a_P and a_S respectively). The predictions of material properties (here sediment) depend on the mathematical model used for the interpretation of the acoustic data and visa versa. It is standard practice to infer material dissipation characteristics from dynamic-sinusoidal measurements (Whorolow, 1992) by making the elastic parameters of the solid (or sediment) complex. The corresponding expressions for the first Lamé constant L_s and the second Lamé constant or shear modulus G_s are:

$$L_s^* = L_s + iL_s^{'} \qquad (6.4) \qquad \text{and} \qquad G_s^* = G_s + iG_s^{'} \qquad (6.5)$$

For a sinusoidal single frequency excitation, the material quality (Q) factors are linked to the imaginary and real parts of the Lame´ constants with:

$$\frac{1}{Q_P} = \frac{L_s' + 2G_s^{'}}{L_s + G_s} \qquad (6.6) \qquad \text{and} \qquad \frac{1}{Q_S} = \frac{G_s^{'}}{G_s}, \qquad (6.7)$$

where Q_P and Q_S are the Q-factors for the P- and S-waves respectively. Equations (6.6) and (6.7) are valid for any kind of sinusoidal single-frequency dynamic excitations; but here the discussion is restricted to acoustic excitations. Furthermore the Q-factors of equations (6.6) and (6.7) are related with the corresponding sound speeds c and attenuation coefficients a (nepers/m) and logarithmic decrement (δ) through:

$$\frac{1}{Q} = \frac{\pi f}{ac} = \frac{\delta}{\pi}. \qquad (6.8)$$

Equation (6.8) is valid under the assumption that the attenuation per wavelength λ is small (i.e. $a\lambda << 1$), as follows from the general wave theory as described in Kolsky (1953) and Ferry (1980).

Expressions for sound speed and attenuation

The above-mentioned general theory forms the basis of Hamilton's viscoelastic model (Hamilton, 1971). This model is semi empirical because equations (6.4) to (6.8) are combined with relationships between speed and attenuation which were established by experimental observations. Specifically, under the observation that the sound speed of the

compressional (P -) and shear (S -) waves (denoted by c_{P} and c_{S} respectively) exhibit no dispersion, the following relations were established between the real part of the sediment Lamé constants and the sound speeds:

$$c_{\mathrm{P}} = \sqrt{\frac{L_s + 2G_s}{\rho_{\mathrm{s}}}} \tag{6.9}$$

and

$$c_{\mathrm{S}} = \sqrt{\frac{G_s}{\rho_{\mathrm{s}}}}\,. \tag{6.10}$$

The first Lame constant is related to the bulk modulus of elasticity K_s and the shear modulus by:

$$L_{\mathrm{s}} = K_{\mathrm{s}} - \frac{2}{3}G_{\mathrm{s}}\,. \tag{6.11}$$

thus the P-wave sound speed can also be expressed as:

$$c_{\mathrm{P}} = \sqrt{\frac{K_{\mathrm{s}} + \frac{4}{3}G_{\mathrm{s}}}{\rho_{\mathrm{s}}}}\,. \tag{6.12}$$

Application of equations (6.9) and (6.12) for sediments assumes that the system grains and fluid form a closed system (i.e. there is no relative skeletal frame-fluid motion). The bulk modulus, K_{s} , entering equation (6.12) follows Gassmann's formulation (Gassmann, 1951). That is, the system mineral grains and water forms an effective medium. This medium has an equivalent bulk modulus, expressed as a function of the grain bulk modulus K_{g} , the fluid (water) bulk modulus K_{w} and the solid frame (drained) bulk modulus K_{f} (that is the porous framework out mineral grains):

$$K_{\mathrm{s}} = K_{\mathrm{g}}\frac{K_{\mathrm{f}} + \Upsilon}{K_{\mathrm{g}} + \Upsilon}, \tag{6.13}$$

where:

$$\Upsilon = \frac{K_w\left(K_g + K_f\right)}{\xi\left(K_g + K_w\right)}. \qquad (6.14)$$

Equations (6.12), (6.13) and (6.14) show that porosity is among the basic sediment parameters that characterise the P - wave speed because it enters the elastic moduli and the saturated sediment density. The velocity versus porosity relationship is shown in Figure 6.5 according to experimental results of Hamilton and Bachman (1982).

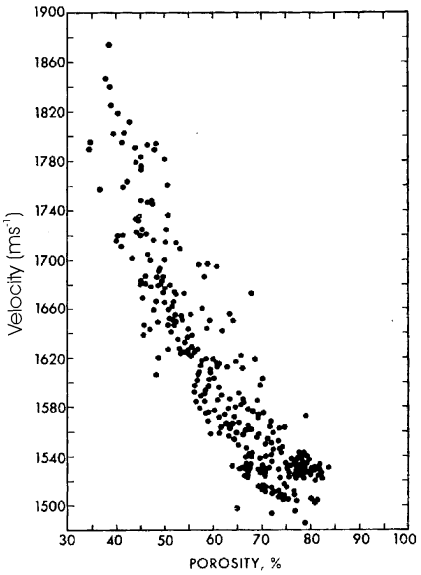

Figure 6.5: Velocity versus porosity versus for continental shelf sediment. From Hamilton and Bachman (1982).

The closed system assumption is retained for the determination of the shear modulus G_s. However as fluids cannot bear shear forces, the values for the dry and saturated shear modulus are the same. The shear modulus G_s entering equations (6.10) and (6.12) represents the shear modulus of the skeleton frame. This is different from the shear modulus of the mineral grains and its value is a geotechnical property extracted from *in situ* or laboratory measurements. The sediment characterization according to Hamilton's model is completed with the observation (Hamilton, 1972) that the attenuation of both compressional and shear waves vary with frequency according to:

$a_P = K_P f^p$ (6.15) and $a_s = K_S f^s$ (6.16) respectively.

The constants of proportionality K_P and K_S (dB/m/kHz) and the exponential parameters p and s are sediment specific. The majority of experimental work with cohesive sediments showed that the parameters p and s take values equal or close to unity (see section 6. 3). If the exponential parameter equals unity the wave Q-factor becomes constant; then the model falls into the category of 'constant Q'. The empirical relationship between K_P and porosity, according to Hamilton (1972), is displayed in Figure 6.6. For this empirical fit, the exponent p was assumed equal to unity.

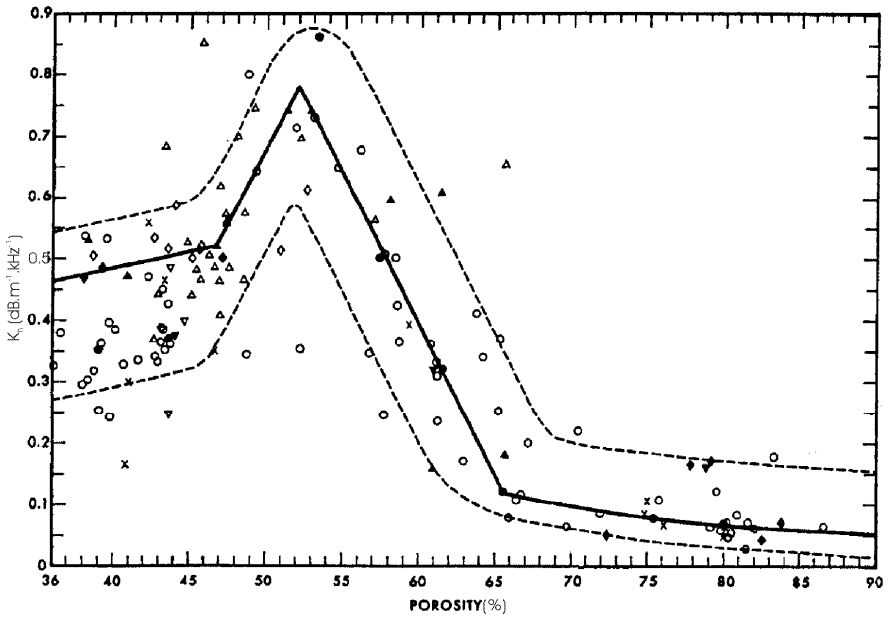

Figure 6.6: Porosity (given as percentage %) versus the proportionality parameter K_P as published by Hamilton (1972). The solid lines are empirical fits and the dashed lines indicate the 'area where most data should fall'. Symbols denote different literature sources from which K_P values have been obtained; details are available in the original paper (Hamilton, 1972).

Hamilton's semi-empirical model shows, in general, good agreement in sediments with high silt and/or clay content. In contrast, acoustic measurements in sandy sediments show poor agreement with Hamilton's viscoelastic model, as found in Hamilton (1980) and Stoll (1985). This is mainly because fluid effects in sandy sediments are important and these effects are neglected in Hamilton's model. Biot (Biot, 1956 a, b) was the first to introduce global flow effects into wave propagation in porous media. Biot's model is discussed in the following section.

6.2.2 Biot model

Biot (1956 a, b) was the first to introduce global flow effects into the equations of wave propagation in water-saturated sediments by allowing relative motion of water and mineral grains. This theory predicts the existence of two compressional waves, a fast and a slow wave, denoted here by $c_{\mathrm{P+}}$ and $c_{\mathrm{P-}}$ respectively, and one shear wave c_{S}. The corresponding expressions are:

$$\frac{1}{c_{\mathrm{P}\pm}^2} = \frac{-\mathrm{A} \pm \sqrt{\mathrm{A}^2 + 4 \cdot \mathrm{B} \cdot \Gamma}}{2 \cdot \mathrm{B}} \qquad (6.17)$$

$$\frac{1}{c_{\mathrm{s}}^2} = \frac{\Gamma}{\overline{\rho} G_{\mathrm{s}}} \qquad (6.18)$$

The ancillary parameters A, B and Γ are defined as:

$$\mathrm{A} = H\overline{\rho} + M\rho_{\mathrm{s}} - 2C\rho_{\mathrm{w}} \qquad (6.19)$$

$$\mathrm{B} = C^2 - MH \qquad (6.20)$$

$$\Gamma = \overline{\rho}\rho_{\mathrm{s}} - \rho_{\mathrm{w}}^2 \qquad (6.21)$$

where

$$H = K_{\mathrm{f}} + \frac{4}{3}G_{\mathrm{s}} + \frac{\left(K_{\mathrm{m}} - K_{\mathrm{f}}\right)^2}{D - K_{\mathrm{f}}} \qquad (6.22)$$

$$C = \frac{\left(K_{\mathrm{m}} - K_{\mathrm{f}}\right)K_{\mathrm{m}}}{\left(D - K_{\mathrm{f}}\right)} \qquad (6.23)$$

$$M = \frac{K_m^2}{\left(D - K_{\mathrm{f}}\right)} \qquad (6.24)$$

$$D = K_{\mathrm{m}}\left[1 + \xi\left(\frac{K_{\mathrm{m}}}{K_{\mathrm{w}}} - 1\right)\right] \qquad (6.25)$$

$$\overline{\rho} = \frac{\alpha_\infty \rho_w}{\xi} - \frac{i\eta_w F(\zeta)}{\omega B} \tag{6.26}$$

$$F(\zeta) = \frac{1}{4}\frac{\zeta \mathrm{T}(\zeta)}{1 + 2i\mathrm{T}(\zeta)/\zeta} \tag{6.27}$$

The viscodynamic operator $F(\zeta)$, equation (6.27), is defined by means of the frequency dependent function $\mathrm{T}(\zeta)$:

$$\mathrm{T}(\zeta) = \frac{e^{i3\pi/4} J_1\left(\zeta e^{i\pi/4}\right)}{J_0\left(\zeta e^{i\pi/4}\right)} \tag{6.28}$$

where J_0 is the zero, and J_1 the first, order Bessel function. This operator incorporates the frequency dependence of the viscous drag through the frequency dependent parameter ζ:

$$\zeta = \alpha_p \sqrt{\frac{\omega \rho_w}{\eta_w}}, \tag{6.29}$$

where α_p is the pore size parameter, a parameter that depends on the dimensions and the shape of the pore space and the water viscosity η_w. This operator $F(\zeta)$ is active at frequencies higher than the critical frequency f_c, equation (6.30). As seen from the equation (6.17), Biot theory predicts the existence of two simultaneously propagating P-waves: the fast and the slow waves. The fast wave is the bulk wave corresponding to the wave propagating when there is no relative motion between the frame and the fluid, i.e. there is inertial coupling between these masses. The slow wave is a diffusive-type wave that is induced by the relative motion of the fluid relative to the frame and becomes important in the high frequency range. The transition from the low to the high frequency range occurs at a critical frequency:

$$f_c = \frac{\zeta \eta_w}{2\pi \rho_w B} \tag{6.30}$$

The remainder of this section studies the Biot theory for a sandy sediment and a muddy sediment. The study focuses on the shear wave and the fast P-wave, which is typically

observed in sediment acoustics. The input values are given in Table 6.2. The pore fluid is assumed to be water with salinity 10 ppt at 10°C. These values were chosen to mach the experimental conditions at intertidal sediments so that the simulated Biot results can be compared later to experimental observations. The values for the pore size parameters were calculated assuming for both types of sediments spherical pores. The following expression was used (Hovem, 1976):

$$\alpha_{\mathrm{p}} = \frac{d_{\mathrm{m}}}{3}\frac{\xi}{(1-\xi)} \tag{6.31}$$

In Figure 6.7, simulation results are shown computed on the above described Biot theory. In the upper plot the phase velocity of the first compressional wave is plotted against frequency for sandy sediment (blue dashed line) and a muddy sediment (black dashed line) the corresponding horizontal lines represent the low frequency Gassmann approximation. The corresponding wave attenuations, as $1/Q_{\mathrm{P}}$ factors, are plotted against frequency in the lower plot of Figure 6.7. The $1/Q_{\mathrm{P}}$ factor for the $c_{\mathrm{P+}}$ in muddy sediment is converted to attenuation a_{P} in dB/m and plotted in a logarithmic scale against frequency in Figure 6.8. In the same figure the effect of the viscodynamic operator, given in equation (6.27), is demonstrated by setting $F(\zeta)$ equal to 1 and retaining all other inputs as in Table 6.2. The purpose of this is to assess a viscoelastic model to the Biot model. If $F(\zeta)$ could be set equal to unity, the Biot model would have a viscoelastic analogue with a relaxation frequency given by equation (6.30). Hence a simple vicoelastic model could be assigned to the gas-free sediment and it would be possible to combine it with the bubble model.

The compressional sound speed for the muddy sediment varies from 1438-1536 m/s and for sand 1646-1715 m/s which are typical values for sandy and muddy sediments respectively. In Figure 6.8 the Biot theoretical results (black solid line) for attenuation are compared with an experimentally observed attenuation trend (red dashed line) for muddy sediments, which has a linear frequency dependence according to $a_{\mathrm{P}} = K_{\mathrm{P}} f$ with K_{P}=0.2 dB/m/kHz. This value for K_{P} falls into the range of values reported by Hamilton (1972) and is discussed further in section 6.3. In the same figure results of the Biot model without the addition of the viscodynamic operator $F(\zeta)$ are shown with the black solid line.

Table 6.2: Input parameters for simulations (temperature 10°C and salinity 10 ppt)

Input parameters	Sand	Mud
Bulk modulus of the grains (GPa) (quartz)	36	36
Bulk modulus of fluid (GPa)	2.1423	2.1423
Bulk modulus of frame (GPa)	0.5	0.1
Shear modulus of frame (MPa)	80	2.6
Grain density (kg/m^3)	2650	2650
Fluid density (kg/m^3)	1007	1007
Fluid viscosity η_w (Pas)	0.0013	0.0013
Pore-size parameter α (μm)	50	9.058
Porosity ξ (-)	0.40	0.66
Permeability (m^2)	6.1x10^{-12}	0.2x10^{-13}
Grain size d_m (mm)	0.250	0.014
grain shape factor, $\wp$ (-)	0.5	0.2

Retaining the input parameters of Table 6.2, Figure 6.9 shows the results for the shear wave sound speed and attenuation as predicted from the original Biot theory. In Figure 6.10 these attenuation results are compared with a linear shear attenuation trend (black solid line) according to $a_s = K_S f$ where K_S=20 dB/m/kHz. This value for K_S is an average value resulted from the literature review as discussed in section 6.3. In the same picture the black dotted line indicates the attenuation predicted from Biot theory by setting the viscodynamic operator F equal to unity.

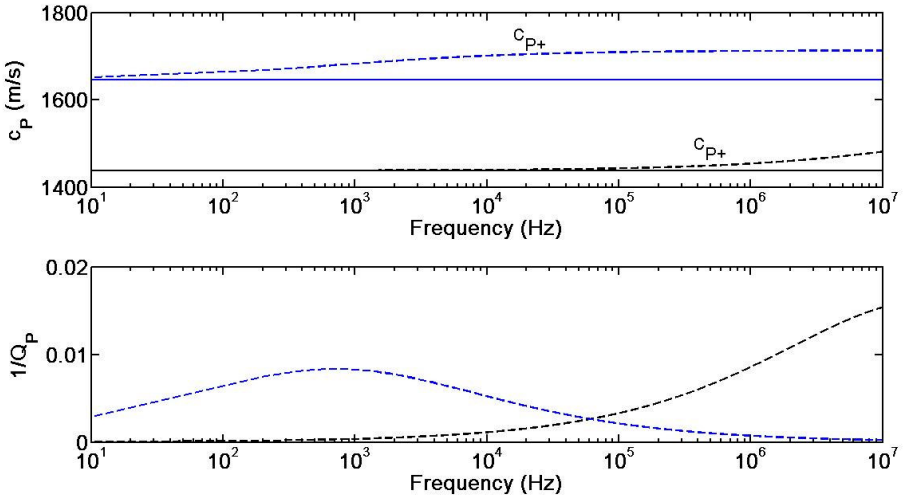

Figure 6.7: Sound speed of fast wave and attenuation of a sandy and muddy sediment (blue and black lines respectively) according to Biot model for the input parameters in Table 6.2. The horizontal lines indicate the low frequency approximation using Gassmann's approximation, equation (6.13).

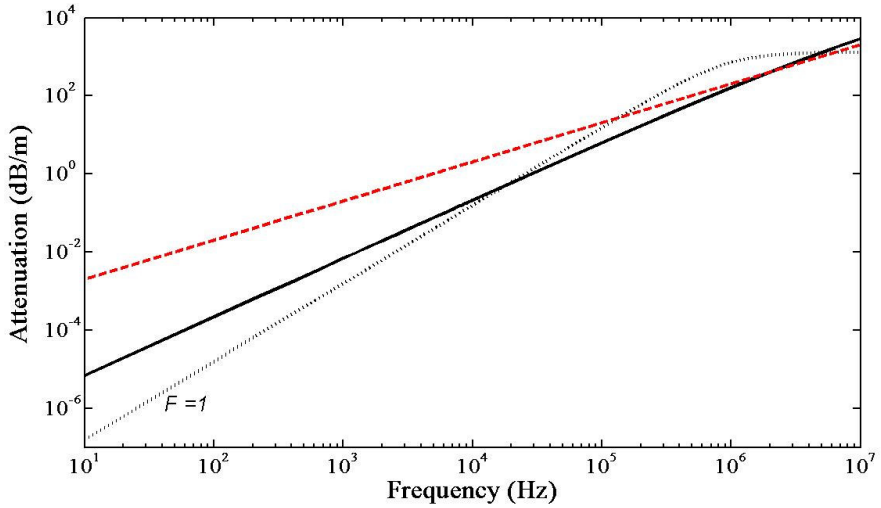

Figure 6.8: Attenuation of fast compressional waves for muddy sediment according to the Biot model (black solid line) with the input parameters of Table 6.2. The dotted black line indicates the Biot attenuation predictions if the viscodynamic operator F is not applied (i.e. set equal to unity). The red dashed line shows an experimentally observed attenuation trend for muddy sediments with a linear frequency dependence according to $a_P = K_P f$ *with* K_P *=0.2 dB/m/kHz (Hamilton, 1972).*

The simulation results presented in this section implemented the Biot theory in the original version using equations (6.17) and (6.18). The practical application of this version is rather limited because of two other forms of attenuation mechanism. The first is losses in the

skeletal frame and the second is the local fluid losses in a direction perpendicular to the direction of wave propagation, which are not included

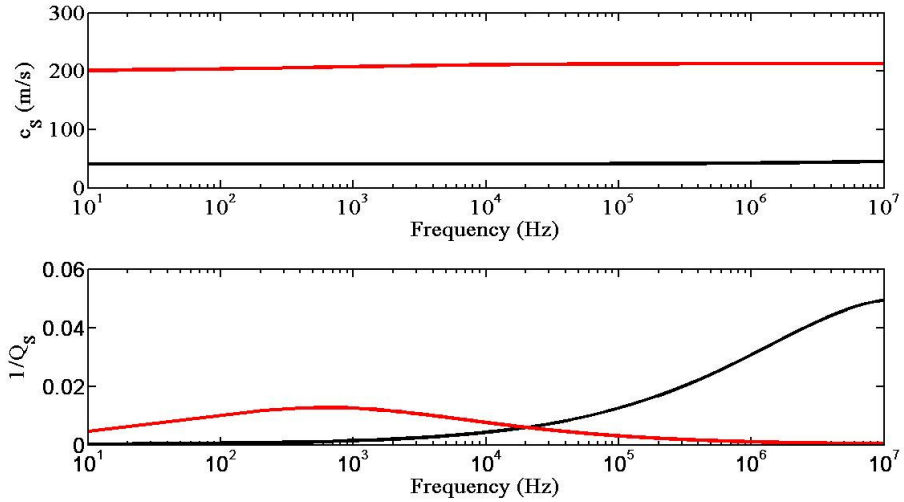

Figure 6.9: Sound speed of shear wave and attenuation ($1/Q_S$) of a muddy (black line) and sandy (red line) sediment according to the Biot model with the input parameters of the Table 6.2.

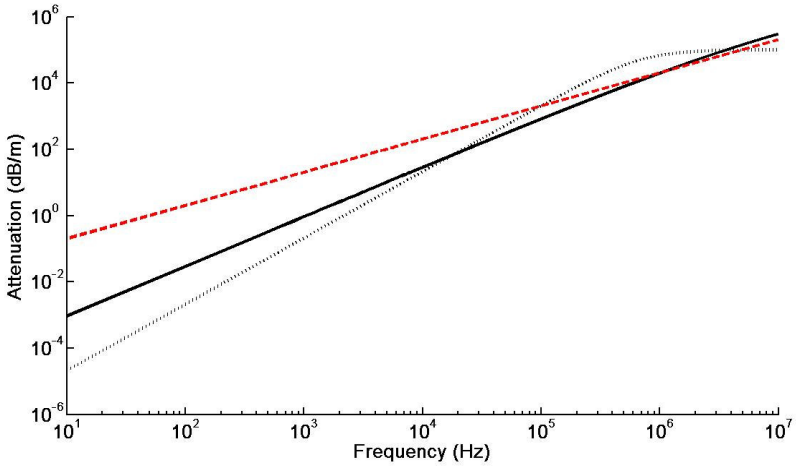

Figure 6.10: Attenuation of shear waves for a muddy sediment according to the Biot model with the input parameters of Table 6.2 (black solid line). The dotted black line indicates the Biot attenuation predictions if the viscodynamic operator F is not applied (i.e. set equal to unity). The red dashed line shows a linear attenuation trend according to $a_s = K_S f$ with K_S =20 dB/m/kHz an average value as resulted from literature review, see Table 6.7

More advanced geoacoustic models

The first attenuation mechanism was integrated in the Biot model in later works of Bryan (1969) and Stoll (1980). This was done by assuming the skeletal frame shear and bulk moduli to be complex in order to account for the various forms of energy dissipation that occur at the grain contacts. Practical limitation of this approach is that these quantities are difficult to obtain experimentally and the number of the unknown input variables for the model increases. Another limitation of this approach is that such a model is ''pseudo-harmonic'' because the wave propagation is in the time domain but some parameters are described in the frequency domain. Therefore there is no straightforward assessment of an equivalent viscoelastic model to the behaviour of the sediment. The second attenuation mechanism is also known as the squirt flow loss mechanism. A rigorous description of this phenomenon was given in the works of (Dvorkin and Nur, 1993; Dvorkin *et al*., 1994). In these papers the Biot theory unified with the squirt flow mechanism (BISQ) is presented with focus on the P-wave propagation. The BISQ model appears more suitable for rocks and sandstones (Marketos and Best, 2010). The BISQ model does not integrate the squirt effect to the modelling of shear waves. The expression for the shear waves is the same with the original Biot theory without the viscoelastic operator.

A novel geoacoustic model which predicts a linear dependence of attenuation with frequency has been proposed by Buckingham (2000). This model is controversial many issues have been raised concerning the underlying theory (Chotiros and Isakson, 2010; Buckingham, 2010). Additionally no good agreement was found with experimental results in sandy (Buchanan, 2006) and muddy (Robb *et al*., 2006) sediments. For these reasons it was not considered further in this PhD work.

6.3 Literature review on sound velocity and attenuation

This section discusses published experimental results on compressional and shear wave velocity and attenuation with the focus on shallow muddy sediments. These results will be used to guide the interpretation of laboratory and *in situ* experiments carried out during this study at intertidal sites. Also these results are used to select an appropriate geoacoustic model for these muddy sediments, based on experimental observations of the dependence of sound speed and attenuation on frequency.

6.3.1 *P*-waves in sediments

A number of experimental results have been published on measurements of sound speed and attenuation in marine sediments. The earliest of these results have been obtained at distinct frequencies (Shumway, 1960 a, b; Hamilton, 1956, 1970, 1972) whereas later experimental results cover a frequency range (Richardson *et al.*, 2001; Robb *et al.*, 2006). Most of the recently published work was carried out in sandy sediments (Turgut and Yamamoto, 1990; Richardson *et al.*, 2001) or poorly sorted muddy environments with very high sand content (Best *et al.,* 2001; Yang *et al.*, 2008) or gas content (Fu *et al.*, 1996; Richardson and Briggs, 1996). Experimental results reported as being from pure mud are rather scarce and most dated back in 1970s, 1980s and 1990s. In the following paragraphs, the velocity and attenuation dependence on frequency is studied by reviewing existing literature on non-gassy muddy sediments. It has to be mentioned that values from the literature can serve only as guidelines because the sediment composition and the experimental conditions are unique for every experiment. Even if experiments are from the same geographical location changes of whether condition, currents and sediment transport may alter the seafloor composition.

Following observations of Bowles (1997), the compressional wave attenuation for frequencies from 10 Hz to 500 kHz has a linear dependence with frequency. An earlier data compilation of Kibblewhite (1989) reports 'some nonlinear dependence of attenuation around 10-100 Hz in the sands and 10^3-10^4 Hz in the silts'. According to Kibblewhite (1989) these data showed ambiguities and the general view of having a linear dependence with frequency is accepted for silts. Early extensive studies of sound speed and attenuation was carried out by Shumway (1960 a, b) and Hamilton (1972). Some results from Shumway's study from resonant column measurements on core samples taken from shallow waters (less than 45 m) of San Diego Bay are given in Table 6.3. According to his study no dispersion is reported and for high porosity sediments the attenuation follows the relationship of equation (6.15) with the exponent p taking the average value of 1.79 with a standard deviation of 0.98. The sound speed measurements are considered accurate within ± 10 m/s Shumway (1960 a). Table 6.3 gives also published results from *in situ* measurements in the same geographical environment (Hamilton, 1972) for comparison. Although Hamilton's results deviate numerically from those of Shumway, no dispersion is reported and the linear dependence of attenuation with frequency according to equation

(6.15) is supported. Values for the attenuation constant and the exponent that resulted from combination of *in situ* and laboratory measurements are given in Table 6.4 and Table 6.5. Wood and Weston (1964) investigated marine muds utilising 5 discreet frequencies between 4 kHz and 50 kHz for their *in situ* measurements. They estimate the value of p to be equal to unity. McLeroy and DeLorach (1968) conducted tank experiments with marine sediments at frequencies between 15 kHz and 1500 kHz and report similarly a unity value for the attenuation exponent p for silty and clay sediments. In these works the sound speed appears as a fraction of the sound speed in the seawater above the sediment. The results of Wood and Weston (1964) and McLeroy and DeLorach (1968) are summarised in Table 6.5.

Table 6.3: Compressional wave sound speed and attenuation data at distinct frequencies for shallow water sediments, as measured in the laboratory (Shumway, 1960 a) and in situ (Hamilton, 1972).

c_P (m/s)	a_P (dB/m)	water depth (m)	f (kHz)	sediment type	reference
1484	8.62	<45	30.2	medium silt	(Shumway, 1960a)
1492	11.54	<45	30.4	medium silt	(Shumway, 1960a)
1465	15.9	15	100	silt	(Hamilton, 1972)
1490	59.7	17	100	sand-silt-clay	(Hamilton, 1972)
1464	18.0	22	100	clayey silt	(Hamilton, 1972)
1483	0.7	4	14	sand silt clay	(Hamilton, 1972)

Table 6.4: Compressional sound speed and best-fit attenuation parameters from experimental data in marine sediments for the frequency range 3.5-100 kHz

c_P (m/s)	K_P (dB/m/kHz)	p (-)	sediment type	reference
1450	0.19 ± 0.01	0.95 ± 0.03	clayey silt	(Hamilton, 1972)
1450	0.18 ± 0.03	0.97 ± 0.05	clayey silt	(Hamilton, 1972)

Table 6.5: Compressional-wave sound speed and best-fit attenuation parameters from early experimental data in muddy sediments.

c_P / c_w (-)	K_P (dB/m/kHz)	p (-)	depth (m)	sediment type	reference
0.95	0.065	1		in situ measurements at tidal mudflats at depth up to 55 m	(Wood and Weston, 1964)
0.999	0.072	1		laboratory measurements with 0.61 m layer of sediment	(McLeroy and DeLorach, 1968)
0.997	0.075	1			(McLeroy and DeLorach, 1968)

Values greater than unity are given by Courtney and Mayer (1993) for the attenuation exponent p. Their results, summarised in Table 6.6, were based on core measurements (cores taken from the top 20 metres) of Emerald Basin at ultrasonic frequencies.

Table 6.6: Compressional sound speed and attenuation data from experimental data core measurements taken at 500 kHz at Emerald Basin.

c_P (m/s)	a_P (dB/m)	p (-)	sediment type	reference
1450-1475	50-100	1.2-2.0	silty clays	(Courtney and Mayer, 1993)

In situ measurements of acoustic profiles of the uppermost metres of the seafloor at Kiel Bay in the frequency range of 3 -20 kHz (Fu *et al.*,1996) indicate velocity values within the range 1430-1465 m/s for the non-gassy sites (the average bottom water velocity was estimated to be 1480 m/s). The shallow marine sediments of Kiel Bay comprise non-gassy zones covering mainly the top metre below sea floor and gassy zones starting at about 3 metres below sea floor. According to the results of Fu *et al.* (1996) the sound speed in the non-gassy zones showed no variability whereas in the gassy zone it showed great variability. Sound speed values in the gassy zones varied from 852-1489 m/s.

Later acoustical data from measurements in shallow waters with silty-sand sediments confirm that the P-wave attenuation varies linearly with frequency and that sound speed exhibits a small dispersion. Here reference is made to measurements during the Shallow Water 2006 program on the New Jersey Shelf. Turgut and Yamamoto (2008) estimate that

for the silty-sand sites examined on the New Jersey shelf the attenuation exponent takes values between 0.6 and unity within the frequency band of 10-80 kHz. Chirp data (1.5 - 4.5 kHz) from the same environment indicate that the attenuation constant K_P takes values between 0.09 and 0.103 dB/m/kHz (Jiang and Chapman, 2010). For these measurements the mean sound speed is estimated to be 1598 m/s and the maximum dispersion observed is approximately 15 m/s. However these results involve muddy sediments with high sand content, hence not directly comparable to the muddy sediments which are of interest here.

6.3.2 S-waves in sediments

Shear waves have been studied to a lesser extent than compressional waves and experimental data appear rather sparse in the literature. Available data have been reviewed by Hamilton (1976) and Bowles (1997). The attenuation of shear waves follows the generally accepted relationship given by equation (6.16).

According to the review of Hamilton (1976), the exponential s equals unity. According to the same review the logarithmic decrement δ, equation (6.8) for shear waves in silts and clays takes values 0.2 ± 0.1. Also the observed dispersion according to Hamilton is negligible for frequencies 'from a few Hertz to at least 1 MHz' and the S-wave attenuation has a linear relationship with frequency in analogy with the P- wave attenuation. The observation is supported by Kudo and Shima (1970) whereas Muir *et al*. (1991) concluded that a value of s =1.5 gives a better fit to data. Experimental studies of Stoll (1979) do not agree with the relationship of equation (6.16). However these involved measurements in sands or silts with low porosity. The experimental work of Brunson and Johnson (1980) confirms such a nonlinear relation between attenuation and frequency for sands only. Based on these results muddy sediments follow, most probably, the accepted relation of equation (6.16) with $s = 1$. In Table 6.7 some shear wave measurements are listed where cast in the form of Bowles (1997). The first column gives the S-wave sound speed and the second column the frequency at which the data were taken. The third column contains a best fit value for the attenuation parameter K_s .As shown in the second table of Bowles (1997), shear wave measurements were carried out at much lower frequencies than those for P-waves, the main reason being the high attenuation of these waves compared to the corresponding compressional waves.

Table 6.7: Shear-wave sound speed and attenuation data.

c_s (m/s)	f (Hz)	K_s (dB/m/kHz)	depth (m)	sediment type	reference
90	5	18.9	1	bay mud	(Warrick, 1974)
139	8	3.6	15	mud	(Muir et al., 1991)
68	40	18.4	1	mud	(Muir et al., 1991)
73	100	43.8	2	mud	(Muir et al., 1991)
102	20	13.4	15	alluvial silt	(Kudo and Shima, 1970)

Table 6.8: Selected information from table 1 of (Richardson et al., 1987).

c_P (m/s)	c_S (m/s)	f (Hz)	ρ_s (Kg/m^3)	depth[6] (cm)	sediment type
1452	13.2	563	1570	62-72	Silty clay
1651	60	1300	1980	20-30	sandy silt
1449	12.8	500	1610	49-59	clayey silt

As there are few data available for shear waves and shear measurements have proved difficult, many studies have concentrated on finding relationships between the P-and S-waves regarding velocity and attenuation. Such examples are the works of Best *et al*. (1994) and Richardson *et al*. (1987). A few of these studies are relevant to muddy and/or cohesive sediments. The Table 6.8 shows some values for sound speed from core measurements collected from the Adriatic Sea (Richardson *et al*., 1987); no attenuation data were available. Work performed in same environment by Caiti *et al*. (1994) concludes values between 30 and 50 m/s for shear waves in soft sediments and 100 m/s to 300 m/s in sandy sediments. Moreover many simplifications are employed to approximate the shear loss mechanism. Frequently the shear wave logarithmic decrement is set equal to the P-wave logarithmic decrement. However the only justification in making this assumption is that the same mechanisms are involved in losses of both processes (Kolsky, 1953), that is here the compressional and shear wave propagation. In this work, these semi-empirical

[6] depth below sea floor

relationships are taken into consideration for the characterisation of the gas-free sediment, which was assumed to be a counterpart of the gassy sediment examined experimentally as described in chapter 7.

6.4 Viscoelastic models for sediments

In this section an overview of characteristics of acoustic propagation through viscoelastic media is given. The behaviour of various viscoelastic elements (i.e. simple dashpot–spring configurations) is studied in order to find a simple viscoelastic model that conforms to Hamilton's model and experimental observations for sound speed and attenuation for mud in the frequency range of interest in this study. The aim is to link the shear attenuation experimental data with the parameters of a suitable viscoelastic element which will enter the bubble dynamics model described in paragraph 3.2.

In Figure 6.11 basic viscoelastic models are depicted. The first model, shown in Figure 6.11 (a), is the Voigt (also named Kelvin) model with constant parameters representing the medium viscosity and shear modulus of elasticity G_s. It consists of a spring and a dashpot in parallel. An acoustic wave propagating in a material behaving like a Voigt solid exhibits no dispersion and has a logarithmic decrement which varies proportionally to the excitation frequency when $\eta\omega/G_s < 1$, i.e. the attenuation varies proportionally to the second power of frequency. For frequencies greater than the relaxation frequency the attenuation grows to infinity. A constant wave speed and a linear dependence of attenuation on frequency are described by the modified Voigt model shown in Figure 6.11(b). In this model the viscosity is set equal to (Whorolow, 1992):

$$\eta = \frac{G_s'(\omega)}{\omega}, \tag{6.32}$$

under the assumption that the shear modulus of the material is complex, according to equation (6.5), with the real part being a constant. Maxwell's model, shown Figure 6.11(d) exhibits the opposite behaviour of the Voigt model: it has a logarithmic decrement which varies inversely with the frequency of excitation. The usefulness of both models is limited in describing qualitatively material losses with the use of the viscosity concept (Kolsky, 1953). More realistic results are obtained from the Voigt model with auxiliary spring

shown in figure 6.9 (c). It is also called the standard solid model and is frequently encountered in sediment acoustics (Mavko *et al*., 1998). In the low frequency limit, that is for the frequencies much lower than the reciprocal of the relaxation time of the Voigt element ($\tau = \eta / G_1$), it behaves like an elastic solid with modulus G_{S0}:

$$G_{S0} = \frac{G_1 G_2}{G_1 + G_2}, \quad \omega \to 0 \tag{6.33}$$

whilst at high frequencies the spring of the Voigt model is inoperative:

$$G_{S\infty} = G_2, \quad \omega \to \infty . \tag{6.34}$$

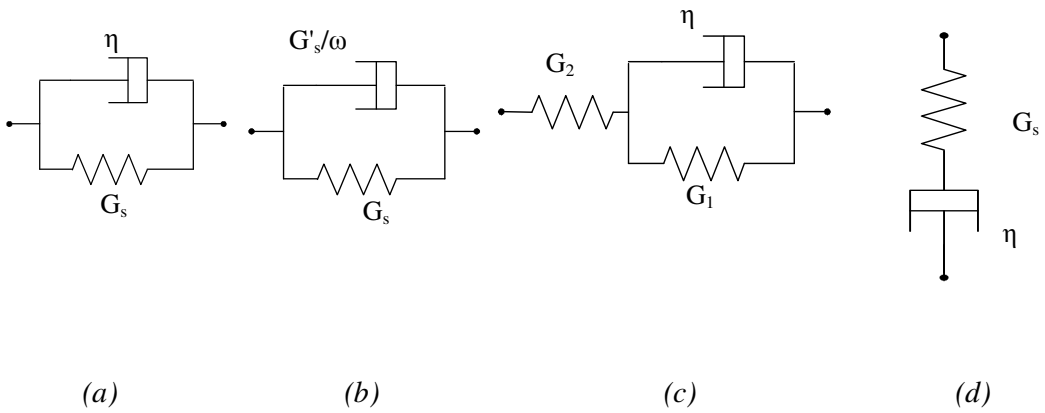

Figure 6.11: Mechanical spring-dashpot analogues to a harmonic stress: (a)Voigt(named also Kelvin) model with constant parameters, (b) Modified Voigt model with the dashpot parameter inversely proportional to frequency, (c) Voigt model with auxiliary spring (standard solid model) and (d) Maxwell with constant parameters

According to this model, a regime can be found where the attenuation in linearly increases with increasing frequency (Kolsky, 1953). However, the logarithmic decrement of this model approaches zero for very small and very high frequencies and exhibits a peak at $\omega = \sqrt{G_1(G_1 + G_2)/\eta}$. Hence the simplest way to represent Hamilton's model is by the modified Voigt model. This model is practically the same as the Hamilton model when $\eta_s \omega / G_s < 1$, when one frequency is under consideration. Therefore data from shear wave attenuation can be used to find suitable values for the shear viscosity using equations (6.32), (6.7) and (6.7).

The theory of linear viscoelasticity and the principle of causality require the attenuation to be accompanied by dispersion (Brennan and Smylie, 1981; Wingham, 1985). In other words a wave attenuated without being dispersed is acausal. The Voigt model predicts a constant sound speed and thus violates the principle of causality. However this model is used in this PhD work to represent the forces acting on the bubble and not the acoustic propagation in the medium (i.e. mud) therefore being acausal in terms of acoustic propagation has no consequences on entering the bubble dynamics model described in Chapter 3.

6.5 Summary

Sediment properties and geoacoustic models were studied in this chapter. The main purpose of this study is to find a viscoelastic analogue for gas-free mud. Only if such analogue exists the bubble model of equation (3.21) can be applied directly to sediments. It was attempted to find a geoacoustic model for gas-free mud to conform to experimental observations and have a spring-damper analogue. There is still a debate over the frequency dependence of both compressional wave velocity and attenuation. The general trend appearing in literature, is that the sound speed in high porosity muddy sediments is slightly lower than in water whereas in sandy sediments much higher. In overall good agreement, the P-wave attenuation varies linearly with frequency except for sediments with high sand content.

To model gas-free mud, Hamilton's viscoelastic model was chosen because it predicts a linear attenuation dependence with frequency. Using this model it is straightforward to link the elastic properties of water-saturated sediment with the linear viscoelastic equations. Another geoacoustic model with viscoelastic analogue, is the original Biot poroelastic model that considers fluid flow effects. It can be converted into a simple viscoelastic model with one relaxation frequency, i.e. it has a spring-damper analogue, provided that the viscodynamic operator is set equal to unity. However it is not adequate for model muddy sediments because in these sediments the permeability is low and therefore the global flow phenomena are not of great importance.

Based on these observations, it was decided to model mud as a viscoelastic medium using the modified Voigt model, i.e. with viscosity η_s entering equation (3.21), equals $\eta_s = G_s^{'}(\omega)/\omega$, which can be fitted accordingly for the frequencies of interest. Based on the literature study, it is concluded that the shear viscosity, which is required for the bubble dynamics model, can be obtained either from shear wave attenuation measurements or from low frequency dynamic loading measurements.

CHAPTER 7: BUBBLE COUNTING IN GASSY SEDIMENTS: MODELS & MEASUREMENTS

In this chapter, acoustic transmission and backscattering measurements are employed with the theory of bubble dynamics in order to investigate to what extent gas pockets in marine sediments can be modelled as monopole sources (i.e. 'acoustically spherical'), which in turn is an indication that their pocket shape is geometrically close to spherical and that their size is significant smaller than the wavelength. The studies concern the top metre of intertidal sediments along the South Coast of England. The two inversion methods which were discussed in chapters 4 and 5, are applied here to sediments. Just as in water, the presence of gas alters the acoustic properties of marine sediment by changing its physical properties such as the elastic modulus. Additionally, when this gas is in the form of 'acoustically spherical' bubbles, resonance phenomena can occur through the coupling of that gas to the surrounding host medium as the bubble undergoes acoustically driven volume-changing pulsations. These resonance phenomena are key characteristics of a new method developed to distinguish between the gas in the form of bubbles from the rest of the gas existing in the form of, for example, cracks or pockets. This new method employs two frequencies and is based on monitoring the scattered spectral components, which are generated from bubble nonlinear pulsations under acoustic excitation (this is the same method which was applied to predict the bubble size distributions in bubbly water, see section 5.2). Independent transmission acoustic measurements along a hydrophone array were taken and inverted following the well-established method of inferring bubble populations from attenuation measurements. The first inversion method is able to detect and measure only 'acoustically spherical' bubbles whereas the latter inversion assumes that all attenuation originates from acoustically spherical bubbles. Hence, comparison of the two bubble population estimates provides information about the gas shape present in the site.

The bubble dynamics theory developed in sections 3.2 and 3.4 is combined with the geoacoustic models of gas-free sediments discussed in chapter 6 to interpret sound scattering and propagation in gassy sediments. Section 7.1 explains how the new bubble model is applied to model linear and nonlinear bubble pulsations under acoustic excitation and how it is used for the interpretation of transmission and scattering measurements. As

mentioned in Chapter 3, the model requires as input parameters the density, shear modulus and viscosity and the compressional wave speed in the gas-free sediment. Laboratory measurements provided the values for the density and shear modulus. Literature experimental data gave indicative values for the compressional wave speed for gas-free sediments. The viscosity of the sediment was inferred from shear wave attenuation values which where found in the literature.

In section 7.2, *in situ* and laboratory measurements are discussed. Laboratory measurements aided the sediment characterisation and the choice of the input parameters for the bubble model. In section 7.3 *in situ* scattering measurements and their interpretation are discussed. In section 7.4 the inversion results from independent *in situ* sets of measurements are compared and discussed.

7.1 Modelling of sound propagation and scattering in gassy sediments

A literature review for existing bubble models in sediments reveals the necessity to develop a new model. As already discussed in section 3.4, the most widely used bubble model, the one of Anderson and Hampton (1980 a, b), was developed for linear scattering interpretation. This model is based on the approach of fitting linear bubble damping constants and this approach may be a reasonable approximation for linear scattering but it cannot be extended for the interpretation of nonlinear scattering from bubbles either under one or two frequency insonification.

Moreover, the double paper by Anderson and Hampton (1980 a, b) presented a model for sound speed and attenuation in gas-bearing sediments but there is no objective way to invert their formulation as mentioned in Chapter 4. In this work, this ambiguity is eliminated using the formulation of Foldy (1944) for the complex sound speed of a wave propagating through random scatterers. The characteristics of the bubble pulsations, as derived from the nonlinear bubble dynamics model, enter Foldy's formulation through the scattering form function as it is explained in the following paragraphs.

7.1.1 Application of the bubble model to intertidal sediments

In this work, the response of a single bubble in sediment was modelled using equation (3.21) with the input parameters given in Table 6.4. These input parameters were inferred from measurements and literature data. In particular, as the experiments took place one to three hours after tidal exposure and the measured density ($\rho_s = 1640 \pm 50\,\mathrm{kg/m^3}$) suggests sediment porosity between 60% and 70%, the medium surrounding the bubble could not be assumed fluid but an elastic solid framework and a viscoelastic model is assigned to it in order to model the internal friction losses. The viscosity entering this model was inferred from the shear wave attenuation using equation (6.32). Unfortunately no shear wave attenuation measurements were possible during this PhD work. For this reason the viscosity entering the bubble model was computed using experimental data for the logarithmic decrement of the shear waves as outlined in section 3.4.

For the modelling of a single gas bubble in sediments has assumed (a) volumetric oscillations, i.e. pulsations and (b) a spherical shape for the bubble. The first assumption is justified from the fact that, only zero order oscillations, i.e. pulsations, are efficient sources of sound. Higher order oscillations, which correspond to changes in shape rather than in volume, are inefficient sources of sound (Strasberg, 1956). However the second assumption needs further consideration because bubbles in sediments tend not to be spherical and the term 'acoustically spherical' bubbles is used to indicate that these pockets have sufficient sphericity[7] in order to radiate as a strong monopole source when insonified with wavelengths much larger than their size.

It is known that deformed bubbles have also the potential to pulsate. The problem was first treated by Strasberg (1953) who compared the resonance frequency of ellipsoidal bubbles with the resonance frequency of a spherical bubble of equal volume. Later Weston (1967) analysed further this problem and found that if the aspect ratio of the major to minor axis of a spheroid is equal to or smaller than 4 the resonance frequencies of deformed and spherical bubbles are essentially the same. The problem was treated more rigorously by Feuillade and Werby (1994) who confirmed the results of Weston (1967). As shown in

[7] The term 'sphericity' is defined in the same way for gas bubbles and mineral grains, see section 6.1 for the definition of the term.

figure 4a of Feuillade and Werby (1994), a bubble with the ratio of the major to minor axis equal to 4 will have, at resonance, approximately 0.1 % less scattering amplitude than that of a perfectly spherical bubble of equal volume. For more elongated shapes the scattering strength reduction is much more pronounced. Thus, based on these works, the analysis that follows in the next paragraphs is valid for spherical and near-spherical gas bubbles, with the term 'acoustically spherical' encompassing spherical shapes, prolate or oblate, having their major to minor aspect ratio less or equal to 4.

Apart from defining the tolerance on sphericity, it is necessary to relate the resonant bubble sizes with the grain size. In other words, to interpret the experimental results, it is essential to relate the magnitude of the bubbles in the saturated (gas-free) sediment with the grain size. For the acoustic measurements in intertidal sediments the same devices and the same frequency combinations were used. Thus, according to equation (3.31), the bubbles resonant at the pump frequencies have approximately a diameter between 0.2 and 0.8 mm. Bubbles resonant at the difference frequency have a diameter between 0.1 and 0.2 mm. According to Table 6.1, bubbles resonant at the pump frequencies are of the order of magnitude of the grain size of coarse to medium sand whereas bubbles resonant at the difference frequency have sizes similar to the grains of very fine to fine sand. If resonant bubbles are present, they will not be characterised by the third model presented by Anderson *et al*., (1990) and shown in Figure 1.2. Current theoretical models, for gas bubbles in sediments tend to consider the two limiting cases of Anderson *et al.,* (1990) i.e. the existence of large bubbles as for example the works of Wheeler (1990; 1999) and the existence of very small bubbles existing in the interstitial water of the sediment (Gregory, 1976). Thus the size of the resonant bubbles in proportion to the water-saturated sediments is virtualised by Figure 7.1 (b) which a case of Figure 7.1 (a), both been sediment-displacing bubbles.

As mentioned in chapter 1, the form of gas in sediments depends on the sediment type which in turn depends on the grain size (see also section 6.1). Studies have shown that in sandy sediments bubbles tend to be spherical whereas in muddy sediments these tend to form prolate (i.e. coin-like) spheroids (Schubel, 1974; Lyons *et al*., 1996; Tang, 1996; Lyons *et al*., 1996; Tang, 1996; Best *et al*., 2004; Boudreau *et al*., 2005; Reed *et al*., 2005). However in these studies the scanning resolution was limited to 0.5 mm and the length of the cracks of fissures were typically few millimetres or greater (Schubel, 1974; Best *et al*.,

2004). Hence the size of the bubbles considered in this work is comparable to the size of the grains which approaches the limits of the CT scan resolution. Bubbles of these sizes can be visualised in fine sand as shown in Figure 7.1 (b) whereas in muddy sediments such small sizes is possible to be trapped between platy minerals.

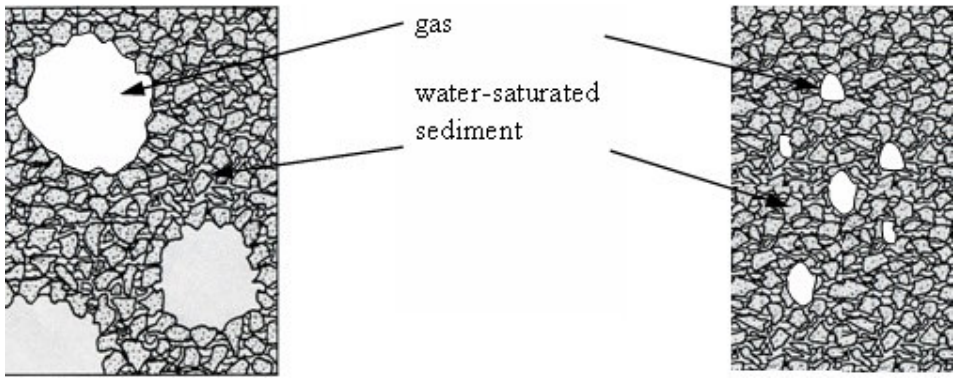

(a) *(b)*

Figure 7.1: Gas bubbles in fine grained sediment as considered (a) much larger than the grain size (Wheeler, 1988) and (b) equal or a factor ten larger than the grain size.

In summary the resonant bubble sizes under investigation in this work have sizes equal to or at maximum ten times bigger than the grain size of the host medium depending on the local properties of the site. Thus the gas configuration corresponding to bubble sizes resonant at the frequencies used for the experimental work (mentioned in chapter 5 and will be discussed further in chapter 7) is similar to that of Figure 7.1 (b). This situation is between the two extreme cases of small and large bubbles described by Wheeler (1988). Assuming such gas formation in sediment, the presence of resonances depends on the bubble sphericity allowed by the water-saturated sediment. In muds such non-spherical bubbles can be characterised as 'elongated occlusions' or small cracks.

7.1.2 Modelling of the collective bubble effect in muddy sediments.

As for the tank experiments, so for the field experiments, transmission and scattering data were taken and inverted using the same linear and nonlinear inversion techniques. The effect of bubbles being present in the propagation path of an acoustic wave propagating in muddy sediment is modelled using the theory of chapter 4 and equation (4.61). Since in

mud the pore-fluid motion relative to the skeletal frame is negligible, the bubble ambient medium has one compressional speed c_{P}. Using the notation of chapter 6 and the bubble natural frequency and damping factors derived in chapter 3 the complex sound speed in bubbly sediments (c_{bP}) is:

$$\frac{c_{\mathrm{P}}^2}{c_{\mathrm{bP}}^2} = 1 + 2\pi c_{\mathrm{P}}^2 \int_{R_{0\,\max}}^{R_{0\,\max}} \frac{R_0 n(R_0)}{\omega_{0\mathrm{s}}^2 - \omega^2 + 2j\beta_{\mathrm{HK\_tot}}\omega} dR_0, \tag{7.1}$$

where the bubble natural frequency in sediments is given by equation (7.2) and the total damping constant is:

$$\beta_{\mathrm{HK\_tot}} = \beta_{\mathrm{HK}} + \beta_{\mathrm{el}}, \tag{7.2}$$

following the analysis of section 3.2. Using equation (7.1) the bubble size distribution $n(R_0)$ is found unambiguously by converting the integral equation (7.1) into a matrix equation in the form of equation (4.56), following the procedures described in chapter 4.

Nonlinear scattering form an ensemble of bubbles in muddy sediment is modelled as the scattering from an ensemble of bubbles in water using equation (4.48). The effects of the shear strength of the sediment are taken into account through the bubble scattering cross sections defined by equations (4.33) and (4.34). The pressure spectral components entering equations (4.33) and (4.34) are computed numerically using equation (4.29). Then the nonlinear scattering cross sections were calculated and used to compose a matrix equation in the form of equation (4.57). The bubble radius and its derivatives are all inputted from the bubble model of equation (3.21). The results from both linear and nonlinear inversions are shown in section 7.4.

7.2 Transmission measurements

The in situ propagation results shown in this section were produced by Dr. G. Robb with the 'stacking method' described in (Robb et al, 2006). The rig of fieldwork was designed by Prof. Leighton. The in situ experiments were carried out in collaboration with Dr. G. Robb, Dr. J. Dix and Dr. A. I. Best. The laboratory experiments and results were carried out in collaboration with Dr. A. I. Best.

The experiments for this study took place at two intertidal sites on south coast of England, the one named Calshot and the other Mercury. The seafloor sediment of these locations falls into the broad category of muddy sediments but the sand grade and the organic

content of these two locations were different. The sediment characteristics for these locations are given in Table 7.1. For both locations, first acoustic transmission measurements were carried out *in situ* and in the laboratory on core samples and then scattering experiments were carried out. The propagation measurements took place during different times of the year and consequently the water temperature was different for the experiments at the two sites. Only one set of measurements was taken at each site. This information is summarized in Table 7.2. In the next paragraphs these experiments and results are described.

Table 7.1: Geotechnical properties of the intertidal sites examined in this work: locations, sediment type, mean grain diameter, porosity and fractions of the constituent sediment grades.

Location	Mean grain diameter(ϕ)	Porosity n (%)	Sand (%)	Silt (%)	Clay (%)	Organic content (%)
N 50° 48'56'' W 001°18'4'' (Calshot)	6.0±0.5	62.0±5.0	27.5±7.0	69.7±6.5	2.8±0.4	3 ±0.5
N 50°52'56" W 001°18'34" (Mercury)	6.7±0.2	60.0±2.5	7.6±5.0	82±3	9±3	9±0.5

Table 7.2: Water temperature and salinity for the time of the year when propagation experiments were carried out.

Location	Salinity (ppt)	Temperature(ºC)	Date	Number of data sets
50°48' 56'' N 001°18' 4'' W (Calshot)	10±2	9±1	March 2008	1
50° 52' 56" N 001°18' 34" W (Mercury)	9.5±0.5	19.5±0.5	June 2008	1

7.2.1 *In situ* transmission measurements in Calshot

The *in situ* transmission experiments were carried out with the rig shown schematically in Figure 7.2. The acoustic source was buried just below the sediment surface at an angle of 45 degrees with respect to the sediment surface. The acoustic axis of the source was aligned with three hydrophones as shown in the same figure. The source was sending 1 ms pulses of frequencies from 26 kHz to 100 kHz at 2 kHz steps. The measurements took place between one and three hours after tidal exposure.

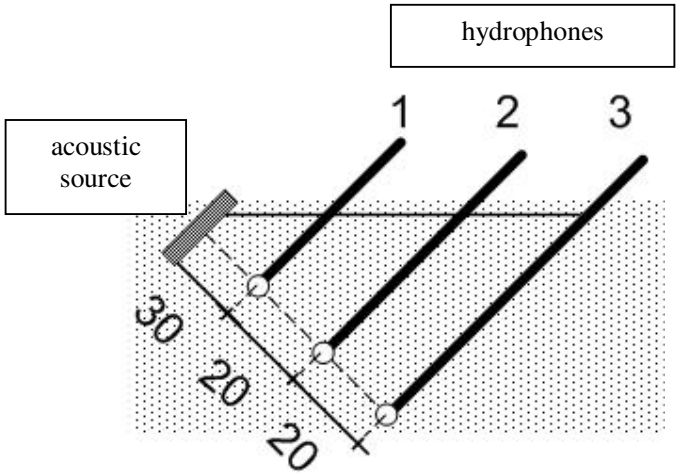

Figure 7.2: Schematics of the propagation set up, the distances are in cm (drawing not in scale)

The *in situ* transmission results are shown in Figure 7.3. The blue line represents results from the first hydrophone pair (hydrophone 1 and 2) and the red line from the second hydrophone pair (hydrophones 2 and 3). The *in situ* results from the first hydrophone pair give a mean value for the sound speed of 1724 m/s with standard deviation 99 m/s. Assuming a linear dependence of attenuation with frequency according to equation (6.15), the best fit line results for $K_{\mathrm{P}} = 0.54$ dB/m/kHz.

The second hydrophone pair measured an average sound speed of 1346 m/s with standard deviation 71 m/s. Assuming a linear dependence of attenuation with frequency according to equation (6.15) the best fit line results for $K_{\mathrm{P}} = 0.56$ dB/m/kHz. The great difference in sound speed measured by the two hydrophone pairs indicates differences in the sediment composition. Based on literature values for P-waves in muddy and sandy sediments, it can

be concluded that in the area of the first pair of hydrophones that sand content was high. This was later confirmed by splitting the core and seeing intermitted sandy layers at the first top 30 cm of the core (Figure 7.5). Moreover, as indicated by Hamilton (1972), the P-wave attenuation is much less sensitive to grade changes (see Figure 6.6) than the velocity is (see Figure 6.5).

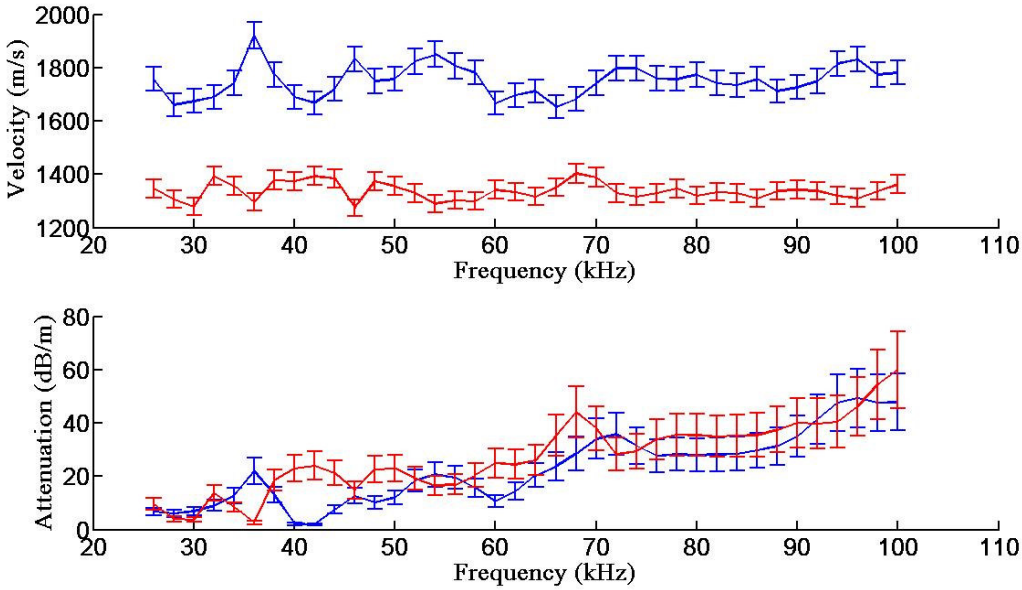

Figure 7.3: Sound speed and attenuation over the frequency range of 26 to 100 kHz as measured by the hydrophones 1 and 2(blue lines) and hydrophones 2 and 3(red lines) of the propagation rig Figure 7.2 in Calshot. The error bars indicate intrinsic errors.

7.2.2 Laboratory measurements with Calshot core

P-wave measurements

Core transmission measurements for the Calshot site, were carried out in the ultrasonic range with a transducer of 500 kHz resonance frequency. The core length from the Calshot location was 50 cm and the measurements took place from the top to the bottom of the core at 2 cm intervals starting at a core depth of 7 cm. Figure 7.4 shows transmission data along the core. The P-wave velocity lies between 1430 m/s and 1550 m/s. If a linear attenuation trend according to equation (6.15) were to be fitted to the attenuation measurements then the value of K_P would be between 0.46 dB/m/kHz and 1 dB/m/kHz.

Given that the second hydrophone was located at an approximate depth of 28 cm, the core measurements exhibit the same trends with the *in situ* measurements: that is in the upper sediment layer exhibits higher attenuation and sound speed than the lower layer. It has to be noted that discrepancies between the *in situ* and laboratory results can also be attributed to sediment disturbance during coring.

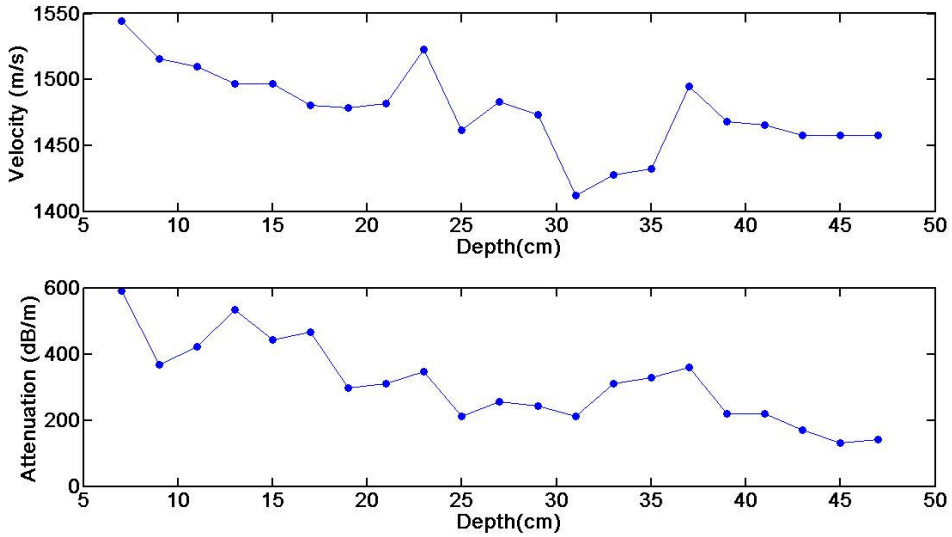

Figure 7.4: P-wave sound speed and attenuation core profiles for Mercury site as computed from transmission ultrasonic core measurements along the core in steps of 2 cm.

After the transmission experiments the core was split in two halves to measure shear wave sound speed. As shown in Figure 7.5, the upper part of the core, the first 25 cm-30 cm has very thin sandy layers appearing distinctively in the grey mud. These explain the higher measured *P*-wave speed *in situ* from hydrophones 1-2. The dark grey colour of the sediment in the core as well as the odour of the hydrogen sulphide indicated that the measurements took in the sulphate reduction zone. The sediment below the sandy layers is grey mud which exhibits homogeneity.

Figure 7.5: Split core from Calshot site.

Discussion on the transmission measurements at the Calshot site

Having seen the sediment structure of the split core, it can be concluded that the measurements which show low sound speed correspond to the muddy layer at the lowest part of the core; whereas measurement with high P-wave sound speed correspond to the sandy layer. This is also easily inferred from the rig lay out (Figure 7.2) because the first hydrophone was buried at a depth of approximately 21 cm, the second one at 35 cm and the third one at 50 cm. Hence the transmission distance between the first hydrophone pair covered the sandy layer whereas the second one covered only the muddy layer. The value of K_P of the muddy sediment below the sandy layer can be estimated to be 0.5 dB/m/kHz, which is a rough approximation resulting from both the *in situ* and core measurements. This value for K_P is approximately one order of magnitude higher than that encountered in literature values for K_P in gas free muddy sediments (see Table 6.3). This is strong evidence of gas presence as typically in gassy sediments, attenuation across all frequencies increases significantly even in the presence of minute amounts of gas (Anderson and Hampton, 1980a, b; Fu *et al.*, 1996)

Moreover the sound speed in the muddy part (sediment layer approximately below 30 cm), depending on the transmission frequency, takes values lower or higher than the values encountered for muddy gas-free sediments (see Table 6.3). This great variation of sound speed is explained from the bubble resonances. At frequencies above resonance the compressional speed is unaffected by bubbles, at frequencies below resonance compressibility effects dominate and the speed is lower than bubble-free sediments. At resonance the effect of bubbles is great and it is manifested as peaks (Wilkens and Richardson, 1998). However, as a bubble distribution instead of a single size bubbles are

expected to be present, the net effect of the bubble resonances will depend on the percentage of bubbles resonant from the whole bubble population.

S -wave measurements

After the P-wave transmission measurements took place, the core was split in two halves to measure shear wave velocity in order to estimate the sediment shear modulus. The shear wave velocity was measured by inserting bender elements in the core; the muddy homogeneous part of the core was examined. The part of the core with the sandy layers was not of interest because it was not possible to receive backscattered signal when such layers are present. This happened when the scattering experiment was set up in the area with the sandy layers no backscattering signal could be received. So the bender elements were inserted in the muddy part only. The measurements in the muddy part of the core were taken with 10 cm separation between the bender elements. The average measured velocity was 40 m/s in the kilohertz frequency range. The shear modulus (G_s) was estimated from equation (6.10) to have an average value of 2.62 MPa, a value which was calculated under the assumption that no dispersion takes place. Attenuation measurements with the available bender elements were not possible because the beam pattern was unknown and therefore spreading corrections could not be applied.

As mentioned in section 7.1 and further discussed in section 7.3, the bubble model for sediments needs the gas-free shear modulus as an input parameter. Although this value for G_s was found by measurements in gassy sediments, it will be assumed that the gas-free sediment shear modulus has the same value. According to observations, the presence of gas has little impact on shear wave velocity and attenuation, especially when compared to the impact of gas on compressional wave propagation (Richardson and Briggs, 1996). Laboratory measurements in kaolin containing methane bubbles have confirmed the low impact of the gas presence on the sediment shear modulus when small strains, such as those induced by acoustic excitation, are involved (Duffy *et al.*, 1994).

7.2.3 *In situ* transmission measurements at Mercury

In situ and laboratory transmission measurements were carried out using the same materials and methods for the intertidal site named Mercury (N 50° 52' 56", W 001°18' 34), see Table 7.1 for average geotechnical properties and Table 7.2 for salinity and temperature values. The in situ transmission results are shown in Figure 7.6. The blue line represents results from the first hydrophone pair (hydrophone 1 and 2) and the red line from the second hydrophone pair (hydrophones 2 and 3). The first hydrophone pair measured an average P-wave sound speed of 1323 m/s and a standard deviation 110 m/s. If a linear dependence of attenuation with frequency were to be fitted to these data, then according to equation (6.15) the value of K_P would equal to 0.32 dB/m/kHz. The second hydrophone pair measured an average sound speed of 1250 m/s with a standard deviation of 240 m/s. Assuming again a linear dependence of attenuation with frequency, the value of K_P equals 1.1 dB/m/kHz. The values of K_P serve only as baselines for comparing attenuation trends between in situ and core measurements.

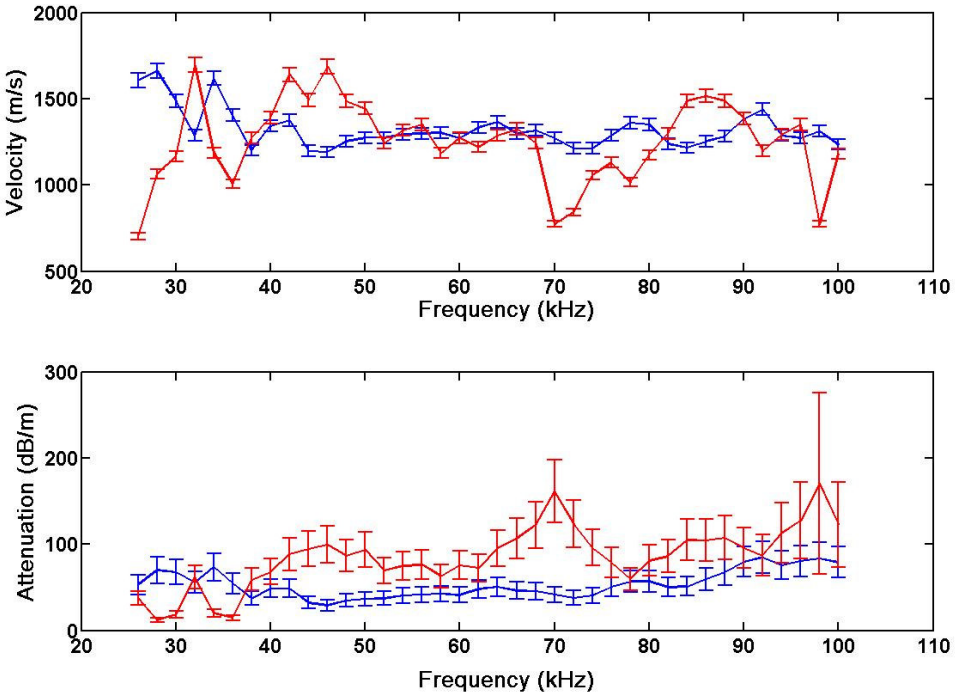

Figure 7.6: Sound speed and attenuation over the frequency range of 26 to 100 kHz as measured by the hydrophones 1 and 2(blue lines) and hydrophones 2 and 3 (red lines) of the propagation rig Figure 7.2 at Mercury site. The error bars indicate intrinsic errors.

7.2.4 Laboratory measurements with Mercury core

Core transmission measurements for the Mercury site were carried out in the same manner as for the Calshot site at 500kHz. The core length is 40 cm and the measurements took place from the top 8 cm to the bottom of the core at 2 cm intervals. Figure 7.7 shows transmission measurement results for P-wave sound speed and attenuation along the core. Data from the lower part of the Mercury core exhibit greater variability than those taken at the upper part and the core data from the Calshot site. As shown in Figure 7.7, at a depth of 24 to 28 cm the average P-wave velocity is 1415 m/s. If a linear dependence of attenuation with frequency is assumed, then the parameter K_P would take values between 0.7 and 0.9 dB/m/kHz for this depth.

Looking at the core profiles, abrupt changes in attenuation and velocity are observed which suggest differences in gas distribution with depth. The split core, shown in Figure 7.8, looked homogenous to the naked eye which indicates that no distinct sandy layers existed. The core measurements show the same trends with the *in situ* measurements: the attenuation increases and the sound speed decreases with the depth, which indicates that the gas content of the sediment increases with depth.

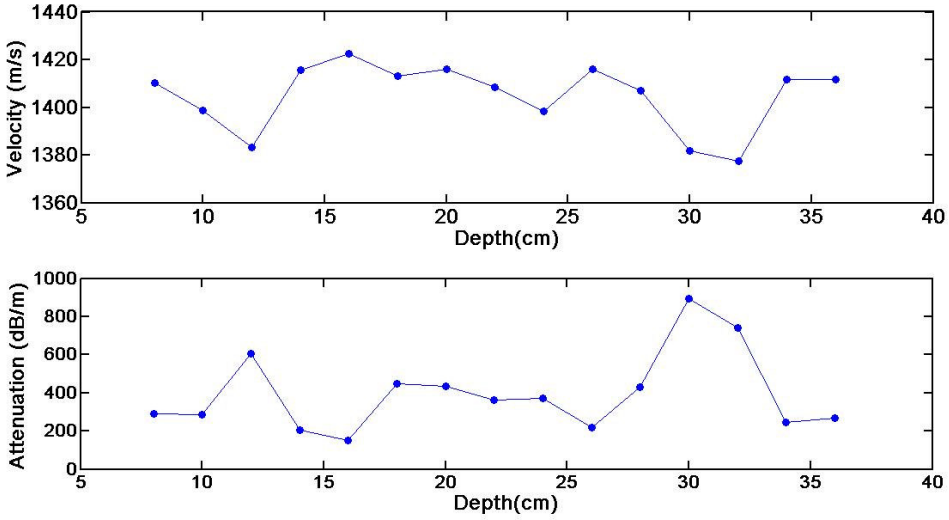

Figure 7.7: P-wave sound speed and attenuation core profiles for Mercury site as computed from transmission ultrasonic core measurements along the core in steps of 2 cm.

Figure 7.8: Split core from Mercury site.

Further characterisation of the gas shape cannot be achieved using the available velocity and attenuation measurements. That is to say, these data alone cannot answer the question of whether the whole amount of gas present is in the form of resonant or non-resonant bubbles. The bubble resonance the sound speed and attenuation are greatly affected. This appears as attenuation peaks and abrupt changes in velocity (Best 2004; Fu *et al*., 1996). For the *in situ* measurements, carried out in Calshot and Mercury, such peaks were not always possible to resolve. However, the bubble Q-factor was predicted to be much larger in sediments than in water, therefore these peaks are not resolvable because of the small frequency steps in transmission measurements (2 kHz).

7.3 The combination frequency inversion technique applied to sediments

To investigate further the gas present in the intertidal sites of Calshot and Mercury, scattering measurements were carried out within approximately 1 metre of the location of the transmission experiments. All scattering experiments were conducted the same time of the year thus the environmental conditions were assumed the same for all experiments. However the scattering experiments took place during summer as opposed to transmission experiments that took place in spring.

In order to interpret the scattering from the gas bubbles existing in the top seafloor layer, first the scattering from a single bubble was modelled and then extended to an ensemble of bubbles. For these inversions, incoherent (back) scattering was assumed and the methodology was exactly the same applied to water inversions as described in chapter 4

and 5. The water tests (Figure 5.12) gave confidence in this approach because in water (where all bubbles were 'acoustically spherical') the two-frequency technique gave the same results as the bubble population derived by the transmission method.

7.3.1 Combination frequency scattering measurements in intertidal sediments

The combination frequency apparatus (Figure 5.1) was deployed vertically such that the surface of the pump source aligns with the seafloor as shown in Figure 7.9. The experiments were carried out in the same manner as the tank experiments. The imaging frequency f_i was kept constant at 220 kHz and the pump frequency f_p varied from 30 kHz to 100 kHz in increments of 2 kHz. The wavelengths involved in all measurements (i.e. the wavelength emitted by the imager and pump source and the wavelengths of the difference and twice the pump frequencies) are an order of magnitude or greater than the equilibrium sizes of the estimation bubble distribution. Hence the assumption of omnidirectional scattering could be retained. Moreover the highest value of the quantity kR_0 is 0.1, which conforms to the initial assumption of unidirectional scattering from all 'acoustically spherical' bubbles. Hence, the matrix formulation of equation (4.48) was applied here without any additional directivity corrections. The insonification volume is, for twice the pump frequency, at maximum 10^{-4} m^3 (see Figure 7.10), which gives to the scattering results local validity rather than the ability to characterise the whole site.

As explained in Chapter 5, the sensing volume was computed as the 3 dB intensity fall of from the rig focus point F (see Figure 5.2). This volume is the volume where the beams of the three devices overlap an is located in the centre of the rig, an indication is given by the red dotted line in Figure 7.9. As already mentioned this sensing volume varies with frequency and the lower the frequency the greater this volume is. Figure 7.10 shows how this sensing volume varies (a) at twice the pump and (b) at the difference frequency for the range of frequencies used for the scattering experiments.

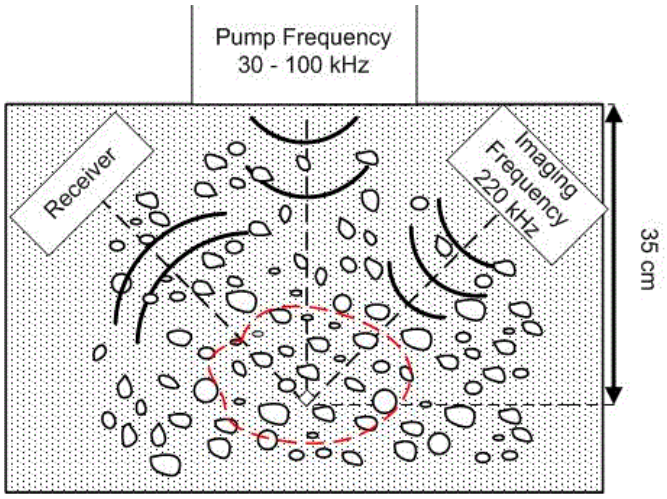

Figure 7.9: Side view of the combination-frequency apparatus in sediments with gas bubbles at the common focal point showing schematically the relative distance of the three devices which are pictured in figure 5.1.

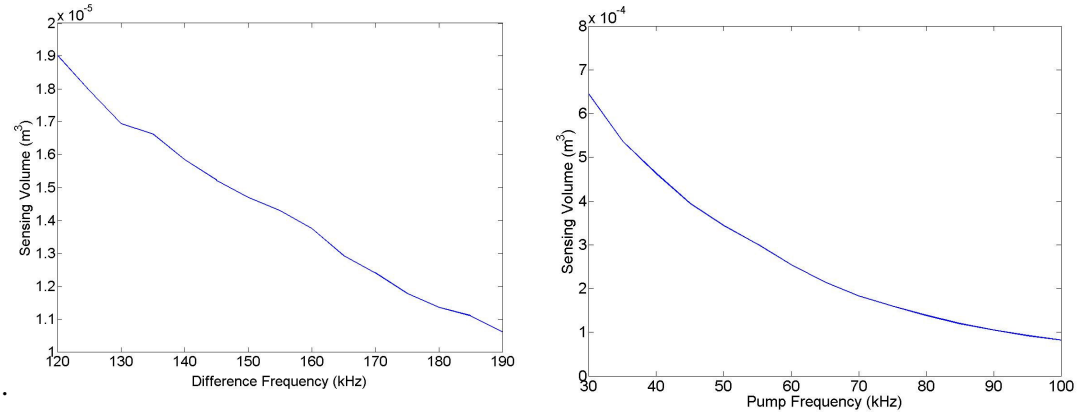

(a) *(b)*

Figure 7.10: Sensing volume of the receiver of the combination frequency apparatus (a) as function of the difference frequency varying from 120 kHz to 190 kHz and (b) as function of the pump frequency varying from 30 kHz to 100 kHz.

As for the tank experiments the acoustic sources were adjusted such that at the focal point of the rig the pressure stays constant for all frequencies. The pressure levels at the focus were calibrated so that the pressure (zero-to-peak) of the imaging source was 60 kPa for the all datasets, which were used for inversions, and for the pump source 5 kPa. These two frequency signals were generated as a 2 ms square pulse. These pressure levels were measured and chosen by trial and error process in the field, taking into account, apart from

the physical limitations of the devices, that: (a) there is an almost linear relationship between attenuation coefficient and frequency (see section 6.3), (b) the pressure levels at all sites must be kept the same. The second condition helps in comparing all sites with the same methodology and prevents introducing errors when compensating for different experimental conditions.

It was possible to 'calibrate' the combination frequency apparatus, i.e. to estimate the non-bubble mediated nonlinearity only in water. The pressure levels of the components stemming from the nonlinearity of the medium, i.e. the bubble-free mud, and possible nonlinear electronic effects due to high pressure levels, were unknown. To distinguish between the bubble-mediated and other sources of nonlinearity, a series of experiments were conducted at both sites with varying pressure levels.

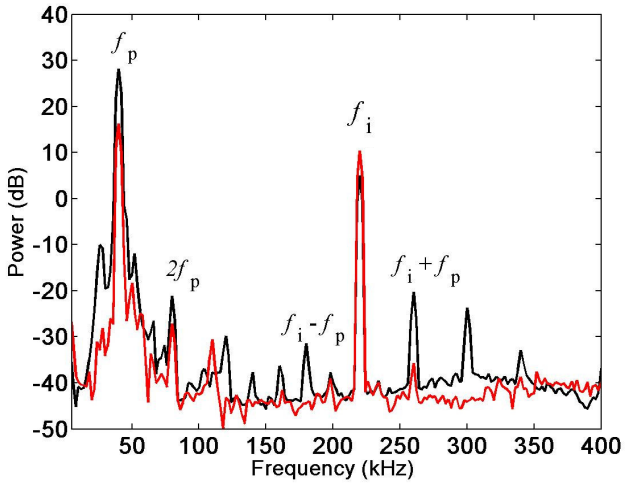

Figure 7.11: The mean-square power spectrum is plotted in dB scale with reference the unity rms acoustic power is plotted against frequency for two different patches(red and black lines) at the Calshot site, for an imaging frequency of 220 kHz and pump frequency of 40 kHz with a zero-to-peak amplitudes of 60 kPa and 5kPa respectively. The frequencies between 5 kHz and 400 kHz are shown.

Figure 7.11 shows the power of the scattered spectrum of the signal measured at two different patches at the Calshot site using the same pressure levels. The pump signal was emitting at 40 kHz and had a zero-to-peak amplitude of 5 kPa. The imaging signal was emitting at 220 kHz and had a zero-to-peak amplitude of 60 kPa. In line with the spectral representation of all previous chapters, the mean-square power spectrum is plotted in dB

scale with reference the unity rms acoustic power[8] versus frequency, thus the power at a specific frequency is indicated on the plot. This approach is valid here because, as for the tank experiments, the steady state part of the received signal, which corresponds to the steady state pulsations of the bubbles, is of interest.

The spectra of Figure 7.11 give evidence that the one patch has gas in form of (near) spherical bubbles (black line) whereas the other patch (red line) has no bubbles or there are just a few of these bubbles such that the signal-to-noise ratio is too low to produce discernible peaks. The conclusion is drawn from the nonlinear peaks: the one patch (black line) exhibits clear nonlinear peaks at all expected combinations of f_p, f_i whereas the red line has no peak at the difference frequency.

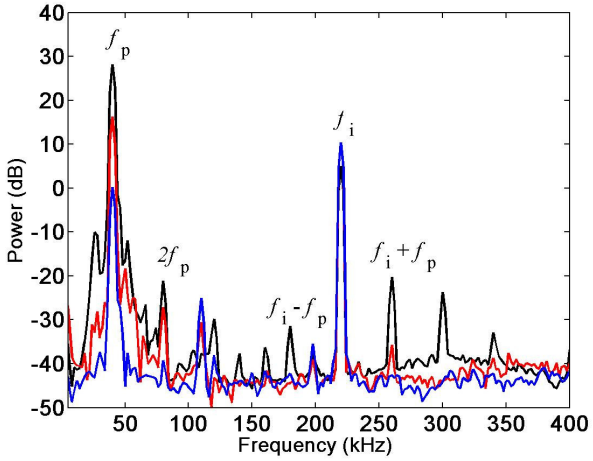

Figure 7.12: The mean-square power spectrum is plotted in dB scale with reference the unity rms acoustic power is plotted against frequency for two different patches at the Calshot site (red and black lines) and for a patch at Mercury (blue line). All conditions are the same as for Figure 7.11. The frequencies between 5 kHz and 400 kHz are shown.

In Figure 7.12 the spectra of Figure 7.11 are plotted together with the acquired spectra from a patch of the Mercury site using the same frequencies and pressure levels. As observed in Figure 7.12 the spectra from this Mercury patch (blue line) exhibit no peak at the difference frequency or the sum frequency; thus it can be concluded that the other peaks are medium and/or electronic nonlinearity rather than bubble mediated. This is verified by the power spectrum of another patch from the Mercury site, which is shown in Figure 7.13 as a green line. The frequency and source levels of the sources and other

[8] With this convention a sine wave of $\sqrt{2}$ zero-to-peak amplitude gives the reference unity power.

experimental settings were kept exactly the same as for the measurements shown in Figure 7.11 and Figure 7.12. The spectra of all four patches are also shown in Figure 7.13 for comparison. Clearly the resonance peaks are higher for this Mercury patch (green line) than for the Calshot site which also exhibited resonances (black line).

To investigate the effect of the appearance of nonlinear components due to the pressure level increase, higher pressure levels were tested at the patch on the Mercury site where no combination harmonics were measured (blue line of Figure 7.12 and Figure 7.13). These results are shown in Figure 7.14 where the mean-square power spectrum is plotted against frequency. As in the experimental results of Figure 7.11 to Figure 7.13, the pump source was emitting at 40 kHz and the imaging source as 220 kHz.

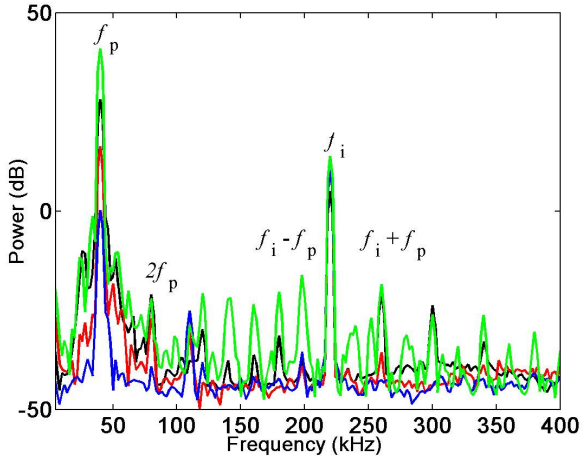

Figure 7.13: The mean-square power spectrum is plotted in dB scale with reference the unity rms acoustic power is plotted against frequency for two different patches at the Calshot site (red and black lines) and for two patches at Mercury site (blue and green lines). All conditions are the same as for Figure 7.11 and Figure 7.12. The frequencies between 5 kHz and 400 kHz are shown.

The blue solid line indicates the spectrum for a zero-to-peak pressure of the imaging and pump source of 60 kPa and 5 kPa respectively, as in Figure 7.12 and Figure 7.13. The black dashed line shows the power spectrum when these amplitudes were raised to 80 kPa and 10 kPa respectively and the blue dashed line the same spectrum when these pressures were raised to 100 kPa and 20 kPa respectively. The appearance of peaks at combination frequencies occurs at high acoustic amplitudes and even then these are much lower than the $2f_p$ or $3f_p$ peaks.

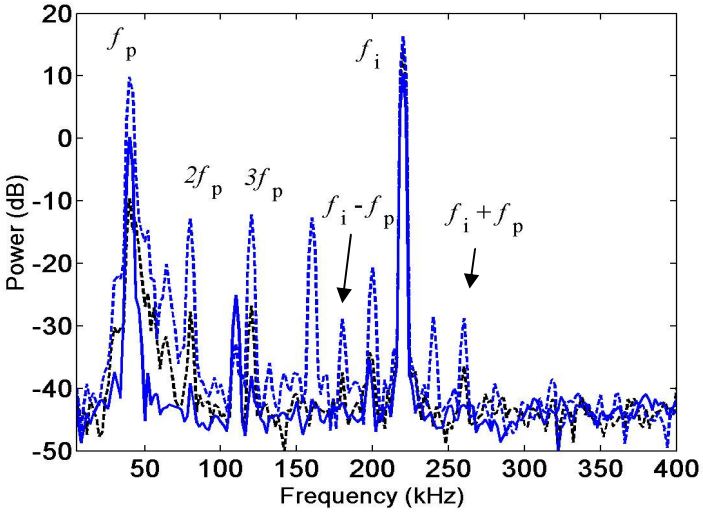

Figure 7.14: The mean-square power spectrum in dB scale with reference the unity rms acoustic power is plotted against frequency for the patch at Mercury exhibiting no resonances (blue line of Figure 7.12 and Figure 7.13). On the same figure for the same patch the mean-square power spectrum is plotted for a zero-to-peak pressure of the imaging and pump source of 80 kPa and 10 kPa respectively (black dashed line) and of 100 kPa and 20 kPa respectively (blue dashed line) .The spectral frequencies between 5 kHz and 400 kHz are shown.

Based on these experimental observations, the datasets which exhibit clear resonances at combination frequencies were selected for inversion. After establishing the thresholds for the noise level and the system mediated nonlinearity, the interpretation of the scattering data from intertidal sediments followed the same line with the inversion process for the tank scattering data (chapter 5).

7.3.2 Construction of the inversion matrix

To invert the scattering data taken with the combination frequency apparatus the inversion matrix was constructed in the same manner as the inversion matrix for the water-based inversions. First the individual bubble response was computed by solving numerically equation (3.21), then the pressure scattered from each bubble was computed using equation (4.29) and lastly the corresponding bubble cross sections were computed at the difference frequency, i.e. $\sigma_{ds-}(\omega_-, R_0)$, and twice the pump frequency , i.e. $\sigma_{ds\,2\omega_p}(\omega_{2p}, R_0)$, using equations (4.33) and (4.34) respectively. This procedure of computing bubble cross sections was repeated for a range of bubble sizes (R_0). This range was defined by the

bubble sizes resonant at twice the pump and the difference frequencies. The computed cross sections were stored in an inversion matrix $\boldsymbol{\sigma}$, such that each row of this matrix gives the contribution of each bubble bin size at the nonlinear component under consideration whereas each column of this matrix gives the importance of a certain bubble size for the nonlinear component under consideration (at ω_{2p} or ω_-).

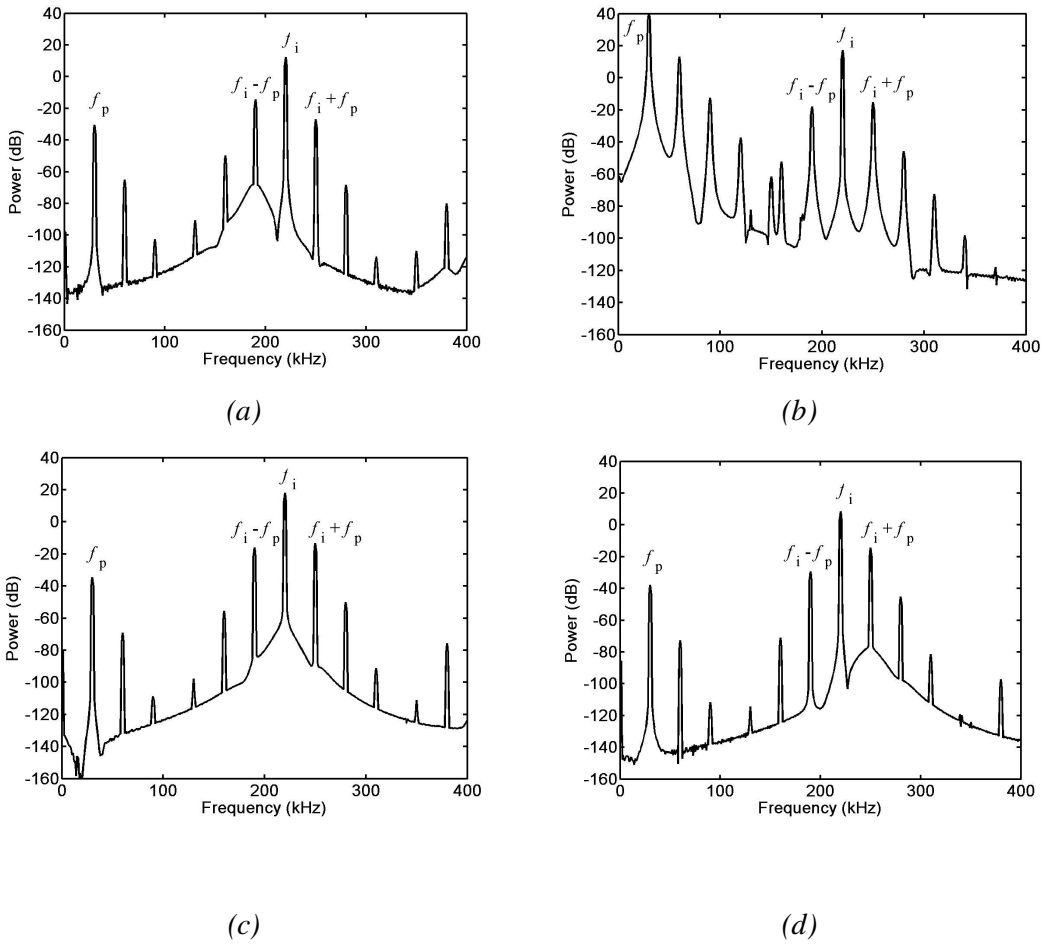

Figure 7.15: Power spectrum of scattered pressure at 1 m from a single bubble of size resonant at (a) $f_i - f_p$ 190 kHz, (b) f_p =30 kHz (c) f_i =220 kHz and (d) $f_i + f_p$ = 250 kHz. The bubble is insonified by a wave at 30 kHz and another at 220 kHz. Both waves have pressure amplitude of 15 kPa (0-peak). Note that for the simulations the damping terms have been modified to accommodate the difference frequency

The application of the same inversion technique to sediments was possible because according to the model of equation (3.21) the single bubble response exhibits qualitatively similar spectra. Also, as for gas bubble distributions in water, bubbles in muddy sediments insonified by the frequency combinations chosen in this work generate nonlinear components which arise from more than one resonant bubble size. Therefore in a similar

way, monitoring the component at twice the pump frequency adds the necessary information to the inversion matrix. This is demonstrated with the following two simulation sets. Figure 7.15 shows the power spectra obtained for a single bubble insonified by f_p=30 kHz and f_i= 220 kHz both of pressure amplitudes 30 kPa (0-peak). These simulations show the mean-square power for bubble sizes resonant at: (a) $f_i - f_p$=190 kHz, i.e. $R_0 \approx 68\mu$m, (b) f_p=30 kHz i.e. $R_0 \approx 413\ \mu$m, (c) f_i= 220 kHz i.e. $R_0 \approx 58\ \mu$m, and (d) $f_i + f_p$=250 kHz, i.e. $R_0 \approx 51\ \mu$m (compare with Figure 5.5). Another example is shown in Figure 7.16 where the power spectra are plotted for a single bubble insonified by f_p=55 kHz and f_i= 220 kHz, both of pressure amplitudes are of 30 kPa (0-peak). These simulations show the mean-square power for bubble sizes resonant at: (a) $f_i - f_p$=165 kHz, i.e. $R_0 \approx 78\mu$m, (b) f_p=55 kHz i.e. $R_0 \approx 235\ \mu$m, (c) f_i= 220 kHz i.e. $R_0 \approx 58\ \mu$m, and (d) $f_i + f_p$=250 kHz, i.e. $R_0 \approx 47\ \mu$m (compare with Figure 5.6).

To summarise, the simulation results show that there is not a one-to-one mapping between the resonant bubble sizes and the pressure component at the difference frequency. Bubbles resonant at the pump frequency produce almost the same amount of nonlinearity at ω_- with those sizes resonant at the difference-frequency. Moreover there is a fixed amount of nonlinearity at ω_- that stems always from those bubbles resonant at the imaging frequency as indicated by Figure 7.15(c) and Figure 7.16 (c).

Following the same approach as for bubble sizing in the water tank, the information about the bubble sizes resonant at the pump frequencies will be extracted via monitoring the scattered pressure component at twice the pump frequency. As discussed in chapter 5, the spectral component at $\omega_{2\mathrm{p}}$ is a non cooperative nonlinear component, i.e. it is independent of the presence of the imaging frequency and stems only from bubbles resonant at the pump frequency. Therefore monitoring the $\left|\tilde{p}_{\mathrm{b}}(r,\omega)\right|^2_{\omega=\omega_{2\mathrm{p}}}$ provides the necessary information about that proportion of bubble sizes that are resonant at the pump and contribute to the spectral component $\left|\tilde{p}_{\mathrm{b}}(r,\omega)\right|^2_{\omega=\omega_-}$.

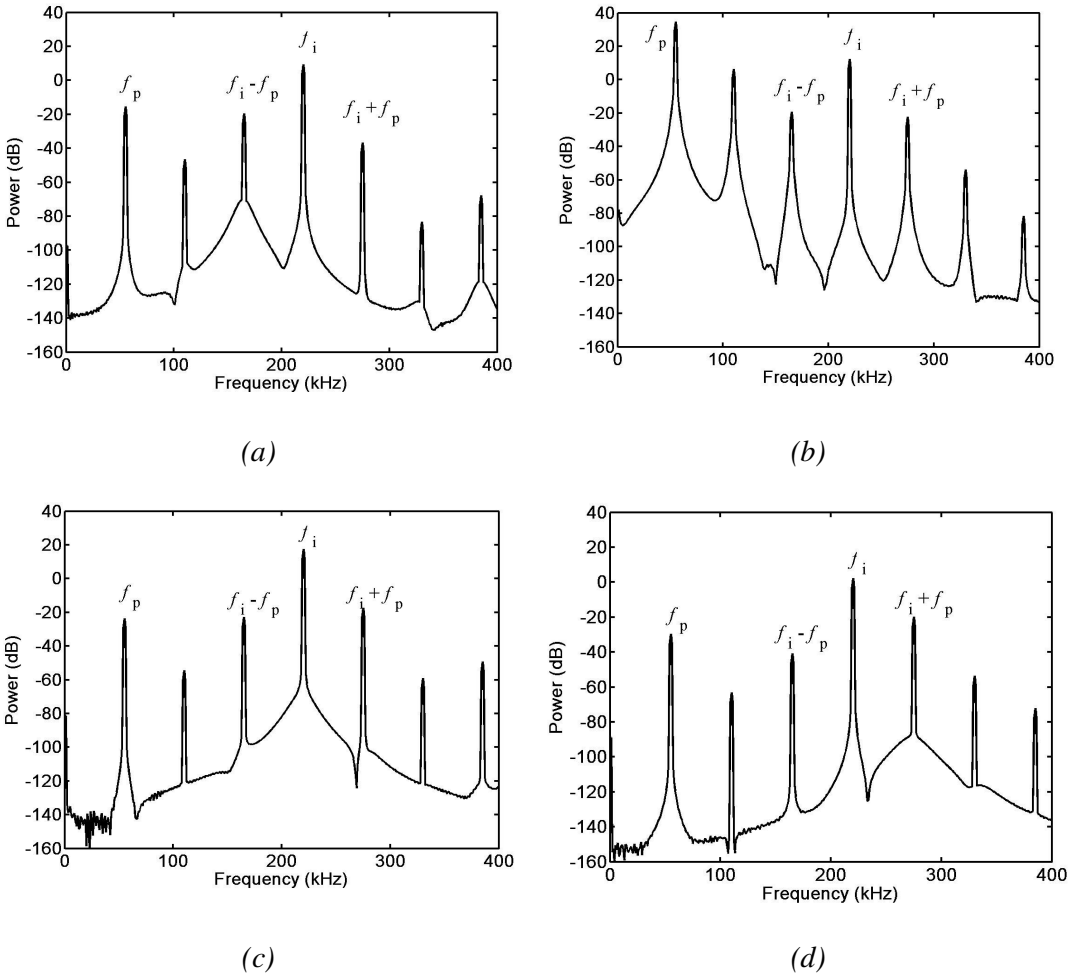

Figure 7.16: Power spectrum of scattered pressure at 1 m from a single bubble of size resonant at (a) $f_i - f_p$ =165 kHz, (b) f_p =55 kHz, (c) f_i =220 kHz and (d) $f_i + f_p$ = 275 kHz. The bubble is insonified by a wave at 55 kHz and another at 220 kHz. Both waves have pressure amplitude of 15 kPa (0-peak). Note that for the simulations the damping terms have been modified to accommodate the difference frequency.

7.4 Inversion results

This section discusses inversion results from transmission and scattering measurements from those patches where bubble nonlinear resonances were present observed. During the same day three patches were examined at each site but bubble nonlinear resonances were observed only in one or two patches, i.e. data sets. That is the datasets other than those given in Table 7.3 did not exhibit clear nonlinear resonances as explained in section 7.3.1.

The water temperature and salinity as well as the dates when scattering experiments were conducted are given in Table 7.3.

Table 7.3 Water temperature and salinity for the time of the year when scattering experiments were carried out.

Location	Salinity (ppt)	Temperature (ºC)	Date	Number of data sets usable for inversion
50°48' 56'' N 001°18'4'' W (Calshot)	11±0.5	21±0.5	July 2008	1 (out of 3)
50°52'56" N 001°18'34" W (Mercury)	12±1	20±1	July 2008	2 (out of 3)

The predicted bubble distributions are presented as bands to indicate uncertainty margins. For the inversion or transmission data only the intrinsic errors were taken into account. For the inversion of scattering data the intrinsic errors plus the maximum possible error due to beam pattern calculations were taken into account. The large 'dips' (or minima) of the bubble population curves are numerical artefacts of the inversion, attributed to the oscillatory behaviour of the regularisation scheme as discussed in section 4.4. No attempt was made to increase the regularisation parameter because this would results into additional errors (see discussion of section 5.4). All data were filtered prior to being inverted using a third order Savitzky-Golay smoothing filter in the same way the data from the tank scattering experiments were filtered. That is they were filtered by minimizing the least-squares error in fitting a third order polynomial to frames of noisy data.

7.4.1 Bubble size distributions at the Mercury site

Figure 7.17 shows the bubble population distributions as computed from the propagation data taken at the Mercury site with the first (blue line) and the second (red line) pair of hydrophones of the propagation rig (see Figure 7.2). The attenuation data cover the frequency range of 26 kHz to 100 kHz (see section 7.2). For the inversions this attenuation is attributed only to bubbles resonant at these frequencies, i.e. bubbles with equilibrium radii between 0.1 and 0.4 millimetres. The bubble size distribution, as predicted from these attenuation measurements covers this size range shown in Figure 7.17. The raw, filtered

and forward fitted data from the attenuation measurements from the first and the second hydrophone pair are shown in Figure 7.18 (a) and (b) respectively. The blue lines indicate the raw data and the green lines the filtered data which were inverted. The red lines indicate the forward fitted data, i.e. the attenuation estimate, which is obtained when the estimated bubble population is inserted into the matrix equation (see equation (4.55) and discussion of section 4.3). As seen in Figure 7.18 (a) and (b) the green and red lines overlap, i.e. the inverse and forward problem give the same results when the input data are filtered.

Figure 7.17 shows also the bubble population as resulted from inversion of scattering data taken at the first patch at Mercury (purple line). As explained in chapter 5, the combination frequency inversion technique developed in this PhD work uses two nonlinearly scattered components, the one at the difference frequency and the other at twice the pump frequency, in order to estimate a certain bubble population. As for gas bubbles in water, simulations showed that only the bubbles which are resonant at the pump frequency will give strong nonlinear peaks at twice the pump frequency, which means that there is unambiguous correspondence between the nonlinear scattering at $2f_{\mathrm{p}}$ and the bubble sizes resonant at f_{p}. This bubble size range coincides with the bubble size estimation from the inversions of the attenuation data. On the other hand, the measured scattering at the difference frequency (f_{-}) is the additive result from bubble sizes resonant at the f_{p} and the f_{-}. Simulations (see Figure 7.15 and Figure 7.16) showed that bubbles resonant at the difference-frequency give stronger scattering than those resonant at the pump frequency; however the difference in their contributions is not so great to neglect the contribution of the sizes resonant at $2f_{\mathrm{p}}$.

The double ended arrow in Figure 7.17 indicates that proportion of the population which results predominantly from scattering at f_{-}. The input information at these two sets of frequencies, i.e. at $2f_{\mathrm{p}}$ and f_{-} is presented as separate curves in Figure 7.19, but they were joined together for the inversion according to the scheme of equation (4.57). The raw scattering data are plotted with blue lines, the filtered inversion input data with green lines and the backward fitted data with red lines.

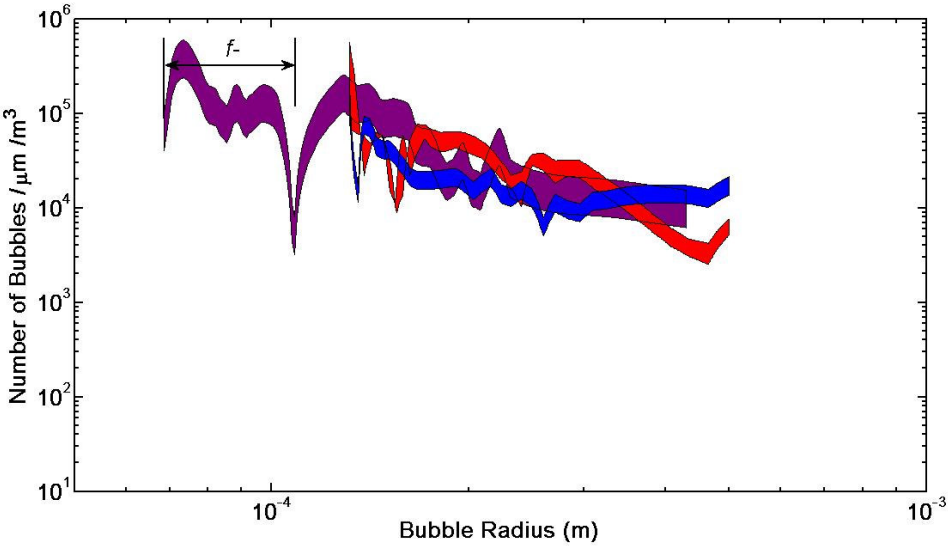

Figure 7.17: Bubble population estimate plotted as number of bubbles per cubic metre per micrometer radius range versus bubble size, as resulted from measurements taken at the Mercury site. The blue and red curves resulted from inversion of the (filtered) transmission data taken from the first and the second pair of hydrophones respectively (Figure 7.2). The purple curve indicates the bubble population which resulted from inversion of the (filtered) scattering data from the first patch examined at the same site. The double sided arrow indicates the proportion of the population which resulted predominantly from the inversion of the spectral components at the difference-frequency.

As shown in Figure 7.18 the input filtered and the forward fitted data overlap which indicates the algorithm selection to minimise $\left|\hat{\mathbf{P}}-\mathbf{P}\right|$. Although one patch is not sufficient to obtain statistically meaningful results, here the results are discussed with the assumption that the filtered data inputted into the inversion scheme were representing the mean scattered value of the pressure spectral components. This is shown in Figure 7.19; although the raw input data plot out a curve which is very jagged, in contrast the inputted filtered data (green line) plots a curve which passes through the raw data as being their mean value.

The great dip seen in the purple curve of Figure 7.17, is an inherent characteristic of the inversion scheme used through this work. The double ended vector indicates the proportion of the population which originates from bubbles mainly resonant at f_-. A large oscillation occurs at the end of this range of bubble sizes mapped out by the resonance of the difference frequency (in the same fashion as occurred in the estimated bubble populations in water – section 5.4). As discussed in section 4.4, this event originates from the scattering

submatrix $\boldsymbol{\sigma}_{i\text{-}p}$, which (as it did for water) for sediments has rapidly varying components that are not damped by the regularisation parameter beta (see discussion at the end of section 4.4).

At this point the assumption of zero attenuation of the background medium should be discussed. The results of Figure 7.17 were produced under the assumption that the waves reach the sensing volume unattenuated. The results taking into account attenuation outside the scattering volume are shown in Figure 7.20.

(a)

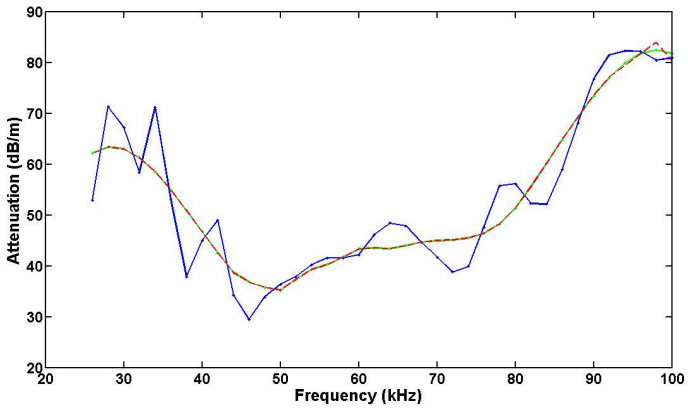

(b)

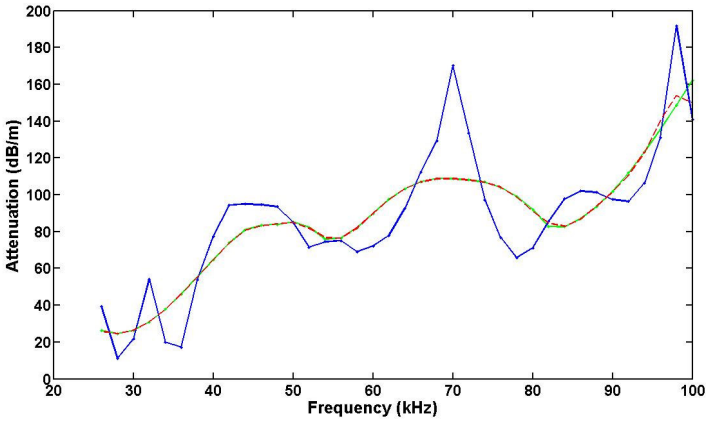

Figure 7.18: Attenuation (dB/m) versus frequency at the Mercury site. Raw data (blue lines), filtered data (green lines) and forward fitted data (red lines) versus frequency range from (a) the first hydrophone pair and (b) the second hydrophone pair of the propagation rig as numbered in Figure 7.2. The sound speed and the measurement errors which correspond to these raw attenuation data (blue lines) are shown in Figure 7.7.

The assumption of zero attenuation loss outside the scattering volume is clearly valid in the case of bubble scattering from the water tank because the rising bubbles were forming a curtain in front of the combination frequency rig and the attenuation of water is negligible

for the distances involved in the experimental set up. However in the case of gassy sediments in the top centimetres of the seafloor these assumptions may not be valid, depending on the composition of the mudflat surface and the depth where the bubbles are located at the moment of the data acquisition. To examine the potential effect of attenuation, the *measured* attenuation was taken into account. The integrals $I(\omega)$, given by equation (4.41), were calculated as:

$$I(\omega) = e^{-\alpha_{\mathrm{P}} r_{\mathrm{r}}} e^{-\alpha_{\mathrm{P}} r_{\mathrm{t}}} \int_V P_{\mathrm{i}}^2 \frac{r_0^2 \Omega_{\mathrm{r}}^2 \Omega_{\mathrm{t}}^2}{r_{\mathrm{r}}^2 r_{\mathrm{t}}^2} dV \,. \qquad (7.1)$$

Equation (7.1) is similar to equation (4.41). The difference is that different attenuations have been assigned to the emitting and scattered signal. This is due to the fact that the attenuation here is the attenuation of the gassy sediment which was also assumed to vary proportionally with the frequency. Thus for nonlinear scattering at f_-, the attenuation of the scattered wave is proportional to that frequency (f_-) whilst the attenuation entering for the transmitted signal corresponds to the imaging frequency.

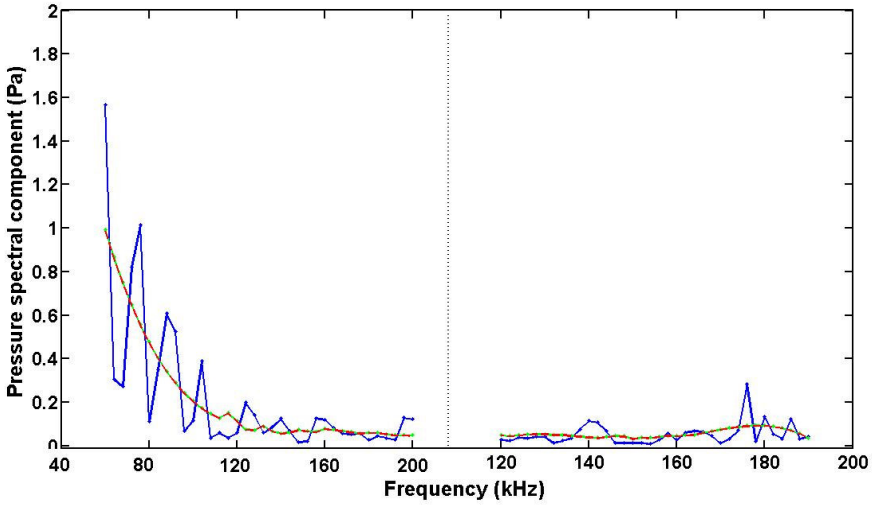

Figure 7.19: Measured pressure spectral components at the first patch of the Mercury site. The left hand side of the graph shows the measured spectral component at $2f_{\mathrm{p}}$ and the right hand side of the graph shows the corresponding spectral component at f_-. The raw data are plotted with blue lines. The filtered data are plotted with green lines and the forward fitted data with red lines. The frequency varies on the abscissa from 60 kHz to 200 kHz for the signal power at $2f_{\mathrm{p}}$ and from 120 kHz to 190 kHz for the signal power at f_-.

Accordingly for scattering at twice the pump frequency, the attenuation for the scattered signal is proportional to f_{2p} and for the transmitted is proportional to f_p. Thus although

for all waves the attenuation is given by the same equation (namely equation (6.15) with the exponent p equal to unity) the values differ for each frequency combination used for the experiments.

The inversion results, using this iteration approach are shown in Figure 7.20 superimposed with the results of Figure 7.17. This approach results in a greater bubble distribution because adjusting for attenuation loss effectively increases the signal strength of the scattering volume.

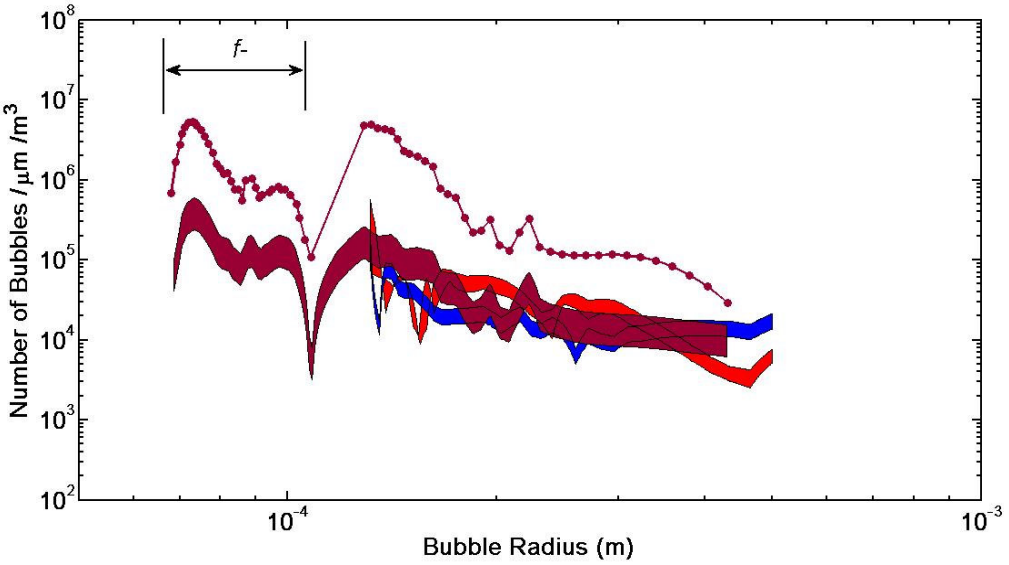

Figure 7.20: Blockplots as in Figure 7.17, The dotted purple line shows the mean bubble distribution which resulted from inversion of the filtered scattering data, as the purple blockplot, taking in addition into account the attenuation of the medium (gassy sediment). The error band that corresponds to this inversion is assumed to be the same with the purple band.

At the Mercury site another patch about two metres away from the first patch was examined with the combination frequency rig. The results from the scattering inversions in Mercury from this second patch are plotted with green line in Figure 7.21. The blue and red curves are the same as those of Figure 7.17. The raw, filtered and forward fitted data for this second patch are plotted in Figure 7.22.

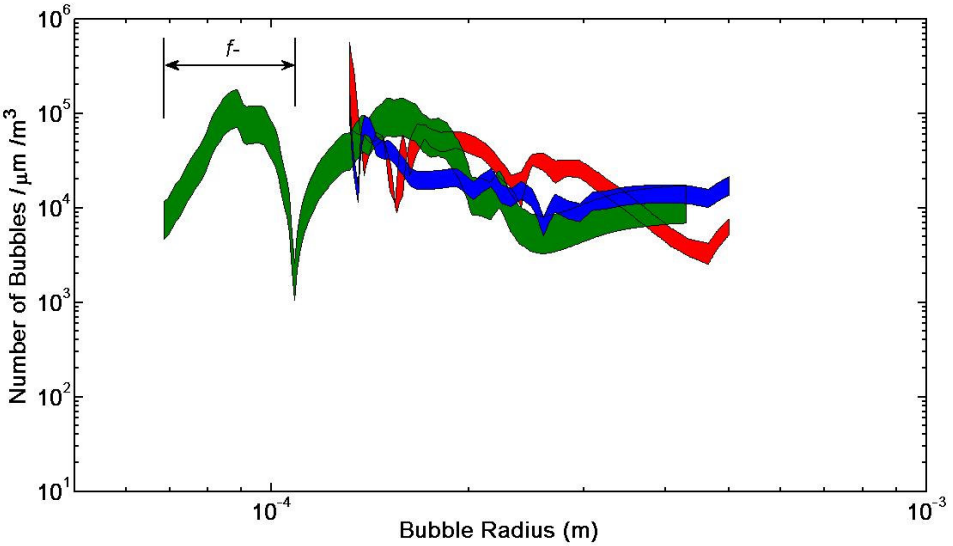

Figure 7.21: Bubble population estimate plotted as number of bubbles per cubic metre per micrometer radius range versus bubble size, as resulted from measurements taken at the Mercury site. The blue and red curves resulted from inversion of the (filtered) transmission data taken from the first and the second pair of hydrophones respectively (Figure 7.2). The green curve indicates the bubble population which resulted from inversion of the (filtered) scattering data from the second patch examined at the same site. The double sided arrow indicates the proportion of the population which resulted predominantly from the inversion of the spectral components at the difference-frequency.

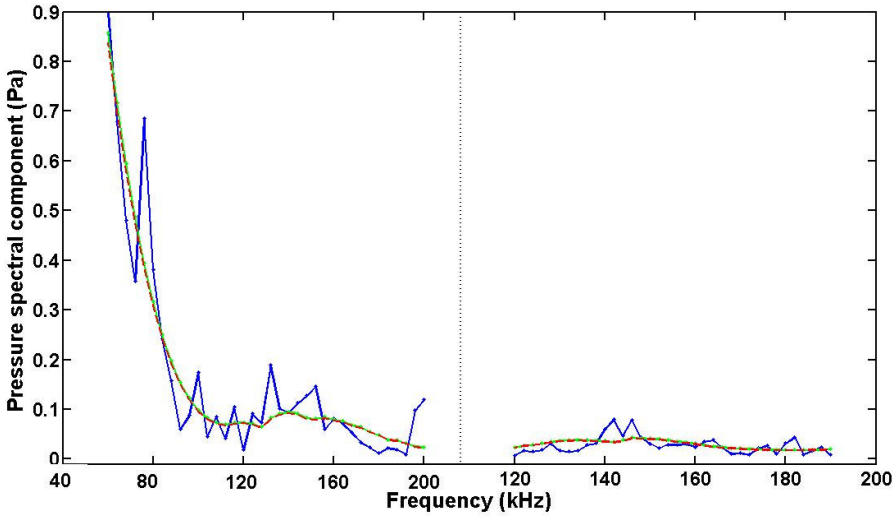

Figure 7.22: Measured pressure spectral components at the second patch of the Mercury site. The left hand side of the graph shows the measured spectral component at $2f_p$ and the right hand side of the graph shows corresponding spectral component at f_-. The raw, filtered and forward data are plotted with blue, green and red lines respectively. The frequency varies on the abscissa from 60 kHz to 200 kHz for the signal at $2f_p$ and from 120 kHz to 190 kHz for the signal at f_-

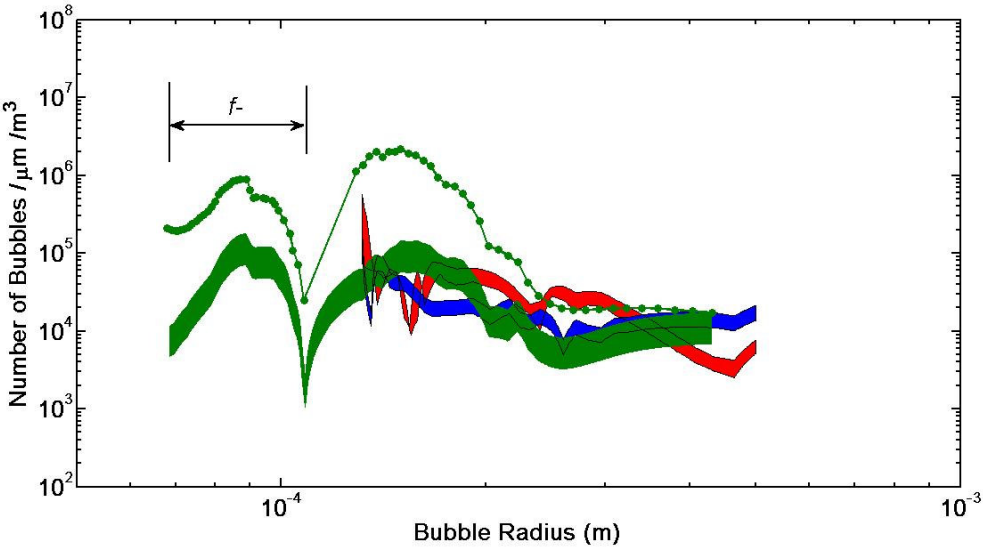

Figure 7.23: Blockplots as in Figure 7.21and Figure 7.17, the dotted green line shows the mean bubble distribution which resulted from inversion of the filtered scattering data, as the green blockplot, taking in addition into account the attenuation of the medium (gassy sediment). The error band that corresponds to this inversion is assumed to be the same with the green band.

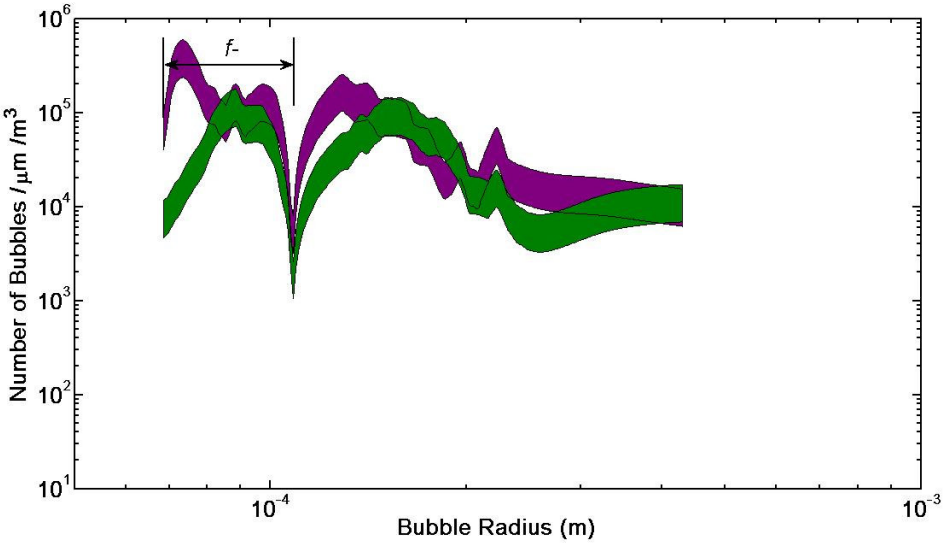

Figure 7.24: Bubble population estimate plotted as number of bubbles per cubic metre per micrometer radius range versus bubble size, as resulted from scattering measurements taken in the Mercury site. The purple curve indicates the bubble population estimate as resulted from inversion of the scattering data from the first patch. The green curve is the bubble population estimate from the second patch. The double sided arrow denotes the proportion of the population which resulted predominantly from inversion of the spectral components at the difference-frequency.

The bubble size distributions which resulted from inversions of scattering data from the two patches at the Mercury site are plotted in Figure 7.24 for comparison. There is an overall agreement of the two curves with their predictions, which suggests that the two patches have approximately the same bubble size distribution. The estimations of these two curves of Figure 7.24, i.e. the green and the purple lines deviate around an order of magnitude for bubble sizes of equilibrium radius between 0.2 mm and 0.3 mm and around two orders of magnitude for bubble sizes of equilibrium radius between 70 and 80 microns. These discrepancies can be attributed to the local character of these measurements. As shown in Figure 7.10 (a) and (b) the sensing volume is at maximum 10^{-4} m^3 and higher the frequency the smaller the sensing volume. In other words the inversion results for the small bubbles are more sensitive to local characteristics of the site than for the bigger bubbles.

Without taking into account the results of the second iteration bubble sizing (purple and green dotted lines in Figure 7.20 and Figure 7.23 respectively), The bubble size distributions computed from scattering data seem to agree better with those computed by inverting the attenuation data from the first hydrophone pair (blue line of Figure 7.17 and Figure 7.21) rather than by inverting attenuation data from the second hydrophone pair (red line of Figure 7.17 and Figure 7.21). This is expected, because the first hydrophone pair covers the depth the scattering sensing volume as opposed to the second pair. However the large uncertainty margins of these predictions obscure the above mentioned trends of the inversion results.

To draw conclusions on these bubble population results, the *statistical mean* bubble size should be considered. As here it was not possible, the mean distributions as measured from scattering measurements, was inserted in the integral equation (7.1) to give the phase speed and attenuation of sound in this bubbly sediment. The results are shown in Figure 7.25 together with the sound speed and attenuation resulted from transmission experiments, i.e. the results of Figure 7.6.

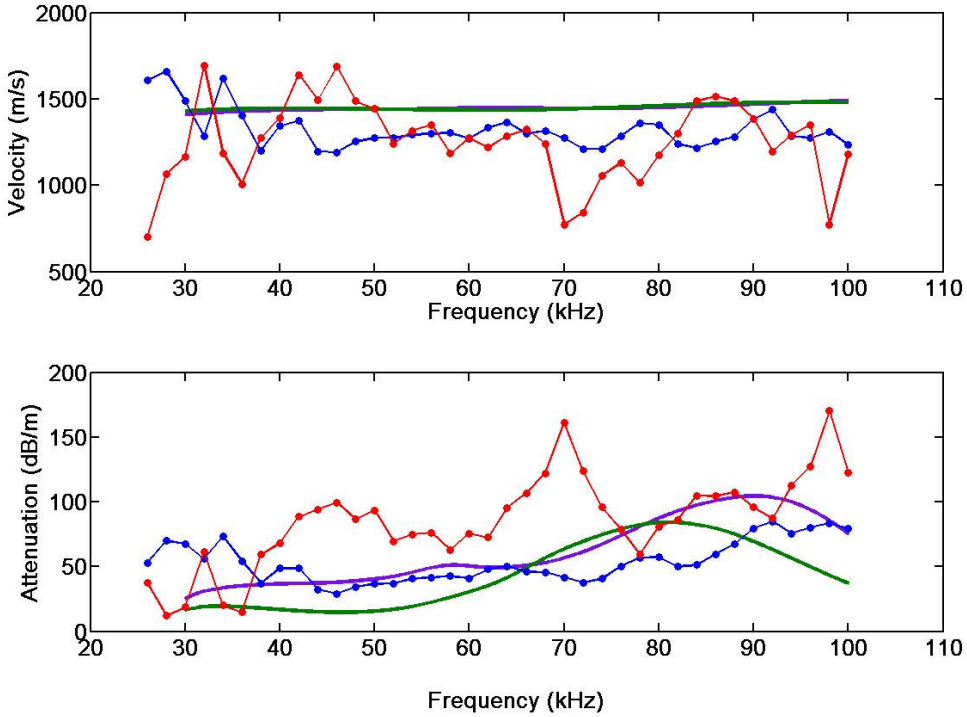

Figure 7.25: Sound speed and attenuation over the frequency range of 26 to 100 kHz as measured at the Mercury site by the hydrophones 1 and 2 (blue lines) and hydrophones 2 and 3 (red lines) of the propagation rig shown in Figure 7.2. The purple and green lines were obtained by inserting the bubble size distributions of the first and the second patch, plotted with the same colours in Figure 7.24 into the forward integral equation for sound propagation in bubbly sediment. The purple and green lines cover the frequency range from 30 kHz to 100 kHz and overlap on their sound speed predictions.

To explain the results of Figure 7.25, it must be recalled that the sound speed and attenuation measured from the two pairs of hydrophones is the overall sound speed and attenuation. That is, scattering from present pebbles and/ or organic matter and change of the sediment bulk properties due to gas in from of cracks are all possible causes of these results. However the sound speed and attenuation curves (purple and green lines) computed from bubble size distributions estimated by the combination frequency technique take into account only the presence of 'acoustically spherical' bubbles estimated from a small volume of the site. As expected, the attenuation measurements from the first hydrophone pair are closer to the results of the forward problem compared to the attenuation measurements from the second hydrophone pair, which was located at a greater depth than the insonification volume of the combination frequency rig (see Figure 7.2 and Figure 7.9). However no linear trend can be assigned to the attenuation as a function of

frequency and therefore, these attenuation curves cannot be extrapolated to lower or higher frequencies. Nevertheless the attenuation curves from the first hydrophone pair and the forward problem agree well for the frequency range of 38 to 70 kHz which corresponds to attenuation from bubbles of equilibrium radius between 340 and 185 microns approximately. This good agreement indicates that these resonant bubble sizes are the main attenuation mechanism for these frequencies at this location. These bubble sizes lie in the range of sand grain sizes whereas the gas-free sediment of the site is mainly silt. In other words these bubbles are about ten times greater than the grain size, as pictured Figure 7.1(b).

Inserting the bubble distributions that resulted from the second iteration (purple and green dotted lines in Figure 7.20 and Figure 7.23 respectively), gave much higher attenuation values (not shown here). This suggests that, given the clear resonances present in the examined patches, this approach overestimates the bubble distributions. The approach of taking into account attenuation is discussed later in this chapter.

7.4.2 Bubble size distributions at the Calshot site

Following the same methods and procedures, bubble populations were inferred from transmission and scattering measurements carried out in the Calshot location. At Calshot three patches were examined but only one had sufficient signal-to-noise ratio to be used for inversions. Additionally for this site only the attenuation data from the second hydrophone pair were used for inversions. The reason was the sandy layer, which was present at the top layer of the seafloor (see section 7.2.1 and Figure 7.5) during the time of the year when the experiments were conducted.

Figure 7.26 shows the bubble population as resulted from inversion of scattering data taken from the only patch examined which exhibited nonlinear resonances (blue line) and from inversion of the attenuation data (red line) as measured from the hydrophones 2 and 3 for the rig shown in Figure 7.2. The raw attenuation data from these measurements are plotted in Figure 7.27 together with the filtered data as inputted in the inversion code (green line) and the forward fitted data (red line).

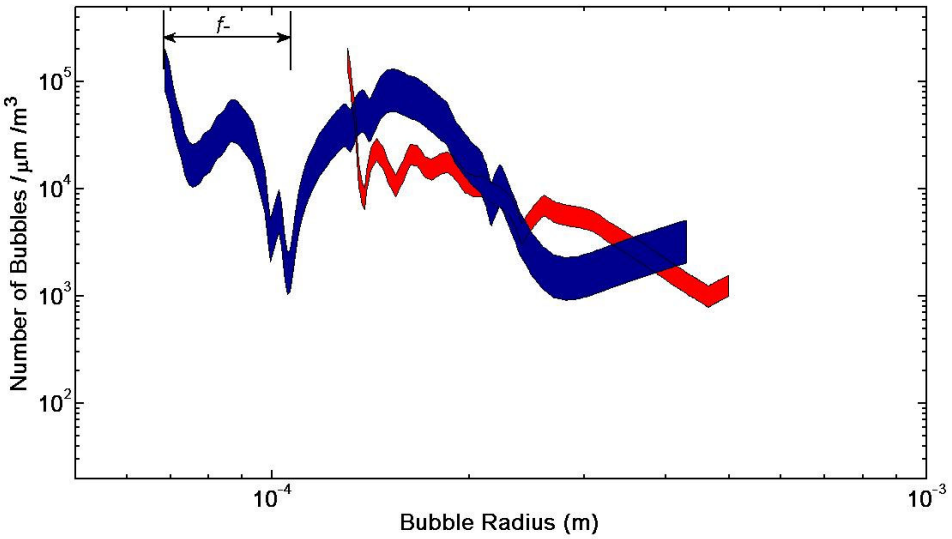

Figure 7.26: Bubble size distribution estimate plotted as number of bubbles per cubic metre per micrometer radius range versus bubble size, as resulted from measurements taken at the Calshot site. The red curve resulted from inversion of the filtered transmission data taken from the second pair of hydrophones as numbered for the rig of Figure 7.2. The blue curve shows the bubble population which resulted from inversion of the (filtered) scattering data from the patch examined at the same site.

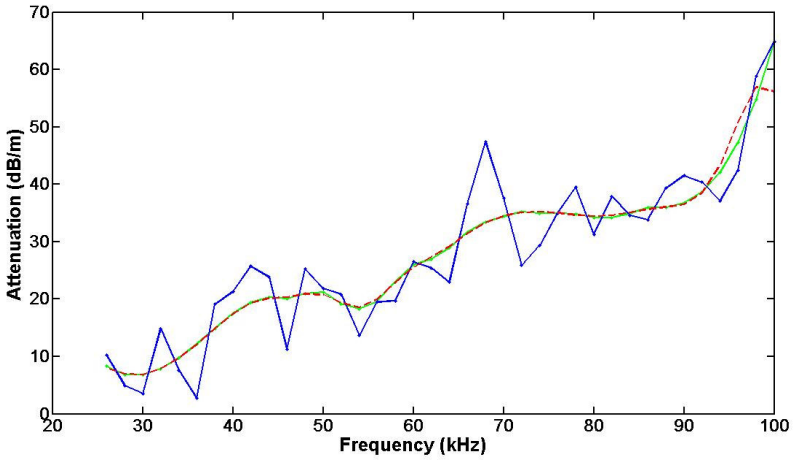

Figure 7.27: Attenuation (dB/m) versus frequency at the mercury site. Raw data (blue line), filtered data (green line) and forward fitted data (red line) versus frequency range from the second hydrophone pair of the propagation rig as numbered in Figure 7.2. The sound speed and the measurement errors which correspond to these raw attenuation data (blue line) are shown in Figure 7.3.

The input information for the inversion using the combination frequency scattering technique is shown in Figure 7.28. As with the other scattering data, the spectral

components at these two sets of frequencies, i.e. at $2f_p$ and f_- is presented as separate curves. The raw measured data are plotted with blue lines, the filtered data with green lines and the forward fitted data with red lines.

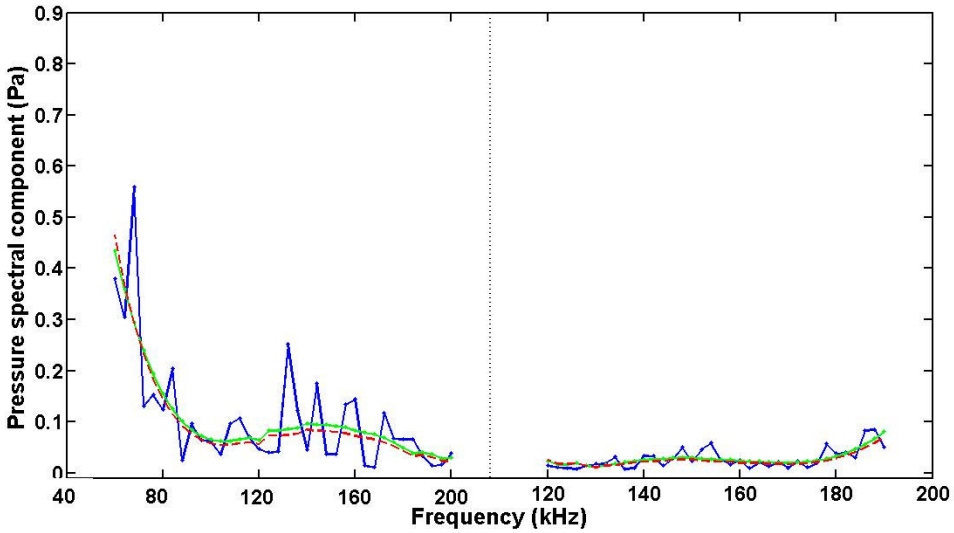

Figure 7.28: Measured pressure spectral components at the patch of the Calshot site. The left hand side of the graph shows the measured spectral component at $2f_p$ and the right hand side of the graph shows corresponding spectral component at f_-. The raw, filtered and forward data are plotted with blue, green and red lines respectively. The frequency varies on the abscissa from 60 kHz to 200 kHz for the signal at $2f_p$ and from 120 kHz to 190 kHz for the signal at f_-

To complete the study, the measured attenuation from the *in situ* propagation measurements is compared to the attenuation stemming from the resonant bubbles as measured from the combination frequency apparatus. The bubble size distribution of Figure 7.26 (blue line) is inputted in the integral equation (7.1) to give the sound speed and attenuation of muddy sediment which contains only 'acoustically spherical' bubbles with the size distribution shown in Figure 7.26 (blue line). The results are shown in Figure 7.29 with blue lines. There is a rather good agreement at the low frequencies but not at the higher ones. This suggests that the combination-frequency apparatus had measured more small bubbles than those encountered at the propagation path of the transmission rig. This could be justified from the local validity of these measurements. However definite conclusions cannot be drawn since the scattering volume and the hydrophone pair were located at different depths. If in spite of this fact, we wish to relate the attenuation with the sphericity of the gas, first we have to relate the frequency range where good agreement of

the attenuation is on the curves of Figure 7.29 with the corresponding bubble sizes. The frequency range from 30 to 68 kHz corresponds to resonant bubble sizes of equilibrium radius between 430 and 190 microns. Comparing these bubble sizes with the expected grain size for the sediment of this site (Table 7.1); shows that the measured bubble sizes have the size of sand grains, hence it may be inferred that these bubbles were trapped in the sandy rather than in the silty parts of the sediment.

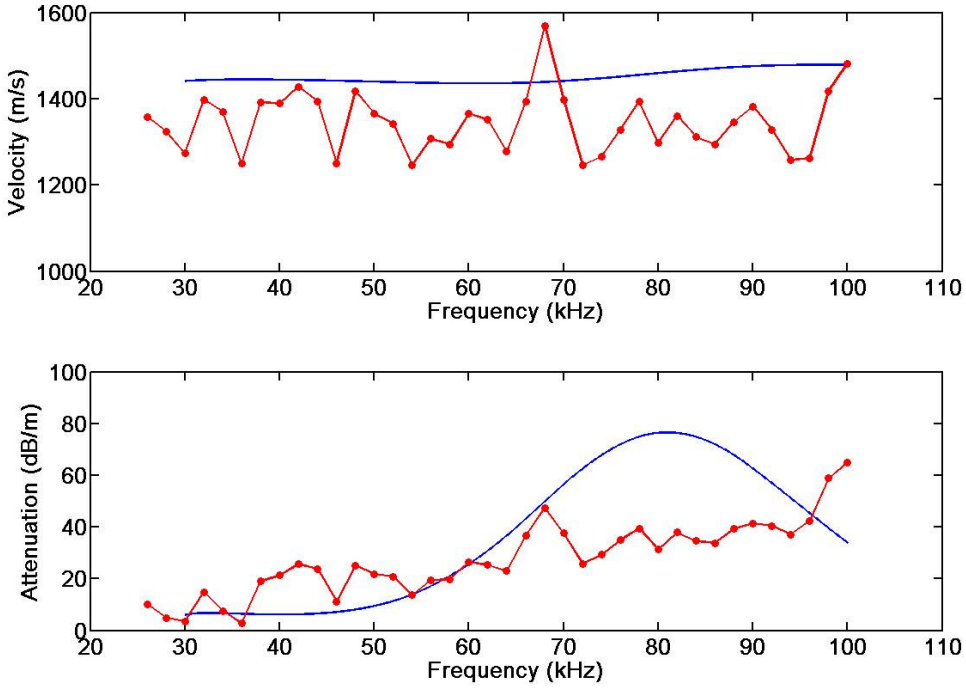

Figure 7.29: Sound speed and attenuation over the frequency range of 26 to 100 kHz as measured at the Calshot site by the second pair of hydrophones (red lines) of the propagation rig shown in Figure 7.2. The blue lines were obtained by inserting the bubble size distribution of the combination frequency scattering experiment into the forward integral equation for sound propagation in bubbly sediment. The forward predicted sound speed and attenuation curves cover the frequency range from 30 kHz to 100 kHz.

As second bubble size distribution was computed taking into account the attenuation of the gassy sediment in exactly the same manner as for the Mercury patches. The results are shown in Figure 7.30. Again here the population resulted from this inversion is much higher than this obtained without taking into account attenuation. However the available attenuation data were originating from a greater depth, where higher attenuation values are observed. Therefore this adjustment is likely to give an overestimated bubble population. Hence a better approach might be to insert in equation (7.1) the *gas-free* attenuation instead of the attenuation of the gassy sediment. Unfortunately degasifying the cores taken

from these patches and conducting propagation measurements was not possible during this PhD work.

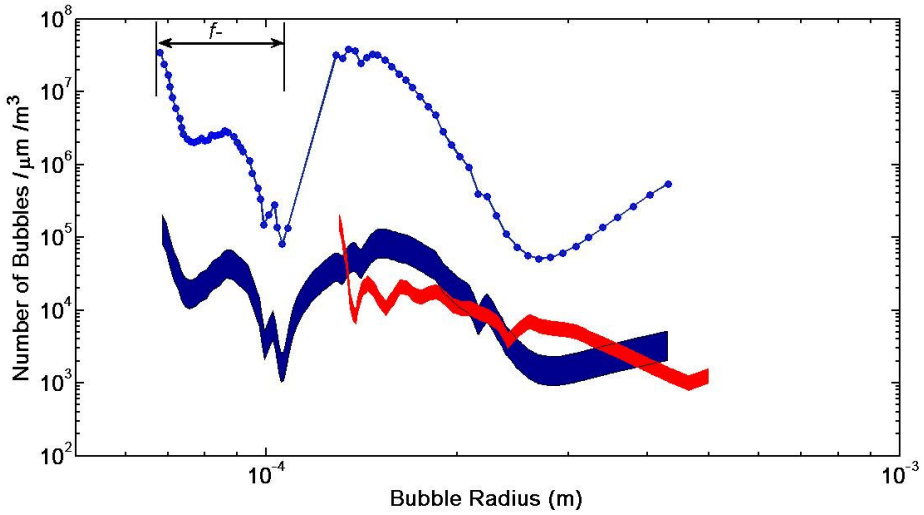

Figure 7.30: Blockplots as in Figure 7.28, the dotted blue line shows the mean bubble distribution which resulted from inversion of the filtered scattering data, as the blue blockplot, taking in addition into account the attenuation of the medium (gassy sediment). The error band that corresponds to this inversion is assumed to be the same with the blue band.

7.5 Summary

This chapter has described the application of the combination frequency technique for bubble counting in intertidal sediments. Existing approaches of modelling the acoustic effects of bubbles in sediments have been discussed and the advantages of applying a viscoelastic bubble dynamics model to sediments were outlined. It was explained how such a model can be applied to sediments and what parameters need to be estimated or taken from the literature. This model was used to interpret nonlinear resonant scattering measurements into bubble size distributions. Additionally these bubble size distributions were inserted into the forward problem, i.e. into the complex sound speed integral equation. The results gave the speed and the attenuation of sound as function of frequency under the assumption that only these resonant bubbles were present in the sediment.

Knowing that (a) gas in sediment may exist in form other than 'acoustically spherical' bubbles and (b) only resonant bubbles produce nonlinear scattering, some conclusions were drawn on the gas shape of bubbles by comparing *in situ* measured attenuation with

the attenuation originating only from resonant bubbles using the bubble distributions measured with the combination frequency rig. However the datasets were not enough to draw statistically meaningful conclusions and to quantify the results. It was attempted to estimate mean value by applying least squares fitting (Savinsky-Golay filtering) to the acquired data. Additionally it was attempted to take into account the attenuation of the transmitted and received waves by accounting for the attenuation of gassy sediment using measured values for K_{P}. Results showed that this approach overestimated the bubble population.

Using qualitative experimental results and observations, it is concluded that gas formations with size comparable to the grain size are almost all in the form of 'acoustically spherical' bubbles. The sound speed and attenuation results do not show a clear trend as function of the frequency for the gassy patches where experiments were conducted. Thus it was not possible to find a relationship between frequency and attenuation. Such a relationship might have allowed comparison between the literature results and the findings of this work.

.

Chapter 8: Conclusions and suggestions for future work

The theory and experiments presented in this thesis deal with the development of a new nonlinear inversion method for estimation of the size distribution applicable to gas bubbles in water and to 'acoustically spherical' bubbles in marine sediments. This method aimed to use the cooperative nonlinear scattered component at the difference frequency and twice the pump frequency from bubbles when insonified with two frequencies.

The method was applied first in bubbly water and the results were compared with those from a well-established linear method. Comparison of the two methods suggests that the new method has the potential to predict correctly the bubble size distribution in fluid media. However the frequencies chosen for the pump and the imaging frequencies resulted into a very limited prediction range of bubble sizes in water. These frequencies were deemed suitable for bubble sizing in sediments and were used for water in order to keep the experimental approach the exactly same for the two media. For populations measured in water, the majority of the population was predicted from the nonlinear component at twice the pump frequency, which is by good approximation independent of the presence of the second frequency. This observation suggests that this method would be simpler to apply if only the nonlinear scattered component at twice the pump frequency were used. Indeed the nonlinear component at twice the pump frequency can be uniquely related to bubble size as opposed to the component at the difference frequency which originates from bubbles resonant at the pump as well as the difference frequency. Additionally the scattering matrix corresponding to f_{2p} is well conditioned as opposed to the scattering matrix corresponding to f_{-}. So the inversion matrix which is composed by these two matrices becomes also ill conditioned and a suitable regularisation scheme had to be applied in order to retrieve the bubble population. The regularisation scheme used in this work succeeded in finding a positive bubble population with the minimum error, however it was not optimised for smoothness and large dips occurred in the bubble distribution curves. These dips occurred at the end of bubble size range, which predominantly originates from the difference frequency data.

To summarise the advantage of using two frequencies is that it is beneficial because more bubble sizes can be detected using the same devices. However the three disadvantages are: 1) complicated common sensing volume calculations because of the presence of three beams, 2) ill-conditioned scattering matrix and 3) signals at the difference frequency with low signal to noise ratio. Following these observations, it appears that using only the nonlinear scattered component at twice the insonification frequency has the potential to produce correct results with less complicated experimental and computational procedure.

The above mentioned drawbacks and suggestions are also valid for application of this bubble sizing technique using f_{2p} and f_{-} to sediments. However application to sediments brings about additional complications. Firstly the frequencies must be carefully chosen. Study of the bubble dynamics models showed that the range of the bubble sizes that may be predicted using an acoustic method depends on the frequency choice and the medium properties which determine the natural frequencies of the bubbles. For bubbles in muddy marine sediments, the gass-free mud shear modulus determines mainly the bubble resonant frequency. Thus the shear modulus of the background medium should be found (experimentally or based on literature data) in order to choose the right frequency range, which is not a trivial task.

The sediments examined in this work and the choice of insonification frequency range, resulted in a difference frequency covering a very narrow bandwidth of the bubble sizes whilst the greater part was covered from the nonlinear component at twice the pump frequency. The bubble sizes covered with both the linear and the nonlinear inversion methods were those comparable with the grain size of the gas-free sediment, approximately ten times larger. Such sizes are by definition ‘acoustically spherical’ for the frequency range used in this PhD work. The results from these methods for ‘acoustically spherical’ bubbles were tested in bubbly water and were in a good agreement, which proved the efficacy of the new method for such bubbles. However in marine sediment the possibility of ‘non-acoustically spherical’ bubbles to be present is a major issue for application of this nonlinear bubble sizing technique without parallel use of transmission measurement. One way to estimate the ‘non-acoustically spherical’ gas is to take both transmission and scattering measurement and to compare them having *additional* information about the attenuation of the background medium, i.e. the attenuation that

corresponds to the gas-free counterpart of the sediment. This requirement of knowing the attenuation of the background medium poses substantial difficulties. One has to take cores, inspect the sediment of the site and then either make measurements using the degasified sediment or resort to literature values for gas-free sediments of comparable type with the type of sediment present in the gassy site under investigation. Having this information, the bubble populations resulted from transmission and scattering measurements can be compared. If both predictions are the same then the site contains only 'acoustically-spherical' bubbles. If they differ, then their difference represents the gas in 'non-acoustically-spherical' bubbles. This is a rather convoluted method, however currently no other method exists to infer gas content in sediments using acoustic methods; which is valuable information for geophysical explorations and other sea operations that require knowledge of the seafloor composition.

Bibliography

Abegg, F., and Anderson, A. L. (**1997**). "The acoustic turbid layer in muddy sediments of Eckernforde Bay, Western Baltic: methane concentration, saturation and bubble characteristics," Marine Geology **137**, 137-147.

Abousleiman, Y., Cheng, A. H. D., C.Jiang, and Roegiers, J. C. (**1996**). "Poroviscoelastic analisis of borehole and Cylinder problems," Acta Mechanica **119**, 199-219.

Ainslie, M. A., and Leighton, T. G. (**2009**). "Near resonant bubble acoustic cross-section corrections, including examples from oceanography, volcanology, and biomedical ultrasound," J. Acoust. Soc. Am. **126**, 2163-2175.

Allen, J. R. L. (**1992**). *Principles of Physical Sendimentology* (Chapman & Hall).

Anderson, A. L., Abegg, F., Hawkins, J. A., Duncan, M. E., and Lyons, A. P. (**1998**). "Bubble populations and acoustic interaction with the gassy floor of Eckernforde Bay," Continental Shelf Research **18**, 1807-1838.

Anderson, A. L., and Hampton, L. D. (**1980a**). "Acoustics of gas-bearing sediments I. Background," J. Acoust. Soc. Am. **67**, 1865-1889.

Anderson, A. L., and Hampton, L. D. (**1980b**). "Acoustics of gas-bearing sediments II.Measurements and models," J. Acoust. Soc. Am. **67**, 1890-1903.

Anderson, V. C. (**1950**). "Sound scattering from a fluid sphere," J. Acoust. Soc. Am. **22**, 426-431.

Andreeva, I. B. (**1964**). "Scattering of sound by air bladders of fish in deep sound-scattering ocean layers," Sov. Phys.Acoust. **10**, 17-20.

Asada, T., Watanabe, Y., and Urabe, Y. (**1990**). "Control of parametric amplification using the nonlinear vibration of bubbles under water.," Jpn.J. Appl. Phys **29**, 74-76.
Backus, M. M. (**1959**). "Water reverberations- their nature and elimination," Geophysics **24**, 233-261.

Bear, J. (**1972**). *Dynamics of Fluids in Porous Media* (American Elsevier, Haifa).

Berryman, J. G. (**1980**). "Confirmation of Biot's theory," Appl. Phys.Lett **37**, 382-384.

Best, A. I., Huggett, Q. J., and Harris, A. J. K. (**2001**). "Comparison of in situ and laboratory acoustic measurementson Lough Hyne marine sediments," J. Acoust. Soc. Am. **110**, 695-709.

Best, A. I., McCann, C., and Sothcott, J. (**1994**). "The relationships beteween the velocities, attenuations and petrophysical properties of reservoir sedimentary rocks," Geophysical Prospecting **42**, 151-178.

Best, A. I., Tuffin, M. D. J., Dix, J. K., and Bull, J. M. (**2004**). "Tidal height and frequency dependance of acoustic velocity and attenuatiomn in shallow gassy marine sediments," J. Geophys. Res. **109**.

Biot, M. A. (**1956a**). "Theory of propagation of elastic waves in a fluid saturated porous solid, I. Low frequency range," J. Acoust. Soc. Am. **28**, 168-178.

Biot, M. A. (**1956b**). "Theory of propagation of elastic waves in a fluid saturated porous solid, II. High frequency range," J. Acoust. Soc. Am. **28**, 179-191.

Biran, A., and Breiner, M. (**1999**). *Matlab 5 for engineers* (Addison-Wesley).

Boudreau, B. P., Algar, C., Johnson, B. D., Croudace, I., Reed, A., Furukawa, Y., Dorgan, K. M., Jumars, P. A., Grader, A. S., and Gardiner, B. S. (**2005**). "Bubble growth and rise in soft sediments," Geology **33**, 517-520.

Boudreau, B. P., and Maysman, F. J. R. (**2006**). "Predicted tortuosity of muds," Geology **34**, 693-696.

Bowles, F. A. (**1997**). "Observations on attenuation and shear-wave velocity in fine-grained marine sediments," J. Acoust. Soc. Am. **101** 3385-3397.

Boyle, F. A., and Chotiros, N. P. (**1995a**). "A model for acoustic backscatter from muddy sediments," J. Acoust. Soc. Am. **98**, 525-530.

Boyle, F. A., and Chotiros, N. P. (**1995b**). "A model for high-frequency acoustic backscatter from gas bubbles in sandy sediments at shallow grazing angles," J. Acoust. Soc. Am. **98**, 531-541.

Boyle, F. A., and Chotiros, N. P. (**1998**). "Nonlinear acoustic scattering from a gassy poroelastic seabed," J. Acoust. Soc. Am. **103**, 1328-1336.

Brennan, B. J., and D.E.Smylie (**1981**). "Linear Viscoelasticity and Dispersion in Seismic Wave propagation," Reviews of Geophysics ans Space Physics **19**, 233-246.

Brunson, B. A., and Johnson, R. K. (**1980**). "Laboratory measurements of shear wave attenuation in saturated sand," J. Acoust. Soc. Am. **68**, 1371–1375.

Buchanan, J. L. (**2006**). "A comparison of broandband models for sand sediments," J. Acoust. Soc. Am **120**, 3584-3598.

Buckingham, M. J. (**2000**). "Wave propagation, stress relaxation, and grain-tograin shearing in saturated, unconsolidated marine sediments," J. Acoust. Soc. Am. **108**, 2796–2815.

Buckingham, M. J. (**2010**). "Response to “Comments on ‘Pore fluid viscosity and the wave properties of saturated granular materials including marine sediments [J. Acoust. Soc. Am. 127, 2095–2098 (2010)]’ ”," J. Acoust. Soc. Am. **127**, 2099-2102.

Buckingham, M. J., and Richardson, M. D. (**2002**). "On Tone-Burst Measurements of Sound Speed and Attenuation in Sandy Marine Sediments," IEEE J. Ocean. Eng. **27** 429-453.

Burdic, W. S. (**1984**). *Underwater acoustic system analysis* (Prentice-Hall).

Caiti, A., Akal, T., and Stoll, R. D. (**1994**). "Estimation of Shear Wave Velocity in Shallow Marine Sediments," IEEE J. Ocean. Eng. **19**, 58-72.

Cartensen, E. L., and Foldy, L. L. (**1947**). "Propagation of Sound Through a Liquid Containing Bubbles," J. Acoust. Soc. Am. **19**, 481-501.

Chotiros, N. P., and Isakson, M. J. (**2010**). "Comments on "On pore fluid viscosity and the wave properties of saturated granular materials including marine sediments "[J. Acoust. Soc. Am. 122, 1486–1501 (2007)]," J. Acoust. Soc. Am. **127**, 2095-2098.

Church, C. C. (**1995**). "The effects of an elastic solid surface layer on the radial pulsations of gas bubbles," J. Acoust. Soc. Am. **97**, 1510-1521.

Clarke, J. W. L., and Leighton, T. G. (**2000**). "A method for estimating time-dependent acoustic cross-sections of bubbles and bubble clouds prior to the steady state," J. Acoust. Soc. Am. **107**, 1922-1929.

Clay, C. S., and Medwin, H. (**1977**). *Acoustical oceanography : principles and applications* (New York : Wiley).

Claypool, G. E., and Kaplan, I. R. (**1974**). "The origin and distribution of methane in marine sediments," in *Natural Gases in Marine Sediments*, edited by I. R. Kaplan (Plenum, New York), pp. 99–139.

Clift, R., J.R.Grace, and M.E.Weber (**1978**). *Bubbles, Drops and Particles* (Academic Press, London, UK).

Coles, D. G. H. (**2009**). "Measurements of Sub-Surface Bubble Populations and the Modelling of Air-Sea Gas flux," *PhD report ISVR* (University of Southampton).

Coles, D. G. H., and Leighton, T. G. (**2007**). "Autonomous spar-buoy measurements of bubble populations under breaking waves in the Sea of the Hebrides.," in *Proceedings of the Second International Conference on Underwater Acoustic Measurements, Technologies and Results* (Heraklion, Crete), pp. 543-548.

Commander, K., and McDonald, R. J. (**1991**). "Finite-element solution of the inverse problem in bubble swarm acoustics," J. Acoust. Soc. Am. **89**, 592-597.

Commander, K., and Moritz, E. (**1989**). "Off-resonance contributions to acoustical bubble spectra," J. Acoust. Soc. Am. **85**, 2665-2669.

Commander, K. W., and Prosperetti, A. (**1989**). "Linear pressure waves in bubbly liquids: Comparison betweentheory and experiments," J. Acoust. Soc. Am. **85**, 732-746.

Courtney, R. C., and Mayer, L. (**1993**). "Acoustic properties of fine-grained sediments from Emerald Basin: Toward an inversion for physical properties using Biot-Stoll model.," J. Acoust. Soc. Am. **93**, 3193-3200.

Devin, C. (**1959**). "Survey of Thermal, Radiation, and Viscous Damping of Pulsating Air Bubbles in Water," J. Acoust. Soc. Am. **31**, 1654-1667.

Duffy, S. M., Wheeler, S. J., and Bennell, J. D. (**1994**). "Shear modulus of kaolin containing methane bubbles," J. Geotech. Eng. **120**, 781-796.

Duraiswami, R., Prabhukumar, S., and Chahine, G. L. (**1998**). "Bubble counting using an inverse acoustic scattering method," J. Acoust. Soc. Am. **104**, 2699-2717.

Dvorkin, J., Nolen-Hoeksema, R., and Nur, A. (**1994**). "The squirt-flow mechanism: Macroscopic description," Geophysics **59**, 428-438.

Dvorkin, J., and Nur, A. (**1993**). "Dynamic poroelasticity: A unified model with the squirt and the Biot mechanisms," Geophysics **58**, 524-532.

Eller, A., and Finn, H. (**1969**). "Generation of Subharmonics of Order One-Half by Bubbles in a Sound Field," J. Acoust. Soc. Am. **46**, 722-727.

Eller, A. I. (**1970**). "Damping Constants of Pulsating Bubbles," J. Acoust. Soc. Am. **47**, 1469-1470.

Ferry, J. D. (**1980**). *Viscoelastic properties of polymers* (New York : John Wiley & Sons).

Feuillade, C., and Werby, M. (**1994**). "Resonances of deformed gas bubbles in liquids," J. Acoust. Soc. Am. **96**, 3684-3692

Fleischer, P., Orsi, T. H., and Richardson, M. D. (**2001**). "Distribution of free gas in marine sediments: a global overview," Geo-Marine Letters **21**, 103-122.

Flemming, B. W. (**2000**). "A revised textural classification of gravel-free muddy sediments on the basis of ternary diagrams," Continental Shelf Research **20**, 1125-1137.

Foldy, L. L. (**1945**). "Multiple scattering of waves," Physical Review **67**, 107-119.

Forsberg, F., Merton, D. A., Liu, J. B., Needleman, L., and Goldberg, B. B. (**1998**). "Clinical applications of ultrasound contrast agents," Ultrasonics **36**, 695- 701.

Forsythe, G., Malcolm, M., and Moler, C. (**1977**). *Computer Methods for Mathematical Computations* (Prentice Hall).

Fu, S. S., Wilkens, R. H., and Frazer, L. N. (**1996**). "In situ velosity profiles in gassy sediments: Kiel Bay," Geo-Marine Letters **16**, 249-253.

Futterman, W. I. (**1962**). "Dispersive body waves," J. Geophys. Res. **67**, 5279-5291.

Gardner, T. (**2003**). "Modeling signal loss in surficial marine sediments containing occluded gas," J. Acoust. Soc. Am. **113**, 1368-1378.

Gardner, T. N., and Sills, G. C. (**2001**). "An examination of the parameters that govern the acoustic behavior of sea bed sediments containing gas bubbles," J. Acoust. Soc. Am. **110**, 1878- 1889.

Gassmann, F. (**1951**). "Über die Elastizität poröser Medien," Vierteljahrsschrift der Naturforschenden Gesellschaft in Zürich **96**, 1-23.

Gaunaurd, G. C., and Uberall, H. M. (**1981**). "Effective Properties of Perforated Solids, Including Effects of Ultrasonic Resonances," Ultrasonics Symposium, 469-473.

Geyer, R. A. (**1983**). *Handbook of Geophysical Exploration at Sea* (CRC Press).

Golubitsky, M., and Deliniz, M. (**1999**). *Linear algebra and differential equations using MATLAB* (Cole Publications, California).

Hamilton, E. L. (**1970**). "Sound velocity and related properties of marine sediments, North Pacific," J. Geophys. Res. **75**, 4423-4446.

Hamilton, E. L. (**1971**). "Elastic Properties of Marine Sediments," J.Geophys. Res **76**, 579-604.

Hamilton, E. L. (**1972**). "Compressional-wave attenuation in marine sediments," Geophysics **37**, 620-646.

Hamilton, E. L. (**1976**). "Attenuation of shear waves in marine sediments," J. Acoust. Soc. Am. **60**, 334-338.

Hamilton, E. L. (**1980**). "Geoacoustic modeling of the sea floor," J. Acoust. Soc. Am. **68**, 1313-1339.

Hamilton, E. L., and Bachman, R. T. (**1982**). "Sound velocity and related properties of marine sediments," J. Acoust. Soc. Am. **72**, 1891-1904.

Hamilton, E. L., Bucker, H. P., Keir, D. L., and Whitney, J. A. (**1970**). "Velocities of Compressional and Shear Waves in Marine Sediments Determined In Situ from a Research Submersible," J. Geophys. Res. **75**, 4039-4049.

Hamilton, E. L., G.Shumway, Menard, H. W., and C.J.Shipek (**1956**). "Acoustics and Other Physical Properties of Shallow-Water Sediments off San Diego," J. Acoust. Soc. Am. **28**, 1-15.

Hashiba, K., and Masuzawa, H. (**2003**). "Effect of Micro-Bubbles in water. ," Jpn. J.Appl. Phys. **42**, 3227-3232.

Hay, A. E., and Burling, R. W. (**1982**). "On sound scattering and attenuation in suspensions with marine applications," J. Acoust. Soc. Am. **72**, 950-959.

Henyey, F. S. (**1999**). "Corrections to Foldy's effective medium theory for propagation in bubble clouds and other collections of very small scatterers," J. Acoust. Soc. Am. **105**, 2149-2154.

Herrin, D. W., and Wu, T. W. (**2000**). "Case study evaluation of the Rayleigh integral " J. Acoust. Soc. Am. **108**, 2451-2451.

Herring, C. (**1941**). "Theory of pulsations of the gas bubble produced by underwater explosion," in *OSRD No 236*.

Hovem, J.M., **(1976)**. "Viscous attenuation of sound in saturated sand " J. Acoust. Soc. Am. **66**, 1807-1812.

Isimaru, A. (**1978**). *Wave Propagation and Scattering in Random Media* (Academic Press, , London, UK).

Jiang, Y., and Chapman, N. R. (**2010**). "Measurement of Low-Frequency Sound Attenuation in Marine Sediment," IEEE J. Ocean. Eng. **35**, 70-78.

Johnson, D. L., and Plona, T. J. (**1982**). "Acoustic slow waves and the consolidation transition," J. Acoust. Soc. Am. **72**, 556-565.

Judd, A. G. (**2004**). "Natural seabed gas seeps as sources of atmospheric methane," Environmental Geology **46**, 988-996.

Judd, A. G., and Hovland, M. (**1992**). "The evidence of shallow gas in marine sediments " Continental Shelf Research **12**, 1081-1095.

Judd, A. G., Hovland, M., Dimitrov, L. I., Gil, S. G., and Jukes, V. (**2002**). "The geological methane budget at Continental Margins and its influence on climate change.," Geofluids **2**, 109-126.

Juel, T. J. (**1997**). "Chaotic Vibrations," in *Vibrations and stability order and chaos*, edited by The technical university of Denmark (McGraw Hill).

Jumikis, A. R. (**1977**). *Thermal geotechnics* (Rutgers University Press, New Jersey).

Junger, M. C. (**1981**). "Dilatational waves in an elastic solid containing lined, gas filled spherical cavities," J. Acoust. Soc. Am. **69**, 1573-1576.

Kamath, V., and Prosperetti, A. (**1989**). "Numerical integration methods in gas-bubble dynamics," J. Acoust.Soc. Am. **85**, 1538-1548.

Kargl, S. (**2002**). "Effective medium approach to linear acoustics in bubbly liquids," J. Acoust. Soc. Am. **111**, 168-173.

Kaye, G. W. C., and Laby, T. H. (**1972**). *Tables of Physical and Chemical Constants and some mathematical functions* (Longman University Press).

Keller, J., and Kolonder, I. (**1956**). "Damping of Underwater Explosion Bubble Oscillations," J. Appl. Phys. **27**, 1152-1161.

Keller, J. B., and Miksis, M. (**1980**). "Bubble oscillations of large amplitude," J. Acoust. Soc. Am. **68**, 628-633.

Kibblewhite, A. C. (**1989**). "Attenuation of sound in marine sediments: A review with emphasis on new low-frequency data," J. Acoust. Soc. Am. **86**, 716-738.

Kimura, M. (**2007**). "Study on the Biot-Stoll model for porous marine sediments," Acoust. Sci. & Tech. **28**, 230-243.

Kinsler, L., Frey, A., Coppens, A., and Sanders, J. (**1999**). *Foundamentals of acoustics* (John Wiley & Sons).

Kjartansson, E. (**1979**). "Constant Q-wave propagation and attenuation," J. Geophys. Res. **84**, 4737-4748.

Klusek, Z., Sutin, A., Matveev, A., and Potapov, A. (**1995**). "Observation of nonlinear scattering of acoustical waves at sea sediments," Acoustical Letters **18**, 198-203.

Koller, D., Li, Y., Shankar, P. M., and Newhouse, V. L. (**1992**). "High-speed bubble sizing using the double frequency technique for oceanographic applications. ," IEEE Journal of Ocean Engineering **17**, 288-291.

Kolsky, H. (**1953**). *Stress Waves in Solids* (Oxford University Press).

Kudo, K., and Shima, E. (**1970**). "Attenuation of shear waves in soil," Bull. Earthquake Res. Inst. Univ. Tokyo **48**, 145-158.

Landau, L. D., and Lifshitz, E. M. (**1959**). *Fluid Mechanics* (Pergamon Press).

Lauterborn, W. (**1976**). "Numerical investigation of nonlinear oscillations of gas bubbles in liquids," J. Acoust. Soc. Am. **59**, 283-293.

Lauterborn, W., and Parlitz, U. (**1988**). "Methods of chaos physics and their application to acoustics," J. Acoust. Soc. Am. **84**, 1975-1993.

Lax, M. (**1951**). "Multiple Scattering of Waves," Reviews of Modern Physics **23**, 287-310.

Leighton, T. G. (**1994**). *The Acoustic Bubble* (Academic Press, London, UK).

Leighton, T. G. (**2007**). "Theory for acoustic propagation in marine sediment containing gas bubbles which may pulsate in a non-stationary nonlinear manner," Geophysical Research Letters **34**.

Leighton, T. G. (**2008a**). "The Rayleigh-Plesset equation in terms of volume with explicit shear losses," Ultrasonics **48**, 85-90.

Leighton, T. G., Mantouka, A., White, P., and Klusek, Z. (**2008b**). "Towards field measurements of populations of methane gas bubbles in marine sediment: An inversion method required for interpreting two-frequency insonification data from sediment containing gas bubbles," Hydroacoustics **11**, 203-224.

Leighton, T. G., Meers, S. D., and White, P. R. (**2004**). "Propagation through nonlinear timedependent bubble clouds and the estimation of bubble populations from measured acoustic characteristics.," Proceedings of the Royal Society **460**, 2521-2550.

Leighton, T. G., and Robb, G. B. N. (**2008b**). "Preliminary mapping of void fractions and sound speeds in gassy marine sediments from subbotom profiles," J. Acoust. Soc. Am. EL313-EL320 **124**, 313-320.

Leurera, K. C., and Brown, C. (**2008**). "Acoustics of marine sediment under compaction: Binary grain-size model and viscoelastic extension of Biot's theory," J. Acoust. Soc. Am. **123,** 1941–1951.

Linz, P., and Wang, R. L. C. (**2003**). *Exploring numerical methods* (Jones and Bartlett publishers).

Lockwood, J. C., and Willette, J. G. (**1973**). "High-speed method for computing the exact solution for the pressure variations in the nearfield of a baffled piston," J. Acoust. Soc. Am. **53**, 735-741.

Lyons, A. P., Duncan, M. E., Anderson, A. L., and Hawkins, J. A. (**1996**). "Predictions of the acoustic scattering response of free-methane bubbles in muddy sediments," J. Acoust. Soc. Am. **99**, 163-171.

MacDonald, C. A., Sboros, V., Gomatam, J., Pye, S. D., Moran, C. M., and McDicken, W. N. (**2004**). "A numerical investigation of the resonance of gas-filled microbubbles: resonance dependence on acoustic pressure amplitude," Ultrasonics **43**, 113-122.

Maksimov, A. (**1997**). "On the subharmonic emission of gas bubbles under two-frequency excitation," Ultrasonics **35**, 79-85.

Maksimov, A., and Sosedko, E. V. (**2000**). "Anomalous Bubble Response to Low Frequency Modulation of Driving Pressure," *In Proc. 2nd Intern. Conf. Control of Oscillations and Chaos* (eds F.L. Chernousko, A.L. Fradkov) Proc. SPIE V. 3, Washington, pp. 548-551.

Marketos, G., and Best, A. I. (**2010**). "Application of the BISQ model to clay squirt flow in reservoir sandstones," J.Geophys. Res. **115**.

Martens, C., and Berner, R. A. (**1974**). "Methane Production in the Interstitial Waters of Sulfate-Depleted Marine Sediments " Science **185**, 1167-1169.

Martens, C. S., Albert, D. B., and Alperin, M. J. (**1998**). "Biogeochemical processes controlling methane in gassy coastal sediments-Part 1. A model coupling organic matter fux to gas production, oxidation and transport," Continental Shelf Research **18**, 1741-1770.

Mavko, G., Mukerji, T., and Dvorkin, J. (**1998**). *The rock physics handbook: tools for seismic analysis in porous media.* (Cambridge).

McAnally, W. H., Friedrichs;, C., Hamilton;, D., Hayter, E., Shrestha;, P., Rodriguez;, H., Sheremet;, A., and Teeter, A. (**2007**). "Management of Fluid Mud in Estuaries, Bays, and Lakes I: Present State of Understanding on Character and Behavior," J. Hydraulic. Eng., 9-22.

McLeroy, E. G., and DeLorach, A. (**1968**). "Sound Speed and Attenuation, from 15 to 1500 kHz Measured in Natural Sea-Floor Sediments," J. Acoust. Soc. Am. **44**, 1148-1150.

Mechalas, B. J. (**1974**). "Pathways and environmental requirements for biogenic gas production in the ocean," in *Natural Gases in Marine Sediments*, edited by I. R. Kaplan (Plenum, New York), 11-25.

Medwin, H. (**1977**). "Counting Bubbles acoustically: a review," Ultrasonics **15**, 7-13.

Medwin, H. (**2005**). *Sounds in the Sea, From Ocean Acoustics to Acoustical Oceanography.* (Cambridge University Press).

Medwin, H., and Clay, C. S. (**1998**). *Fundamentals of Acoustical Oceanography* (Academic Press, London, UK).

Meers, S. D. (**2005**). "The estimation of bubble populations in the surf-zone by inversion of acoustic propagation," in *ISVR* (Southampton).

Michaelides, E. E. (**2006**). *Particles, Bubbles & Drops Their Motion, Heat and Mass Transfer* (World Scientific Publishing).

Miksis, M. J., and Ting, L. (**1987**). "A numerical study of thermal effects on nonlinear bubble oscillations," J. Acoust. Soc. Am. **81**, 1331-1340.

Miller, D. (**1981**). "Ultrasonic detection of resonant cavitation bubbles in a flow tube by their second-harmonic emissions," Ultrasonics, 217-223.

Morse, P. M., and Feshbach, H. (**1953**). *Methods of theoretical physics* (McGraw-Hill).

Muir, T. G., Akal, T., Richardson, M. D., Stoll, R. D., Caiti, A., and Hovem, J. M. (**1991**). "Comparison of techniques for shear wave velocity and attenuation measurements," in in Shear Waves in Marine Sediments, edited by J. M. Hovem, M. D. Richardson and R. D. Stoll (Kluwer, Dordrecht), pp. 283-294.

Nayfeh and Hasan (**1933**). *Nonlinear oscillations* (Willey, New York).

Newhouse, V. L., and Shankar, P. M. (**1984**). "Bubble size measurements using the nonlinear mixing of two frequencies," J. Acoust. Soc. Am. **75**, 1473-1477.

Nishi, R. Y. (**1975**). "The scattering and absorptionof sound waves by a gas bubble in a viscous liquid," Acustica **33**, 65-74.

Olowofela, J. A., and Adegoke, J. A. (**2004**). "Modelling effective rheologies for viscoelastic porous media with application to silt and medium and croase sand," J.Geophys. Eng. **1**, 240-243.

Orfanides, S. J. (**1996**). *Introduction to signal processing* (Prentice-Hall).

Ostrovsky, L. A., Sutin, A.M., Soustova, I.A., Matveyev, A. L., Potapov, A. I. and Kluzek, Z. (**2003**). "Nonlinear scattering of acoustic waves by natural and artificially generated subsurface bubble layers in sea," J. Acoust. Soc. Am. **113**, 741-749.

Parlitz, U., Englisch, V., Scheffczyka, C., and Lauterborn, W. (**1990**). "Bifurcation structure of bubble oscillators," J. Acoust. Soc. Am. **88**, 1061-1077.

Parra, J. O. (**1997**). "The transversely isotropic poroelastic wave equation including the Biot and the squirt mechanisms:Theory and application," Geophysics **62**, 309-318.

Phelps, A. D., and Leighton, T. G. (**1997**). "The Subharmonic Oscillations and Combination-Frequency Subharmonic Emissions from a Resonant Bubble: Their Properties and Generation Mechanisms," Acustica **83**, 59-66.

Phelps, A. D., and Leighton, T. G. (**1998**). "Oceanic bubble population measurements using a buoy-deployed combination frequency technique," IEEE J. Oceanic Eng. **23**, 400-410.

Prosperetti, A. (**1974**). "Nonliner oscillations of gas bubbles in liquids: steady-state solutions," J. Acoust. Soc. Am. **56**, 878-885.

Prosperetti, A. (**1976**). "Subharmonics and ultraharmonics in the forced oscillations of weakly nonlinear systems," J. Acoust. Soc. Am. **44**, 548-554.

Prosperetti, A. (**1977a**). "Application of the subharmonic threshold to the measurement of the damping of oscillating gas bubbles," J. Acoust. Soc. Am. **61**, 11-16.

Prosperetti, A. (**1977b**). "Thermal effects and damping mechanisms in the forced radial oscillations of gas bubbles in liquids," J. Acoust. Soc. Am. **61**, 17-27.

Prosperetti, A., Crum, L. A., and Commander, K. W. (**1988**). "Nonlinear bubble dynamics," J. Acoust. Soc. Am. **83**, 502-514.

Prosperetti, A., and Lezzi, A. (**1986**). "Bubble dynamics in a compressible liquid. Part 1. First order theory," J. Fluid. Mech. **168**, 457-478.

Ramble, D. (**1997**). "Characterisation of bubbles in liquids using acoustic techniques," *PhD report* (ISVR).

Rayleigh, L. (**1917**). "On the pressure developed in a liquid during the collapse of a spherical cavity," Phil Mag, 94-98.

Reeburgh, W. S. (**1983**). "Rates of Biogeochemical Processes in Anoxic Sediments," Annual Rev. Earth Planetary Science 11, 269-298.

Reed, A. H., Boudreau, B. P., Alga, C., and Furukawa, Y. (**2005**). "Morphology of gas bubbles in mud: A microcomputed tomographic evaluation.," in *Proceedings of the First*

International Conference on Underwater Acoustic Measurements, Technologies and Results (Heraklion, Crete).

Reismann, H., and Pawlik, P. S. (**1980**). "Elasticity: theory and applications," (John Wiley & Sons, New York), pp 425.

Richardson, M. D., and Briggs, K. B. (**1996**). "In situ and laboratory geoacoustic measurements in soft mud and hard-packed sand sediments: Implications for high-frequency acoustic propagation and scattering.," Geo-Marine Letters **16**, 196-203.

Richardson, M. D., Briggs, K. B., Bibee, L. D., Jumars, P. A., Sawyer, W. B., Albert, D. B., Bennett, R. H., Berger, T. K., Buckingham, M. J., Chotiros, N. P., Dahl, P. H., Dewitt, N. T., Fleischer, P., Flood, R., Greenlaw, C. F., Holliday, D. V., Hulbert, M. H., Hutnak, M. P., Jackson, P. D., Jaffe, J. S., Johnson, H. P., Lavoie, D. L., A. P. Lyons, Martens, C. S., McGehee, D. E., Moore, K. D., Orsi, T. H., Piper, J. N., Ray, R. I., Reed, A. H., Self, R. F. L., Schmidt, J. L., Schock, S. G., Simonet, F., Stoll, R. D., Tang, D., Thistle, D. E., Thorsos, E. I., Walter, D. J., and Wheatcroft, R. A. (**2001**). "Overview of SAX99: Environmental Considerations," IEEE J. Ocean. Eng. **26**, 26-53.

Richardson, M. D., Curzsi, P. V., Muzi, E., Miaschi, B., and Barbagelata, A. (**1987**). "Measurement of shear wave velocity in marine sediments," in *Acoustics and ocean bottom* (Consejo Superior de Investigaciones Cientificas, Madrid), 75-84.

Robb, G. B. N., Best, A. I., Dix, J. K., Bull, J. M., Leighton, T. G., and White, P. R. (**2006a**). "The frequency dependence of compressional wave velocity and attenuation coefficient of intertidal marine sediments," J. Acoust. Soc. Am. **120**, 2526-2537.

Robb, G. B. N., Best, A. I., Dix, J. K., White, P. R., Leighton, T. G., Bull, J. M., and Harris, A. (**2007**). "Measurement of the In Situ Compressional Wave Properties of Marine Sediments," IEEE J. Oceanic Eng. **32**, 484-495.

Robb, G. B. N., Leighton, T. G., Dix, J. K., Best, A. I., V.F.Humpfrey, and White, P. R. (**2006b**). "Measuring bubble populations in gassy marine sedimens: A review," Proceedings of the Institute of Acoustics **28**, 60-68.

Robb, G. B. N., Leighton, T. G., Dix, J. K., Best, A. I., V.F.Humphrey, and White, P. R. (**2006c**). "Measuring bubble populations in gassy marine sediments: A review," Proceedings of the Institute of Acoustics **28**, 60-68.

Sarkar, K., and Prosperetti, A. (**1994**). "Coherent and incoherent scattering by oceanic bubbles," J. Acoust. Soc. Am. **96**, 332-341.

Schanz, M., and Cheng, A. H. D. (**2001**). "Dynamic Analysis of a One-Dimensional Poroviscoelastic Column," Transactions of ASME **68**, 192-198.

Schubel, J. R. (**1974**). "Gas bubbles and the acoustically impenetrable or turbid character of some estuarine sediments.," in *Natural Gases in Marine Sediments*, edited by I. R. Kaplan (Plenum, New York), 275-298.

Shepard, F. P. (**1954**). "Nomenclature based on sand-silt-clay ratios," J.Sediment. Pertology **24**, 151-158.

Shumway, G. (**1960a**). "Sound speed and absorption studies of marine sediment by a resonance method," Geophysics **25**, 451-467.

Shumway, G. (**1960b**). "Sound speed and absorption studies of marine sediment by a resonance method-Part II," Geophysics **25**, 659-681.

Silberman, E. (**1957**). "Sound Velocity and Attenuation in Bubbly Mixtures Measured in Standing Wave Tubes," J. Acoust. Soc. Am. **29**, 925-933.

Sinayoko, S., Joseph, P., and McAlpine, A. (**2009**). "Multimode radiation from an unflanged, semi-infinite circular duct with uniform flow," J. Acoust. Soc. Am. **127**, 2159-2168.

Spitzer, L. J. (**1943**). "Acoustic properties of gas bubbles in a liquid," in *NDRC 1705* (Division of War Research).

Stoll, R. D. (**1979**). "Experimental studies of attenuation in sediments," J. Acoust. Soc. Am. **66**, 1152-1160.

Stoll, R. D. (**1980**). "Theoretical aspects of sound transmission in sediments," J. Acoust. Soc. Am. **68**, 1341-1350.

Stoll, R. D. (**1983**). *Sediment Acoustics, Lecture Notes in Earth Science*, (Springer-Verlag, The Netherlands)

Stoll, R. D. (**1985**). "Marine sediment acoustics," J. Acoust. Soc. Am. **77**, 1789-1799.

Stoll, R. D. (**1991**). "Shear waves in marine sediments-Bridging the gap from theory to field applications," in *Acoustics and ocean bottom* (Consejo Superior de Investigaciones Cientificas, Madrid).

Stoll, R. D., and Bautista, E. O. (**1998**). "Using the Biot theory to establish a baseline geoacoustic model for seafoor sediments," Continental Shelf Research **18**, 1839-1857.

Stoll, R. D., and Bryan, G. M. (**1969**). "Wave attenuation in saturated sediments," J. Acoust. Soc. Am. **47**, 1440–1447.

Strasberg, M. (**1956**). "Gas Bubbles as Sources of Sound in Liquids," J. Acoust. Soc. Am. **28**, 20-26.

Strasburg, M. (**1953**). "The pulsation frequency of nonspherical gas bubbles in liquids," J. Acoust. Soc. Am. **25**, 536–537.

Sutin, A., Yoon, S., and, E. K., and Didenkulov, I. (**1998**). "Nonlinear acoustic method for bubble density measurements in water," J. Acoust. Soc. Am. **103**, 2377-2384.

Tang, D. (**1996**). "Modeling high-frequency backscattering from gas voids buried in sediments," Geo-Marine Letters **16**, 261-265.

Tegowski, J., Klusek, Z., and Jakaki, J. (**2006**). "Nonlinear acoustical methods in the detection of gassy sediments," in *Acoustic sensing techniques for the shallow water environment*, edited by A. Caiti, N. R. Chapman, J. P. Hermand, and S. M. Jesus (Springer Netherlands), pp. 125-136.

Terrill, E. J., and Melville, W. K. (**2000**). "A Broadband Acoustic Technique for Measuring Bubble Size Distributions: Laboratory and Shallow Water Measurements," J. Atmosph. Ocean. Tech. **17**, 220-240.

Thießen, O., Schmidt, M., Theilen, F., Schmitt, M., and Klein, G. (**2006**). "Methane formation and distribution of acoustic turbidity in organic-rich surface sediments in the Arkona Basin, Baltic Sea " Continental Shelf Research **26**, 2469-2483

Thorne, P. D., P.J.Hardcastle, and Soulby, R. L. (**1993**). "Analysis of acoustic measurements of suspended sediments," J. Geophys. Res. **98**, 899-910.

Tikhonov, A. N., and Arsenin, V. Y. (**1977**). *Solution of ill-posed problems* (John Wiley & Sons).

Tuffin, J. M. D. (**2001**). "Properties of shallow gas-bearing sediments," in *School of Ocean and Earth Sciences* (University of Southamton).

Turgut, A. and Yamamoto T. (**1990**). "Measurements of acoustic wave velocities and attenuations in marine sediment," J. Acoust. Soc. Am. **87**, 2376-2383.

Turgut, A. and Yamamoto T. (**2008**). "In situ measurements of velocity dispersion and attenuation in New Jersey Shelf sediments," J. Acoust. Soc. Am. EL **124**, 122-127.

Vagle, S., and Farmer, D. M. (**1992**). "The Measurement of Bubble-Size Distributions by Acoustical Backscatter," J. Atmosph.Ocean. Tech. **9**, 630-644.

Vokurka, K. (**1985**). "On Rayleigh's model of a freely oscillating bubble," Czech.J.Phys. **35**, 28-40.

Wadell, H. (**1935**). "Volume, Shape and Roundness of Quartz Particles," J. Geology **43**, 250-280.

Warrick, R. (**1974**). "Seismic investigation of a San Francisco Bay mud site," Bull. Seismol. Soc. Am. **64**, 375-385.

Wentworth, C. K. (**1922**). "A Scale of Grade and Class Terms for Clastic Sediments," The Journal of Geology **30**, 377-392.

Weston, D. E. (**1967**). "Sound propagation in the presence of bladder fish," in *Underwater Acoustics*, edited by V. M. Albers (Plenum, New York), 55-88.

Wever, T. F., Abegg, F., Fiedler, H. M., Fechner, G., and Stender, I. H. (**1998**). "Shallow gas in the muddy sediments of Eckernforde Bay, Germany," Continental Shelf Research **18,** 1715-1739.

Wheeler, S. J. (**1988**). "A conceptual model for soils containing large gas bubbles," Geotechnique **38**, 389-397.

Wheeler, S. J. (**1990**). "Movement of Large Gas Bubbles in Unsaturated Fine-Grained Sediments," Marine Geotechnology **9**, 113-129.

Whitehouse, R., Soulsby, R., Roberts, W., and Mitchener, H. (**2000**). *Dynamics of estuarine muds* (Thomas Telford Publishing).

Whorolow, R. W. (**1992**). *Rheological Techniques*. (Ellis Horwood, Chichester), pp. 460.

Wilkens, R. H., and Richardson, M. D. (**1998**). "The influence of gas bubbles on sediment acoustic properties: in situ, laboratory and theoretical results from Eckernforde Bay, Baltic sea," Continental Shelf Research **18**, 1859-1892.

Wingham, D. J. (**1985**). "The dispersion of sound in sediment," J. Acoust. Soc. Am **78** 1757-1760.

Wood, A. B., and Weston, D. E. (**1964**). "The Propagation of Sound in Mud," Acustica **14**, 156-162.

Yang, J., Tang, D., and Williams, K. L. (**2008**). "Direct measurement of sediment sound speed in ShallowWater '06," J. Acoust. Soc. Am. EL **124**, 116-121.

Yang, X., and Church, C. C. (**2005**). "A model for the dynamics of gas bubbles in soft tissue," J. Acoust. Soc. Am. **118**, 3595-3606.

Zabolotskaya, E. A., and Soluyan, S. I. (**1967**). "A possible approach to the amplification of sound waves.," Sov.Phys.Acoust. **13**, 254-256.

A. Appendix A: Asymptotic solutions of the Rayleigh-Plesset equation

The aim is to obtain expressions for the amplitudes and phases of the various frequency components which describe the radial bubble wall displacements under a two frequency insonification. The analysis begins with the general case of two insofication waves and proceeds with the examination of special cases in order to cross check with the works of Newhouse and Shankar (1985) and Miller (1981). To obtain the desired expressions, series of simultaneous equations are constructed by substituting the bubble radius in the form of equation (2.12) into the low-amplitude expansion of the Rayleigh-Plesset equation (2.10). The dimensionless variable x is assumed much smaller than unity and it is approximated with the asymptotic series expansion:

$$\begin{aligned} x = {} & A_0 + A_1\cos(\omega_1 t) + B_1\sin(\omega_1 t) \\ & + A_2\cos(\omega_2 t) + B_2\sin(\omega_2 t) \\ & + A_3\cos(2\omega_1 t) + B_3\sin(2\omega_1 t) \\ & + A_4\cos(2\omega_2 t) + B_4\sin(2\omega_2 t) \\ & + A_5\cos((\omega_1+\omega_2)t) + B_5\sin((\omega_1+\omega_2)t) \\ & + A_6\cos((\omega_1-\omega_2)t) + B_6\sin((\omega_1-\omega_2)t) \end{aligned} \qquad \text{(A.1)}$$

The amplitudes of the sine harmonic terms are of the same order of magnitude with the corresponding cosine terms, i.e. $O(A_1) = O(B_1)$ and $O(A_2) = O(B_2)$ etc., and considered to converge as follows:

$$A_1, B_1, A_2, B_2 > A_0 > A_3, B_3, A_4, B_4 > A_5, B_5, A_6, B_6 \qquad \text{(A.2)}$$

Each frequency component of x, which consists of a pair of sin and cosine terms (A.1), can be converted to a single term using amplitude and phase representation (equation (2.16)) through [9]:

$$A_{\omega_n} = \sqrt{A_n^2 + B_n^2} \qquad \text{(A.3)}$$

and

$$\phi_{\omega_n} = \tan^{-1} - \left(\frac{B_n}{A_n}\right). \qquad \text{(A.4)}$$

[9] Every $A_n\cos\omega_n t + B_n\sin\omega_n t$ pair must equal to $A_{\omega n}\cos(\omega_n t+\phi_{\omega n}) = A_{\omega n}\cos\omega_n t\sin\phi_{\omega n} - A_{\omega n}\sin\omega_n t\cos\phi_{\omega n}$. Then $A_n = A_{\omega n}\sin\phi_{\omega n}$ and $B_n = -A_{\omega n}\cos\phi_{\omega n}$, which gives equations (A.3) and (A.4). Note there is a sign ambiguity in the phase due to the inversion of the tangent.

The mathematic manipulations are facilitated if the Rayleigh-Plesset equation in terms of x, as given by equation (2.10), is written, as:

$$C_0\,\ddot{x}+C_0\,\ddot{x}\,x+C_1\,\dot{x}^2+(C_3-C_5)x-\left(C_4-C_5\right)x^2+C_6\,\dot{x}+C_6\,\dot{x}\,x+P(t)=0 \tag{A.5}$$

where:

$$C_0=\rho_0 R_0^2\,, \tag{A.6}$$

$$C_3=3\kappa\left(p_0+\frac{2\sigma}{R_0}-p_{\mathrm{v}}\right)$$

$$C_4=\frac{3}{2}\kappa\left(3\kappa+1\right)\left(p_0+\frac{2\sigma}{R_0}-p_{\mathrm{v}}\right),$$

$$C_5=\frac{2\sigma}{R_0}\text{, and}$$

$$C_6=4\eta$$

The applied pressure field is assumed to be the sum of two sinusoidal waves which have initially the same phase. Thus it can be written in the following form:

$$P(t)=P_1\cos\omega_1 t+P_2\cos\left(\omega_2 t+\psi\right)\,. \tag{A.7}$$

The analytic solutions were obtained by the following procedure:

- substitution of equation (A.1) and (A.7) into equation (A.5); then
- grouping the terms having the same harmonic components; then
- equating the terms having the same coefficients to the right part of equation (A.6) to zero; then
- solving the homogenous system of equations.

The contribution of each term to the corresponding harmonic component is listed in table A.1. We are interested in a solution of second order therefore, as follows from the relationship (A.2); the following terms should be retained:

$$A_0, A_1, B_1, A_2, B_2, A_3, B_3, A_4, B_4, A_5, B_5, A_6, B_6, A_1B_1, A_2B_2, A_1B_2, A_2B_1, A_1^2, B_1^2, A_2^2, B_2^2$$

The resulting system must have a nonzero solution, therefore all the coefficients of the polynomial that correspond to harmonics of the bubble pulsation must equal zero. This procedure is demonstrated in the following paragraphs where the results of Miller (1981) and Newhouse and Shankar (1984) are reproduced.

Table A.1

	$\ddot{x}$	$\ddot{x}x$	$\dot{x}^2$	x	x^2	$\dot{x}$	$\dot{x}x$
coefficients:	C_0	C_0	C_1	$C_3 - C_5$	$C_4 - C_5$	C_6	C_6
DC	0	$-\frac{1}{2}(A_1^2 + B_1^2)\omega_1^2$ $-\frac{1}{2}(A_2^2 + B_2^2)\omega_2^2$	$\frac{1}{2}(A_1^2 + B_1^2)\omega_1^2$ $+\frac{1}{2}(A_2^2 + B_2^2)\omega_2^2$	A_0	$\frac{1}{2}(A_1^2 + B_1^2)$ $+\frac{1}{2}(A_2^2 + B_2^2)$	0	0
$\cos(\omega_1 t)$	$-A_1\omega_1^2$	0	0	A_1	0	$B_1\omega_1$	0
$\sin(\omega_1 t)$	$-B_1\omega_1^2$	0	0	B_1	0	$-A_1\omega_1$	0
$\cos(\omega_2 t)$	$-A_2\omega_2^2$	0	0	A_2	0	$B_2\omega_2$	0
$\sin(\omega_2 t)$	$-B_2\omega_2^2$	0	0	B_2	0	$-A_2\omega_2$	0
$\cos(2\omega_1 t)$	$-4A_3\omega_1^2$	$-\frac{1}{2}\omega_1^2(A_1 - B_1)(A_1 + B_1)$	$-\frac{1}{2}\omega_1^2(A_1 - B_1)(A_1 + B_1)$	A_3	$\frac{1}{2}(A_1 - B_1)(A_1 + B_1)$	$2B_3\omega_1$	$A_1B_1\omega_1$
$\sin(2\omega_1 t)$	$-4B_3\omega_1^2$	$-A_1B_1\omega_1^2$	$-A_1B_1\omega_1^2$	B_3	A_1B_1	$-2A_3\omega_1$	$-\frac{1}{2}\omega_1(A_1 - B_1)(A_1 + B_1)$
$\cos(2\omega_2 t)$	$-4A_4\omega_2^2$	$-\frac{1}{2}\omega_2^2(A_2 - B_2)(A_2 + B_2)$	$-\frac{1}{2}\omega_2^2(A_2 - B_2)(A_2 + B_2)$	A_4	$\frac{1}{2}(A_2 - B_2)(A_2 + B_2)$	$2B_4\omega_2$	$A_2B_2\omega_2$
$\sin(2\omega_2 t)$	$-4B_4\omega_2^2$	$-A_2B_2\omega_2^2$	$-A_2B_2\omega_2^2$	B_4	A_2B_2	$-2A_4\omega_2$	$\frac{1}{2}\omega_2(B_2 - A_2)(B_2 + A_2)$
$\cos(\omega_1 + \omega_2)t$	$-A_5(\omega_1 + \omega_2)^2$	$-\frac{1}{2}(\omega_1^2 + \omega_2^2)(A_1A_2 - B_1B_2)$	$-\omega_2\omega_1(A_1A_2 - B_1B_2)$	A_5	$A_1A_2 - B_2B_1$	$B_5(\omega_1 + \omega_2)$	$\frac{1}{2}(\omega_1 + \omega_2)(A_2B_1 + A_1B_2)$
$\sin(\omega_1 + \omega_2)t$	$-B_5(\omega_1 + \omega_2)^2$	$-\frac{1}{2}(\omega_1^2 + \omega_2^2)(A_1B_2 + A_2B_1)$	$-\omega_2\omega_1(A_1B_2 + A_2B_1)$	B_5	$A_1B_2 - A_2B_1$	$-A_5(\omega_1 + \omega_2)$	$\frac{1}{2}(\omega_1 + \omega_2)(B_1B_2 - A_1A_2)$

Table A.1 (continued)

	$\ddot{x}$	$\ddot{x}x$	$\dot{x}^2$	x	x^2	$\dot{x}$	$\dot{x}x$
coefficients:	C_0	C_0	C_1	$C_4 - C_5$	$C_4 - C_5$	C_6	C_6
$\cos(\omega_1 - \omega_2)t$	$-A_6(\omega_1 - \omega_2)^2$	$-\frac{1}{2}(\omega_1^2 + \omega_2^2)(A_1A_2 + B_1B_2)$	$\omega_2\omega_1(A_1A_2 + B_2B_1)$	A_6	$A_1A_2 + B_2B_1$	$B_6(\omega_1 - \omega_2)$	$\frac{1}{2}(\omega_1 - \omega_2)(A_2B_1 - A_1B_2)$
$\sin(\omega_1 - \omega_2)t$	$-B_6(\omega_1 - \omega_2)^2$	$-\frac{1}{2}(\omega_1^2 + \omega_2^2)(A_2B_1 - A_1B_2)$	$\omega_2\omega_1(A_2B_1 - A_1B_2)$	B_6	$-A_1B_2 + A_2B_1$	$-A_6(\omega_1 - \omega_2)$	$-\frac{1}{2}(\omega_1 - \omega_2)(B_1B_2 + A_1A_2)$

A.1 Analytical solutions for single frequency insonification

The analytical solutions for the case of single-frequency insonification $P(t) = P_1 \cos \omega_1 t$, are obtained with the above mentioned procedure by retaining the terms of equation (A.1) with coefficients $A_0, A_1, B_1, A_3, B_3, A_1B_1, A_1^2, B_1^2$ whilst setting the others equal to zero. Thus in this case the only relevant rows of the table A.1 are the 1st, 2nd , 3rd , 6th and 7th. To obtain the first harmonic component from the table A.1, the 2nd and 3rd row are multiplied with the corresponding coefficient. The resulting set of equations with unknowns A_1 and B_1 is:

$$\left(-C_0\omega_1^2 + (C_3 - C_5)\right) A_1 + C_6\omega_1 B_1 + P_1 = 0 \ , \tag{A.8}$$

$$\left(-\omega_1 C_6\right) A_1 + \left(-C_0\omega_1^2 + (C_3 - C_5)\right) B_1 = 0 \ . \tag{A.9}$$

which can be written in matrix formulation as:

$$\begin{bmatrix} a_1 & b_1 \\ -b_1 & a_1 \end{bmatrix} \begin{bmatrix} A_1 \\ B_1 \end{bmatrix} = \begin{bmatrix} -P_1 \\ 0 \end{bmatrix} \tag{A.10}$$

where

$$a_1 = -C_0\omega_1^2 + (C_3 - C_5), \tag{A.11}$$

and

$$b_1 = C_6\omega_1 . \tag{A.12}$$

The system is solved by matrix inversion and yields:

$$\begin{bmatrix} A_1 \\ B_1 \end{bmatrix} = \begin{bmatrix} \dfrac{a_1}{a_1^2 + b_1^2} & -\dfrac{b_1}{a_1^2 + b_1^2} \\ \dfrac{b_1}{a_1^2 + b_1^2} & \dfrac{a_1}{a_1^2 + b_1^2} \end{bmatrix} \begin{bmatrix} -P_1 \\ 0 \end{bmatrix}. \tag{A.13}$$

Using (A.13), the amplitudes of the first harmonic components are:

$$A_1 = -\frac{a_1}{a_1^2 + b_1^2} P_1 \tag{A.14}$$

and

$$B_1 = -\frac{b_1}{a_1^2 + b_1^2} P_1 . \tag{A.15}$$

The equivalent representation of the first harmonic in terms of amplitude and phase information (equation (2.15)) is obtained through the relationships

$$A_{\omega 1} = \sqrt{A_1^2 + B_1^2} \tag{A.16}$$

and

$$\phi_{\omega 1} = \tan^{-1} - \left(\frac{B_1}{A_1} \right). \tag{A.17}$$

Substitution of (A.14) and (A.15) into (A.16) yields:

$$A_{\omega 1} = \sqrt{A_1^2 + B_1^2} \Rightarrow A_{\omega 1} = \frac{P_1}{\sqrt{a_1^2 + b_1^2}} = \frac{P_1}{\sqrt{\left(-C_0 \omega_1^2 + (C_3 - C_5)\right)^2 + \left(C_6 \omega_1\right)^2}}, \tag{A.18}$$

Observing that $\omega_0^2 = \frac{C_3 - C_5}{C_0}$, see also equation (2.19), equation (A.18) can be written in the alternative form (equation (2.28)):

$$A_{\omega 1} = \frac{P_1}{\rho_0 R_0^2 \sqrt{\left(\omega_0^2 - \omega_1^2\right)^2 + \left(2\beta_{\text{vis}} \omega_1\right)^2}}, \tag{A.19}$$

where β_{vis} is as defined with (2.24).

If a normalised damping parameter is defined as:

$$\delta_n = \frac{C_6}{\omega_0 C_0} \tag{A.20}$$

and a normalised insonification frequency as:

$$\Omega_1 = \frac{\omega_1}{\omega_0}, \tag{A.21}$$

then equation (A.19) can be written in the manner appearing in the paper of Miller (1981) by replacing the damping and natural frequency expressions with their normalised counter parts:

$$A_{\omega 1} = \frac{P_1}{\rho_0 R_0^2 \omega_0^2 \sqrt{(1-\Omega_1^2)^2 + \delta_n^2 \Omega_1^2}}. \tag{A.22}$$

The phase information is obtained through substitution of (A.14) and (A.15) in (A.17). After some manipulation we obtain:

$$\tan \phi_{\omega 1} = -\frac{2\beta_{vis}}{\omega_0^2 - \omega_1^2}. \tag{A.23}$$

The expression for the second harmonic term is obtained via repeating the procedure outlined above for the 6th and 7th rows. The resulting set of equations with unknowns A_3 and B_3 is:

$$\left(-4\omega_1^2 C_0 + (C_3 - C_5)\right) A_3 + C_6 \omega_1 B_3 + Z = 0 \ , \tag{A.24}$$

$$\left(-2\omega_1 C_6\right) A_3 + \left(-4\omega_1^2 C_0 + (C_3 - C_5)\right) B_3 + Q = 0 \ , \tag{A.25}$$

where the auxiliary variables Z and Q equal

$$Z = -\frac{1}{2}\omega_1^2 \left(A_1 - B_1\right)^2 \left(C_0 + C_1\right) + \frac{1}{2}\left(A_1 - B_1\right)^2 \left(C_4 - C_5\right) \tag{A.26}$$

and

$$Q = -A_1 B_1 \omega_1^2 \left(C_0 + C_1\right) \text{ respectively.} \tag{A.27}$$

Equations (A.24) and (A.25) form a system with unknowns the A_3 and B_3. Repeating the matrix inversion method for this set of equations results in the following expression for A_3 and B_3;

$$A_3 = -\frac{a_3}{{a_3}^2 + {b_3}^2} Z + \frac{b_3}{{a_3}^2 + {b_3}^2} Q \tag{A.28}$$

and

$$B_3 = -\frac{b_3}{{a_3}^2 + {b_3}^2} P_1 - \frac{a_3}{{a_3}^2 + {b_3}^2} Q \tag{A.29}$$

where

$$a_3 = -4\omega_1^2 C_0 + (C_3 - C_5) \ , \tag{A.30}$$

and

$$b_3 = 2\omega_1 C_6 . \tag{A.31}$$

To find an amplitude phase representation for this harmonic (A.28) and (A.29) are substituted in (according to the general expression (A.3)):

$$A_{2\omega 1} = \sqrt{A_3^2 + B_3^2} \tag{A.32}$$

which after some manipulation gives:

$$A_{2\omega 1} = \frac{1}{2} A_{\omega 1}^2 \sqrt{\frac{\left(2.5\omega_1^2 \rho_0 R_0^2 + 1.5\kappa(3\kappa+1)\left(p_0 + \frac{2\sigma}{R_0} - p_v\right) - \frac{4\sigma}{R_0}\right)^2 + \left(2\beta_{vis}\omega_1\right)^2}{\left(\left(\rho_0 R_0^2\right)^2 \left(\omega_0^2 - 4\omega_1^2\right)^2 + \left(4\beta_{vis}\omega_1\right)^2\right)}} \tag{A.33}$$

Using as previously the concepts of normalised damping constant and frequency, the resulting expression for the second harmonic amplitude is:

$$A_{2\omega 1} = \frac{1}{2} A_{\omega 1}^2 \sqrt{\frac{\left(\frac{2.5\Omega_1^2 + 1.5\kappa(3\kappa+1)(p_0 + 2\sigma/R_0 - p_v) - 4\sigma/R_0}{2\omega_0^2 \rho_0 R_0^2}\right)^2 + \delta_n^2 \Omega_1^2}{\left(\left(1 - 4\Omega_1^2\right)^2 + 4\delta_n^2 \Omega_1^2\right)}} \tag{A.34}$$

and the phase information can be found from:

$$\phi_{2\omega 1} = \tan^{-1} - \left(\frac{B_3}{A_3}\right). \tag{A.35}$$

The expression for the DC term is obtained from the first row of the table A.1 as function of the first harmonic amplitudes:

$$A_0 = \frac{A_{\omega 1}^2}{2\omega_0^2 \rho_0 R_0^2}\left[\left(\frac{1}{2}\rho_0\omega_0^2 R_0^2 - \frac{1}{4}\rho_0\omega_1^2 R_0^2\right) + \frac{9\kappa^2}{2}\left(p_0 + \frac{2\sigma}{R_0} - p_v\right) - \frac{2\sigma}{R_0}\right] \quad \text{(A.36)}$$

A.2 Analytical solutions for two frequency insonification

Analytical solutions for bubble pulsation under a two frequency insonification ω_1 and ω_2 can be found using table A.1 and the method outlined in section A.1. The harmonic components at ω_1 and $2\omega_1$ have a similar form with those at ω_2 and $2\omega_2$ respectively. This is observed from the similarity between the 2nd and 3rd row with 4th and 5th rows and between the 6th and 7th rows with 8th and 9th rows. For example, the amplitude of the harmonic at ω_2 is found from the 4th and 5th rows of the table A.1, with the procedure followed for the derivation of the harmonic at ω_1 when single frequency insonification was considered. The corresponding system of equations is:

$$\left(-C_0\omega_2^2 + (C_3 - C_5)\right)A_2 + C_6\omega_2 B_2 + P_2 = 0 \ , \quad \text{(A.37)}$$

$$\left(-\omega_2 C_6\right)A_2 + \left(-C_0\omega_2^2 + (C_3 - C_5)\right)B_2 = 0 \ . \quad \text{(A.38)}$$

where:

$$a_2 = \left(-C_0\omega_2^2 + (C_3 - C_5)\right) \quad \text{(A.39)}$$

and

$$b_2 = C_6\omega_2 \ . \quad \text{(A.40)}$$

Application of the matrix inversion method to solve the system of equations (A.37) and (A.38) results in:

$$A_2 = -\frac{a_2}{a_2^{\,2} + b_2^{\,2}}P_2 \quad \text{(A.41)}$$

$$B_2 = -\frac{b_2}{a_2^2 + b_2^2}P_2$$

In line with the derivation of the harmonic component of x at ω_1, the amplitude corresponding to the second drive frequency is:

$$A_{\omega 2} = \frac{P_1}{\rho_0 R_0^2 \omega_0^2 \sqrt{(1-\Omega_2^2)^2 + \delta_n^2 \Omega_2^2}}, \tag{A.42}$$

where Ω_2 is the normalised second frequency:

$$\Omega_2 = \frac{\omega_2}{\omega_0} \tag{A.43}$$

The phase information is obtained through the relationship (A.4):

$$\tan\phi_{\omega_2} = -\frac{\dfrac{2\beta_{vis}}{\omega_0^2 - \omega_2^2} + \tan\psi}{\dfrac{2\beta_{vis}}{\omega_0^2 - \omega_2^2}\tan\psi - 1}. \tag{A.44}$$

The harmonics at $\omega_1 - \omega_2$ and $\omega_1 + \omega_2$ result from the interaction of the two insonifing fields. The component at difference frequency which is of major importance for this work, is found from the last two rows for table A.1. The expression for the amplitude of the difference frequency harmonic is:

$$A_{\omega-} = \frac{\sqrt{\left(B_2^2 + A_2^2\right)\left(A_1^2 + B_1^2\right)}}{\sqrt{a_{1-2}^2 + b_{1-2}^2}}\left(\left(\frac{1}{2}\left(\omega_1^2 + \omega_2^2\right)C_0 - \omega_2\omega_1 C_1 + \left(C_4 - C_5\right)\right)^2 + \left(\frac{1}{2}\left(\omega_1 - \omega_2\right)C_6\right)^2\right)^{1/2} \tag{A.45}$$

,

where:

$$a_{1-2} = \left(-C_0\left(\omega_1 - \omega_2\right)^2 + \left(C_3 - C_5\right)\right) \tag{A.46}$$

and

$$b_{1-2} = C_6\left(\omega_1 - \omega_2\right) \tag{A.47}$$

or in a more compact form:

$$A_{\omega-}=\frac{A_{\omega 1}A_{\omega 2}}{\sqrt{\left(\omega_0^2-(\omega_1-\omega_2)^2\right)^2+\left(2\beta_{\text{vis}}(\omega_1-\omega_2)\right)^2}}$$
$$\sqrt{\left(\frac{1}{2}\left(\omega_1^2+\omega_2^2\right)-\frac{3}{2}\omega_2\omega_1+\frac{\frac{3}{2}\kappa(3\kappa+1)\left(p_0+\frac{2\sigma}{R_0}-p_{\text{v}}\right)-\frac{2\sigma}{R_0}}{\rho_0 R_0^2}\right)^2+\left((\omega_1-\omega_2)^2\,4\beta_{\text{vis}}^2\right)} \quad \text{(A.48)}$$

After some manipulation of equation (A.48) the form of the dimensionless amplitude $A_{\omega-}$ becomes:

$$A_{\omega-}=\frac{A_{\omega 1}A_{\omega 2}}{\sqrt{(1-\Omega_-{}^2)^2+\delta_{\text{n}}^2\Omega_-{}^2}}$$
$$\sqrt{\left(\frac{\left(\Omega_1^2+\Omega_2^2\right)}{2}-\frac{3}{2}\Omega_1\Omega_2+\frac{3\kappa(3\kappa+1)\left(p_0+\frac{2\sigma}{R_0}\right)-\frac{4\sigma}{R_0}}{2\rho R_0^2\omega_0^2}\right)^2+\frac{\delta_{\text{n}}^2}{4}\Omega_-^2} \quad \text{(A.49)}$$

where the normalized angular frequency Ω_- is defined as:

$$\Omega_-=\frac{\omega_1-\omega_2}{\omega_0}. \quad \text{(A.50)}$$

Equations (A.42) and (A.49) are equations 10 and 15 as appear on the paper of Newhouse and Shankar (1984). The phase of this component found from:

$$\phi_-=\tan^{-1}-\left(\frac{B_6}{A_6}\right) \quad \text{(A.51)}$$

which after substitution of A_6 and B_6 rearrangement of the terms is can be written as:

$$\tan\phi_-=-\frac{(1+\theta)}{(1-\theta)}, \quad \text{(A.52)}$$

where the ancillary parameter θ equals:

$$\theta = \frac{2\beta_{\text{vis}}\frac{\omega_1-\omega_2}{\omega_0}\left(\tan\psi\left(\frac{\omega_1^2+\omega_2^2}{\omega_0^2}-3\frac{\omega_2\omega_1}{\omega_0^2}+\frac{3\kappa(3\kappa+1)\left(p_0+\frac{2\sigma}{R_0}-p_{\text{v}}\right)-\frac{4\sigma}{R_0}}{2\rho_0 R_0^2\omega_0^2}\right)+2\beta_{\text{vis}}\frac{\omega_1-\omega_2}{\omega_0}\right)}{\left(1-\left(\frac{\omega_1-\omega_2}{\omega_0}\right)^2\right)\left(\left(\frac{\omega_1^2+\omega_2^2}{\omega_0^2}-3\frac{\omega_2\omega_1}{\omega_0^2}+\frac{3\kappa(3\kappa+1)\left(p_0+\frac{2\sigma}{R_0}-p_{\text{v}}\right)-\frac{4\sigma}{R_0}}{2\rho_0 R_0^2\omega_0^2}\right)-2\beta_{\text{vis}}\frac{\omega_1-\omega_2}{\omega_0}\tan\psi\right)}$$

(A.53)

.

B. Appendix B: Beam patterns of low frequency device.

Here the calibrated directivity of the low frequency transducer is compared with simulation results to estimate the accuracy of the numerical code used for beam pattern calculations. The comparison is carried out for three frequencies: 30 kHz, 60 kHz and 90 kHz.

B.1 Directivities at 30 kHz

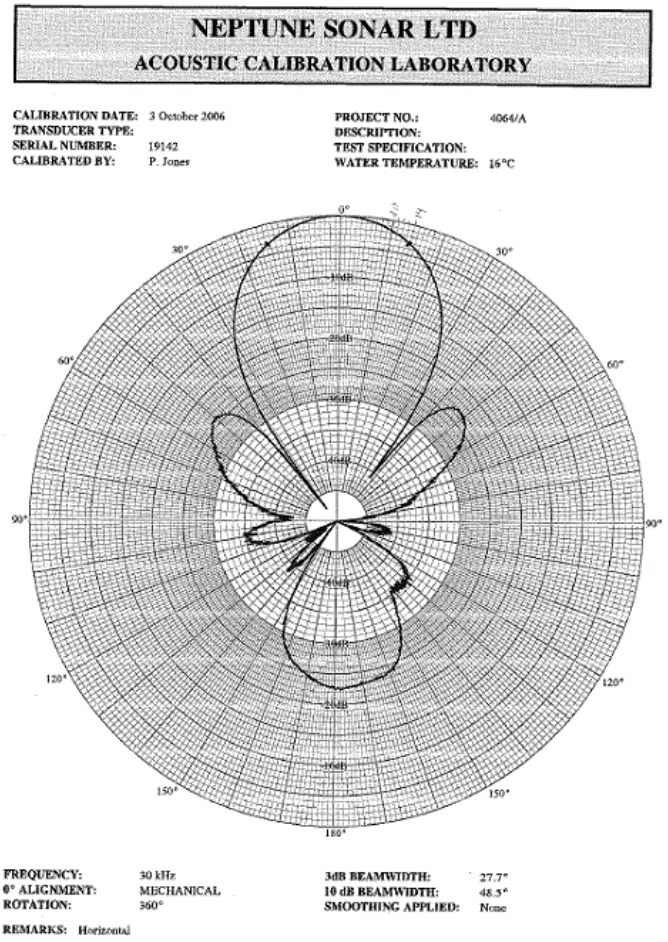

Figure B.1: Calibrated beam pattern at 30 kHz.

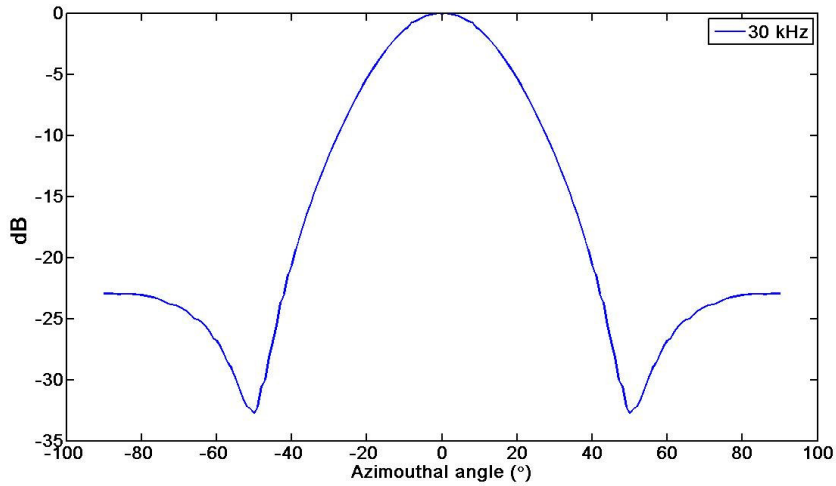

Figure B.2: Beam directivity at 30 kHz, as computed with Matlab

B.2 Directivities at 60 kHz

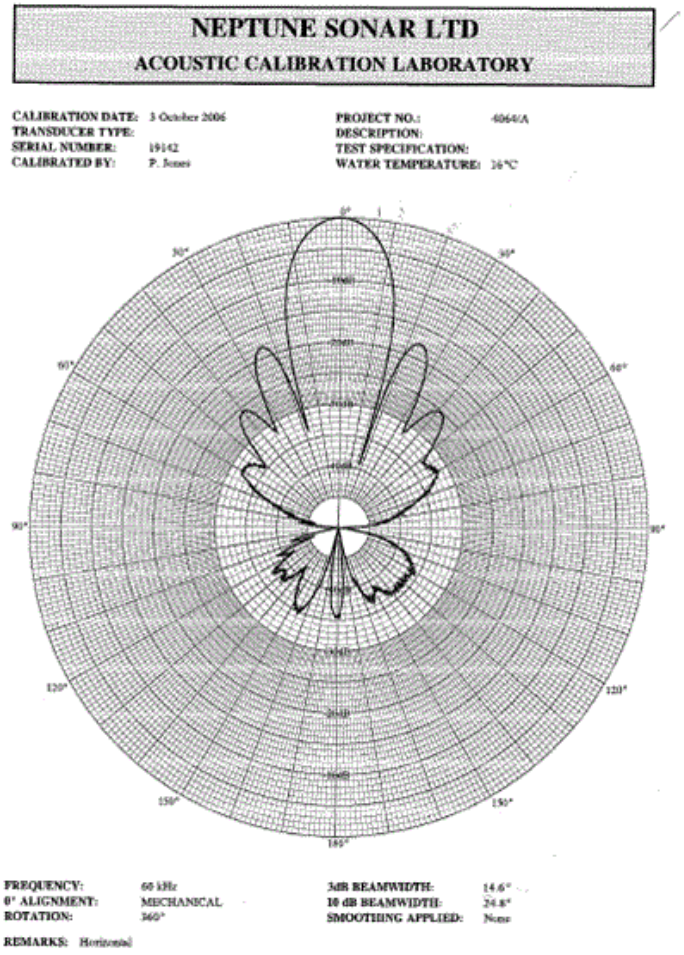

Figure B.3: Calibrated beam pattern at 60 kHz.

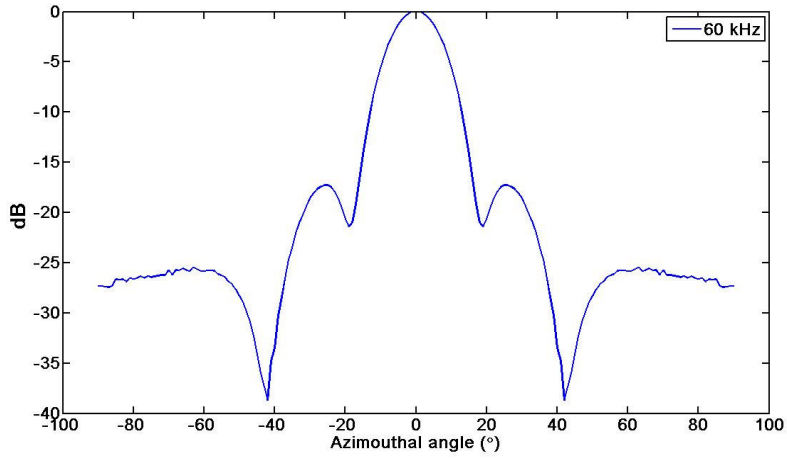

Figure B.4: Beam directivity at 60 kHz, as computed with matlab

B.3 Directivities at 90 kHz

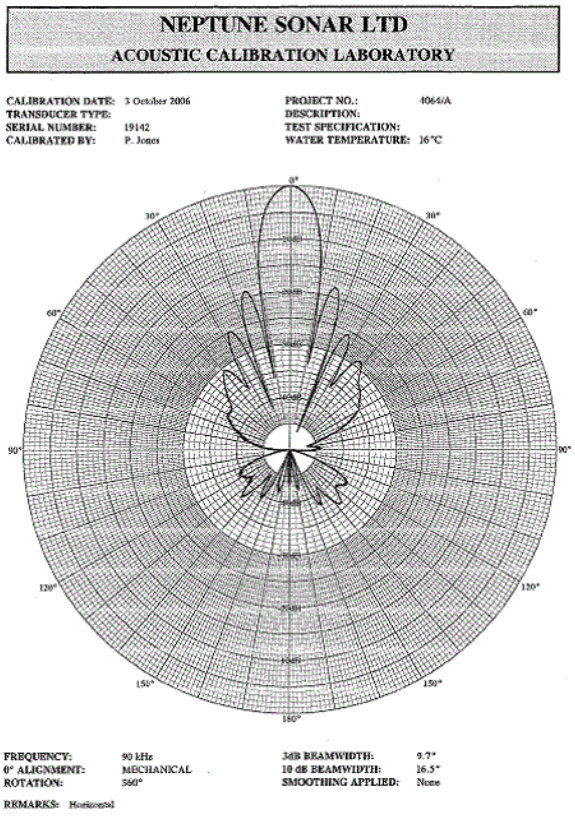

Figure B.5: Calibrated beam pattern at 60 kHz.

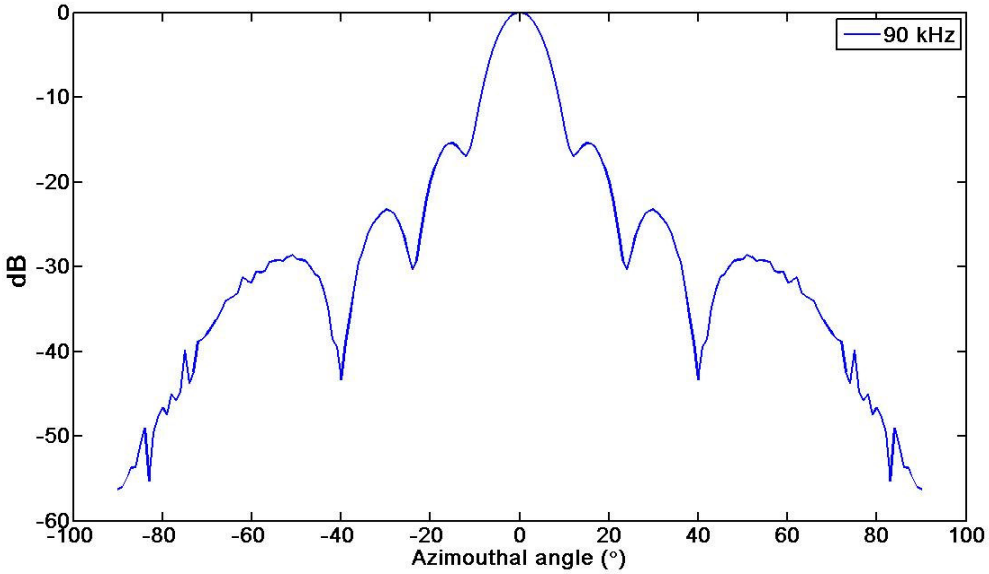

Figure B.6: Beam directivity at 90 kHz, as computed with matlab